


Doctoral Dissertation
Doctoral Program in Electrical, Electronic and Communication Engineering
(33^{rd} cycle)

Generalized Sensorless and Advanced Control of Synchronous Reluctance Machines

Anantaram Varatharajan

* * * * * *

Supervisor
Prof. Gianmario Pellegrino

Doctoral Examination Committee:
Prof. Fernando Briz, Referee, University of Oviedo, Spain
Prof. Roberto Petrella, Referee, University of Udine, Italy
Prof. Seung-Ki Sul, Seoul National University, South Korea
Prof. Marko Hinkkanen, Aalto University, Finland
Prof. Paolo Guglielmi, Politecnico di Torino, Italy

Politecnico di Torino
January 22, 2021

I hereby declare that, the contents and organisation of this dissertation constitute my own original work and does not compromise in any way the rights of third parties, including those relating to the security of personal data.

. . . . . .

Anantaram Varatharajan
Turin, January 22, 2021

Summary

For their higher efficiency and power density, the synchronous machines have become prominent in variable-speed-drives (VSD). In keeping with the growing energy-efficiency standards and high-performance requirements, research on the control of motor drives have sought to push the boundaries, in synergy with the advancements in motor design and semiconductors. Within the scope of control of synchronous machines, this work focuses of three aspects, namely: *(i)* Sensorless control; *(ii)* Self-Commissioning and *(iii)* Direct Flux Vector Control (DFVC).

Sensorless control is pursued for cost reduction, reliability and redundancy. A generalized projection vector framework is developed for design and analysis of the flux observer-based position estimation techniques. A few known sensorless schemes in literature are reviewed within the projection vector framework to identify regions of instability. Following, a new auxiliary-flux position observer (AUX) is designed for stable operation. A main contribution is the development of adaptive projection vector for position error estimation (APP) scheme that has a unique property of stator resistance immunity for operating points on the maximum-torque-per-ampere (MTPA) trajectory. Concurrent with the position estimation, the feasibility of speed error estimation and parameter adaptation are explored. A novel model-based torque control strategy is designed with APP position observer for accurate torque control under parameter errors. In addition to the work on fundamental back-emf based sensorless control techniques, an injection-less sensorless control scheme is investigated for operations at zero to low speeds region.

Given the nonlinearity of the magnetic model of synchronous machines, it becomes imperative to have an accurate flux-map for optimal operations as well as stable sensorless control. To this end, the self-commissioning involves identification of magnetic model without a dedicated lab environment. Two self-commissioning techniques for synchronous reluctance (SyR) machines are discussed of which one is a sensorless variant at standstill condition while the other uses position transducer at free-shaft for alternating acceleration-deceleration.

Thirdly, the DFVC is explored as a high-performance control strategy, particularly for its ease of operation in flux-weakening regions. With respect to the state-of-art, an accurate model of control dynamics in stator flux oriented reference frame is developed accounting for the magnetic saturation. The proposed nonlinear

decoupling is shown to achieve higher bandwidths for a uniform performance at all operating points. In addition, a new small-signal model based optimal reference generation is designed with stator flux magnitude and load angle as the controlled variables that permits operation at the MTPV limit and thus, exploiting the extremums of the speed-torque characteristics. All proposed schemes are supported with experimental validation.

Acknowledgements

I have been fortunate that a great many things conspired together for the successful completion of my PhD.

I wish to express my gratitude to Prof. Gianmario Pellegrino for his faith in me, for the ceaseless inspiration and encouragement, and for entertaining my whims and fancies. It is very rewarding to have a mentor and a friend in one's supervisor. Thank you Jimmy!

The realization of experimental results would have been far from easy without the magic touch of Prof. Eric Armando. I'm thankful to Dr. Paolo Pescetto for I stood on his shoulders, and helped jump-start my work. My gratitude to the fellow colleagues and friends, Fabio, Stefano, Simone, Fausto, Sandro, Davide and Matteo, for keeping the air light and jovial. The collaboration with Prof. Marko Hinkkannen of Aalto University has been very enriching, both technical and otherwise.

The last words I wish to dedicate to my family, for the perseverance of my father Varatharajan and the boundless compassion of my sister Niketana. Finally, my mother Savithri, whatever little I have accomplished is squarely on her account.

Contents

List of Tables

List of Figures

Chapter 1

Introduction

This manuscript describes and discusses the research and development that transpired during the three years of PhD program from 1 November 2017 to 31 October 2020 at the Power Electronics Innovation Center (PEIC), Politecnico di Torino. The title **Generalized Sensorless and Advanced Control of Synchronous Reluctance Machines** summarizes the research's findings in the fields of adaptive and sensorless control, identification, and the advancements in mathematical modeling and control of synchronous machines.

1.1 Background and Significance

Presently, the electric motor systems account for the single largest global energy consumption of around 40% which is more than twice as much as the second largest, lighting. Within the industrial section, it represents about 70% of the electricity consumption with pumps, fans and compressors among the most important loads. The motors of size 0.75 kW to 375 kW comprise of 10% of the deployed stock and account for 68% of the electricity consumed [1]–[6].

In the wake of global warming and climate change, the United Nation Environment Program foresees a reduction in the global electricity demand by 20% to 30% by 2030 with a transition to energy-efficient motor systems [5]. As the lifetime of motors is about 20 years or more, it becomes imperative to emphasize and steer the research as well as the global environmental policies towards high-efficiency motor drives. Following the energy crisis in 1970's, a concerted effort was put to promote variable-speed-drives (VSD) to reduce power losses. The steady diffusion of VSD, AC drives in particular, into the market have been further aided by policy mandates for the use of energy-efficient products.

The International Electrotechnical Commission (IEC) published the standard IEC 60034-30-1 [7] on March 6, 2014, for global harmonization of energy-efficiency classes of electric motors. As a function of rated power output, the normative

efficiency classes defined are: Standard Efficiency (IE1), High Efficiency (IE2), Premium Efficiency (IE3), Super-Premium Efficiency (IE4) and Ultra-Premium Efficiency (IE5). The testing methods to assess the motor efficiency are specified in standard IEC 60034-2-1 and for the converter-fed VSD in standard IEC 60034-2-3. Minimum energy performance standard (MEPS) are regulations that prescribe the efficiency class of motors that can be sold in a market. MEPS vary by countries and regions, dictated by the local markets and policy makers. Since January 1, 2017, European Union (EU) MEPS has mandated IE3 as the minimum efficiency class for motors with rated output 0.75 kW to 375 kW. A concession of class IE2 is granted for VSD to encourage its proliferation. The efficiency regulations are expected to get further stringent in the future.

For their ruggedness, simplicity and the direct on-line grid connectivity, the asynchronous squirrel-cage induction motors (IM) are a popular workhorse since late 19^{th} century and hold more than 80% of the global market share. They have long been the bastion in fixed speed applications where they are expected to continue their reign. However, in converter-fed variable speed applications, the permanent magnet (PM) and synchronous reluctance (SyR) machines offer a better alternative to IM in terms of power density and efficiency [8], [9]. Besides, the SyR and interior permanent magnet (IPM) machines are more conducive to closed-loop sensorless control due to the saliency of the anisotropic rotor [10].

Pertinent to the current evolution of motor drives, this thesis focuses on the control techniques of converter-fed synchronous machines for variable speed applications. The title bears the keyword *synchronous reluctance machine* as the proposed solutions have hitherto been only validated on a SyR motor test-bench. However, a vast majority of the work is general in nature, applicable to the family of anisotropic synchronous machines. Within the paradigm of motor drives, this work broadly covers three topics: *(i)* Sensorless Control; *(ii)* Self-Commissioning and *(iii)* Direct Flux Vector Control.

1.1.1 Appeal for Sensorless Control

The operation without a rotor position transducer in motor drives has been long sought after and has been a subject of research for over three decades. The control techniques developed towards this end are commonly known as sensorless control, also referred as self-sensing and encoderless control is some literature.

Typical speed and position transducers include potentiometer, tachometer, hall-effect sensor, optical encoder and resolver. The main motivation for eliminating these sensors are:

- The cost reduction is a major incentive in pursing sensorless control; besides the cost of the sensor itself, the supplementary expense incurred in cabling and assembly can also be avoided.

- The resolution of position sensor imposes a limitation on the maximum operable speed whereas the sensorless techniques are known to be very reliable, particularly at high speeds.
- A prospective application for sensorless control is the hostile environments that is not conducive for position sensors such as high temperature, liquid immersion, long cabling, etc.
- In cases of sensitive equipment, the sensorless control provides redundancy and a contingency plan should the position sensor fail, aiding in fault-tolerance.

Thus, the research in the field of sensorless control aims at eliminating the position sensor while providing a reliable speed and position estimation at all operating points.

1.1.2 Need for Automatic Commissioning

Commissioning the drive comprises of identifying the parameters of the motor and the inverter. The characterization of inverter involves mapping the voltage drop due to dead-time and switching losses. This work addresses the automatic or self-commissioning of the motors for magnetic model characterization.

Synchronous machines often exhibit nonlinear magnetic characteristics with self-saturation and cross-coupling phenomenon. The knowledge of the motor flux-map is mandatory for the accurate control of synchronous motor drives for the following reasons:

- For a given speed and torque, the dq operating point for optimal efficiency is dependent on the flux-map of the machine. Thus, for high-efficiency drives, the flux-map information is vital.
- The tuning of linear regulators for torque control is reliant on the flux-map of the machine for a uniform dynamic performance at all operating points. Needless to say, the model-based control schemes such as model-predictive-control (MPC) and deadbeat control (DBC) are at the mercy of accurate model parameters.
- The efficacy of most sensorless techniques is directly proportional to the accuracy of the flux-map; parameter errors could potentially lead to loss of control and instability. Besides position estimation, the flux-map helps in reliable torque and stator flux estimation that benefits high-performance drives.

Having established the need for accurate magnetic model, methods for identification without an elaborate and a dedicated test-bench finds interest in industrial applications. To this end, self-commissioning techniques are developed for flux-map identification that is not limited to a lab environment.

1.1.3 Control Strategies

A robust control technique is essential to exploit the merit of an electrical drive. The development of new semiconductor devices and faster control processing platforms have fostered continuous evolution in the control strategies of motor drives. The two most commercial and prominent classical control strategies are the linear proportional-integral (PI) controller-based field-oriented-control (FOC) and the hysteresis controller-based direct-torque-control (DTC). The merits and demerits of the two have been long debated and well-documented. Some features that are desired out of a notable control scheme are:

- Good dynamic performance and uniform bandwidth at all operating points with reasonably low torque/current ripples and acoustic noise.
- Ability to extend operation beyond rated speed and generate optimal references for flux-weakening region with ease.
- Resilience to parameter detuning and less dependency on offline preprocessed optimal reference tables.

Direct flux vector control (DFVC) is an amalgamation of sorts of FOC and DTC. While the aforementioned features can be attained by various control schemes, this work focuses on DFVC as a high-performance control strategy.

1.2 Thesis Outline

As alluded to earlier, the thesis focuses on three aspects of the control of motor drives. The sensorless control is the primary topic of the work, incurring a lion's share of time and resources. The manuscript is organized as follows:

- **Chapter 2** defines the symbols and notation, and introduces the synchronous machine model. The experimental setup and the two SyR motors under test are discussed.
- **Chapter 3** presents the sensorless control framework as a basis for the projection vector-based position estimation techniques. The stator flux, speed and position observers are introduced and the generalized stability analysis is formulated.
- **Chapter 4** contains a review of three common back-emf based sensorless schemes from literature. The stability is assessed to reveal problematic operating regions through the common prism of the projection vector framework.
- **Chapter 5** presents a new auxiliary-flux position observer (AUX) to mitigate the instability of the fundamental-wave excitation techniques.

- **Chapter 6** presents a new adaptive projection vector for position error estimation (APP) scheme for sensorless control of synchronous machines. Following the sensitivity analysis to parameter errors, a stator resistance and flux adaptation mechanism is designed.

- **Chapter 7** introduces a new model-based torque control scheme with adaptive MTPA tracking. A new current-model flux adaptation is supplemented to the APP position observer to mitigate error in torque estimation and realize accurate torque control under flux-map errors.

- **Chapter 8** deals with the sensorless control techniques for the zero to low speeds region where the position information is retrieved from the high-frequency excitation of the machine. An injection-less sensorless control with finite-control-set model-predictive-control (FCS-MPC) is discussed.

- **Chapter 9** presents the self-commissioning techniques for SyR machines. An online flux adaptation during alternate acceleration-deceleration at free-shaft is presented. A sensorless variant at standstill condition is also explored.

- **Chapter 10** talks about the contributions to DFVC in terms of accurate modeling of the nonlinear dynamics that help realizing high bandwidth control. A new small-signal model based online optimal reference generation is investigated.

- **Chapter 11** concludes the thesis by summarizing the contributions and discussing future works.

In addition to the work discussed in the manuscript, two industrial contracts were managed during the course of PhD. The first activity from 1 April to 30 June 2018 involved a hardware-in-loop (HiL) modeling and experimental validation of an elevator drive-train. The second activity is a two year research contract from 1 April 2019 to 31 March 2021 to investigate developments in sensorless control of SyR machines. Within this contract, a new low speed sensorless control without the need for flux-map was designed for plug-and-play systems. A patent on this technique is jointly held with the industrial partner; this new scheme is not discussed in the manuscript to refrain from imposing an 18 month embargo on the thesis.

Besides the work on motor drives, the early days required a brief involvement in an inter-disciplinary project on exploring the feasibility of plastic optic-fibers for real-time control and synchronization of different power converters, primarily in assisting with the power electronic hardware setup.

1.3 List of Publications

Journal Papers

1. A. Varatharajan, G. Pellegrino, E. Armando and M. Hinkkanen, "Sensorless Synchronous Motor Drives: A Review of Flux Observer-based Position Estimation Schemes using the Projection Vector Framework," in *IEEE Transactions on Power Electronics*, DOI: 10.1109/TPEL.2020.3048922.

2. A. Varatharajan, G. Pellegrino, E. Armando and M. Hinkkanen, "Sensorless Control of Synchronous Motor Drives: Accurate Torque Estimation and Control under Parameter Errors," in *IEEE Journal of Emerging and Selected Topics in Power Electronics*, 2020, DOI: 10.1109/JESTPE.2020.3037792.

3. A. Varatharajan, G. Pellegrino and E. Armando, "Sensorless Synchronous Reluctance Motor Drives: Auxiliary Flux based Position Observer," in *IEEE Journal of Emerging and Selected Topics in Power Electronics*, 2020, DOI: 10.1109/JESTPE.2020.3019568.

4. A. Varatharajan and G. Pellegrino, "Sensorless Synchronous Reluctance Motor Drives: A Projection Vector Approach for Stator Resistance Immunity and Parameter Adaptation," in *IEEE Transactions on Industry Applications*, vol. 56, no. 5, pp. 5003-5012, Sept.-Oct. 2020, DOI: 10.1109/TIA.2020.3009641.

5. A. Varatharajan, P. Pescetto and G. Pellegrino, "Sensorless Synchronous Reluctance Motor Drives: A Full-Speed Scheme Using Finite-Control-Set MPC in a Projection Vector Framework," in *IEEE Transactions on Industry Applications*, vol. 56, no. 4, pp. 3809-3818, July-Aug. 2020, DOI: 10.1109/TIA.2020.2990834.

6. A. Varatharajan and G. Pellegrino, "Sensorless Synchronous Reluctance Motor Drives: A General Adaptive Projection Vector Approach for Position Estimation," in *IEEE Transactions on Industry Applications*, vol. 56, no. 2, pp. 1495-1504, March-April 2020, DOI: 10.1109/TIA.2019.2961986.

7. Savio P, Varatharajan A, Vizzaccaro E, Abdelfattah S, Franco G, Abrate S, Pellegrino G, Curri V: "Control of Power Electronics through a Photonic Bus: Feasibility and Prospects," in *Journal of Sensor and Actuator Networks*. 2018; 7(4):53.

Conference Papers

1. A. Varatharajan, G. Pellegrino and E. Armando, "Self-Commissioning of Synchronous Reluctance Motor Drives: Magnetic Model Identification with Online Adaptation," *2020 IEEE Energy Conversion Congress and Exposition*

(ECCE), Detroit, USA, 2020.

2. A. Varatharajan, P. Pescetto and G. Pellegrino, "Sensorless Self-Commissioning of Synchronous Reluctance Machine with Rotor Self-Locking Mechanism," *2019 IEEE Energy Conversion Congress and Exposition (ECCE)*, Baltimore, MD, USA, 2019, pp. 812-817, DOI: 10.1109/ECCE.2019.8913023.

3. A. Varatharajan and G. Pellegrino, "Sensorless Synchronous Reluctance Motor Drives: A Sensitivity Analysis Framework and Design to Achieve Stator Resistance Immunity," *2019 IEEE 10th International Symposium on Sensorless Control for Electrical Drives (SLED)*, Turin, Italy, 2019, pp. 1-6, DOI: 10.1109/SLED.2019.8896282.

4. A. Varatharajan and G. Pellegrino, "Sensorless Control of Synchronous Reluctance Motor Drives: Improved Modeling and Analysis Beyond Active Flux," *2019 IEEE International Electric Machines & Drives Conference (IEMDC)*, San Diego, CA, USA, 2019, pp. 419-426, DOI: 10.1109/IEMDC.2019.8785315.

5. A. Varatharajan, P. Pescetto and G. Pellegrino, "Injectionless Sensorless Control of Synchronous Reluctance Machine for Zero to Low Speeds Region," *2018 IEEE 9th International Symposium on Sensorless Control for Electrical Drives (SLED)*, Helsinki, 2018, pp. 72-77, DOI: 10.1109/SLED.2018.8486061.

6. A. Varatharajan, P. Savio, E. Vizzaccaro, S. Abrate, G. Pellegrino and V. Curri, "Remotized Control of Power Electronic Devices Exploiting a Plastic Optical Fiber Photonic Bus," *2018 20th International Conference on Transparent Optical Networks (ICTON)*, Bucharest, 2018, pp. 1-4, DOI: 10.1109/ICTON.2018.8473992.

List of Submitted Papers

S1 A. Varatharajan, G. Pellegrino and E. Armando, "Direct Flux Vector Control of Synchronous Motor Drives: A Small-Signal Model for Optimal Reference Generation," in *IEEE Transactions of Power Electronics*, 2020.

S2 A. Varatharajan, G. Pellegrino and E. Armando, "Direct Flux Vector Control of Synchronous Motor Drives: Accurate Decoupled Control with Online Adaptive MTPA and MTPV Evaluation," in *IEEE Transactions of Industrial Electronics*, 2020.

Chapter 2

Synchronous Machines

The analytical formulation of MTPA criterion using the auxiliary-flux vector is published in [11], [12].

2.1 Introduction

Since the turn of 21st century, the synchronous machines have begun to grow prominent in high-efficiency VSD. For the same stack and inverter size, a comparison of three motors, IM, surface permanent magnet (SPM) and interior permanent magnet (IPM), shows that a well-designed high-salient IPM synchronous motor has a better overall performance in power overload curve and efficiency [13]. The SPM motors hold a poor reputation for flux-weakening capability as the characteristic current often exceeds the rated current, limiting the achievable constant-power speed range (CPSR) [14]. Even when the characteristic current is achievable (like in concentrated winding SPM machines), it is not convenient to shoot against the PMs for efficiency reasons. The IPM motor is assisted with a reluctance torque component in addition to the magnetic torque and is known to have a wider CPSR with better flux-weakening capability. A realizable characteristic current provides better fault-tolerant operation as it is the phase current during three-phase short-circuit fault.

In early 2010, the price of rare-earth metal neodymium (Nd) skyrocketed in unprecedented proportions that disrupted the PM synchronous motor industry and brought to light the undue reliance and the monopolistic nature of the rare-earth metal market [15]. This prompted the investigation for alternative high performance machines to shield the exposure to price swings and volatility of the rare-earth magnets [16]. Ferrite ceramic magnets have been commercially successful despite their lower remanent flux density due to their lower cost and higher Curie temperature [17].

A search for rare-earth free machines led to the rediscovery of SyR machines

as the inverter technology evolved [18]. The theoretical principles of reluctance torque production in SyR machine were introduced by Kostko in 1923 [19]; early reference on a salient pole synchronous machine without field excitation dates back to 1926 [20]. Despite applications in textile industry as early as 1960's, the SyR machine laid largely dormant until the research interest was revived with the onset of developments in semiconductors. While the PM motors are less sturdy owing to the risk of demagnetization from shocks and over-current faults, the SyR motors are more sturdy for the simplicity of the rotor.

Considering the spectrum of synchronous machines with the non-salient SPM motors with purely magnetic torque at one end and the salient SyR motors with purely reluctance torque at the other, there are numerous combinations of designs that encompass both magnetic and reluctance torque. The IPM motors represent those having a relatively higher proportion of magnetic torque while the permanent magnet assisted synchronous reluctance (PM-SyR) motors have a higher proportion of reluctance torque.

This chapter introduces the mathematical model of a synchronous machine, and the analytical expressions of maximum-torque-per-ampere (MTPA) and maximum-torque-per-volts (MTPV) criteria in Section 2.2. The description of the experimental test-bench, the motors under test and the hardware setup is presented in Section 2.3.

2.2 Theoretical Background

The electrical rotor position is θ and the electrical angular speed is $\omega = s\,\theta$ where s is the differential operator $\frac{\mathrm{d}}{\mathrm{d}t}$. The orthogonal rotational matrix is $\mathbf{J} = \left[\begin{smallmatrix} 0 & -1 \\ 1 & 0 \end{smallmatrix}\right]$ and $\mathbf{I}$ is the identity matrix. Real space vectors will be used; for example, the stator current is $\boldsymbol{i}_{dq} = [i_d, i_q]^{\mathrm{T}}$ where i_d and i_q are the vector components in the dq rotor reference frame. Space vectors in the stationary reference frame are denoted by subscript $\alpha\beta$. Note that the convention of a SyR machine is followed, i.e, d-axis is defined along the maximum inductance path and the magnets, if any, are along the negative q-axis.

2.2.1 Mathematical Model

The voltage equation of a synchronous machine in the dq rotor reference frame is given by

$$s\,\boldsymbol{\lambda}_{dq} = \boldsymbol{v}_{dq} - R_s \boldsymbol{i}_{dq} - \omega\,\mathbf{J}\,\boldsymbol{\lambda}_{dq} \tag{2.1}$$

where R_s is the stator resistance and $\boldsymbol{\lambda}_{dq}$ is the stator flux linkage. The stator flux linkage and its time-derivative are expressed as

$$\boldsymbol{\lambda}_{dq} = \boldsymbol{L}\,\boldsymbol{i}_{dq} + \boldsymbol{\lambda}_m \qquad s\,\boldsymbol{\lambda}_{dq} = \boldsymbol{L}_\partial\, s\,\boldsymbol{i}_{dq} \tag{2.2}$$

where $\boldsymbol{L}$ is the apparent inductance matrix, $\boldsymbol{L}_\partial$ is the incremental inductance matrix and $\boldsymbol{\lambda_m}$ is the open circuit permanent-magnet flux vector. They are given by

$$\boldsymbol{L}(\boldsymbol{i}_{dq}) = \begin{bmatrix} L_d & 0 \\ 0 & L_q \end{bmatrix} \quad \boldsymbol{\lambda}_m = \begin{bmatrix} 0 \\ -\lambda_m \end{bmatrix} \quad \boldsymbol{L}_\partial(\boldsymbol{i}_{dq}) = \begin{bmatrix} l_d & l_{dq} \\ l_{dq} & l_q \end{bmatrix} \tag{2.3}$$

where λ_m is the open circuit permanent-magnet flux linkage, l_d, l_q represents the incremental inductance along direct d and quadrature q axis, respectively, while l_{dq} is the cross-saturation term. Apparent inductances are defined likewise. The inductance matrices are functions of $\boldsymbol{i}_{dq}$. The cross-saturation in apparent inductance is included in the diagonal terms in $\boldsymbol{L}(\boldsymbol{i}_{dq})$. The average electromagnetic torque is given by

$$T = \frac{3p}{2}\, \boldsymbol{i}_{dq}^{\mathrm{T}}\, \mathbf{J}\, \boldsymbol{\lambda}_{dq} \tag{2.4}$$

where p is the number of pole pairs. The dynamics of mechanical speed and position, denoted by the subscript r, of a synchronous machine is given by

$$J \cdot s\, \omega_r = T - T_L - B\, \omega_r \tag{2.5}$$

where J is the shaft inertia, T_L is the load torque and B is the friction coefficient.

Iron losses, being a nonlinear function of the stator flux and the angular frequency, are difficult to model and gain significance at high speeds. For operations around the nominal speed, it is common to neglect the iron losses due to their diminished influence and modeling complexity; besides, it has little detrimental effects on control to warrant complicated control scheme and machine identification stage. Hence, they are not considered in this work.

2.2.2 MTPA Law and Auxiliary-Flux Definition

Let $\gamma = \angle \boldsymbol{i}_{dq}$ denote the current angle in the dq reference frame. The change of torque w.r.t current angle for a given current amplitude $i = |\boldsymbol{i}_{dq}|$ is computed as

$$\left.\frac{\mathrm{d}T}{\mathrm{d}\gamma}\right|_i = \frac{3p}{2} \left(\frac{\mathrm{d}\boldsymbol{i}_{dq}}{\mathrm{d}\gamma}^{\mathrm{T}}\, \mathbf{J}\, \boldsymbol{\lambda}_{dq} + \boldsymbol{i}_{dq}^{\mathrm{T}}\, \mathbf{J}\, \frac{\mathrm{d}\boldsymbol{\lambda}_{dq}}{\mathrm{d}\gamma} \right). \tag{2.6}$$

Upon manipulation,

$$\left.\frac{\mathrm{d}T}{\mathrm{d}\gamma}\right|_i = \frac{3p}{2} \left(\mathbf{J}\, \boldsymbol{\lambda}_{dq} - \boldsymbol{L}_\partial\, \mathbf{J}\, \boldsymbol{i}_{dq} \right)^{\mathrm{T}} \mathbf{J}\, \boldsymbol{i}_{dq}. \tag{2.7}$$

The contours of (2.7) in dq current plane for SyR motor A (see Section 2.3.2 for the motor ratings) is shown in Fig. 2.1(a); the MTPA trajectory is coincident with the zero locus. The auxiliary-flux vector $\boldsymbol{\lambda}_{dq}^a$ is defined as

$$\boldsymbol{\lambda}_{dq}^a = \mathbf{J}\, \boldsymbol{\lambda}_{dq} - \boldsymbol{L}_\partial\, \mathbf{J}\, \boldsymbol{i}_{dq}. \tag{2.8}$$

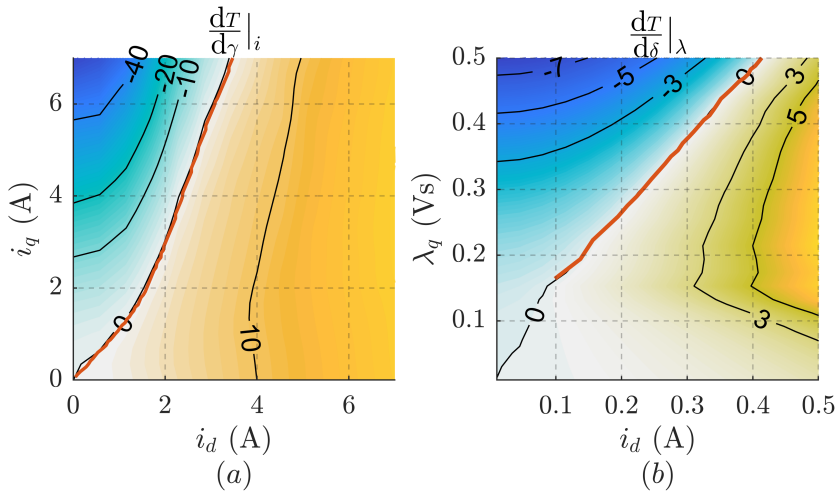

Figure 2.1: (a) Contour of derivative of torque w.r.t current angle (2.7) where the red line is the MTPA trajectory; (b) Contour of derivative of torque w.r.t load angle (2.14) where the red line is the MTPV trajectory. Motor: *A*.

The MTPA law is finally defined as

$$\left.\frac{\mathrm{d}T}{\mathrm{d}\gamma}\right|_i = 0 \implies \left(\boldsymbol{\lambda}^a_{dq}\right)^{\mathrm{T}} \mathbf{J}\, \boldsymbol{i}_{dq} = 0. \tag{2.9}$$

The expression (2.9) dictates that the MTPA criterion is respected *if and only if* the stator current is in phase with the auxiliary-flux vector, i.e., $\gamma_{\mathrm{MTPA}} = \angle \boldsymbol{\lambda}^a_{dq}$.

Physical Insights into Auxiliary-Flux Vector

Let $\hat{d}q$ denote a general reference frame whose $\hat{d}$-axis is shifted from the real rotor d-axis by an angle $\tilde{\theta} = \theta - \hat{\theta}$. In the following chapters on sensorless control, the notation $\hat{d}q$ represents the estimated reference frame having a position error $\tilde{\theta}$. The linearized form of the derivative of stator flux in the general reference frame can be expressed as

$$\mathrm{d}\boldsymbol{\lambda}_{\hat{d}q}\left(\boldsymbol{i}_{\hat{d}q}, \tilde{\theta}\right) = \left.\frac{\delta \boldsymbol{\lambda}_{\hat{d}q}}{\delta \boldsymbol{i}_{\hat{d}q}}\right|_{\tilde{\theta}} \cdot \mathrm{d}\boldsymbol{i}_{\hat{d}q} + \left.\frac{\delta \boldsymbol{\lambda}_{\hat{d}q}}{\delta \tilde{\theta}}\right|_{\boldsymbol{i}_{\hat{d}q}} \cdot \mathrm{d}\tilde{\theta}. \tag{2.10}$$

Examining the second term in (2.10) using (2.2) leads to

$$\left.\frac{\delta \boldsymbol{\lambda}_{\hat{d}q}}{\delta \tilde{\theta}}\right|_{\boldsymbol{i}_{\hat{d}q}} = \mathbf{J}\, \mathrm{e}^{\mathbf{J}\tilde{\theta}}\, \boldsymbol{\lambda}_{dq} - \mathrm{e}^{\mathbf{J}\tilde{\theta}}\, \boldsymbol{L}_{\partial}\, \mathbf{J}\, \mathrm{e}^{-\mathbf{J}\,\tilde{\theta}}\, \boldsymbol{i}_{\hat{d}q}. \tag{2.11}$$

Using the definition of auxiliary-flux vector (2.8), the above expression becomes

$$\left.\frac{\delta \boldsymbol{\lambda}_{\hat{d}q}}{\delta \tilde{\theta}}\right|_{\boldsymbol{i}_{\hat{d}q}} = \mathrm{e}^{\mathbf{J}\tilde{\theta}}\, \boldsymbol{\lambda}^a_{dq} = \boldsymbol{\lambda}^a_{\hat{d}q}. \tag{2.12}$$

The expression (2.12) gives a physical understanding of the auxiliary-flux vector as the change in stator flux w.r.t the position error for a constant stator current vector in the general reference frame.

2.2.3 MTPV Law and Auxiliary-Current Definition

Let $\delta = \angle\boldsymbol{\lambda}_{dq}$ denote the load angle in the dq reference frame. Then, the change of torque w.r.t load angle for a given flux amplitude $\lambda = |\boldsymbol{\lambda}_{dq}|$ is computed as

$$\left.\frac{\mathrm{d}T}{\mathrm{d}\delta}\right|_{\lambda} = \frac{3p}{2}\left(\frac{\mathrm{d}\boldsymbol{i}_{dq}}{\mathrm{d}\delta}^{\mathrm{T}}\,\mathbf{J}\,\boldsymbol{\lambda}_{dq} + \boldsymbol{i}_{dq}^{\mathrm{T}}\,\mathbf{J}\,\frac{\mathrm{d}\boldsymbol{\lambda}_{dq}}{\mathrm{d}\delta}\right). \tag{2.13}$$

Upon manipulation,

$$\left.\frac{\mathrm{d}T}{\mathrm{d}\delta}\right|_{\lambda} = \frac{3p}{2}\,\boldsymbol{\lambda}_{dq}^{\mathrm{T}}\,\mathbf{J}\left(\mathbf{J}\,\boldsymbol{i}_{dq} - \boldsymbol{L}_{\partial}^{-1}\,\mathbf{J}\,\boldsymbol{\lambda}_{dq}\right). \tag{2.14}$$

The contours of (2.14) in dq flux plane for SyR motor A (see Section 2.3.2) is shown in Fig. 2.1(b); the MTPV trajectory is coincident with the zero locus. The auxiliary-current vector $\boldsymbol{i}_{dq}^{a}$ is defined as

$$\boldsymbol{i}_{dq}^{a} = \mathbf{J}\,\boldsymbol{i}_{dq} - \boldsymbol{L}_{\partial}^{-1}\,\mathbf{J}\,\boldsymbol{\lambda}_{dq}. \tag{2.15}$$

Following, the MTPV law is defined as

$$\left.\frac{\mathrm{d}T}{\mathrm{d}\delta}\right|_{\lambda} = 0 \implies \boldsymbol{\lambda}_{dq}^{\mathrm{T}}\,\mathbf{J}\,\boldsymbol{i}_{dq}^{a} = 0. \tag{2.16}$$

The expression (2.16) dictates that the MTPV criterion is respected *if and only if* the auxiliary-current is in phase with the stator flux vector, i.e., $\delta_{\mathrm{MTPV}} = \angle\boldsymbol{i}_{dq}^{a}$.

Physical Insights into Auxiliary-Current Vector

The linearized form of the derivative of stator current in the general reference frame can be expressed as

$$\mathrm{d}\boldsymbol{i}_{\hat{dq}}\left(\boldsymbol{\lambda}_{\hat{dq}}, \tilde{\theta}\right) = \left.\frac{\delta\boldsymbol{i}_{\hat{dq}}}{\delta\boldsymbol{\lambda}_{\hat{dq}}}\right|_{\tilde{\theta}} \cdot \mathrm{d}\boldsymbol{\lambda}_{\hat{dq}} + \left.\frac{\delta\boldsymbol{i}_{\hat{dq}}}{\delta\tilde{\theta}}\right|_{\boldsymbol{\lambda}_{\hat{dq}}} \cdot \mathrm{d}\tilde{\theta}. \tag{2.17}$$

Examining the second term using (2.2) leads to

$$\left.\frac{\delta\boldsymbol{i}_{\hat{dq}}}{\delta\tilde{\theta}}\right|_{\boldsymbol{\lambda}_{\hat{dq}}} = \mathbf{J}\,\mathrm{e}^{-\mathbf{J}\tilde{\theta}}\,\boldsymbol{i}_{dq} - \mathrm{e}^{\mathbf{J}\tilde{\theta}}\,\boldsymbol{L}_{\partial}^{-1}\,\mathbf{J}\,\mathrm{e}^{-\mathbf{J}\tilde{\theta}}\,\boldsymbol{\lambda}_{\hat{dq}}. \tag{2.18}$$

Figure 2.2: Experimental Setup with the custom built inverter, dSPACE DS1103 control platform and HBM GEN 3i data recorder.

Using the definition of auxiliary-current vector (2.15), the above expression becomes

$$\left.\frac{\delta \boldsymbol{i}_{\hat{dq}}}{\delta \tilde{\theta}}\right|_{\boldsymbol{\lambda}_{\hat{dq}}} = \mathrm{e}^{\mathbf{J}\tilde{\theta}}\, \boldsymbol{i}^{a}_{dq} = \boldsymbol{i}^{a}_{\hat{dq}}. \tag{2.19}$$

As a duality to the auxiliary-flux vector,, the expression (2.19) gives a physical understanding of the auxiliary-current vector as the change in stator current w.r.t the position error for a constant stator flux in the general reference frame.

2.3 Experimental Test-Bench

2.3.1 Hardware Setup

A snapshot of the hardware setup is shown in Fig. 2.2. The 3-phase voltage source inverter is custom designed and in-house built, rated at 400 V and 40 A pk with the dc-link at 565 V. The control platform is dSPACE DS1103 that runs at a sampling frequency of 5 - 10 kHz; the precise data are reported in the experimental results section of each chapter. The setup uses synchronous sampling. The inverter dead-time (3μs) is appropriately compensated. The ratio of the switching to the fundamental frequency is over 100; thus, a simple forward Euler integration is adequate for time discretization [21].

2.3.2 Motors under Test

The developed sensorless control techniques in Chapters 3-8 as well as the direct flux vector control in Chapter 10 are valid for all synchronous machines. The

Table 2.1: Motor Parameters

Parameters	**Symbol**	**Motor *A***	**Motor *B***	**Units**
Rated power	P_n	1.1	1.1	kW
Rated voltage	V_n	340	340	V
Rated speed	ω_n	1500	1500	rpm
Rated current	I_n	2.9	2.3	A
Rated torque	T_n	7.1	7.1	Nm
Pole pairs	p	2	2	-
Stator resistance	R_s	6.2	4.5	Ω
Shaft inertia	J	0.04	0.04	kgm^2

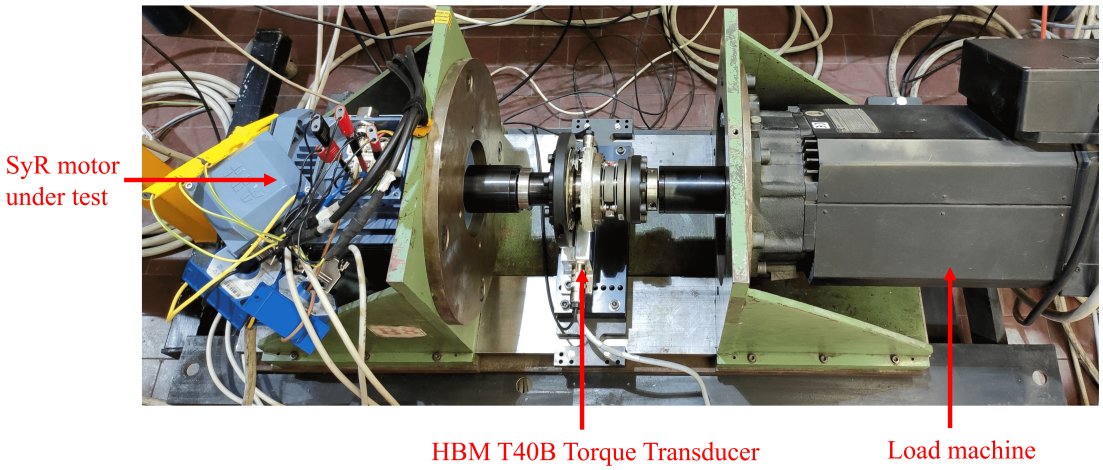

Figure 2.3: Motor test-bench with the SyR machine under test (blue) and the auxiliary load machine (black) coupled through a HBM T40B torque transducer for motor commissioning.

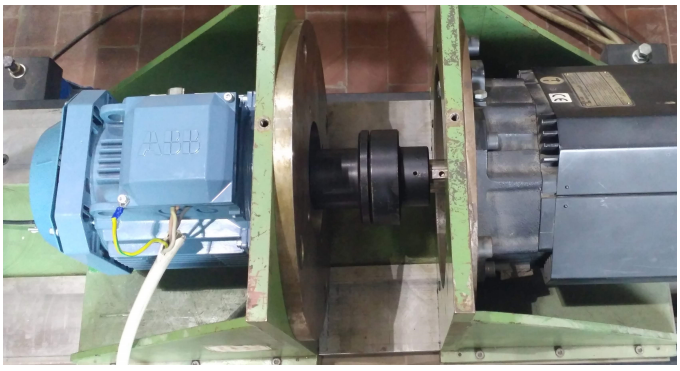

Figure 2.4: Motor test-bench with a hard coupling used for the sensorless control development.

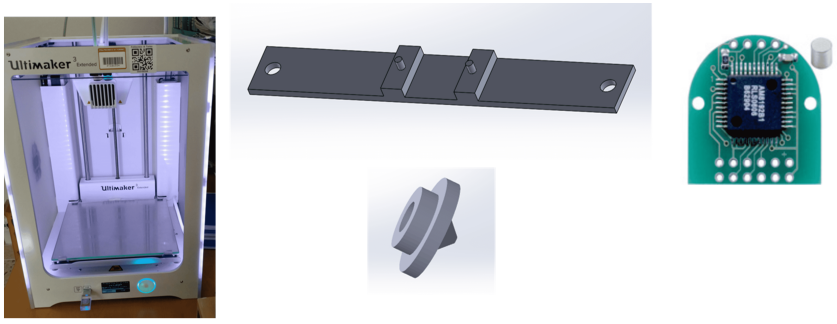

(a) (b) (c)

Figure 2.5: (a) 3D printer Ultimaker 3; (b) Solid Works 3D print design for magnetic encoder adapters; (c) RLS AM8192B Hall sensor-based magnetic incremental encoder.

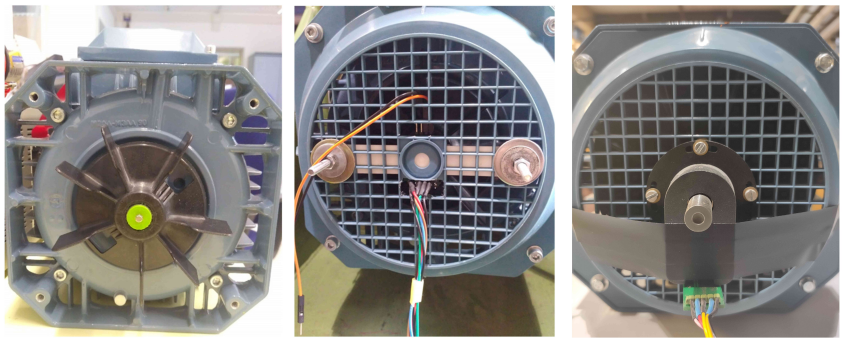

(a) (b) (c)

Figure 2.6: Encoder mounting: (a) Diametrically polarized magnet attached to the shaft of motor A; (b) Hall sensor mounted on the frame of motor A; (c) Optical encoder mounted on the frame of motor B.

experimental validation is presented on two 1.1 kW SyR machines, motor A and motor B.

The motor A is the commercially available ABB 3GAL092513-BSB while the motor B is custom designed starting from an ABB inductor motor. The parameters of the two motors are reported in Table 2.1. Wherein necessary, the motor in use will be indicated in the figures caption in the following chapters.

None of the motor included a position transducer by default. The motor test-bench is shown in Fig. 2.3 with the SyR motor under test (blue) and the load machine (black). The HBM Gen 3i data recorder in Fig. 2.2 and the torque transducer HBM T40B in Fig. 2.3 are mounted only for the initial identification stage (flux and efficiency maps) of the SyR machine. As strong transients are detrimental to the health of torque sensors, it has been the laboratory policy to not use the torque sensor for the tests pertaining to the development stage of sensorless control, sensitivity and stability analysis. Thus, the torque sensor is replaced with a direct

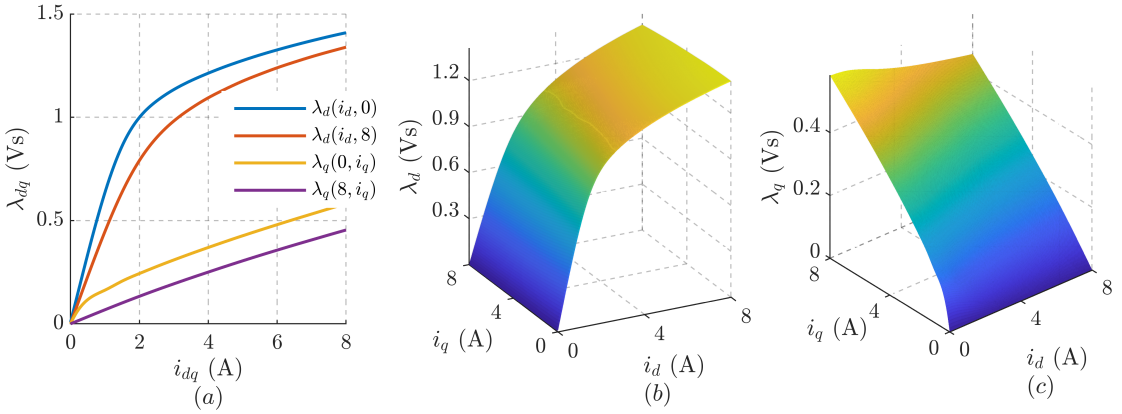

Figure 2.7: Experimentally identified magnetic model of SyR motor A: (a) Overview exhibiting saturation and cross-saturation phenomenon; (b) d-axis flux-map; (c) q-axis flux-map.

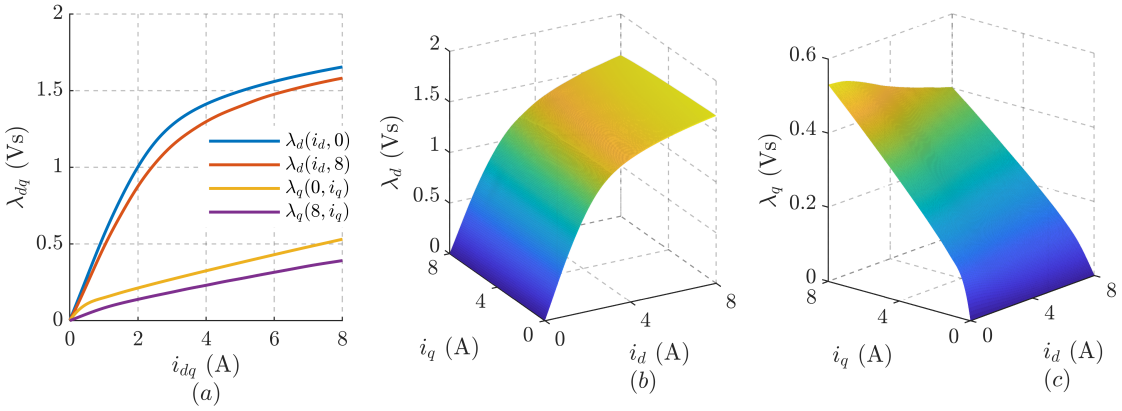

Figure 2.8: Experimentally identified magnetic model of SyR motor B: (a) Overview exhibiting saturation and cross-saturation phenomenon; (b) d-axis flux-map; (c) q-axis flux-map.

coupling as shown in Fig. 2.4.

The motor A is affixed with a 13 bits RLS AM8192B Hall sensor-based magnetic incremental encoder. To aid in mounting the encoder onto the motor, adapters were designed in Solid Works and fabricated with a 3D printer Ultimaker 3 and PLA ink, as shown in Fig. 2.5. The final mounting on the machine is shown in Fig. 2.6. The motor B uses a 12 bits optical encoder mounted behind the shaft, besides the fan, as shown in Fig. 2.6(c).

The magnetic model characteristics of the SyR motors A and B are shown in Figs. 2.7 and 2.8, respectively. The flux-map of the two motors under test is experimentally identified with the constant speed test reported in [22]. Note that the flux-map identification at constant speed extracts the fundamental component that averages out the spacial and slot harmonics. The motors under test exhibit secondary harmonics though it has little bearing on the control techniques discussed

in this work.

2.4 Summary of the Chapter Contributions

The major contributions of this chapter are summarized as follows:

- The analytical expression of the MTPA condition is expressed using the newly defined auxiliary-flux vector. It is shown that, at the MTPA operating point, the stator current vector and the auxiliary-flux vector are in phase. This property is exploited in later chapters to design a real-time MTPA adaptation.
- Similarly, the MTPV condition is analytically expressed using the newly defined auxiliary-current vector and is shown that the stator flux vector is in phase with the auxiliary-current vector at the MTPV operating point. This property is used to design a real-time MTPV limit in Chapter 10.

Chapter 3

Unified Sensorless Control Framework

The projection vector framework for design and analysis of position sensorless control schemes is published in [23], [24]. The nonlinear magnetic model accounting for position error is also reported in [23], [24].

3.1 Introduction

The sensorless control techniques can be broadly classified into two classes: *(i)* fundamental-wave excitation schemes; *(ii)* high-frequency excitation schemes. Those sensorless techniques that extract the position information from the back-emf (equivalently, flux linkage) of the machine fall under the fundamental-wave excitation scheme. They are reviewed and extensively discussed in Chapters 4 - 7.

The fundamental-excitation schemes become unreliable at low speeds due to the diminished back-emf and is inoperable at standstill condition. An alternative is sought with the high-frequency excitation schemes for low speed sensorless control where the local magnetic saliency of the machine is exploited for position estimation. High-frequency excitation schemes will be reviewed and treated in Chapter 8. In medium to high speed region, the high-frequency excitation approach is often relegated in the favor of fundamental-wave excitation approach for reliability and absence of acoustic noise.

This chapter aims to establish a general sensorless control framework upon which the fundamental-wave excitation techniques in Chapters 4 - 7 are constructed, but also applicable to the high-frequency excitation schemes in Chapter 8. The influence of position error on the current-model flux is analyzed for a nonlinear magnetic model in Section 3.2. The hybrid flux observer (HFO) is introduced and the linearized flux estimation error dynamics is drawn in Section 3.3. The position error signal in the form of projection vectors [23]–[26] using the discrepancy between

the observed and the current-model flux for fundamental-wave excitation schemes is introduced in Section 3.4. A phase-locked-loop (PLL) is used as the speed and position observer; a stability analysis for the combined flux and position observer in a general form is introduced.

3.2 Sensorless Control System

The machine model is expressed in coordinates of estimated rotor reference frame, denoted by subscript $\hat{d}\hat{q}$, whose $\hat{d}$-axis is at $\hat{\theta} = \theta - \tilde{\theta}$, where $\tilde{\theta}$ is the position error. Estimated vectors are represented by the superscript $\hat{}$.

3.2.1 Machine Model under Position Error

The voltage equation of a synchronous machine in the estimated rotor reference frame is given by

$$s\,\boldsymbol{\lambda}_{\hat{d}\hat{q}} = \boldsymbol{v}_{\hat{d}\hat{q}} - R_s \boldsymbol{i}_{\hat{d}\hat{q}} - \hat{\omega}\,\mathbf{J}\,\boldsymbol{\lambda}_{\hat{d}\hat{q}} \tag{3.1}$$

where $\hat{\omega}$ is the estimated speed. The average electromagnetic torque resembles (2.4), given by

$$T = \frac{3p}{2}\,\boldsymbol{i}_{\hat{d}\hat{q}}^{\mathrm{T}}\,\mathbf{J}\,\boldsymbol{\lambda}_{\hat{d}\hat{q}}. \tag{3.2}$$

Voltage-Model Stator Flux

The stator flux linkage computed from the voltage equation (3.1) is referred to as voltage-model stator flux, expressed as

$$\boldsymbol{\lambda}_{\hat{d}\hat{q}} = \int \left(\boldsymbol{v}_{\hat{d}\hat{q}} - R_s \boldsymbol{i}_{\hat{d}\hat{q}} - \hat{\omega}\,\mathbf{J}\,\boldsymbol{\lambda}_{\hat{d}\hat{q}}\right)\mathrm{d}t. \tag{3.3}$$

The voltage-model flux is considered to be the exact stator flux in the estimated reference frame, which holds true under precise inverter voltage compensation and accurate stator resistance.

Let $\boldsymbol{\Lambda}_{dq}(\boldsymbol{i}_{dq})$ denote the accurate flux-map LUTs of the synchronous machine. Then, the voltage-model stator flux linkage is transformed to the estimated rotor reference frame under position error as

$$\boldsymbol{\lambda}_{\hat{d}\hat{q}} = \mathrm{e}^{\mathbf{J}\tilde{\theta}}\,\boldsymbol{\Lambda}_{dq}(\boldsymbol{i}_{dq}) = \mathrm{e}^{\mathbf{J}\tilde{\theta}}\,\boldsymbol{L}(\boldsymbol{i}_{dq})\,\mathrm{e}^{-\mathbf{J}\tilde{\theta}}\,\boldsymbol{i}_{\hat{d}\hat{q}} + \mathrm{e}^{\mathbf{J}\tilde{\theta}}\,\boldsymbol{\lambda}_m \tag{3.4}$$

where the inductance matrix are a function of the operating point $\boldsymbol{i}_{dq}$ in the real dq rotor reference frame. The time-derivative of stator flux in estimated reference frame is given by

$$s\,\boldsymbol{\lambda}_{\hat{d}\hat{q}} = \mathrm{e}^{\mathbf{J}\tilde{\theta}}\,\boldsymbol{L}_{\partial}(\boldsymbol{i}_{dq})\,\mathrm{e}^{-\mathbf{J}\tilde{\theta}}\,s\,\boldsymbol{i}_{\hat{d}\hat{q}} + \left(\mathbf{J}\boldsymbol{\lambda}_{\hat{d}\hat{q}} - \mathrm{e}^{\mathbf{J}\tilde{\theta}}\,\boldsymbol{L}_{\partial}(\boldsymbol{i}_{dq})\,\mathrm{e}^{-\mathbf{J}\tilde{\theta}}\,\mathbf{J}\,\boldsymbol{i}_{\hat{d}\hat{q}}\right)\cdot s\,\tilde{\theta} \tag{3.5}$$

where $s\,\tilde{\theta} = 0$ is generally assumed.

Current-Model Stator Flux

The current-model flux linkage, denoted with a superscript i, in the estimated rotor reference frame is given by

$$\boldsymbol{\lambda}^{i}_{\hat{d}\hat{q}} = \boldsymbol{\Lambda}_{dq}(\boldsymbol{i}_{\hat{d}\hat{q}}) = \boldsymbol{L}^{i}(\boldsymbol{i}_{\hat{d}\hat{q}}) \cdot \boldsymbol{i}_{\hat{d}\hat{q}} + \boldsymbol{\lambda}_{m} \tag{3.6}$$

where $\boldsymbol{L}^{i}$ is the current-model apparent inductance matrix that is a function of the operating point $\boldsymbol{i}_{\hat{d}\hat{q}}$ in the estimated $\hat{d}\hat{q}$ reference frame. Only in the absence of position error does the equalities $\boldsymbol{\lambda}_{dq} = \boldsymbol{\lambda}^{i}_{dq}$ and $\boldsymbol{L} = \boldsymbol{L}^{i}$ hold. Likewise, the current-model incremental inductance matrix is denoted by $\boldsymbol{L}^{i}_{\partial}$; however, for small position errors, the equality $\boldsymbol{L}^{i}_{\partial}(\boldsymbol{i}_{\hat{d}\hat{q}}) = \boldsymbol{L}_{\partial}(\boldsymbol{i}_{dq})$ holds.

3.2.2 Magnetic Model Accounting Position Error (MMAP)

The voltage-model stator flux linkage in the estimated rotor reference can be expanded as

$$\boldsymbol{\lambda}_{\hat{d}\hat{q}} = \mathrm{e}^{\mathbf{J}\tilde{\theta}}\, \boldsymbol{\Lambda}_{dq}(\boldsymbol{i}_{dq}) \quad \Rightarrow \quad \boldsymbol{\lambda}_{\hat{d}\hat{q}} = \mathrm{e}^{\mathbf{J}\tilde{\theta}}\, \boldsymbol{\Lambda}_{dq}(\mathrm{e}^{-\mathbf{J}\tilde{\theta}}\boldsymbol{i}_{\hat{d}\hat{q}}). \tag{3.7}$$

The synchronous machine exhibits nonlinear magnetic characteristics due to both saturation and cross-saturation phenomena. Hence, linearizing the term $\boldsymbol{\Lambda}_{dq}(\mathrm{e}^{-\mathbf{J}\tilde{\theta}}\boldsymbol{i}_{\hat{d}\hat{q}})$ in (3.7) around an operating point gives

$$\begin{aligned} \boldsymbol{\Lambda}_{dq}(\mathrm{e}^{-\mathbf{J}\tilde{\theta}}\boldsymbol{i}_{\hat{d}\hat{q}}) = \boldsymbol{\Lambda}_{dq}(\boldsymbol{i}_{\hat{d}\hat{q}} - \tilde{\theta}\,\mathbf{J}\,\boldsymbol{i}_{\hat{d}\hat{q}}) &= \boldsymbol{\Lambda}_{dq}(\boldsymbol{i}_{\hat{d}\hat{q}}) - \tilde{\theta}\,\frac{\mathrm{d}\boldsymbol{\Lambda}_{dq}}{\mathrm{d}\boldsymbol{i}_{\hat{d}\hat{q}}}\,\mathbf{J}\,\boldsymbol{i}_{\hat{d}\hat{q}} \\ \Rightarrow \quad \boldsymbol{\Lambda}_{dq}(\mathrm{e}^{-\mathbf{J}\tilde{\theta}}\boldsymbol{i}_{\hat{d}\hat{q}}) &= \boldsymbol{\lambda}^{i}_{\hat{d}\hat{q}} - \tilde{\theta}\,\boldsymbol{L}_{\partial}\,\mathbf{J}\,\boldsymbol{i}_{\hat{d}\hat{q}}. \end{aligned} \tag{3.8}$$

In the above derivation, the first order approximation holds for small position error, i.e., a constant incremental inductance in the vicinity of the operating point.

Using (3.8) in (3.7) and linearizing, the magnetic model accounting position error (MMAP) that relates the voltage-model and the current-model flux estimates is derived as

$$\boldsymbol{\lambda}_{\hat{d}\hat{q}} = \boldsymbol{\lambda}^{i}_{\hat{d}\hat{q}} + \tilde{\theta}\left(\mathbf{J}\,\boldsymbol{\lambda}^{i}_{\hat{d}\hat{q}} - \boldsymbol{L}_{\partial}\,\mathbf{J}\,\boldsymbol{i}_{\hat{d}\hat{q}}\right). \tag{3.9}$$

Using the definition of auxiliary-flux vector in (2.8), the MMAP relating the current-model and the voltage-model flux in estimated reference frame is given by

$$\boldsymbol{\lambda}_{\hat{d}\hat{q}} = \boldsymbol{\lambda}^{i}_{\hat{d}\hat{q}} + \tilde{\theta}\,\boldsymbol{\lambda}^{a}_{\hat{d}\hat{q}}. \tag{3.10}$$

The MMAP for a SyR machine was introduced as improved inductance model in [24].

3.2.3 Conventional Magnetic Model (CMM)

In the literature, it is common to overlook the position error induced inductance variations and to assume the current-model inductance in the estimated rotor reference frame to be equal to the real inductance, i.e.,

$$\boldsymbol{L}^{i}(\boldsymbol{i}_{\hat{d}\hat{q}}) = \boldsymbol{L}(\boldsymbol{i}_{dq}) \quad \Rightarrow \quad \boldsymbol{\lambda}^{i}_{\hat{d}\hat{q}} = \boldsymbol{L}\,\boldsymbol{i}_{\hat{d}\hat{q}} + \boldsymbol{\lambda}_{m}. \tag{3.11}$$

Linearizing (3.4) and using (3.11) leads to the conventional magnetic model (CMM) as

$$\boldsymbol{\lambda}_{\hat{d}\hat{q}} = \boldsymbol{\lambda}^{i}_{\hat{d}\hat{q}} + \tilde{\theta}\left(\mathbf{J}\,\boldsymbol{\lambda}^{i}_{\hat{d}\hat{q}} - \boldsymbol{L}\,\mathbf{J}\,\boldsymbol{i}_{\hat{d}\hat{q}}\right). \tag{3.12}$$

Drawing equivalence to (3.10), the auxiliary-flux vector for CMM is denoted by a superscript $'$ as

$$\boldsymbol{\lambda}^{a'}_{\hat{d}\hat{q}} = (\mathbf{J}\,\boldsymbol{L} - \boldsymbol{L}\,\mathbf{J})\,\boldsymbol{i}_{\hat{d}\hat{q}}. \tag{3.13}$$

It can be discerned that the CMM (3.12) is equivalent to the MMAP (3.9) only in the linear unsaturated region where the incremental inductance is identical to the apparent inductance.

3.2.4 Parameter Error Definition

Hitherto, exact motor parameters (flux-map LUTs and stator resistance) were considered. This section defines the respective parametric errors.

Current-Model Flux Error

Let $\hat{\boldsymbol{\lambda}}^{i}_{dq} = \hat{\boldsymbol{\Lambda}}_{dq}(\boldsymbol{i}_{dq})$ denote the current-model flux based on the error-ridden flux-map LUTs. Then, the current-model flux error $\tilde{\boldsymbol{\lambda}}^{i}_{dq}$ is given by

$$\tilde{\boldsymbol{\lambda}}^{i}_{dq} = \boldsymbol{\lambda}_{dq} - \hat{\boldsymbol{\lambda}}^{i}_{dq} = \tilde{\boldsymbol{L}} \cdot \boldsymbol{i}_{dq} + \tilde{\boldsymbol{\lambda}}_{m} \tag{3.14}$$

where the $\tilde{\boldsymbol{L}} = \boldsymbol{L} - \hat{\boldsymbol{L}}$ and $\tilde{\boldsymbol{\lambda}}_{m} = \boldsymbol{\lambda}_{m} - \hat{\boldsymbol{\lambda}}_{m}$ are the errors in apparent inductance and permanent magnet flux respectively. Incorporating the parameter error into the MMAP in (3.10) leads to

$$\boldsymbol{\lambda}_{\hat{d}\hat{q}} = \hat{\boldsymbol{\lambda}}^{i}_{\hat{d}\hat{q}} + \tilde{\theta}\,\hat{\boldsymbol{\lambda}}^{a}_{\hat{d}\hat{q}} + \tilde{\boldsymbol{\lambda}}^{i}_{\hat{d}\hat{q}}. \tag{3.15}$$

Stator Resistance and Inverter Voltage Error

Accurate dc-link voltage measurement is assumed. Two potential sources of voltage error are considered: *(i)* discrepancy in temperature-dependent stator resistance estimate; *(ii)* non-ideal dead-time compensation of the inverter. If $\hat{R}_s$ is the resistance used in the control, v_{dc} is the dc-link voltage, f_s is the switching

frequency and $\tilde{t}_d = t_d - \hat{t}_d$ is the error in the compensated dead-time, the voltage error can be expressed as [27]

$$\tilde{\boldsymbol{v}}_{\alpha\beta} = (R_s - \hat{R}_s)\, \boldsymbol{i}_{\alpha\beta} + \frac{4}{3}\, v_{dc}\, f_s\, \tilde{t}_d\, \operatorname{sgn}(\boldsymbol{i}_{abc}) \tag{3.16}$$

where the nonlinear term $\operatorname{sgn}(\boldsymbol{i}_{abc})$ is a signum of the inverter load current, defined as

$$\operatorname{sgn}(\boldsymbol{i}_{abc}) = \frac{1}{2}\left(\operatorname{sgn}(i_a) + \mathrm{e}^{\mathbf{J}\frac{2\pi}{3}} \cdot \operatorname{sgn}(i_b) + \mathrm{e}^{\mathbf{J}\frac{4\pi}{3}} \cdot \operatorname{sgn}(i_c)\right) \tag{3.17}$$

where $\boldsymbol{i}_{abc}$ is the motor current vector expressed in phase components *abc*. The $\operatorname{sgn}(\boldsymbol{i}_{abc})$ vector is a unity vector along one of the six active discrete voltage vectors of a 2-level inverter that is closest to the current vector in the stationary $\alpha\beta$ reference frame. The voltage error related to on-state voltage drop of power devices is included in the dead-time effect and the related compensation. Note that though the parasitic capacitance introduces harmonics in the applied voltage, they have been overlooked since they only marginally affect the fundamental voltage.

The fundamental component of the nonlinear voltage error due to the non-ideal dead-time compensation is in phase with the current vector, just as the voltage error due to the inaccurate stator resistance. Hence, for modeling simplicity, an effective stator resistance error is defined from the fundamental component of (3.16) using Fourier series as

$$\tilde{R}_s = R_s - \hat{R}_s + \frac{1}{i}\,\frac{4}{\pi}\, v_{dc}\, f_s\, \tilde{t}_d \tag{3.18}$$

where $\tilde{R}_s$ incorporates the net voltage error and i is the current vector amplitude.

3.3 Hybrid Flux Observer (HFO)

3.3.1 State Equation and Implementation

The hybrid flux observer state equation in the stationary reference frame is defined as

$$s\hat{\boldsymbol{\lambda}}_{\alpha\beta} = \boldsymbol{v}_{\alpha\beta} - \hat{R}_s \boldsymbol{i}_{\alpha\beta} + \mathrm{e}^{\mathbf{J}\hat{\theta}}\, \boldsymbol{G}\left(\hat{\boldsymbol{\lambda}}^{\,i}_{\hat{d}\hat{q}} - \hat{\boldsymbol{\lambda}}_{\hat{d}\hat{q}}\right) \tag{3.19}$$

where $\boldsymbol{G}$ is a 2×2 gain matrix, and $\hat{\boldsymbol{\lambda}}_{\alpha\beta}$ and $\hat{\boldsymbol{\lambda}}_{\hat{d}\hat{q}}$ are the observed stator flux in the stationary and the estimated rotor reference frame, respectively.

For a diagonal matrix $\boldsymbol{G} = g\,\mathbf{I}$, the gain g acts as a cross-over frequency that dictates the dominance of the current-model flux estimation on the observed flux for electrical speeds less g rad/s while the voltage-model flux estimation prevails for speed over g rad/s. The term $\hat{\boldsymbol{\Lambda}}_{dq}$ in Fig.3.1 is the flux-map LUTs from experimental identification.

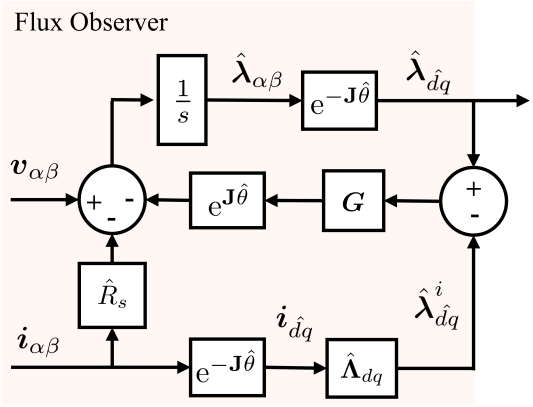

Figure 3.1: Block diagram of the hybrid flux observer implemented in the stator reference frame where the feedback is computed in the estimated rotor reference frame.

The incremental inductance matrix $\hat{\boldsymbol{L}}_{\partial}$ is computed in real-time from the flux-map LUTs; as an example:

$$\hat{l}_d(\boldsymbol{i}_{dq}) = \frac{\hat{\boldsymbol{\Lambda}}_d(i_d + \delta i_d, i_q) - \hat{\boldsymbol{\Lambda}}_d(i_d, i_q)}{\delta i_d} \tag{3.20}$$

where δi_d is a small value ($\approx$ 10 mA). The other incremental inductances are obtained in a similar fashion. This real-time computed incremental inductance will be used extensively; for instance, in the real-time evaluation of the auxiliary-flux vector.

3.3.2 Linearized Error Dynamics

For studying the error dynamics, the state equation (3.19) is transformed to the estimated reference frame as

$$s\,\hat{\boldsymbol{\lambda}}_{\hat{d}q} = \boldsymbol{v}_{\hat{d}q} - \hat{R}_s \boldsymbol{i}_{\hat{d}q} - \hat{\omega}\mathbf{J}\,\hat{\boldsymbol{\lambda}}_{\hat{d}q} + \boldsymbol{G}\left(\hat{\boldsymbol{\lambda}}^{i}_{\hat{d}q} - \hat{\boldsymbol{\lambda}}_{\hat{d}q}\right). \tag{3.21}$$

The nonlinear flux estimation error dynamics is derived from (3.1) and (3.21) as

$$s\,\tilde{\boldsymbol{\lambda}}_{\hat{d}q} = -(\boldsymbol{G} + \hat{\omega}\mathbf{J})\,\tilde{\boldsymbol{\lambda}}_{\hat{d}q} + \boldsymbol{G}\,(\boldsymbol{\lambda}_{\hat{d}q} - \hat{\boldsymbol{\lambda}}^{i}_{\hat{d}q}) - \tilde{R}_s \boldsymbol{i}_{\hat{d}q} \tag{3.22}$$

where $\tilde{\boldsymbol{\lambda}}_{\hat{d}q} = \boldsymbol{\lambda}_{\hat{d}q} - \hat{\boldsymbol{\lambda}}_{\hat{d}q}$ is the flux estimation error. Using the MMAP with the parameter errors in evidence (3.15), the linearized flux estimation error dynamics as functions of errors in position, resistance and current-model flux is derived as

$$\tilde{\boldsymbol{\lambda}}_{\hat{d}q} = (s\mathbf{I} + \boldsymbol{G} + \hat{\omega}\mathbf{J})^{-1}\left[\boldsymbol{G}\,(\hat{\boldsymbol{\lambda}}^{a}_{\hat{d}q}\,\tilde{\theta} + \tilde{\boldsymbol{\lambda}}^{i}_{\hat{d}q}) - \tilde{R}_s \boldsymbol{i}_{\hat{d}q}\right] \tag{3.23}$$

where $\hat{\boldsymbol{\lambda}}^{a}_{\hat{d}q}$ is the auxiliary-flux (2.8) computed using the observed stator flux.

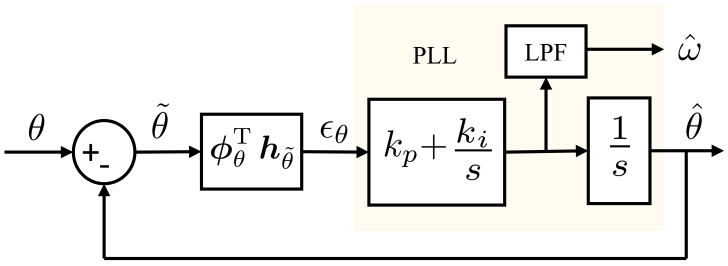

Figure 3.2: Closed-loop analysis of the position observer with a phased-locked-loop.

3.4 Speed and Position Observer

3.4.1 Phase-Locked-Loop (PLL)

A conventional phase-locked-loop (PLL) with a proportional-integral (PI) controller is employed to drive the position error signal ϵ_θ to zero, shown in Fig. 3.2, as

$$\hat{\omega} = k_p\,\epsilon_\theta + \omega_i \qquad \omega_i = \int k_i\,\epsilon_\theta\,\mathrm{d}t \qquad \hat{\theta} = \int \hat{\omega}\,\mathrm{d}t \tag{3.24}$$

where k_p and k_i are the respective gains. The gains of the PLL are tuned for a critically damped response considering $\epsilon_\theta = \tilde{\theta}$ by placing the two poles at $s = -\Omega_\omega$:

$$k_p = 2\,\Omega_\omega \qquad k_i = \Omega_\omega^2. \tag{3.25}$$

3.4.2 Projection Vector Framework

The position error signal ϵ_θ driving the PLL in Fig. 3.2 is expressed in a general form as the projection of the difference in observed and current-model flux estimates on the position projection vector $\boldsymbol{\phi}_\theta$, shown in Fig. 3.3, as [24], [25]

$$\epsilon_\theta = \boldsymbol{\phi}_\theta^{\mathrm{T}}\,(\hat{\boldsymbol{\lambda}}_{\hat{dq}} - \hat{\boldsymbol{\lambda}}_{\hat{dq}}^{\,i}). \tag{3.26}$$

Besides position tracking, the error signal in such general form will be used also for parameter adaptation. Using the flux estimation error $\tilde{\boldsymbol{\lambda}}_{\hat{dq}} = \boldsymbol{\lambda}_{\hat{dq}} - \hat{\boldsymbol{\lambda}}_{\hat{dq}}$ and the MMAP (3.15), the linearized form of (3.26) becomes

$$\epsilon_\theta = \boldsymbol{\phi}_\theta^{\mathrm{T}}\left(\hat{\boldsymbol{\lambda}}_{\hat{dq}}^{\,a}\,\tilde{\theta} + \tilde{\boldsymbol{\lambda}}_{\hat{dq}}^{\,i} - \tilde{\boldsymbol{\lambda}}_{\hat{dq}}\right). \tag{3.27}$$

Following the results of flux estimation error dynamics (3.23), the position error signal (3.27) is decomposed in terms of the constituent errors as

$$\epsilon_\theta = \boldsymbol{\phi}_\theta^{\mathrm{T}}\begin{bmatrix}\boldsymbol{h}_{\tilde{\theta}} & \boldsymbol{H}_{\tilde{\boldsymbol{\lambda}}^i} & \boldsymbol{h}_{\tilde{R}}\end{bmatrix}\tilde{\boldsymbol{x}} \tag{3.28a}$$

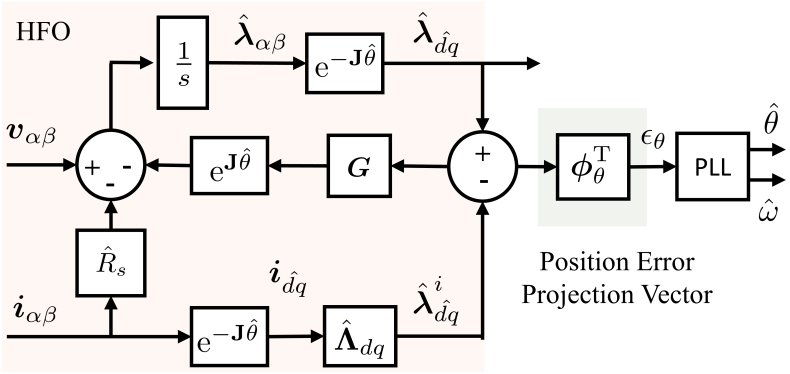

Figure 3.3: Hybrid flux observer (HFO) with projection vector-based position error signal and a phase-locked-loop (PLL) for position tracking.

$$\begin{aligned}
\boldsymbol{h}_{\tilde{\theta}} &= (s\mathbf{I} + \boldsymbol{G} + \omega\mathbf{J})^{-1}(s\mathbf{I} + \omega\mathbf{J})\,\hat{\boldsymbol{\lambda}}^{a}_{\hat{d}q} \\
\boldsymbol{H}_{\tilde{\boldsymbol{\lambda}}^{i}} &= (s\mathbf{I} + \boldsymbol{G} + \omega\mathbf{J})^{-1}(s\mathbf{I} + \omega\mathbf{J}) \\
\boldsymbol{h}_{\tilde{R}} &= (s\mathbf{I} + \boldsymbol{G} + \omega\mathbf{J})^{-1}\,\boldsymbol{i}_{\hat{d}q}
\end{aligned} \tag{3.28b}$$

where $\tilde{\boldsymbol{x}} = \begin{bmatrix}\tilde{\theta} & \left(\tilde{\boldsymbol{\lambda}}^{i}_{\hat{d}q}\right)^{\mathrm{T}} & \tilde{R}_s\end{bmatrix}^{\mathrm{T}}$. The transfer function matrices $\boldsymbol{h}_{\tilde{\theta}}$ and $\boldsymbol{h}_{\tilde{R}}$ are of length 2×1 while $\boldsymbol{H}_{\tilde{\boldsymbol{\lambda}}^{i}}$ is 2×2.

The steady-state position error $\tilde{\theta}_0$ owing to parametric errors can be derived from (3.28) by equating $\epsilon_\theta = 0$ as

$$\tilde{\theta}_0 = -\left.\frac{\boldsymbol{\phi}_\theta^{\mathrm{T}}\left(\boldsymbol{H}_{\tilde{\boldsymbol{\lambda}}^{i}}\,\tilde{\boldsymbol{\lambda}}^{i}_{\hat{d}q} + \boldsymbol{h}_{\tilde{R}_s}\,\tilde{R}_s\right)}{\boldsymbol{\phi}_\theta^{\mathrm{T}}\,\boldsymbol{h}_{\tilde{\theta}}}\right|_{s=0}. \tag{3.29}$$

Note that the expression (3.29) is not valid for large parameter errors as it is obtained from a linearized small-signal model. Steady-state error in the case of parameter adaptation can be derived in a similar fashion.

3.4.3 Stability Analysis

Closed-Loop Transfer Function

For the PLL defined in (3.24), the closed-loop transfer function in Fig. 3.2 is given by

$$\frac{\hat{\theta}(s)}{\theta(s)} = \frac{(sk_p + k_i)\,\boldsymbol{\phi}_\theta^{\mathrm{T}}\,\boldsymbol{h}_{\tilde{\theta}}}{s^2 + (sk_p + k_i)\,\boldsymbol{\phi}_\theta^{\mathrm{T}}\,\boldsymbol{h}_{\tilde{\theta}}} \tag{3.30}$$

where $\boldsymbol{\phi}_\theta^{\mathrm{T}}\,\boldsymbol{h}_{\tilde{\theta}}$ is the transfer function between the position error signal and position error for the projection vector in (3.28), given by

$$\frac{\epsilon_\theta}{\tilde{\theta}} = \boldsymbol{\phi}_\theta^{\mathrm{T}}\,\boldsymbol{h}_{\tilde{\theta}} = \boldsymbol{\phi}_\theta^{\mathrm{T}}\,(s\mathbf{I} + \boldsymbol{G} + \omega\mathbf{J})^{-1}(s\mathbf{I} + \omega\mathbf{J})\,\hat{\boldsymbol{\lambda}}^{a}_{\hat{d}q}. \tag{3.31}$$

The transfer function (3.31) will be used extensively in the following chapters to assess the stability of the fundamental-wave excitation sensorless schemes.

State-Space Model

It is convenient to evaluate the system stability with a state-space model of flux and position observers that can be later expanded to include parameter adaptation. To this end, the error dynamics of the position observer (3.24) can be expressed as

$$s\,\tilde{\theta} = \tilde{\omega}_i - k_p\,\epsilon_\theta \qquad\qquad s\,\tilde{\omega}_i = -k_i\,\epsilon_\theta. \tag{3.32}$$

The combined dynamics of the flux and the position observers is given by

$$s\,\boldsymbol{y} = \boldsymbol{A}\,\boldsymbol{y} \tag{3.33}$$

$$\boldsymbol{A} = \begin{bmatrix} -(\boldsymbol{G} + \omega\,\mathbf{J}) & \boldsymbol{G}\,\hat{\boldsymbol{\lambda}}^{a}_{\hat{d}q} & \mathbf{0} \\ k_p\,\boldsymbol{\phi}_\theta^{\mathrm{T}} & -k_p\,\boldsymbol{\phi}_\theta^{\mathrm{T}}\,\hat{\boldsymbol{\lambda}}^{a}_{\hat{d}q} & 1 \\ k_i\,\boldsymbol{\phi}_\theta^{\mathrm{T}} & -k_i\,\boldsymbol{\phi}_\theta^{\mathrm{T}}\,\hat{\boldsymbol{\lambda}}^{a}_{\hat{d}q} & 0 \end{bmatrix}$$

where $\boldsymbol{y} = \begin{bmatrix} \left(\tilde{\boldsymbol{\lambda}}_{\hat{d}q}\right)^{\mathrm{T}} & \tilde{\theta} & \tilde{\omega}_i \end{bmatrix}^{\mathrm{T}}$. The eigenvalues of (3.33) are computed for each operating point to evaluate the system stability.

3.5 Summary of the Chapter Contributions

The main contributions of this chapter are summarized as follows:

- Through linearization, the effect of the position error on the current-model flux estimation is analytically evaluated for MMAP. This helps to model the dynamics of sensorless control with improved accuracy that benefits analysis and design of stable position estimation techniques.
- Following the flux estimation error dynamics of HFO, the projection vector framework is developed to represent the position error signal in a general form. Parameter errors in stator resistance estimate and the flux-map LUTs estimate are considered.
- For a position observer using PLL, the stability analysis of the combined flux and position observer for a general projection vector is presented.

Chapter 4

Analysis of Fundamental-Wave Excitation Schemes

The findings in the stability analysis of fundamental-wave excitation schemes in literature using the projection vector framework is published in [28].

4.1 Introduction

This chapter concerns the fundamental-wave excitation methods based on back-emf integration for position estimation at medium to high speeds region. The regions of instability and operational limits of the techniques based on the flux observer in Fig. 3.3 are reviewed through the common prism of projection vector framework in similar operating conditions. Accurate parameters are assumed in the stability analysis in this chapter.

The three flux observer-based sensorless schemes for synchronous machines under consideration are: *(i)* Flux cross-product based position observer [29]–[31] in Section 4.2 where the position error function is proportional to the cross-product of the observed and the current-model flux estimates; *(ii)* Active-flux position observer [32]–[35] in Section 4.3 where the position error function is proportional to the q-axis component of the observed active-flux in the estimated rotor reference frame; *(iii)* Fundamental saliency-based position observer [36] in Section 4.4 where the position error function is extracted from the anisotropic component of the stator flux.

This is by no means an exhaustive review but only of those schemes that comply with the structure in Fig. 3.3. Among others, a common fundamental-wave excitation sensorless scheme without flux observer is the extended back-emf approach [37]–[40]. Extended Kalman filter and sliding mode techniques are reported in [41]–[43]. Differing from Fig. 3.3, sensorless schemes based on the flux observer with current feedback are investigated in [44]–[46]; they are mathematically equivalent to

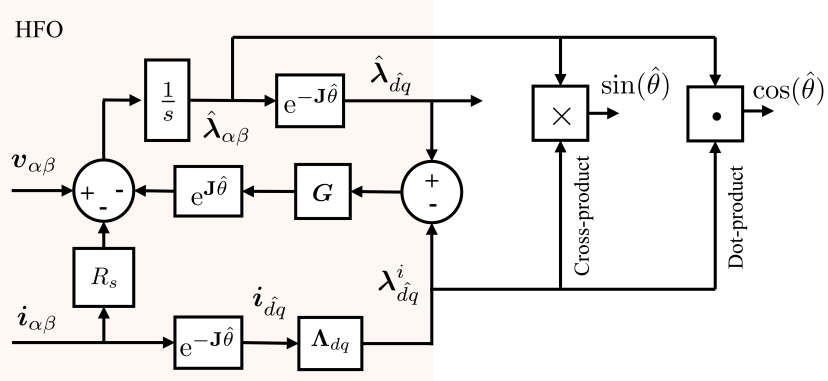

Figure 4.1: Block diagram of the flux cross-product based position observer for direct position estimation without a PLL [30], [31].

Fig. 3.3 only for linear magnetic machines with gains scaled accordingly.

4.2 Flux Cross-Product Position Observer (CP)

The flux cross-product based position observer was introduced in [29]–[31]. The rotor angular position is retrieved using the cross-product of the observed flux in stationary $\alpha\beta$ coordinates and the current-model flux estimate in estimated $\hat{d}\hat{q}$ coordinates, as shown in the block diagram in Fig. 4.1. The sine and cosine of the rotor position are estimated directly as

$$\sin(\hat{\theta}) = \frac{\lambda^{i}_{\hat{d}}\,\hat{\lambda}_{\beta} - \lambda^{i}_{\hat{q}}\,\hat{\lambda}_{\alpha}}{|\boldsymbol{\lambda}^{i}_{\hat{d}\hat{q}}|\,|\hat{\boldsymbol{\lambda}}_{\alpha\beta}|} \qquad \cos(\hat{\theta}) = \frac{\lambda^{i}_{\hat{d}}\,\hat{\lambda}_{\alpha} + \lambda^{i}_{\hat{q}}\,\hat{\lambda}_{\beta}}{|\boldsymbol{\lambda}^{i}_{\hat{d}\hat{q}}|\,|\hat{\boldsymbol{\lambda}}_{\alpha\beta}|}. \tag{4.1}$$

The reference papers do not apparently use a PLL, but it is worthwhile to assess the compatibility of this technique with a PLL for avoiding the direct reverberation of the voltage signal transients on the position and speed estimates.

4.2.1 Projection Vector Design

Using MMAP (2.8), the position error can be expressed as the cross-product of the voltage and the current-model flux estimates as

$$\tilde{\theta} = \frac{1}{\left(\boldsymbol{\lambda}^{i}_{\hat{d}\hat{q}}\right)^{\mathrm{T}} \mathbf{J}\,\boldsymbol{\lambda}^{a}_{\hat{d}\hat{q}}} \left(\boldsymbol{\lambda}^{i}_{\hat{d}\hat{q}}\right)^{\mathrm{T}} \mathbf{J}\,\boldsymbol{\lambda}_{\hat{d}\hat{q}} \tag{4.2}$$

The position error signal ϵ_{cp} that is representative of (4.1) is derived in the form of (4.2) from the cross-product of the observed and the current-model fluxes in the

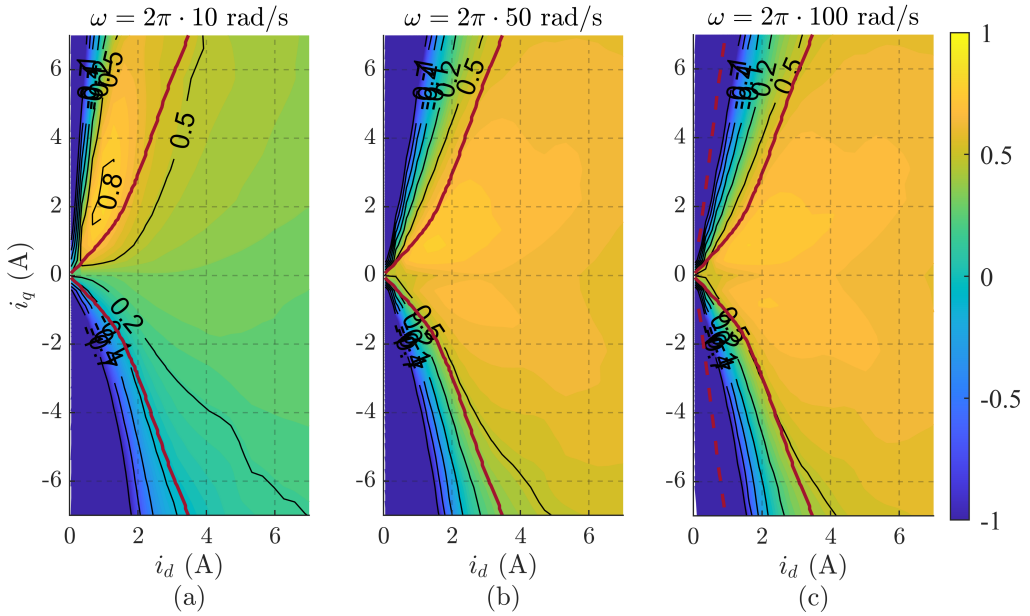

Figure 4.2: The contour plot of transfer function (4.6) for the CP position observer: (a) $\omega = 0.2$ p.u. (b) $\omega = 1$ p.u.; (c) $\omega = 2$ p.u. Flux observer gain is $g = 2\pi \cdot 10$ rad/s. The solid red line is the MTPA trajectory and the dashed red line is the MTPV trajectory. Motor: *A*.

estimated reference frame as

$$\epsilon_{cp} = \frac{\lambda^i_{\hat{d}}\,\hat{\lambda}_{\hat{q}} - \lambda^i_{\hat{q}}\,\hat{\lambda}_{\hat{d}}}{|\boldsymbol{\lambda}^i_{\hat{d}q}|^2} = \frac{-1}{|\boldsymbol{\lambda}^i_{\hat{d}q}|^2}\left(\boldsymbol{\lambda}^i_{\hat{d}q}\right)^{\mathrm{T}} \mathbf{J}\,\hat{\boldsymbol{\lambda}}_{\hat{d}q} \tag{4.3}$$

This scheme will be denoted by the acronym CP and the subscript *cp*, implying cross-product. The error signal is expressed in the projection vector framework as

$$\epsilon_{cp} = \boldsymbol{\phi}^{\mathrm{T}}_{cp}\,(\hat{\boldsymbol{\lambda}}_{\hat{d}q} - \boldsymbol{\lambda}^i_{\hat{d}q}) \tag{4.4}$$

where the projection vector $\boldsymbol{\phi}_{cp}$ corresponding to the error signal (4.3) is given by

$$\boldsymbol{\phi}^{\mathrm{T}}_{cp} = \frac{-1}{|\boldsymbol{\lambda}^i_{\hat{d}q}|^2}\left(\boldsymbol{\lambda}^i_{\hat{d}q}\right)^{\mathrm{T}} \mathbf{J}. \tag{4.5}$$

4.2.2 Stability Analysis

For $\boldsymbol{G} = g\,\mathbf{I}$ and using (4.5), the dc-gain of the transfer function (3.31) between the position error signal and the position error becomes

$$\boldsymbol{\phi}^{\mathrm{T}}_{cp}\,\boldsymbol{h}_{\tilde{\theta}}\Big|_{s=0} = \frac{\omega^2}{g^2+\omega^2}\,\frac{\left(\boldsymbol{\lambda}^i_{\hat{d}q}\right)^{\mathrm{T}}}{|\boldsymbol{\lambda}^i_{\hat{d}q}|^2}\left[\frac{g}{\omega}\,\hat{\boldsymbol{\lambda}}^a_{\hat{d}q} - \mathbf{J}\,\hat{\boldsymbol{\lambda}}^a_{\hat{d}q}\right]. \tag{4.6}$$

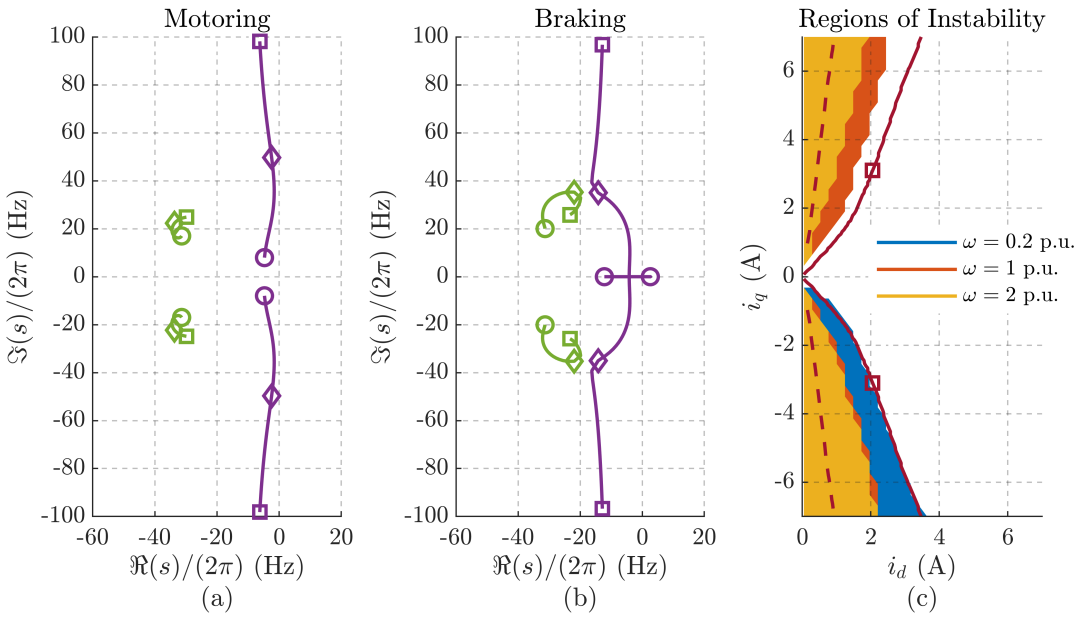

Figure 4.3: Closed-loop stability analysis of the CP position observer: Locus of poles of the flux (purple) and the position (green) observer at the rated torque (MTPA): (a) Motoring; (b) Braking. Speed markers: ∘ is 0.1 p.u., ⋄ is 1 p.u. and □ is 2 p.u. (c) Regions of instability evaluated at different speeds where the marker □ denotes the rated torque at MTPA. Parameters: flux observer gain $g = 2\pi \cdot 10$ rad/s and PLL gain $\Omega_\omega = 2\pi \cdot 50$ rad/s. Motor: A.

The expression (4.6) can be loosely interpreted as an open-loop gain (see Fig. 3.2) and as an indication of strength of the position error signal, i.e., the lower values indicate poor observability of the position error and poor resilience to parameter errors. A negative value implies a positive feedback and instability.

The gain (4.6) is dependent on the operating point $\boldsymbol{i}_{dq}$ and the angular speed ω, and not symmetric in motoring and braking quadrants. The contour of (4.6) in the dq current plane for SyR motor A is shown in Figs. 4.2(a), 4.2(b) and 4.2(c) at low speed (0.2 p.u.), rated speed and twice rated speed (2 p.u.), respectively. For speeds below 0.2 p.u., typically, a high-frequency excitation based scheme is employed in place of the fundamental-wave scheme. The contour map Fig. 4.2(a) indicates that operation in the braking quadrant ($i_q < 0$) is unstable at low speed, as the MTPA trajectory is in the vicinity of zero contour of the dc-gain. Moreover, high speed operations in flux-weakening region shows poor signal strength and can be potentially unstable.The MTPV trajectory is inoperable in Fig. 4.2(c).

The locus of closed-loop poles (3.33) for the projection vector (4.5) at the rated torque in motoring and braking is shown in Figs. 4.3(a) and 4.3(b), respectively. While the motoring condition is observed to be stable at all speeds, the flux observer pole ventures into the positive plane during braking at low speeds in Fig. 4.3(b). For comprehensive stability analysis, the closed-loop poles at all operating point in the dq current plane are evaluated at various speeds and the regions of instability

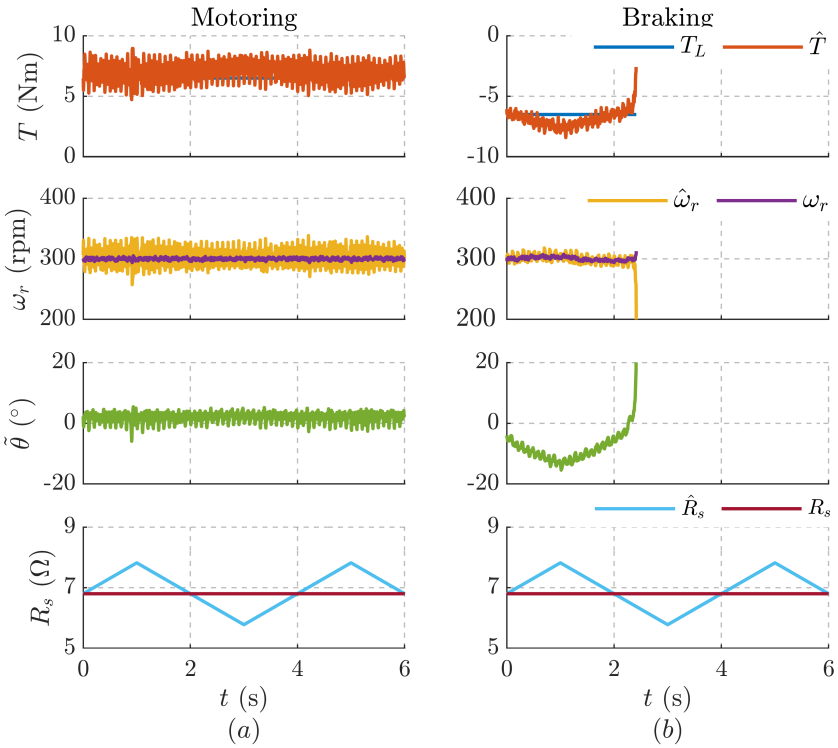

Figure 4.4: CP position observer stability analysis with resistance perturbation of ±15% error, $\tilde{R}_s = \pm 0.15\, R_s$ at 300 rpm (0.2 p.u.) and rated torque: (a) Motoring; (b) Braking. Motor: *A*.

are sketched in Fig. 4.3(c). Low speeds braking and high speeds flux-weakening regions are identified as critical for stability.

4.2.3 Experimental Results

The stability analysis of the sensorless techniques is validated experimentally with SyR motor *A* at a sampling frequency of 10 kHz. Current vector control is used where the *dq* current references are fetched from the MTPA lookup tables (LUTs); the findings also apply to other control schemes. The SyR machine operates in the speed control mode while the load torque is imposed by an auxiliary drive. The speed PI controller is tuned for critically damped poles at $s = -2\pi \cdot 1$ rad/s. A minimum stator current $i_{min} = 1$ A (0.25 p.u.) is set for fundamental excitation at no load.

Reference is made to the instability at low speed; the tests in Fig. 4.4 refer to 300 rpm (0.2 p.u.) speed condition and nominal torque. To evaluate the stability of the sensorless techniques, a small perturbation of ± 15% in the control stator resistance is introduced; Figs. 4.4(a) and 4.4(b) show the motoring and braking operation at rated torque, respectively.

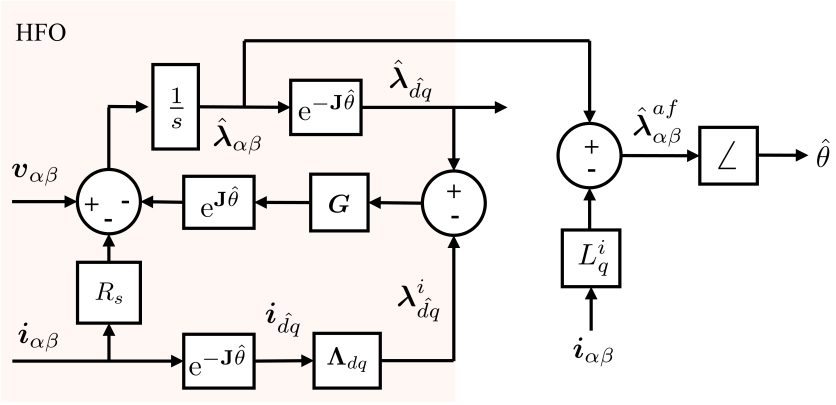

Figure 4.5: Block diagram of the active-flux based position observer for a SyR machine using direct position estimation without a PLL [33].

It can be observed that the motoring operation of the CP observer is stable while the braking runs into instability. The results corroborate the stability analysis in Fig. 4.3(c) where the rated torque at 300 rpm (0.2 p.u.) in braking operation at MTPA (denoted by the marker □) is at close proximity to the unstable region.

4.3 Active-Flux Position Observer (AF)

The active-flux for a SyR machine is defined along the d-axis as an equivalence to the torque produce flux in a non-salient machine as [32]–[35]

$$T = \frac{3p}{2} \overbrace{(L_d - L_q)\, i_d}^{\lambda^{af}_{dq}} i_q \quad \Rightarrow \quad \boldsymbol{\lambda}^{af}_{\alpha\beta} = \boldsymbol{\lambda}_{\alpha\beta} - L_q\, \boldsymbol{i}_{\alpha\beta} \tag{4.7}$$

where $\boldsymbol{\lambda}^{af}_{dq}$ is the active-flux. Thus, the rotor position is estimated from the phase angle of the observed stator flux and the current-model q-axis inductance, shown in the block diagram in Fig. 4.5, as

$$\hat{\theta} = \angle \hat{\boldsymbol{\lambda}}^{af}_{\alpha\beta} = \angle(\hat{\boldsymbol{\lambda}}_{\alpha\beta} - L^i_q\, \boldsymbol{i}_{\alpha\beta}). \tag{4.8}$$

Note that for PM machines, the active flux is defined along the magnetic axis, i.e., along the negative q-axis as per the convention of this text, as

$$T = \frac{3p}{2} \overbrace{\big((L_d - L_q)\, i_q + \lambda_m\big)}^{\lambda^{af}_{dq}} i_d \quad \Rightarrow \quad \boldsymbol{\lambda}^{af}_{\alpha\beta} = \boldsymbol{\lambda}_{\alpha\beta} - L_d\, \boldsymbol{i}_{\alpha\beta}. \tag{4.9}$$

Similar to (4.8), the position for PM machines is estimated as

$$\hat{\theta} = \angle \hat{\boldsymbol{\lambda}}^{af}_{\alpha\beta} + \frac{\pi}{2} = \angle(\hat{\boldsymbol{\lambda}}_{\alpha\beta} - L^i_d\, \boldsymbol{i}_{\alpha\beta}) + \frac{\pi}{2}. \tag{4.10}$$

The following analysis of active-flux position observer using PLL is drawn for a SyR machine but is just as valid for PM machines if the d-axis is defined along the magnetic axis.

4.3.1 Projection Vector Design

The active-flux of a SyR machine in the estimated rotor reference can be expressed as

$$\boldsymbol{\lambda}^{af}_{\hat{d}\hat{q}} = \boldsymbol{\lambda}_{\hat{d}\hat{q}} - L_q\, \boldsymbol{i}_{\hat{d}\hat{q}}. \tag{4.11}$$

Using (3.4) and linearizing leads to

$$\boldsymbol{\lambda}^{af}_{\hat{d}\hat{q}} = \begin{bmatrix} (L_d - L_q)\, i_{\hat{d}} \\ 0 \end{bmatrix} + \tilde{\theta}\, 2\, L_\Delta \begin{bmatrix} i_{\hat{q}} \\ i_{\hat{d}} \end{bmatrix} \tag{4.12}$$

where the q-axis component is proportional to the position error. Reformulating (4.12) gives

$$\tilde{\theta} = \frac{1}{2\, L_\Delta\, i_{\hat{d}}} \begin{bmatrix} 0 \\ 1 \end{bmatrix}^{\mathrm{T}} \left(\boldsymbol{\lambda}_{\hat{d}\hat{q}} - L_q\, \boldsymbol{i}_{\hat{d}\hat{q}} \right). \tag{4.13}$$

Thus, the position error signal can be derived using the observed stator flux ($\boldsymbol{\lambda}_{\hat{d}\hat{q}} \to \hat{\boldsymbol{\lambda}}_{\hat{d}\hat{q}}$) and the current-model inductance ($\boldsymbol{L} \to \boldsymbol{L}^i$) in (4.13) as

$$\epsilon_{af} = \frac{1}{2\, L^i_\Delta\, i_{\hat{d}}} \begin{bmatrix} 0 \\ 1 \end{bmatrix}^{\mathrm{T}} \left(\hat{\boldsymbol{\lambda}}_{\hat{d}\hat{q}} - L^i_q\, \boldsymbol{i}_{\hat{d}\hat{q}} \right). \tag{4.14}$$

This scheme is denoted by the acronym AF and the subscript af. The equivalent projection vector for the error signal (4.14) is given by

$$\boldsymbol{\phi}^{\mathrm{T}}_{af} = \frac{1}{2\, L^i_\Delta\, i_{\hat{d}}} \begin{bmatrix} 0 \\ 1 \end{bmatrix}^{\mathrm{T}}. \tag{4.15}$$

4.3.2 Stability Analysis

Using $\boldsymbol{G} = g\, \mathbf{I}$, the dc-gain of transfer function (3.31) for the active-flux projection vector (4.15) is given by

$$\boldsymbol{\phi}^{\mathrm{T}}_{af}\, \boldsymbol{h}_{\tilde{\theta}}\big|_{s=0} = \frac{\omega^2}{g^2 + \omega^2}\, \frac{1}{2\, L_\Delta\, i_{\hat{d}}} \left[\frac{g}{\omega}\, \hat{\lambda}^a_{\hat{d}} + \hat{\lambda}^a_{\hat{q}} \right]. \tag{4.16}$$

The gain (4.16) is dependent on the operating point $\boldsymbol{i}_{dq}$ and the angular speed ω. The contour plot is shown in Fig. 4.6 at three different speeds where the braking region is observed to have poor signal strength that deteriorates with decreasing

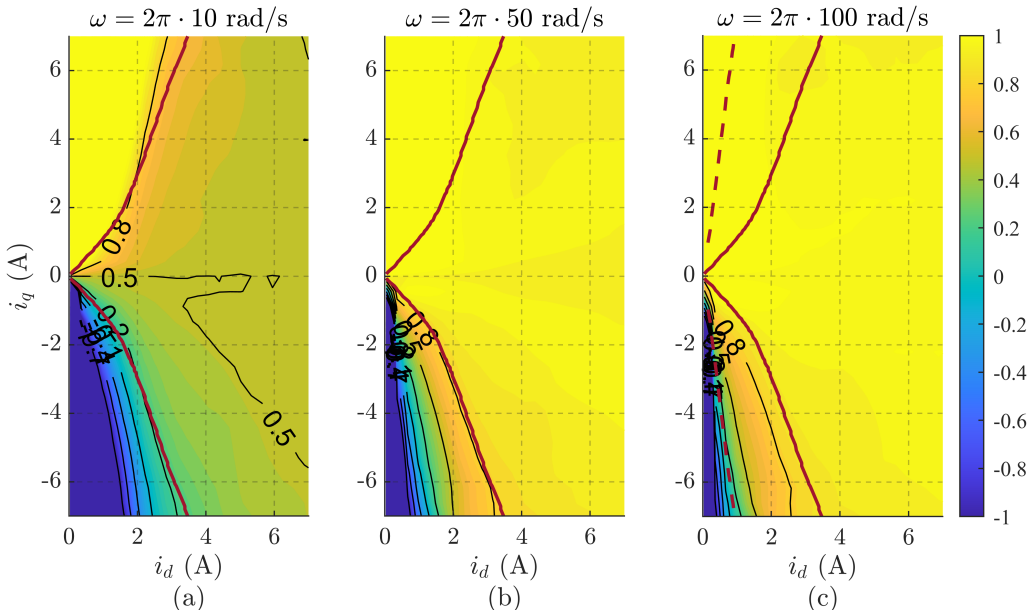

Figure 4.6: The contour plot of transfer function (4.16) for the AF position observer: (a) $\omega = 0.2$ p.u.; (b) $\omega = 1$ p.u.; (c) $\omega = 2$ p.u. Flux observer gain is $g = 2\pi \cdot 10$ rad/s. The solid red line is the MTPA trajectory and the dashed red line is the MTPV trajectory. Motor: A.

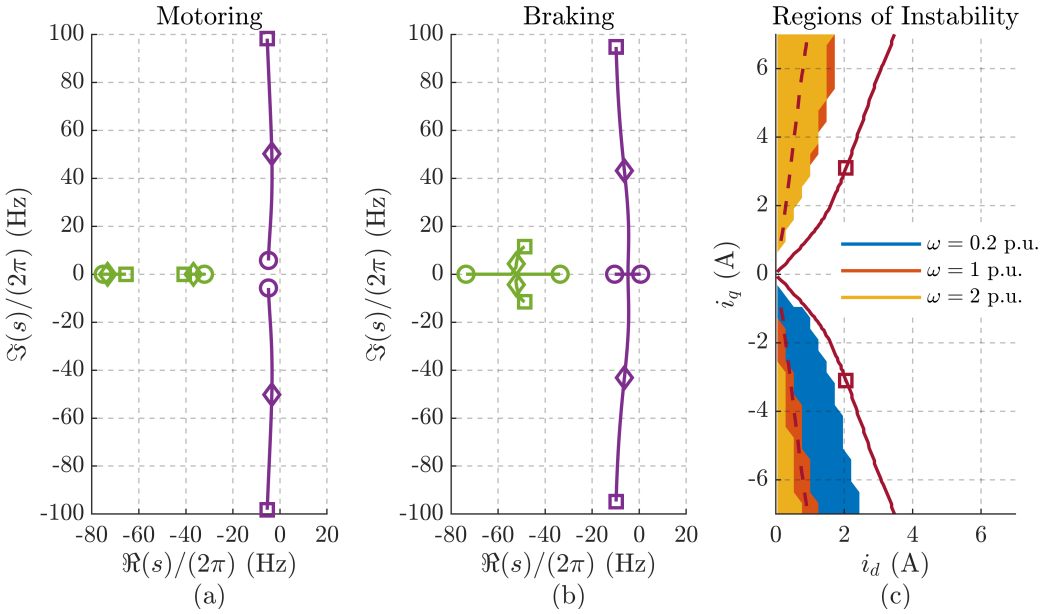

Figure 4.7: Closed-loop stability analysis of the AF position observer. Locus of poles of the flux (purple) and the position (green) observer at the rated torque (MTPA): (a) Motoring; (b) Braking. Speed Markers: ∘ is 0.1 p.u., ⋄ is 1 p.u. and □ is 2 p.u. (c) Regions of instability evaluated at different speeds where the marker □ denotes the rated torque at MTPA. Parameters: flux observer gain $g = 2\pi \cdot 10$ rad/s and PLL gain $\Omega_\omega = 2\pi \cdot 50$ rad/s. Motor: A.

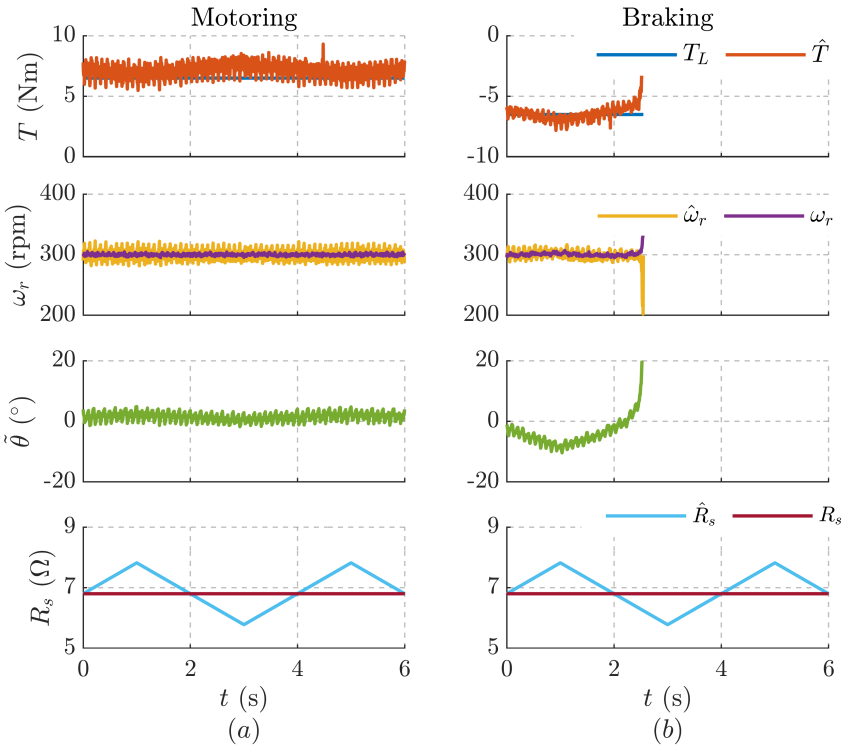

Figure 4.8: AF position observer stability analysis with resistance perturbation of ±15% error, $\tilde{R}_s = \pm 0.15\, R_s$ at 300 rpm (0.2 p.u.) and rated torque: (a) Motoring; (b) Braking. Motor: *A*.

speed. Although the motoring region has largely positive values of dc-gain at all speeds, further analysis shows that instability occurs also in this region.

The locus of poles at the rated torque in motoring is shown in Fig. 4.7(a) which is stable at all speeds. During braking, the flux observer pole approaches the first quadrant at low speeds in Fig. 4.7(b). A comprehensive evaluation for stability in the *dq* current plane at three different speeds is shown in Fig. 4.7(c). As mentioned earlier, the low speed braking regions are susceptible. It is interesting to point out that unstable regions also exist at high speeds motoring despite a healthy signal strength in Figs. 4.6(b) and 4.6(c). This arises due to the dynamic coupling between the flux and the position observer, as shown in [24], [25].

4.3.3 Experimental Results

Figs. 4.8(a) and 4.8(b) show the experimental validation of the stability of AF position observer with a control resistance perturbation in motoring and braking operation, respectively.

The motoring at rated torque and 300 rpm (0.2 p.u.) is stable while the braking becomes unstable. This corroborates the stability analysis in Fig. 4.7(c) where the

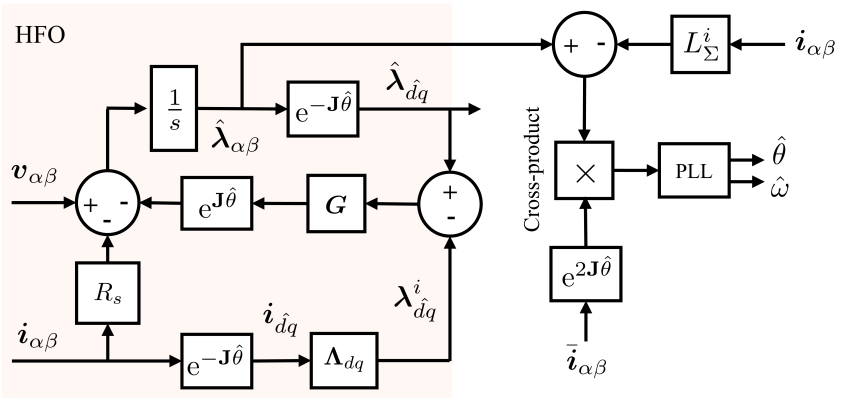

Figure 4.9: Block diagram of the fundamental saliency-based position observer for a SyR machine using a PLL for position tracking [36].

rated torque operation in braking (denoted by the marker □) is near the unstable region at 300 rpm.

4.4 Fundamental Saliency-based Position Observer (FS)

The fundamental saliency-based technique aims to estimate the rotor position from the differential-mode component of the stator flux. It is developed for a SyR machine in [36]; the block diagram is shown in Fig. 4.9. However, it is valid for all synchronous machines in general.

4.4.1 Projection Vector Design

This technique is extended also to the synchronous machines bearing magnets. To this end, decomposing the stator flux in estimated rotor reference frame (3.4) to common-mode and differential-mode terms leads to

$$\boldsymbol{\lambda}_{\hat{d}\hat{q}} = L_\Sigma\, \boldsymbol{i}_{\hat{d}\hat{q}} + L_\Delta\, \mathrm{e}^{2\mathbf{J}\,\tilde{\theta}}\, \bar{\boldsymbol{i}}_{\hat{d}\hat{q}} + \mathrm{e}^{\mathbf{J}\tilde{\theta}}\, \boldsymbol{\lambda}_m \tag{4.17}$$

where $L_\Sigma = \frac{L_d+L_q}{2}$, $L_\Delta = \frac{L_d-L_q}{2}$ and $\bar{\boldsymbol{i}}_{\hat{d}\hat{q}} = \begin{bmatrix} i_{\hat{d}} & -i_{\hat{q}} \end{bmatrix}^{\mathrm{T}}$ is the conjugate vector. Linearizing (4.17) and simplifying leads to

$$\boldsymbol{\lambda}_{\hat{d}\hat{q}} = \boldsymbol{L}\, \boldsymbol{i}_{\hat{d}\hat{q}} + \boldsymbol{\lambda}_m + \tilde{\theta}\, \boldsymbol{\lambda}^{a'}_{\hat{d}\hat{q}} \tag{4.18}$$

where $\boldsymbol{\lambda}^{a'}_{\hat{d}\hat{q}}$ is the CMM-based auxiliary-flux vector (3.13) defined in Section 3.2.3. Reformulating (4.18) leads to

$$\tilde{\theta} = \frac{\left(\boldsymbol{\lambda}^{a'}_{\hat{d}\hat{q}}\right)^{\mathrm{T}}}{|\boldsymbol{\lambda}^{a'}_{\hat{d}\hat{q}}|^2} \left(\boldsymbol{\lambda}_{\hat{d}\hat{q}} - \boldsymbol{L}\, \boldsymbol{i}_{\hat{d}\hat{q}} - \boldsymbol{\lambda}_m\right) \tag{4.19}$$

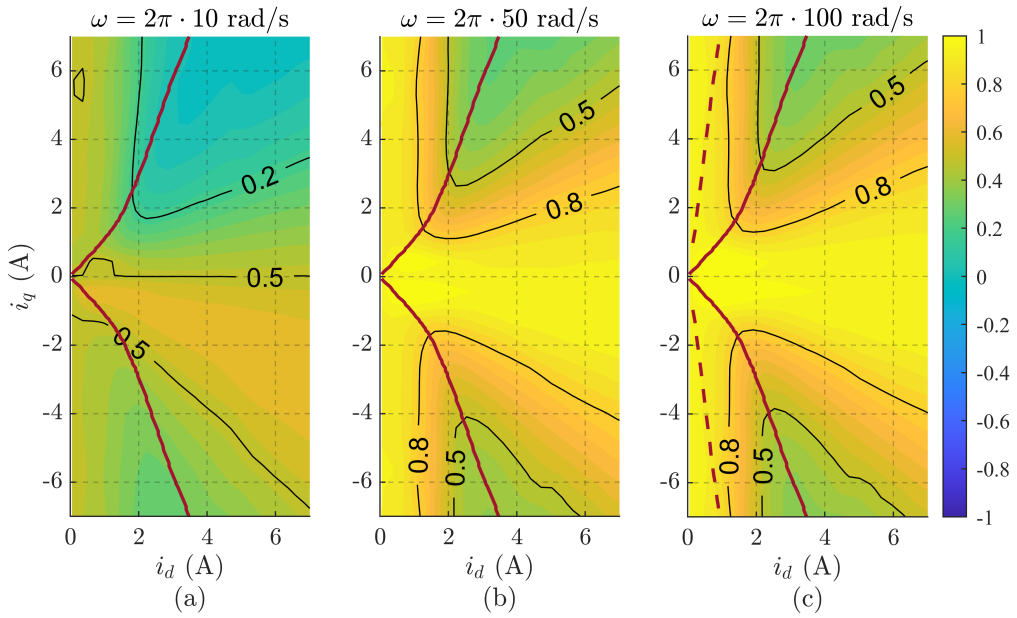

Figure 4.10: The contour plot of transfer function (4.22) for the FS position observer: (a) $\omega = 2\pi \cdot 10$ rad/s (0.2 p.u.); (b) $\omega = 2\pi \cdot 50$ rad/s (1 p.u.); (c) $\omega = 2\pi \cdot 100$ rad/s (2 p.u.). Flux observer gain is $g = 2\pi \cdot 10$ rad/s. The solid red line is the MTPA trajectory and the dashed red line is the MTPV trajectory. Motor: A.

This scheme is denoted by the acronym FS and the subscript fs. To design the position error function following (4.19), the real stator flux is replaced by the observed flux ($\boldsymbol{\lambda}_{\hat{d}\hat{q}} \to \hat{\boldsymbol{\lambda}}_{\hat{d}\hat{q}}$) and the real inductance is replaced by the current-model inductance ($\boldsymbol{L} \to \boldsymbol{L}^i$) as

$$\epsilon_{fs} = \boldsymbol{\phi}_{fs}^{\mathrm{T}} \left(\hat{\boldsymbol{\lambda}}_{\hat{d}\hat{q}} - \boldsymbol{L}^i \, \boldsymbol{i}_{\hat{d}\hat{q}} - \boldsymbol{\lambda}_m \right) = \boldsymbol{\phi}_{fs}^{\mathrm{T}} \left(\hat{\boldsymbol{\lambda}}_{\hat{d}\hat{q}} - \boldsymbol{\lambda}_{\hat{d}\hat{q}}^i \right) \tag{4.20}$$

where the FS projection vector is given by

$$\boldsymbol{\phi}_{fs}^{\mathrm{T}} = \frac{\left(\hat{\boldsymbol{\lambda}}_{\hat{d}\hat{q}}^{a'} \right)^{\mathrm{T}}}{|\hat{\boldsymbol{\lambda}}_{\hat{d}\hat{q}}^{a'}|^2} \tag{4.21}$$

The estimated CMM-based auxiliary-flux vector $\hat{\boldsymbol{\lambda}}_{\hat{d}\hat{q}}^{a'}$ is computed using the observed stator flux and the current-model inductance.

4.4.2 Stability Analysis

The dc-gain of the transfer function (3.31) with $\boldsymbol{G} = g\,\mathbf{I}$ for the FS projection vector (4.21) becomes

$$\boldsymbol{\phi}_{fs}^{\mathrm{T}} \, \boldsymbol{h}_{\tilde{\theta}} \Big|_{s=0} = \frac{\omega^2}{g^2 + \omega^2} \, \frac{1}{|\hat{\boldsymbol{\lambda}}_{\hat{d}\hat{q}}^{a'}|^2} \left[\left(\hat{\boldsymbol{\lambda}}_{\hat{d}\hat{q}}^{a'} \right)^{\mathrm{T}} \hat{\boldsymbol{\lambda}}_{\hat{d}\hat{q}}^{a} + \frac{g}{\omega} \left(\hat{\boldsymbol{\lambda}}_{\hat{d}\hat{q}}^{a'} \right)^{\mathrm{T}} \mathbf{J} \, \hat{\boldsymbol{\lambda}}_{\hat{d}\hat{q}}^{a} \right]. \tag{4.22}$$

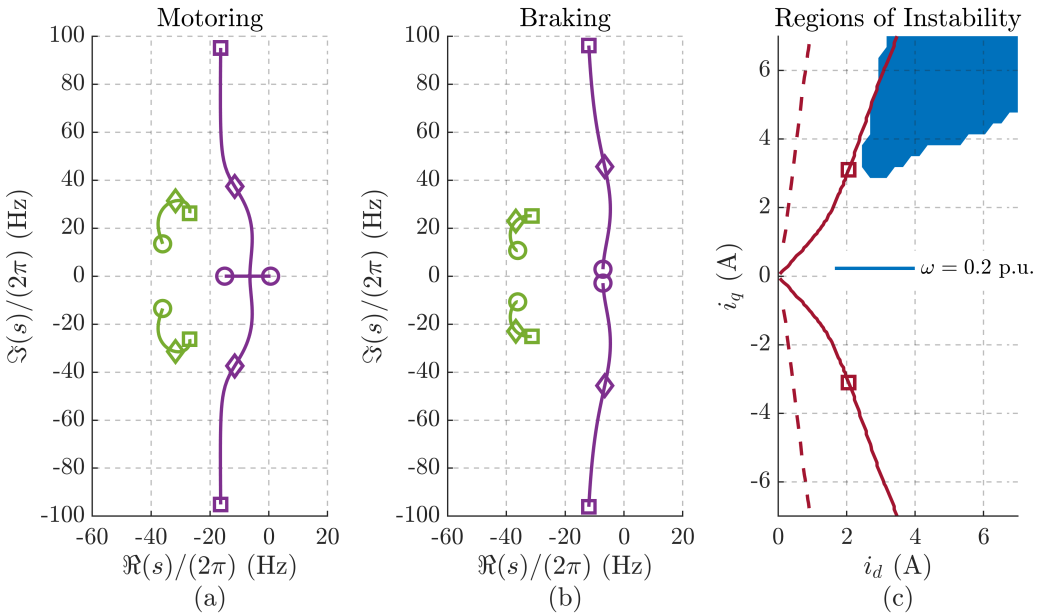

Figure 4.11: Closed-loop stability analysis of the FS position observer. Locus of poles of the flux (purple) and the position (green) observer at the rated torque (MTPA): (a) Motoring; (b) Braking. Speed Markers: ∘ is 0.1 p.u., ⋄ is 1 p.u. and □ is 2 p.u. (c) Regions of instability evaluated at different speeds where the marker □ denotes the rated torque at MTPA. Parameters: flux observer gain $g = 2\pi \cdot 15$ rad/s and PLL gain $\Omega_\omega = 2\pi \cdot 50$ rad/s. Motor: A.

The gain (4.22) is dependent on the operating point $\boldsymbol{i}_{dq}$ and the angular speed ω. The contour in the dq current plane is shown in Fig. 4.10 for three different speeds. Differing from the previous two schemes, it is the motoring operation having poor signal strength at the low speeds region in Fig. 4.10(a) and being vulnerable to instability under parameter errors more than the braking mode.

The locus of the closed-loop poles (3.33) at the rated torque (motoring) is shown in Fig. 4.11(a) where the poles are seen moving towards the positive plane at low speeds. During braking mode in Fig. 4.11(b), the poles are confined to second quadrant at all speeds. The region of instability at low speed (0.2 p.u.) is mapped in the dq current plane in Fig. 4.11(c); the motoring operation at high load is susceptible which is coherent with the poor signal quality in Fig. 4.22(a). No unstable regions were identified at medium and high speeds which makes the FS technique more robust respect to the ones presented so far.

4.4.3 Experimental Results

The stability analysis is validated with the control resistance perturbation at rated torque and 300 rpm (0.2 p.u.) in motoring and braking operation as shown in Figs. 4.12(a) and 4.12(b), respectively.

The motoring operation is observed to be unstable while the braking is stable.

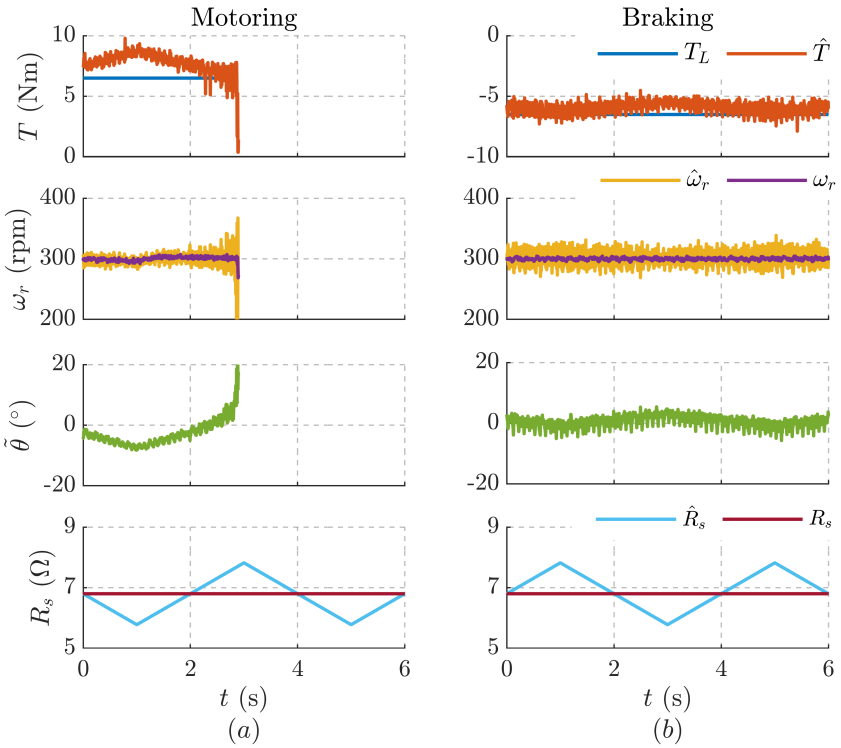

Figure 4.12: FS position observer stability analysis with resistance perturbation of ±15% error, $\tilde{R}_s = \pm 0.15\, R_s$ at 300 rpm (0.2 p.u.) and rated torque: (a) Motoring; (b) Braking. Motor: *A*.

This corroborates the stability analysis in Fig. 4.11(c) where the rated torque in motoring (denoted by the marker □) is at close proximity to the instability region at 300 rpm (0.2 p.u.).

4.5 Summary of the Chapter Contributions

The main contributions of the chapter are enumerated as follows:

1. The generalized projection vector approach defined in Chapter 3 is here used for the direct comparison of different flux-observer-based position observers.

2. Three state-of-art sensorless techniques are comparatively studied under this common lens where each technique is characterized by a unique vector under the common mathematical definition of projection vector. They are subjected to stability analysis at identical operating conditions with a control resistance perturbation test to validate the analytical evaluations.

3. Regions of instability were identified for the three schemes: both CP and AF

position observers are unstable at low speeds braking and at high speeds flux-weakening operation while the FS position observer is found to be unstable at low speeds motoring operation.

Chapter 5

Auxiliary-Flux Position Observer (AUX)

The contributions in the design and development of the auxiliary-flux position observer are published in [47].

5.1 Introduction

Following the review of the known fundamental-wave excitation schemes in Chapter 4 where the regions of instability were identified and experimentally corroborated, two new solution are proposed in this work to ensure stability at all operations points: *(i)* Auxiliary-flux position observer (AUX); *(ii)* Adaptive projection vector for position error estimation (APP). The new APP sensorless scheme, designed for improved stability, is treated separately in the following Chapter 6.

The new auxiliary-flux based position observer is designed in Section 5.2 where the projection vector is defined along the auxiliary-flux vector [47]. It is developed to mitigate the instability problems of established schemes like active-flux observer while retaining its simplicity and computational ease. The sensitivity of the AUX scheme to flux-map LUTs parameter errors is presented in Section 5.3 along with the experimental validation. Finally, the auxiliary-flux position observer with adaptive gain [25] is discussed in Section 5.4 where the flux observer gain $\boldsymbol{G}$ is adapted to decouple the position and the flux observer, resulting in a constant bandwidth at all operating points with fixed poles.

5.2 AUX Position Observer

The auxiliary-flux position observer is introduced in [47] where the projection vector is designed along the observed auxiliary-flux vector. This scheme is denoted

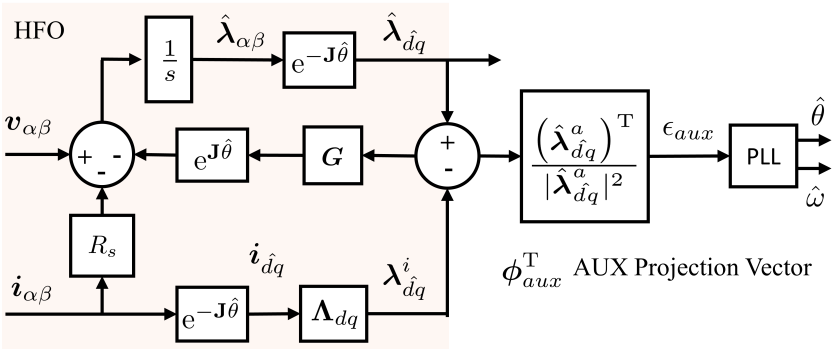

Figure 5.1: Block diagram of the auxiliary-flux based position observer for direct position estimation without a PLL [12].

by the acronym AUX and the subscript aux. The block diagram of the AUX scheme is shown in Fig. 5.1.

5.2.1 Projection Vector Design

To mitigate the instability problems of the former methods while retaining the simplicity, the MMAP-based auxiliary-flux position observer is developed. The auxiliary-flux (3.10) defined in Section 3.2.2 is the discrepancy between the voltage and the current-model flux estimates scaled by the position error, i.e.,

$$\boldsymbol{\lambda}_{\hat{d}\hat{q}} = \boldsymbol{\lambda}^{i}_{\hat{d}\hat{q}} + \tilde{\theta}\,\boldsymbol{\lambda}^{a}_{\hat{d}\hat{q}} = \boldsymbol{L}^{i}\,\boldsymbol{i}_{\hat{d}\hat{q}} + \boldsymbol{\lambda}_{m} + \tilde{\theta}\,\boldsymbol{\lambda}^{a}_{\hat{d}\hat{q}} \tag{5.1}$$

Reformulating (5.1) to obtain the position error leads to

$$\tilde{\theta} = \frac{\left(\boldsymbol{\lambda}^{a}_{\hat{d}\hat{q}}\right)^{\mathrm{T}}}{|\boldsymbol{\lambda}^{a}_{\hat{d}\hat{q}}|^2}\left(\boldsymbol{\lambda}_{\hat{d}\hat{q}} - \boldsymbol{L}^{i}\,\boldsymbol{i}_{\hat{d}\hat{q}} - \boldsymbol{\lambda}_{m}\right) \tag{5.2}$$

The expression (5.2) differs from the equivalent position error of the fundamental saliency method (4.19) in that (5.2) relies on the current-model inductance $\boldsymbol{L}^{i}$ whereas (4.19) on the real inductance $\boldsymbol{L}$. Using the observed stator flux ($\boldsymbol{\lambda}_{\hat{d}\hat{q}} \rightarrow \hat{\boldsymbol{\lambda}}_{\hat{d}\hat{q}}$) in (5.2), a natural choice for the position error signal is along MMAP-based the auxiliary-flux vector as

$$\epsilon_{aux} = \boldsymbol{\phi}^{\mathrm{T}}_{aux}\left(\hat{\boldsymbol{\lambda}}_{\hat{d}\hat{q}} - \boldsymbol{\lambda}^{i}_{\hat{d}\hat{q}}\right) \tag{5.3}$$

where the AUX projection vector is given by

$$\boldsymbol{\phi}^{\mathrm{T}}_{aux} = \frac{\left(\hat{\boldsymbol{\lambda}}^{a}_{\hat{d}\hat{q}}\right)^{\mathrm{T}}}{|\hat{\boldsymbol{\lambda}}^{a}_{\hat{d}\hat{q}}|^2}. \tag{5.4}$$

The comparison of (4.21) and (5.4) suggests that the AUX approach is equivalent to the FS approach, but with the improved MMAP in place of the approximated CMM.

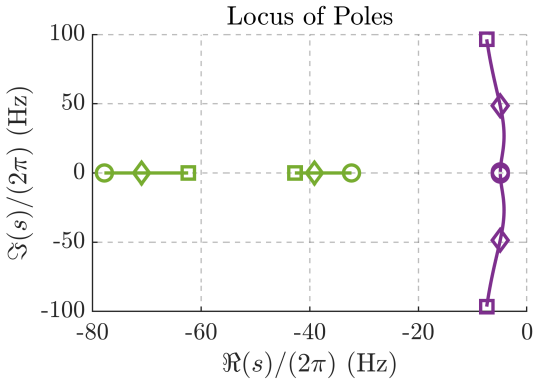

Figure 5.2: Locus of poles of flux (purple) and position (green) observer for AUX position observer. Speed Markers: ∘ is 0.1 p.u., ⋄ is 1 p.u. and □ is 2 p.u. Parameters: flux observer gain $g = 2\pi \cdot 10$ rad/s and PLL gain $\Omega_\omega = 2\,\pi \cdot 50$ rad/s.

5.2.2 Stability Analysis

The dc-gain of transfer function (3.31) with $\boldsymbol{G} = g\,\mathbf{I}$ for the AUX projection vector (5.4) is given by

$$\boldsymbol{\phi}_{aux}^{\mathrm{T}}\,\boldsymbol{h}_{\tilde{\theta}}\Big|_{s=0} = \frac{\omega^2}{g^2+\omega^2}. \tag{5.5}$$

Differing from the former three schemes, the gain (5.5) is only dependent on the square of angular speed ω and not the operating point $\boldsymbol{i}_{dq}$. Hence, a minimum signal strength of 0.5 is ensured at the low speed $\omega = g$ and progressively increasing at higher speeds.

Using (5.4) in (3.33), the eigenvalues are traced in Fig. 5.2 for electrical speeds from zero to twice rated. The poles are confined to the second quadrant at all operating points, thus ensuring stability. This further highlights the significance of MMAP model in designing stable control systems.

5.2.3 Experimental Results

Parameters: switching frequency 5 kHz, flux observer gain $g = 2\pi \cdot 10$ rad/s and PLL gain $\Omega_\omega = 2\pi \cdot 25$ rad/s. The speed PI controller is tuned for critically damped poles at $s = -2\pi \cdot 1$ rad/s. A minimum current $i_d^{min} = 1$ A is imposed for fundamental excitation at high speeds.

Control Resistance Perturbation

The performance of the AUX position observer under control resistance perturbation at rated torque and 300 rpm in motoring and braking operation is shown in Figs. 5.3(a) and 5.3(b), respectively. The control is stable as ascertained in the

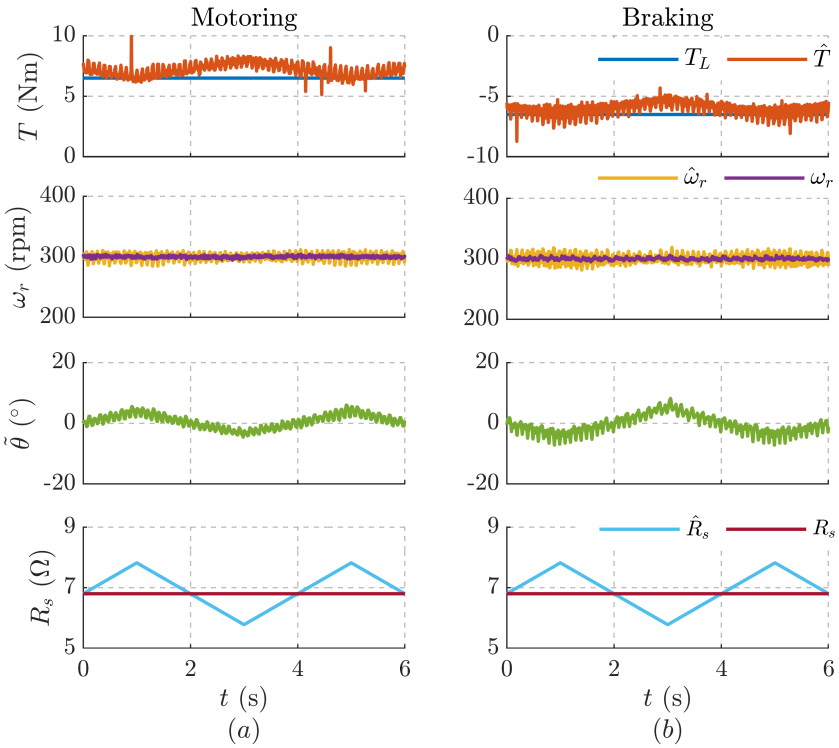

Figure 5.3: AUX position observer stability analysis with resistance perturbation of ±15% error, $\tilde{R}_s = \pm 0.15\, R_s$ at 300 rpm (0.2 p.u.) and rated torque: (a) Motoring; (b) Braking. Motor: *A*.

former analysis. The position error and the estimated torque are observed to be susceptible to the resistance perturbations.

Dynamic Stiffness

The test for dynamic stiffness of the AUX scheme is performed at rated speed with a rated step in load torque in Fig. 5.4(a) and a rated reversal in load torque in Fig. 5.4(b). The position error is observed to be negligible.

To demonstrate faster dynamic performance, a rated torque reversal is imposed at half-rated speed with the poles of speed PI controller at $s = -2\pi \cdot 1$ rad/s and $s = -2\pi \cdot 3$ rad/s in Figs. 5.5(a) and 5.5(b), respectively. About 50% reduction in speed sag is observed from 150 rpm in Fig. 5.5(a) to 75 rpm in Fig. 5.5(b). As expected, the trade-off is the increase in high-frequency noise that can discerned in the measured current and the estimated torque.

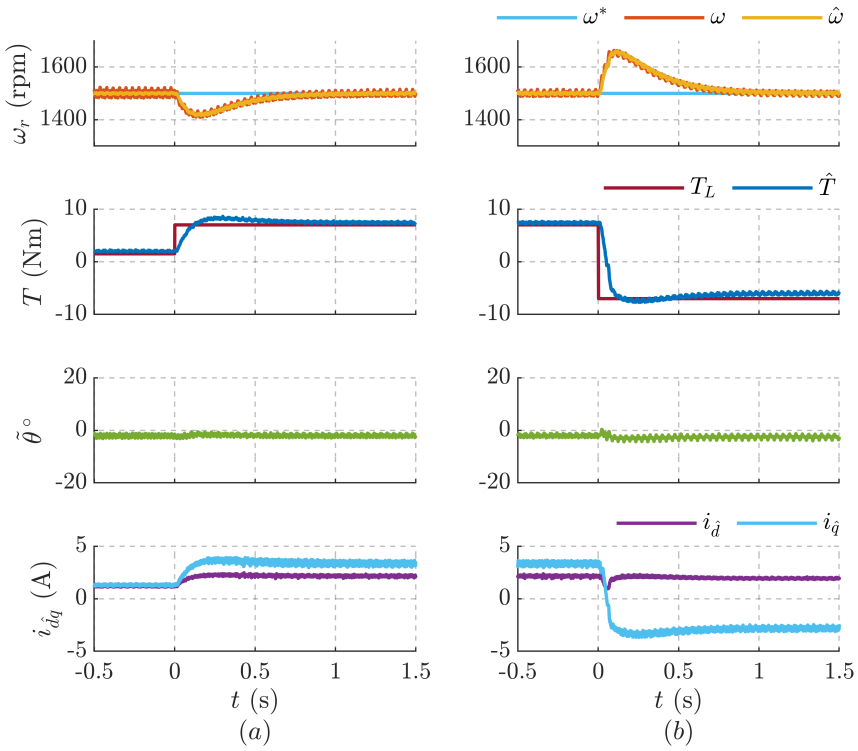

Figure 5.4: Test for dynamic stiffness with rated load torque step at rated speed $\omega = 2\pi \cdot 50$ rad/s: (a) $T_L = 0 \rightarrow 7.1$ Nm at $t = 0$ s; (b) $T_L = +7.1 \rightarrow -7.1$ Nm at $t = 0$ s. Motor: A.

5.3 Sensitivity to Parameter Errors

The sensitivity of the AUX scheme to the current-model flux errors is first evaluated analytically and then corroborated experimentally. Note that the former schemes can be subjected to similar sensitivity analysis.

5.3.1 Susceptibility to Flux-Map Errors

Under inaccurate flux-map LUTs, the steady-state position error for the auxiliary-flux projection vector (5.4) can be computed from (3.29) as

$$\tilde{\theta}_0 = -\frac{\left(\hat{\boldsymbol{\lambda}}^{a}_{\hat{d}\hat{q}}\right)^{\mathrm{T}}}{\omega|\hat{\boldsymbol{\lambda}}^{a}_{\hat{d}\hat{q}}|^2}\left(\omega\mathbf{I} + g\,\mathbf{J}\right)\tilde{\boldsymbol{\lambda}}^{i}_{\hat{d}\hat{q}}. \tag{5.6}$$

Figs. 5.6(a) and 5.6(b) show the contour plots of steady-state position error for +15% error in d-axis, $\hat{\lambda}^{i}_{\hat{d}} = 0.85\,\lambda_{\hat{d}}$, at the electrical speeds $\omega = 2\pi \cdot 15$ rad/s and $\omega = 2\pi \cdot 40$ rad/s, respectively. It can be discerned that the sensitivity to parameter

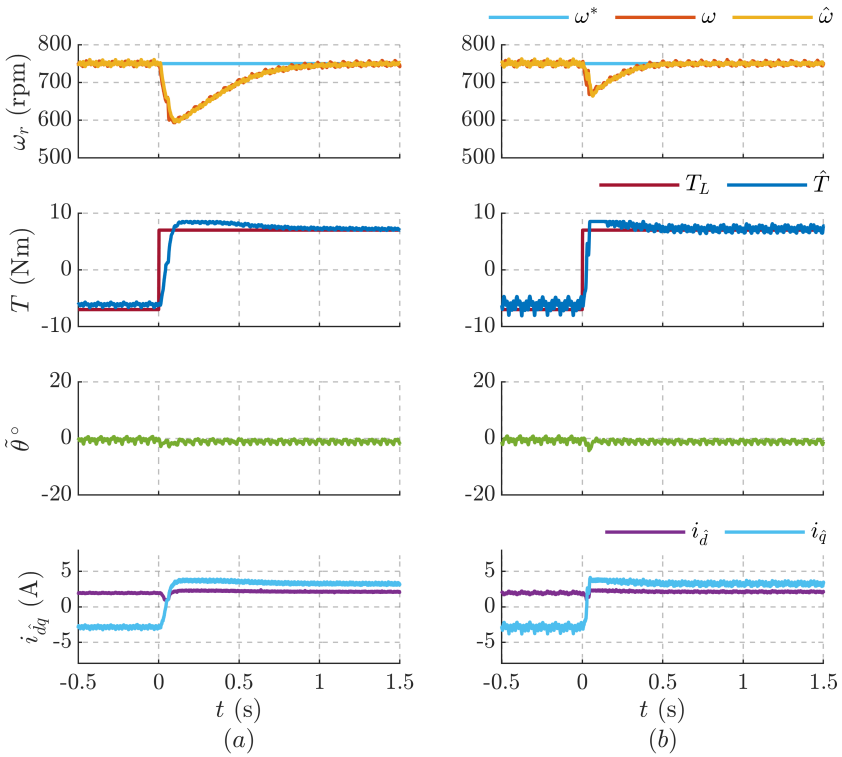

Figure 5.5: Comparative torque step test with speed controller tuned for critical damping at: (a) $s = -2\pi \cdot 1$ rad/s; (b) $s = -2\pi \cdot 3$ rad/s. Rated load torque reversal $T_L = -7.1 \rightarrow +7.1$ Nm at $t = 0$ s and speed $\omega = 2\pi \cdot 25$ rad/s (0.5 p.u). Motor: *A*.

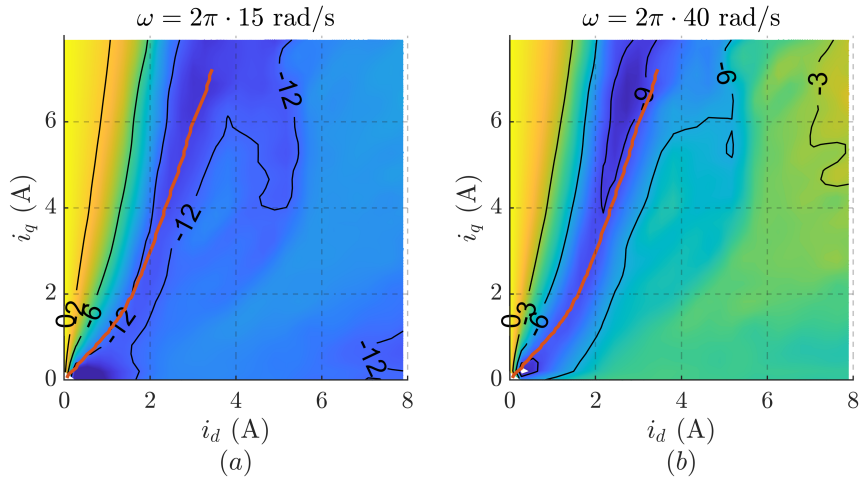

Figure 5.6: The steady-state position error $\tilde{\theta}_0$ in degrees (electrical) for +15% error in d-axis flux-map, $\hat{\lambda}_{\hat{d}}^{i} = 0.85\,\lambda_{\hat{d}}$, at different electrical speeds: (a) $\omega = 2\pi \cdot 15$ rad/s; (b) $\omega = 2\pi \cdot 40$ rad/s. In red is the MTPA trajectory. Motor: *A*.

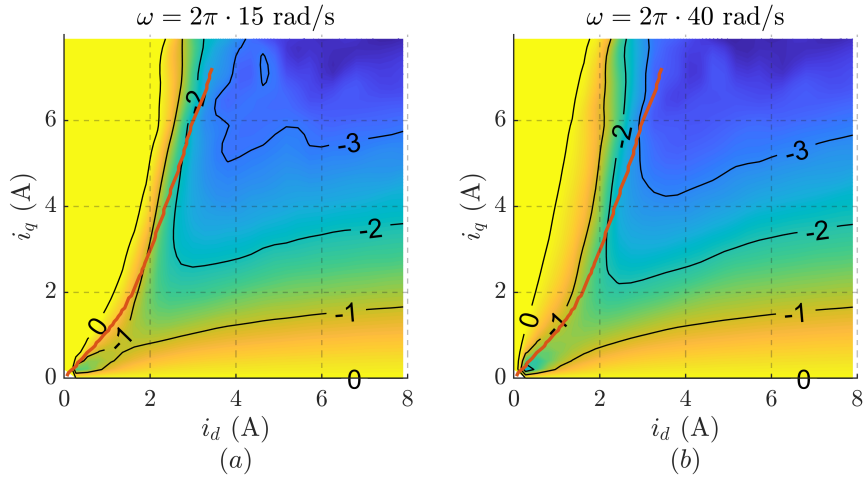

Figure 5.7: The steady-state position error $\tilde{\theta}_0$ in degrees (electrical) for +15% error in q-axis flux-map, $\hat{\lambda}^i_{\hat{q}} = 0.85\,\lambda_{\hat{q}}$, at different electrical speeds: (a) $\omega = 2\pi \cdot 15$ rad/s; (b) $\omega = 2\pi \cdot 40$ rad/s. In red is the MTPA trajectory. Motor: *A*.

error is high at lower speeds with position error of approximately $-12°$ along the MTPA trajectory.

Fig. 5.7 reports the similar evaluation for +15% error in q-axis, $\hat{\lambda}^i_{\hat{q}} = 0.85\,\lambda_{\hat{q}}$ where the maximum position error is approximately $-3°$; as expected, it is less sensitive than d-axis due to the smaller absolute error ($\tilde{\lambda}^i_q < \tilde{\lambda}^i_d$).

5.3.2 Experimental Results

The sensitivity to d-axis flux-map error is evaluated at rated load torque by imposing an incremental error from +15% ($\hat{\lambda}^i_{\hat{d}} = 0.85\,\lambda_{\hat{d}}$) to -15% ($\hat{\lambda}^i_{\hat{d}} = 1.15\,\lambda_{\hat{d}}$) in steps of 5% increment every 0.5 s at two different speeds. The position error for +15% d-axis error ($t < 0.5$ s) at low speed $\omega = 2\pi \cdot 15$ rad/s in Fig. 5.8(a) is approximately $-11°$ and at high speed $\omega = 2\pi \cdot 40$ rad/s in Fig. 5.8(b) is approximately $-7°$. The experimental result corroborates the analytical evaluation of steady-state position error in Fig. 5.6.

In a similar fashion, the sensitivity to q-axis flux-map is evaluated at rated load torque by imposing an incremental error from +15% ($\hat{\lambda}^i_{\hat{q}} = 0.85\,\lambda_{\hat{q}}$) to -15% ($\hat{\lambda}^i_{\hat{q}} = 1.15\,\lambda_{\hat{q}}$) in steps of 5% increment at two different speeds. The position error for +15% q-axis error ($t < 0.5$ s) at either speeds in Fig. 5.9 is approximately $-3°$, corroborating the analytical evaluation of the steady-state position error in Fig. 5.7.

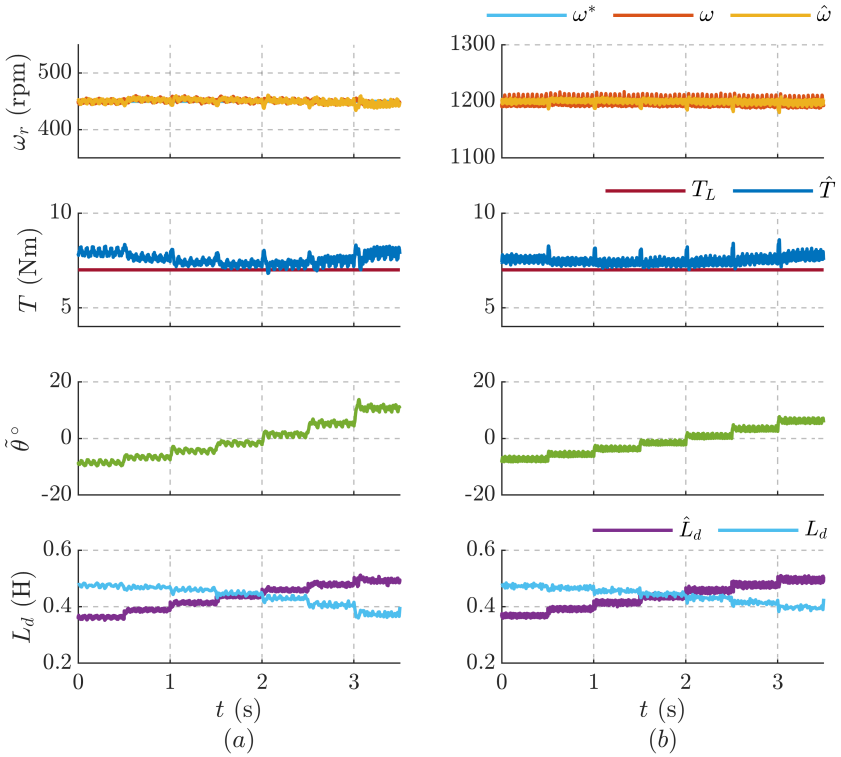

Figure 5.8: Sensitivity to error in d-axis flux-map, +15% ($\hat{\lambda}^i_{\hat{d}} = 0.85\,\lambda_{\hat{d}}$) → -15% ($\hat{\lambda}^i_{\hat{d}} = 1.15\,\lambda_{\hat{d}}$) in steps of 5% increment every 0.5 s at: (a) $\omega = 2\pi \cdot 15$ rad/s; (b) $\omega = 2\pi \cdot 40$ rad/s. Motor: A.

5.4 Auxiliary-Flux Position Observer with Adaptive Gain (AG)

For the sake of completeness, the adaptive gain flux observer proposed in [25] for decoupled position and flux observers is briefly reviewed. This scheme is denoted by the acronym AG.

5.4.1 Design and Stability Analysis

Hitherto, the analysis only examined the dc-gain of the transfer function (3.31) barring the dynamics ($s = 0$). Adaptive-gain position observer is proposed in [25], [26] where the flux observer gain is adapted such that the dynamics of the position and the flux observer are decoupled, i.e.,

$$\boldsymbol{\phi}_{aux}^{\mathrm{T}}\, \boldsymbol{h}_{\tilde{\theta}}(s) = 1 \tag{5.7}$$

To this end, the transfer function (3.31) can be manipulated as

$$\boldsymbol{\phi}_{aux}^{\mathrm{T}}\, \boldsymbol{h}_{\tilde{\theta}}(s) = \boldsymbol{\phi}_{aux}^{\mathrm{T}}\, \hat{\boldsymbol{\lambda}}^a_{\hat{d}q} - \boldsymbol{\phi}_{aux}^{\mathrm{T}}\, (s\mathbf{I} + \boldsymbol{G} + \omega\mathbf{J})^{-1}\, \boldsymbol{G}\, \hat{\boldsymbol{\lambda}}^a_{\hat{d}q}. \tag{5.8}$$

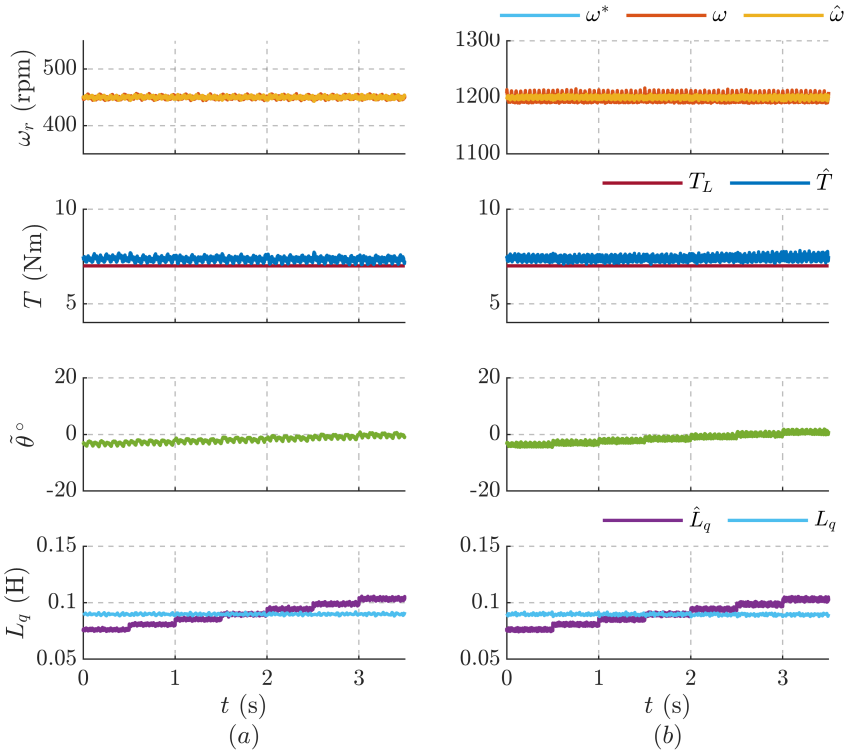

Figure 5.9: Sensitivity to error in q-axis flux-map, +15% ($\hat{\lambda}^i_{\hat{q}} = 0.85\,\lambda_{\hat{q}}$) → -15% ($\hat{\lambda}^i_{\hat{q}} = 1.15\,\lambda_{\hat{q}}$) in steps of 5% increment every 0.5 s at: (a) $\omega = 2\pi \cdot 15$ rad/s; (b) $\omega = 2\pi \cdot 40$ rad/s. Motor: *A*.

If the gain $\boldsymbol{G}$ is adapted such that $\boldsymbol{G}\,\hat{\boldsymbol{\lambda}}^a_{\hat{d}q} = 0$, then it follows from (5.4) and (5.8) that condition for decoupling in (5.7) is satisfied. The adaptive-gain to satisfy the condition $\boldsymbol{G}\,\hat{\boldsymbol{\lambda}}^a_{\hat{d}q} = 0$ is given by

$$\boldsymbol{G} = \begin{bmatrix} k_1 \\ k_2 \end{bmatrix} \frac{\left(\hat{\boldsymbol{\lambda}}^a_{\hat{d}q}\right)^{\mathrm{T}}}{|\hat{\boldsymbol{\lambda}}^a_{\hat{d}q}|^2}\,\mathbf{J} \tag{5.9}$$

where k_1 and k_2 are the additional degrees of freedom to design the locus of the flux observer poles. For comparison with former schemes, the poles are placed at $s = -g \pm \omega$ as

$$\det\left(s\,\mathbf{I} + \boldsymbol{G} + \omega\mathbf{J}\right) = (s+g)^2 + \omega^2. \tag{5.10}$$

Solving, the gains are given by

$$\begin{bmatrix} k_1 \\ k_2 \end{bmatrix} = \frac{g}{\omega} \begin{bmatrix} g & 2\omega \\ -2\omega & g \end{bmatrix} \hat{\boldsymbol{\lambda}}^a_{\hat{d}q}. \tag{5.11}$$

The locus of poles for the adaptive-gain approach is are shown in Fig. 5.10. It

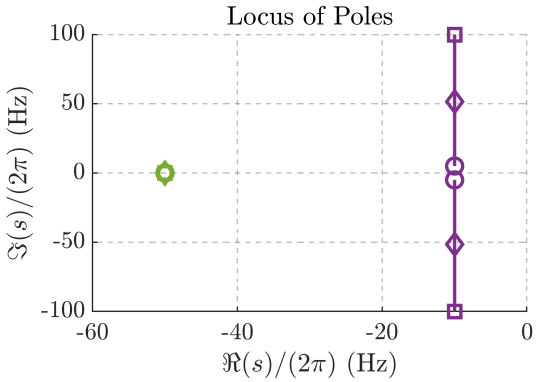

Figure 5.10: Locus of poles of flux (purple) and position (green) observer for AG position observer. Speed Markers: ∘ is 0.1 p.u., ⋄ is 1 p.u. and □ is 2 p.u. Parameters: $g = 2\pi \cdot 10$ rad/s and $\Omega_\omega = 2\,\pi \cdot 50$ rad/s.

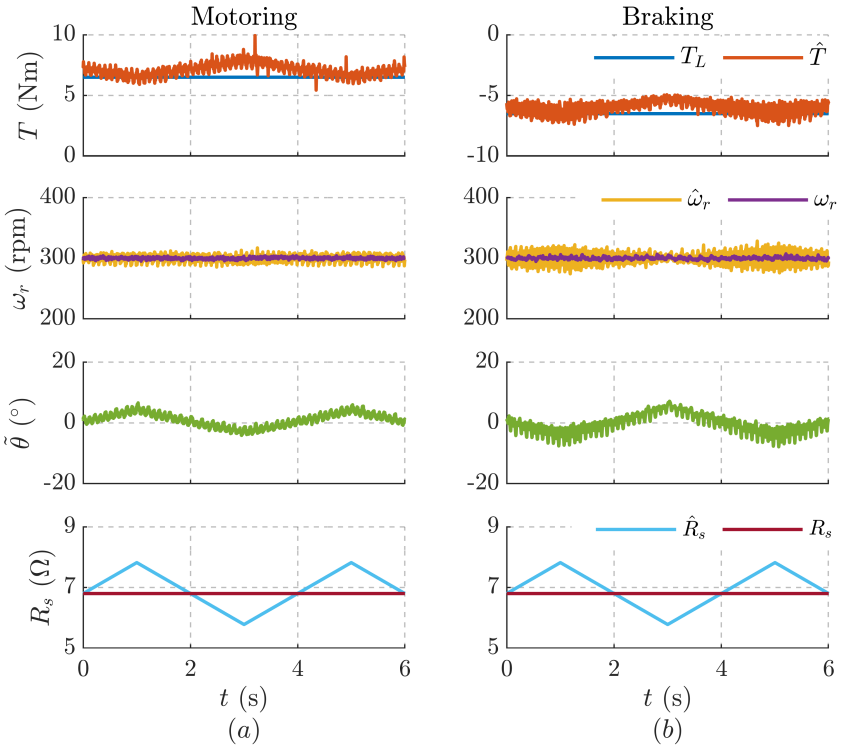

Figure 5.11: AG position observer stability analysis with resistance perturbation of ±15% error, $\tilde{R}_s = \pm\,0.15\,R_s$ at 300 rpm (0.2 p.u.) and rated torque: (a) Motoring; (b) Braking. Motor: *A*.

can be observed that the poles are coincident with the design parameter, unlike the AUX in Fig. 5.2, due to dynamic decoupling of the two observers.

5.4.2 Experimental Results

The experimental validation of AG position observer under control resistance perturbation at rated torque and 300 rpm in Fig. 5.11 shows that the system is stable for motoring and braking operations although the position error is susceptible to the resistance variations.

5.5 Summary of the Chapter Contributions

The main contributions of the chapter are enumerated as follows:

1. A new MMAP-based auxiliary-flux position observer is developed to mitigate the stability problems of the existing techniques while retaining the simplicity and the ease of implementation. The FS scheme is shown to be equivalent to CMM-based auxiliary-flux scheme, thus illustrating the significance of MMAP-based design for stable position observers.

2. The robustness of AUX position observer to the current-model flux error in LUTs is formulated analytically. The experiment results corroborate the steady-state position error from the analytical evaluation.

Chapter 6

Adaptive Projection Vector for Position Error Estimation (APP)

The development of the adaptive projection vector for position error and speed error estimation for high speed sensorless control is published in [23][24]. The findings of the stator resistance immunity property of the APP scheme and parameter adaptation are published in [11][12].

6.1 Introduction

This chapter introduces a new fundamental-excitation based sensorless technique namely adaptive projection vector for position error estimation (APP). The APP projection vector is designed from the results of the flux estimation error dynamics and the linearized error signal (3.28) for obtaining a position tracking response independent of the operating conditions and without regions of instability, as described in succeeding Section 6.2. In addition to position error estimation, this chapter shows that the orthogonal projection vector offers an additional degree of freedom, used in the following either for independent speed error estimation in Section 6.3 or for parameters adaptation in Section 6.5.

The sensitivity of the APP position observer to parameter errors in flux-map LUTs and stator resistance is investigated in Section 6.4. Unlike the former AUX scheme, the APP technique is immune to stator resistance on the MTPA trajectory. The prospect of adaptation for operation under inaccurate parameters is discussed in Section 6.5. The closed-loop stability analysis of the APP scheme with stator resistance adaptation and d-axis current-model flux adaptation is presented. Following the experimental validation, the contributions of this chapter are summarized in Section 6.6.

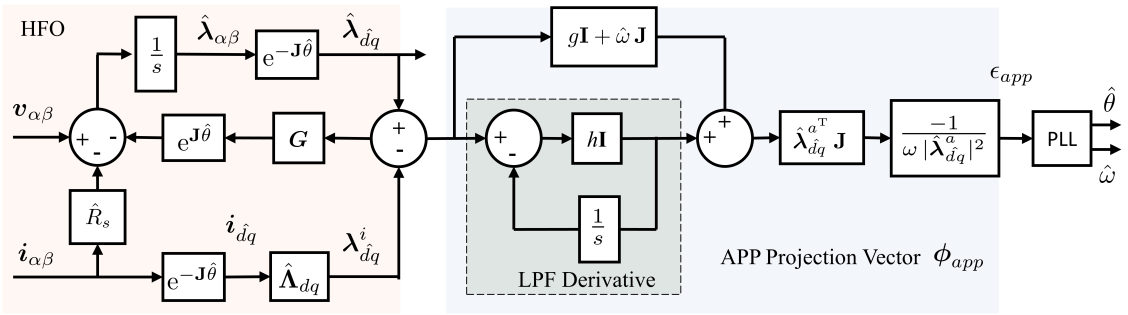

Figure 6.1: Block diagram of the proposed APP position observer where h is the bandwidth of the low-pass-filtered derivative term.

6.2 APP Position Observer

6.2.1 Design and Analysis

Denoted by the acronym APP and the subscript *app*, the APP position error projection vector $\boldsymbol{\phi}_{app}$ is designed to hold the equality between position error signal and position error, $\epsilon_{app} = \tilde{\theta}$, in the absence of parametric errors, i.e., $\boldsymbol{\phi}_{app}^{\mathrm{T}}\,\boldsymbol{h}_{\tilde{\theta}} = 1$. From (3.28), this leads to a projection vector of nature:

$$\boldsymbol{\phi}_{app}^{\mathrm{T}} = \frac{-1}{\omega\,|\hat{\boldsymbol{\lambda}}_{\hat{d}q}^{a}|^2}\,\left(\hat{\boldsymbol{\lambda}}_{\hat{d}q}^{a}\right)^{\mathrm{T}}\mathbf{J}\left(s\,\mathbf{I}+\boldsymbol{G}+\omega\,\mathbf{J}\right). \tag{6.1}$$

However, the ideal derivate term ($s\mathbf{I}$) in the projection vector is practically unfeasible as it is prone to amplify the high frequency noise. Hence, a low-pass-filtered derivative is computed instead with a bandwidth h rad/s as shown in the block diagram in Fig. 6.1. Considering the LPF derivative, the projection vector transforms to

$$\boldsymbol{\phi}_{app}^{\mathrm{T}} = \frac{-1}{\omega\,|\hat{\boldsymbol{\lambda}}_{\hat{d}q}^{a}|^2}\,\left(\hat{\boldsymbol{\lambda}}_{\hat{d}q}^{a}\right)^{\mathrm{T}}\mathbf{J}\left(\frac{sh}{s+h}\,\mathbf{I}+\boldsymbol{G}+\omega\,\mathbf{J}\right). \tag{6.2}$$

For $\boldsymbol{G} = g\,\mathbf{I}$, the transfer function $\boldsymbol{\phi}_{app}^{\mathrm{T}}\,\boldsymbol{h}_{\tilde{\theta}}$ in (3.31) reduces to

$$\boldsymbol{\phi}_{app}^{\mathrm{T}}\,\boldsymbol{h}_{\tilde{\theta}} = \frac{s^2+g^2+\omega^2+s\,g+g\,s\left(\frac{h}{s+h}\right)}{(s+g)^2+\omega^2}. \tag{6.3}$$

As $h\to\infty$, the ideal APP error response $\boldsymbol{\phi}_{app}^{\mathrm{T}}\,\boldsymbol{h}_{\tilde{\theta}} \to 1$ is found, as expected. From (6.3), it is discerned that the $\boldsymbol{\phi}_{app}^{\mathrm{T}}\,\boldsymbol{h}_{\tilde{\theta}}$ is independent of $\hat{\boldsymbol{\lambda}}_{\hat{d}q}^{a}$, $\boldsymbol{i}_{\hat{d}q}$ and the sign of ω. This is valid for any h, including $h=0$, which is a favorable candidate solution as shown in the following.

The frequency response plot of the transfer function (6.3) at various speeds for $h = 0$ rad/s is shown in Fig. 6.2(a), exhibiting a notch filter-like behavior at ω

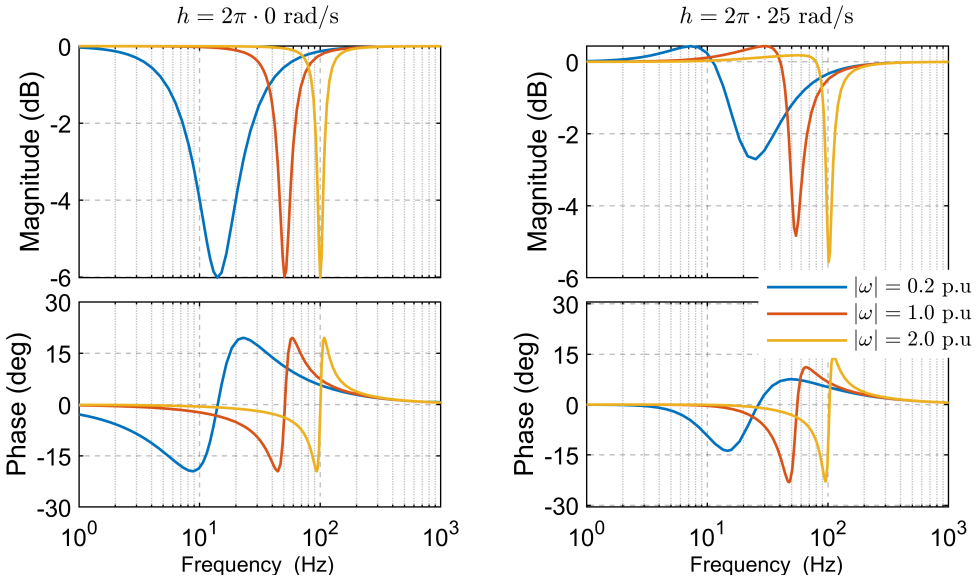

Figure 6.2: Frequency response plot of the transfer function (6.3) at $g = 2\pi \cdot 10$ rad/s exhibiting a notch-filter like behavior: a) $h = 2\pi \cdot 0$ rad/s; b) $h = 2\pi \cdot 25$ rad/s

with -6 dB attenuation of the error amplitude and limited phase distortion. In the presence of derivative term $h = 2\pi \cdot 25$ rad/s in Fig. 6.2(b), a similar band-stop amplitude attenuation is noticed albeit diminished in magnitude.

The locus of poles for the closed loop analysis of position observer (3.33) is shown in Fig. 6.3 at different values of h and is observed to be stable at all operating points. Fig. 6.3(a) shows the poles without the derivative term ($h = 0$) while Fig. 6.3(b) with inclusion of the LPF-derivative term ($h = 2\pi \cdot 25$ rad/s) that introduces an additional pole (yellow). The reference locus of poles with $h = \infty$ for the ideal projection vector (6.1) is shown in Fig 6.3(c) where the flux and the position observers are decoupled.

As inferred from Fig. 6.2, the derivate term brings no substantial benefits to the position error signal to justify the additional complexity and computations. Hence, unless otherwise mentioned, the simplified APP projection vector is used neglecting the derivative term ($h = 0$) as

$$\boldsymbol{\phi}_{app}^{\mathrm{T}} = \frac{-1}{\omega\,|\hat{\boldsymbol{\lambda}}_{\hat{d}\hat{q}}^{a}|^2}\,\left(\hat{\boldsymbol{\lambda}}_{\hat{d}\hat{q}}^{a}\right)^{\mathrm{T}}\mathbf{J}\left(\boldsymbol{G} + \omega\,\mathbf{J}\right). \tag{6.4}$$

Fig. 6.4 shows the frequency response plot of the closed-loop transfer function $\hat{\theta}/\theta$ (3.30) at different operating speeds for the simplified projection vector ($h = 0$) (6.4) and the ideal projection vector with derivative term ($h = \infty$) (6.1). Notice that the closed loop bandwidth is only marginally altered by the absence of derivative term, respect to the reference dashed graph; hence, the simplification is

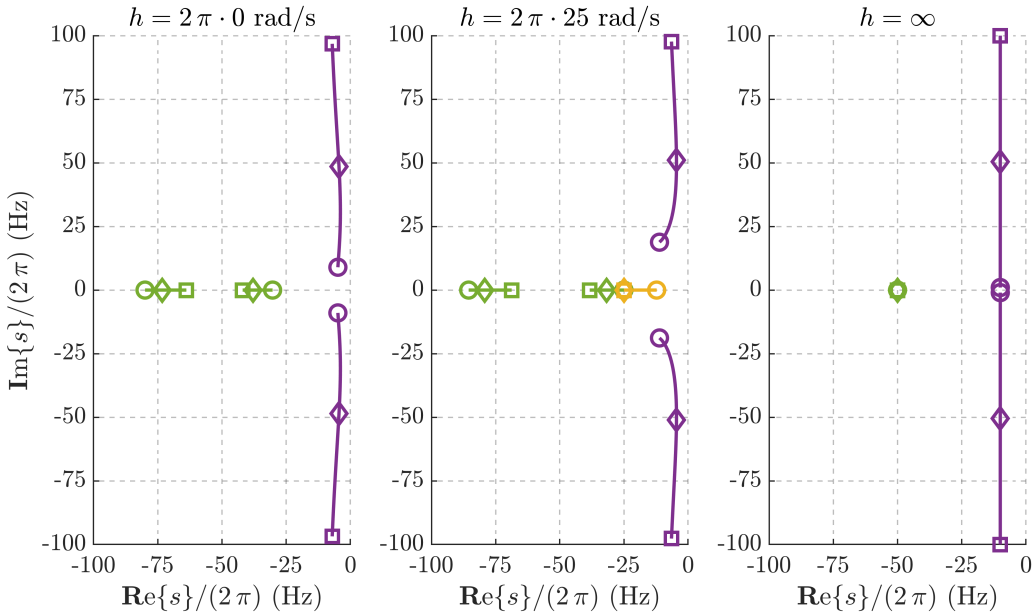

Figure 6.3: Locus of poles of the APP position observer: a) $h = 2\pi \cdot 0$ rad/s; b) $h = 2\pi \cdot 25$ rad/s; (c) $h = \infty$. The circle, diamond and square represents the speeds 0.02 p.u, 1 p.u. and 2 p.u. respectively. The poles of PLL are in green, flux observer in blue and LPF-derivative term in yellow. Parameters: $g = 2\pi \cdot 10$ rad/s and $\Omega_\omega = 2\pi \cdot 50$ rad/s.

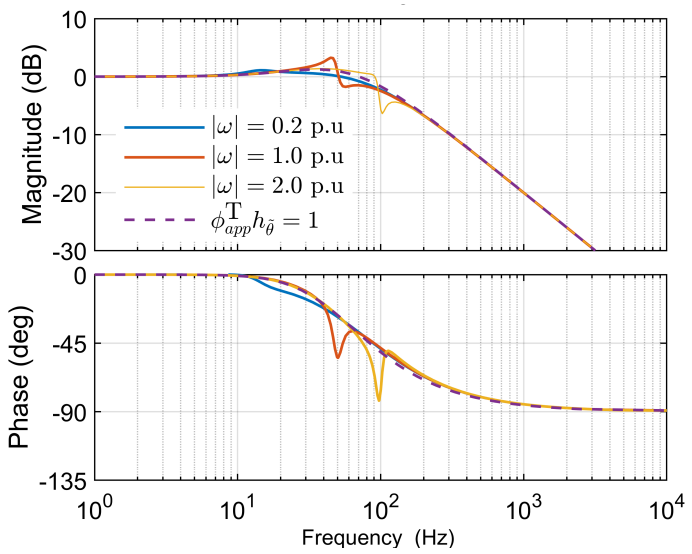

Figure 6.4: Frequency response of closed loop position observer for simplified projection vector (6.4) at three different operating speeds; dotted lines correspond to the ideal projection vector with derivative term (6.1). Parameters: $g = 2\pi \cdot 10$ rad/s, $\Omega_\omega = 2\pi \cdot 50$ rad/s.

considered reasonable.

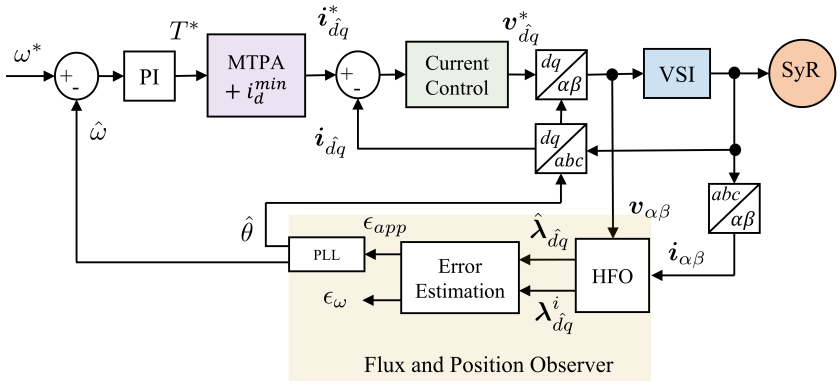

Figure 6.5: Control system depicting the APP position observer aided by hybrid flux observer (HFO). Current vector control can be replaced by any other scheme.

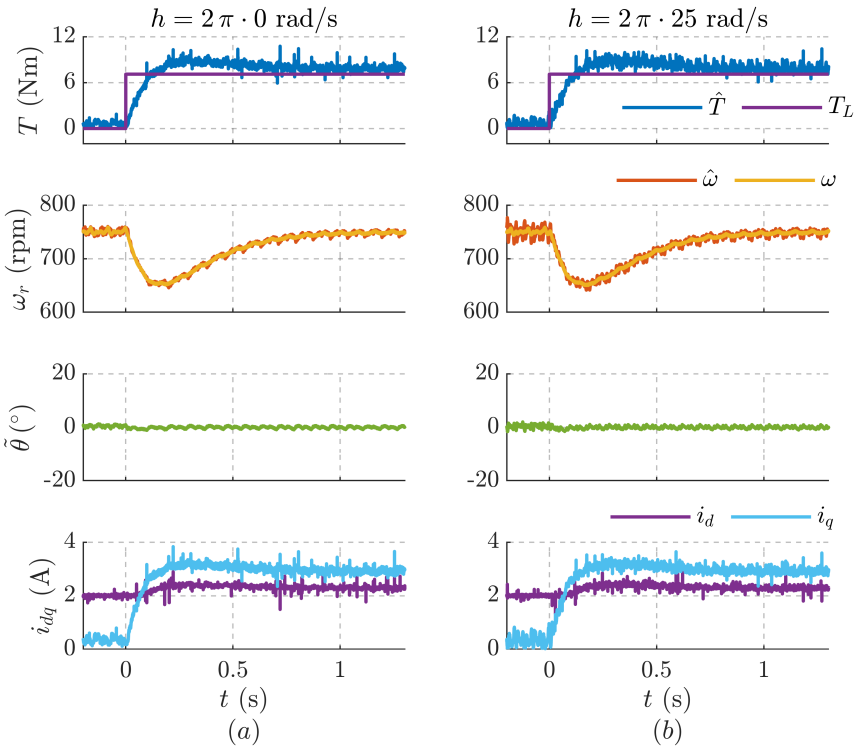

Figure 6.6: Transient performance of the APP technique for a rated step change in load torque, $T_L = 0 \rightarrow 7.1$ p.u, at $\omega = 0.5$ p.u: (a) $h = 2\pi \cdot 0$ rad/s; (b) $h = 2\pi \cdot 25$ rad/s. Motor: *B*.

6.2.2 Experimental Results

The block diagram of the sensorless control system with current vector control is shown in Fig. 6.5. The proposed APP scheme is experimentally validated with SyR motor *B* at a sampling frequency of 10 kHz. The speed controller of the SyR motor

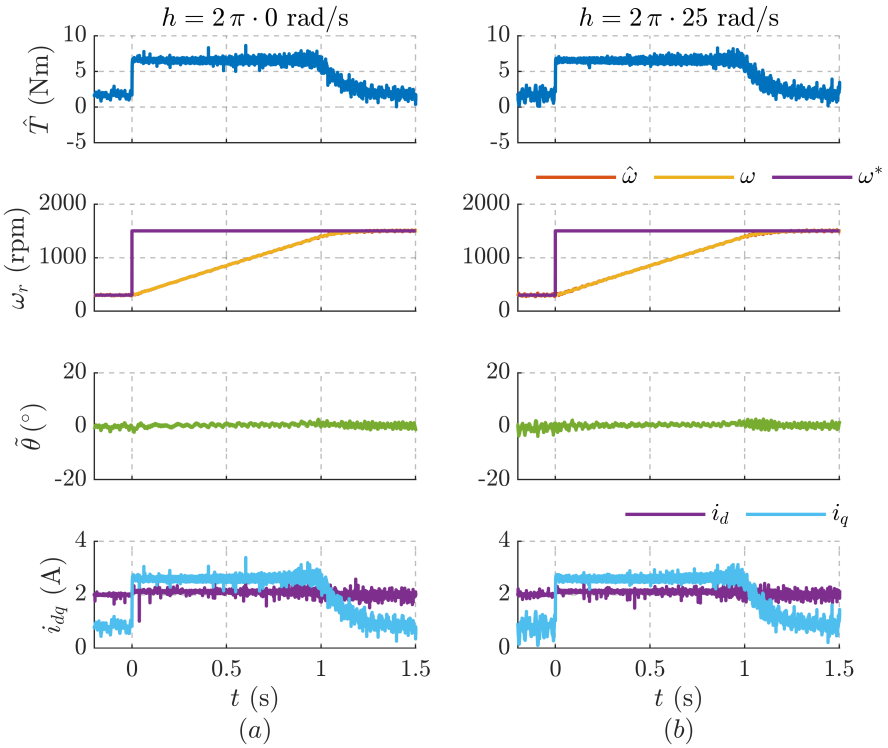

Figure 6.7: Transient performance of the APP technique for a step change in speed reference, $\omega = 0.2 \rightarrow 1$ p.u, at a load torque $T_L = 0.15$ p.u: (a) $h = 2\pi \cdot 0$ rad/s; (b) $h = 2\pi \cdot 25$ rad/s. Motor: *B*.

B is tuned for critical damping at $s = -2\pi \cdot 1$ rad/s while the load torque is imposed by an auxiliary drive. A minimum current $i_d^{min} = 2$ A is imposed for guaranteeing enough saliency and minimum fundamental excitation at no-load. The observer bandwidth $\Omega_\omega = 2\pi \cdot 25$ rad/s is chosen; the estimated speed is low-pass filtered at Ω_ω. The flux observer gain is set to $g = 2\pi \cdot 10$ rad/s.

In addition to the results presented in this section, the validation of APP scheme augmented with a low speed injection-less sensorless technique using finite-control-set model-predictive-control is presented in Section 8.6.4.

Significance of h on Position Estimation

The performance of APP technique with/without the derivative term during transients is analyzed with a step change in load torque and reference speed in Figs. 6.6 and 6.7, respectively. In either case, a negligible transient error in position is observed. This confirms the results of the frequency response analysis: the exclusion of derivative term in Figs. 6.6(a) and 6.7(a) makes little difference as supported by frequency response plot in Fig. 6.2.

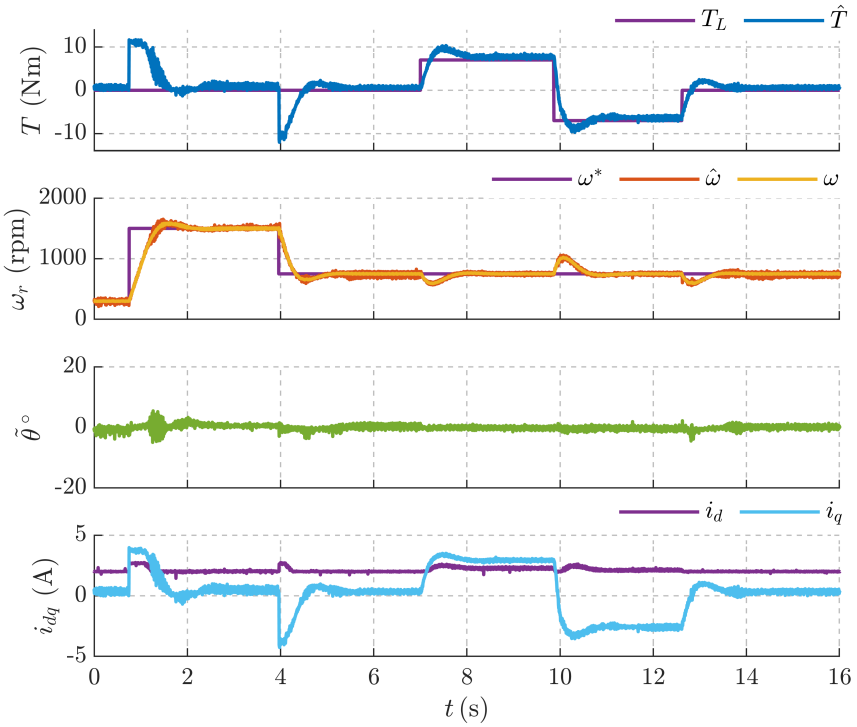

Figure 6.8: Comprehensive performance validation of the APP scheme without the derivative term in motoring and braking operations. Motor: *B*.

Braking Performance Validation

A comprehensive performance validation of the APP scheme without the derivative term ($h = 0$) for operations in motoring and braking regions is shown in Fig. 6.8. The control is discerned to handle the speed step references and the load torque step commands with negligible position error.

6.3 APP with Speed Error Estimation

Recalling the definition of position observer (3.24), the derivative of position error is equivalent to the speed error, $s\,\tilde{\theta} = \tilde{\omega}$ where $\tilde{\omega} = \omega - \hat{\omega}$. Note that the equivalence does not hold for a PID-type mechanical observer [40]. Although the speed error is not employed in the thesis to enhance the PLL performance, it can be a valuable additional input in designing high performance observers [40].

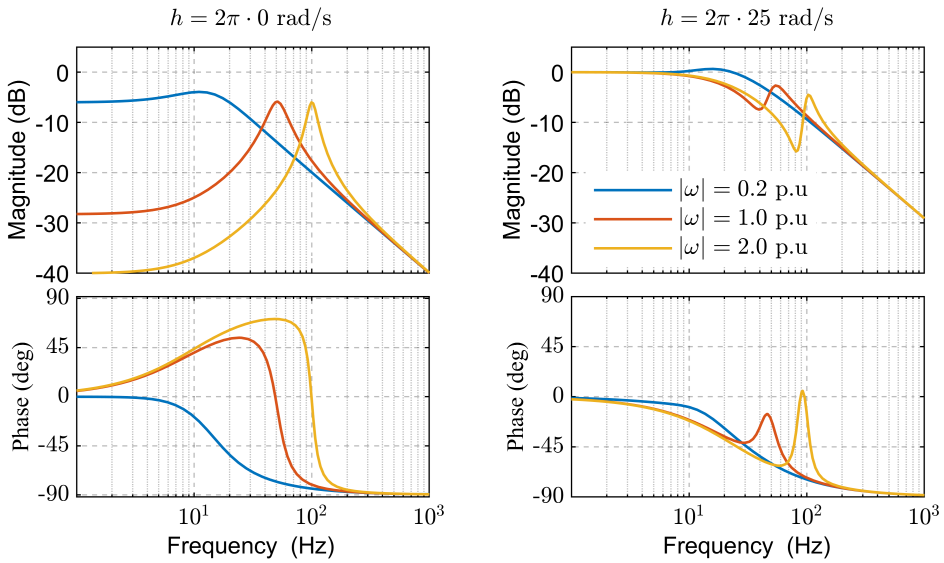

Figure 6.9: Frequency response plot of the transfer function (6.8) at $g = 2\pi \cdot 10$ rad/s exhibiting a LPF behavior: a) $h = 2\pi \cdot 0$ rad/s; b) $h = 2\pi \cdot 25$ rad/s

6.3.1 Design and Analysis

Exploiting the two degrees of freedom of the error domain, a second projection vector orthogonal to the APP vector $\left(\mathbf{J}\,\boldsymbol{\phi}_{app}\right)$ can be utilized for speed error estimation. To this end, the error signal ϵ_j of the orthogonal projection vector is given by

$$\epsilon_j = \left(\mathbf{J}\,\boldsymbol{\phi}_{app}\right)^{\mathrm{T}} (\hat{\boldsymbol{\lambda}}_{\hat{d}q} - \hat{\boldsymbol{\lambda}}^{i}_{\hat{d}q}). \tag{6.5}$$

Under accurate parameters and for $\boldsymbol{G} = g\,\mathbf{I}$, examining (6.5) using the APP projection vector with the derivative term (6.2) leads to

$$\epsilon_j = \left(\mathbf{J}\,\boldsymbol{\phi}_{app}\right)^{\mathrm{T}} \boldsymbol{h}_{\tilde{\theta}}\,\tilde{\theta} = -\frac{g^2 + s\,g + (s^2 + \omega^2 + s\,g)\left(\frac{h}{s+h}\right)}{(s+g)^2 + \omega^2} \cdot s\,\tilde{\theta} \tag{6.6}$$

where, owing to the orthogonality, the steady-state (dc-value) position error has no bearing on the error signal ϵ_j, i.e.,

$$\epsilon_j\Big|_{s=0} = \left(\mathbf{J}\,\boldsymbol{\phi}_{app}\right)^{\mathrm{T}} \boldsymbol{h}_{\tilde{\theta}}\,\tilde{\theta}\Big|_{s=0} = 0. \tag{6.7}$$

The error signal (6.6) is discerned to have a direct correspondence to the speed error. In order to rectify the polarity, the speed error signal is defined as $\epsilon_\omega = -\epsilon_j$; thus, the transfer function between speed error signal and the speed error becomes

$$\frac{\epsilon_\omega}{\tilde{\omega}} = \frac{g^2 + s\,g + (s^2 + \omega^2 + s\,g)\left(\frac{h}{s+h}\right)}{(s+g)^2 + \omega^2}. \tag{6.8}$$

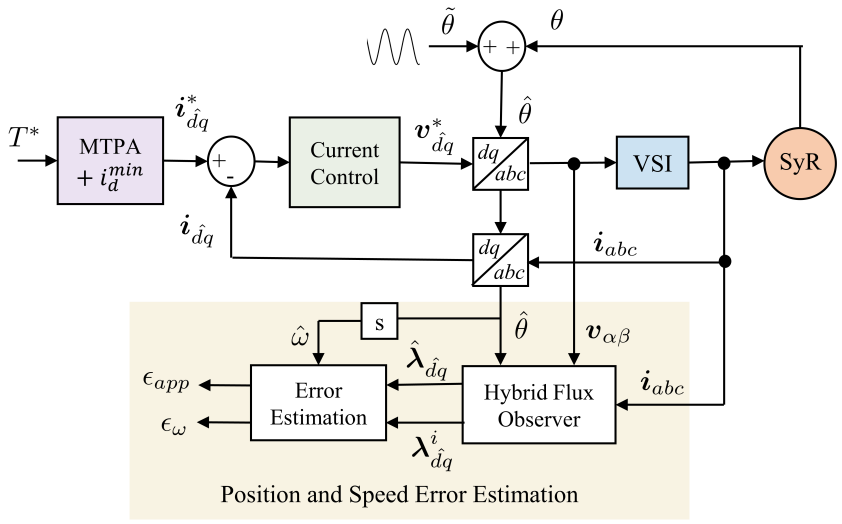

Figure 6.10: Perturbation of encoder measurement to validate speed and position error estimation in the APP sensorless scheme.

Similar to (6.3), the transfer function (6.8) is independent of $\boldsymbol{i}_{\hat{d}q}$ and the sign of ω, and as $h \to \infty$, $\epsilon_\omega \to \tilde{\omega}$.

The frequency response plot of (6.8) at various speeds is shown in Fig. 6.9 where it is seen to be strongly influenced by the derivative term. At $h = 0$ in Fig. 6.9(a), the speed error is unobservable at high speeds due to attenuated amplitude and large phase swing, also a function of speed. Fig. 6.9(b) with $h = 2\pi \cdot 25$ rad/s exhibits a LPF behavior with a cut-off frequency around h. Hence, the derivative term is deemed essential for speed error estimation.

6.3.2 Experimental Results

A perturbation analysis is developed to validate the accuracy of position and speed error estimation. To this end, a sinusoidal disturbance is injected into the encoder position measurement as shown in Fig. 6.10 and the estimated errors are juxtaposed against the reference errors.

Note that the PLL is disabled for this test as the system is no longer sensorless; moreover, the SyR machine is in torque control mode with a constant speed imposed by the auxiliary drive.

Position Error Perturbation Tracking

The position error tracking capability of the APP technique is evaluated with a sinusoidal perturbation of $\tilde{\theta}^* = 10^\circ \sin(2\pi \cdot 25\, t)$ and $\tilde{\theta}^* = 10^\circ \sin(2\pi \cdot 50\, t)$ imposed on the encoder position measurement in Figs. 6.11(a) and 6.11(b), respectively. The notch-filter behavior of the transfer function (6.3) in Fig. 6.2 is experimentally

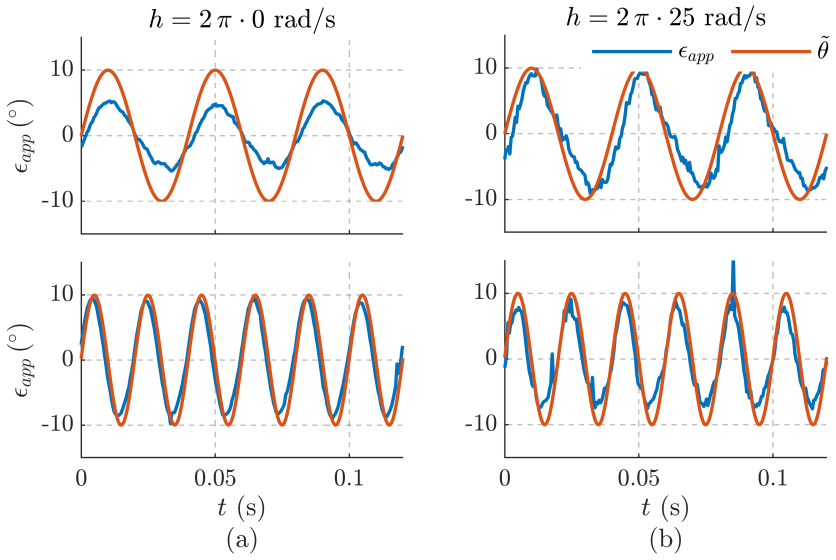

Figure 6.11: Position error estimation of the APP scheme under imposed sinusoidal perturbation of $\tilde{\theta}^* = 10° \sin(2\pi \cdot 25\,t)$ and $\tilde{\theta}^* = 10° \sin(2\pi \cdot 50\,t)$ (electrical) on encoder measurement: a) $h = 2\pi \cdot 0$ rad/s; b) $h = 2\pi \cdot 25$ rad/s . Operating conditions: T = 0.5 p.u. and $\omega = 0.5$ p.u. Motor: *B*.

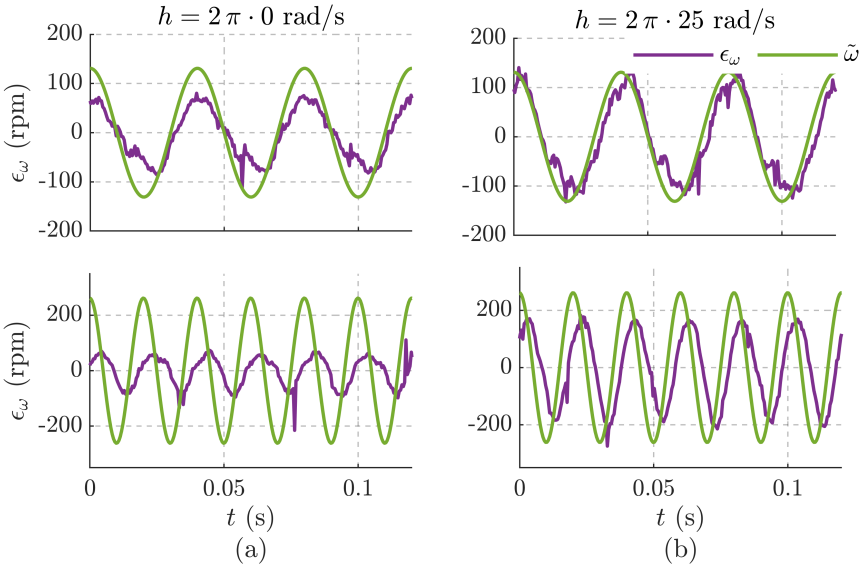

Figure 6.12: Speed error estimation of the APP scheme under imposed sinusoidal perturbation of $\tilde{\theta}^* = 10° \sin(2\pi \cdot 25\,t)$ and $\tilde{\theta}^* = 10° \sin(2\pi \cdot 50\,t)$ (electrical) on encoder measurement: a) $h = 2\pi \cdot 0$ rad/s; b) $h = 2\pi \cdot 25$ rad/s. Operating conditions: T = 0.5 p.u. and $\omega = 0.5$ p.u. Motor: *B*.

corroborated at $\omega = 0.5$ p.u. (25 Hz) and $h = 2\pi \cdot 0$ rad/s in Fig. 6.11(a) where the position error signal ϵ_{app} tracks the $\tilde{\theta}$ oscillations at 50 Hz while it marginally

falters at the notch frequency of 25 Hz. The inclusion of the derivative term aids in tracking the notch frequency as observed in Fig. 6.11(b).

Speed Error Perturbation Tracking

The frequency response plot of the transfer function (6.8) in Fig. 6.9 dictates a low-pass behavior with cut-off frequency at h; accordingly, in Fig. 6.12(b), the speed error signal ϵ_ω at $h = 2\pi \cdot 25$ rad/s tracks accurately the $\tilde{\omega}$ oscillations at 25 Hz but falters at 50 Hz. As expected, the inclusion of derivative term improves the tracking of speed error.

In closing, the analysis demonstrates that the simplified APP ($h = 0$) is an effective alternative to previous fundamental-wave sensorless techniques, providing stable operation, independently of the operating point. If the quadrature projection vector is used for speed error estimation, then the use of the LPF derivative term is essential.

6.4 Sensitivity to Parameter Errors

The sensitivity to parameter errors of the simplified APP projection vector (6.4) is determined by evaluating the steady-state position error $\tilde{\theta}_0$ using (3.29) as

$$\tilde{\theta}_0 = -\frac{\boldsymbol{\phi}_{app}^{\mathrm{T}} \left(\boldsymbol{H}_{\tilde{\boldsymbol{\lambda}}^i} \, \tilde{\boldsymbol{\lambda}}_{\hat{dq}}^{\,i} + \boldsymbol{h}_{\tilde{R}_s} \, \tilde{R}_s \right)}{\boldsymbol{\phi}_{app}^{\mathrm{T}} \, \boldsymbol{h}_{\tilde{\theta}}} \Bigg|_{s=0} = -\boldsymbol{\phi}_{app}^{\mathrm{T}} \left(\boldsymbol{H}_{\tilde{\boldsymbol{\lambda}}^i} \, \tilde{\boldsymbol{\lambda}}_{\hat{dq}}^{\,i} + \boldsymbol{h}_{\tilde{R}_s} \, \tilde{R}_s \right) \Bigg|_{s=0} . \tag{6.9}$$

6.4.1 Stator Resistance Immunity along the MTPA

The sensitivity to stator resistance error is drawn from the steady-state position error expression (6.9) at $\tilde{\boldsymbol{\lambda}}_{\hat{dq}}^{\,i} = 0$ as

$$\tilde{\theta}_0 = -\boldsymbol{\phi}_{app}^{\mathrm{T}} \, \boldsymbol{h}_{\tilde{R}_s} \Big|_{s=0} \cdot \tilde{R}_s = \frac{1}{\omega \, |\hat{\boldsymbol{\lambda}}_{\hat{dq}}^{\,a}|^2} \left(\hat{\boldsymbol{\lambda}}_{\hat{dq}}^{\,a} \right)^{\mathrm{T}} \mathbf{J} \, \boldsymbol{i}_{\hat{dq}} \cdot \tilde{R}_s \tag{6.10}$$

where the term $\left(\hat{\boldsymbol{\lambda}}_{\hat{dq}}^{\,a} \right)^{\mathrm{T}} \mathbf{J} \, \boldsymbol{i}_{\hat{dq}}$ in (6.10) resembles the MTPA law derived in (2.9).

This implies that the APP projection vector (6.4) is immune to stator resistance error so long as the MTPA condition is satisfied. As discussed in Section 3.2.4, the resistance error also encompasses the voltage error due to non-ideal inverter voltage compensation. Thus, the immunity also extends to the errors in dead-time compensation for operations on the MTPA trajectory.

Fig. 6.13(a) shows the contour of the steady-state position error (6.10) for a 25% error in resistance, $\tilde{R}_s = 0.25 \, R_s$, at an operating speed of $\omega = 2\pi \cdot 10$ rad/s. The

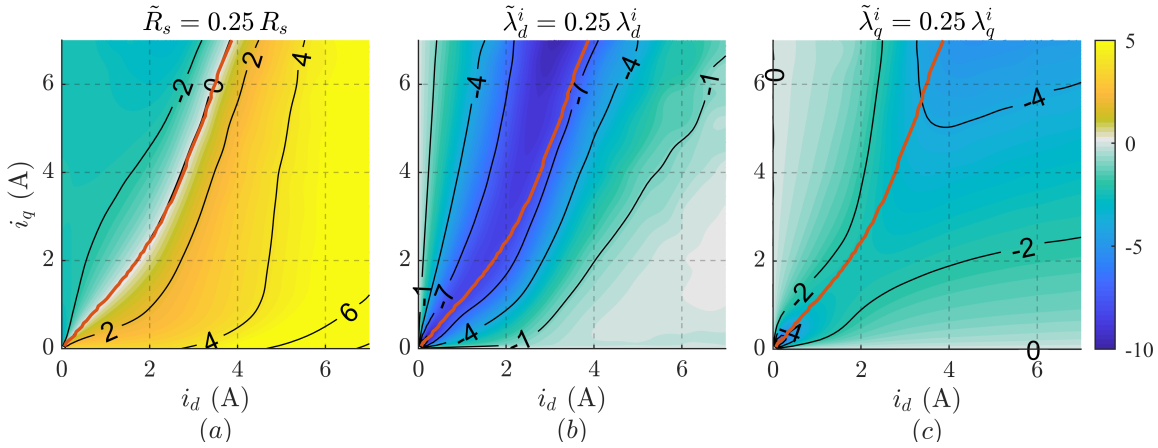

Figure 6.13: Steady-state position error $\tilde{\theta}_0$ in ° (electrical) of APP position observer due to parameter inaccuracies: (a) $\tilde{R}_s = 0.25\,R_s$ at $\omega = 2\pi \cdot 10$ rad/s; (b) $\tilde{\lambda}^i_d = 0.25\,\lambda^i_d$; (c) $\tilde{\lambda}^i_q = 0.25\,\lambda^i_q$. Red line is the MTPA trajectory. Motor: *B*.

position error $\tilde{\theta}_0$ is seen to diminish towards the MTPA trajectory. As the position error in (6.10) is inversely proportional to ω, the $\tilde{R}_s$ becomes less relevant at higher speeds, expectedly.

6.4.2 Susceptibility to Flux-Map Errors

The sensitivity of the APP scheme to flux-map LUTs error is analyzed by evaluating the steady-state position error for the current-model flux errors in d and q-axes in (6.11) and (6.12), respectively, as

$$\tilde{\theta}_0 = -\boldsymbol{\phi}^{\mathrm{T}}_{app}\,\boldsymbol{H}_{\tilde{\boldsymbol{\lambda}}^i} \begin{bmatrix} \tilde{\lambda}^i_d \\ 0 \end{bmatrix}\Bigg|_{s=0} = -\tilde{\lambda}^i_d \frac{\hat{\lambda}^a_{\hat{d}}}{|\hat{\boldsymbol{\lambda}}^a_{\hat{d}\hat{q}}|^2} \tag{6.11}$$

$$\tilde{\theta}_0 = -\boldsymbol{\phi}^{\mathrm{T}}_{app}\,\boldsymbol{H}_{\tilde{\boldsymbol{\lambda}}^i} \begin{bmatrix} 0 \\ \tilde{\lambda}^i_q \end{bmatrix}\Bigg|_{s=0} = -\tilde{\lambda}^i_q \frac{\hat{\lambda}^a_{\hat{q}}}{|\hat{\boldsymbol{\lambda}}^a_{\hat{d}\hat{q}}|^2}. \tag{6.12}$$

Figs. 6.13(b) and 6.13(c) plot the contours of steady-state position error for a 25% current-model flux error in d and q-axes, i.e., $\tilde{\lambda}^i_d = 0.25\,\lambda^i_d$ and $\tilde{\lambda}^i_q = 0.25\,\lambda^i_q$, respectively. It is observed in Fig. 6.13(b) that the regions in the vicinity of MTPA trajectory are particularly sensitive to $\tilde{\lambda}^i_d$, resulting in steady-state position error as high as around $-9°$. APP is relatively less sensitive to $\tilde{\lambda}^i_q$ as shown in Fig. 6.13(c) where the maximum position error is approximately $-5°$ at high loads. Contrary to the resistance error, the influence of current-model flux errors is speed independent.

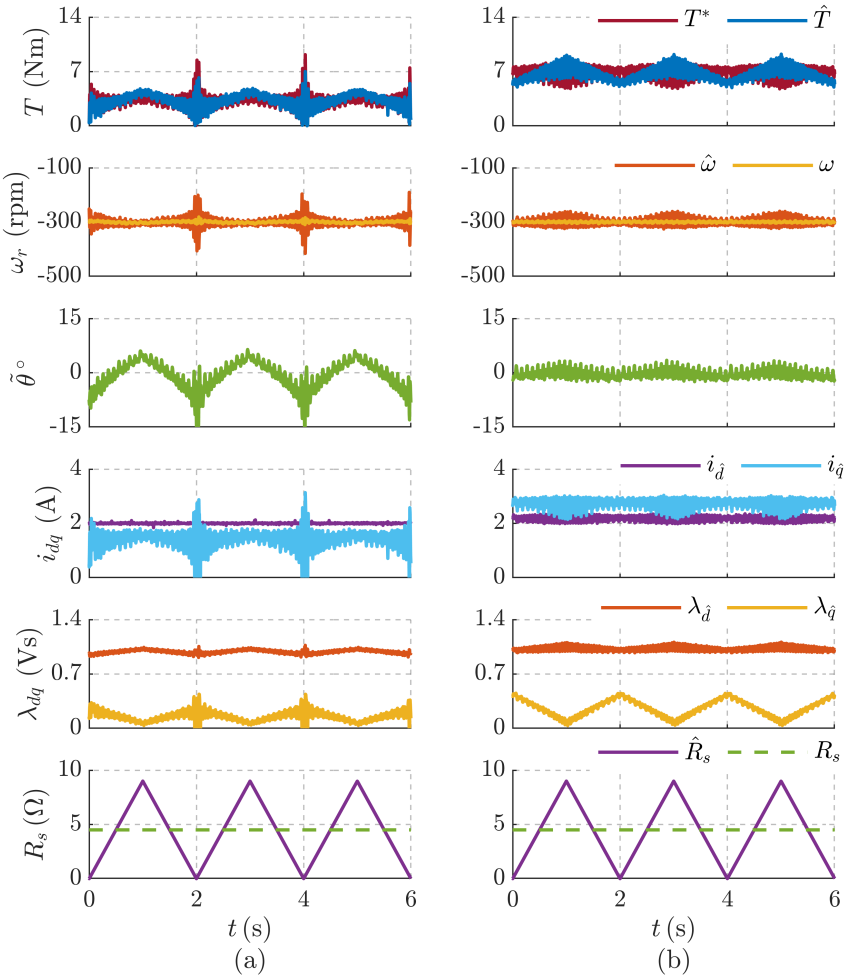

Figure 6.14: Immunity of the APP technique to control resistance variation of $\tilde{R}_s = \pm 1$ p.u. ($\pm 4.5\Omega$) at $\omega = -0.2$ p.u: (a) $T_L = 0.5$ p.u, away from MTPA due to i_d^{min}; (b) $T_L = 1$ p.u, on MTPA trajectory.

6.4.3 Experimental Results

As alluded to in Section 6.2.2, a high minimum current $i_d^{min} = 0.6$ p.u. (2A) is intentionally imposed to move the operation away from the MTPA to facilitate the demonstration of immunity of APP scheme to resistance error.

A perturbation of $\pm 100\%$ is injected to resistance within the control, $\hat{R}_s$, with the physical stator resistance R_s remaining constant. A load torque of $T_L = 0.5$ p.u. (non-MTPA) and $T_L = 1$ p.u. (MTPA) are imposed in Figs. 6.14(a) and 6.14(b), respectively. Despite the variations in observed flux and torque in Fig. 6.14(b), the position is undeterred. However, when the MTPA is not respected as in Fig. 6.14(a),

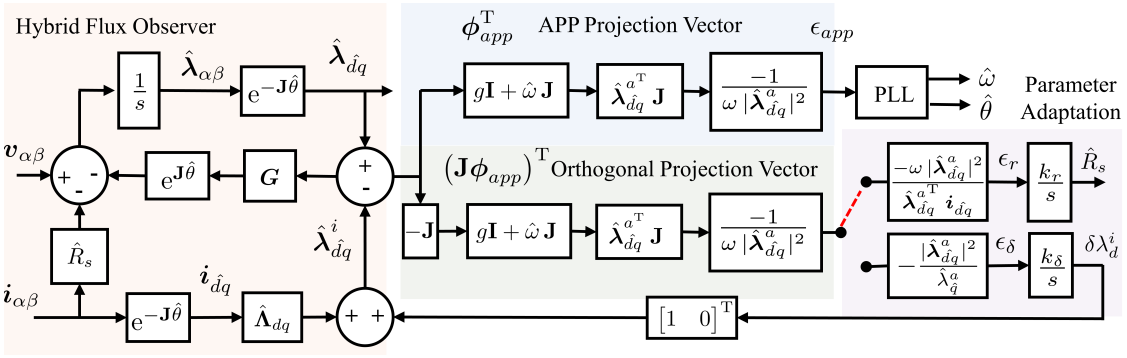

Figure 6.15: Block diagram of the flux and APP position observer supplemented with parameter adaptation exploiting the orthogonal projection vector. Motor: *B*.

the observed position is susceptible to $\tilde{R}_s$. In either scenario, stability is not compromised.

The experimental validation of the APP scheme with errors in flux-map LUTs to corroborate the analytical evaluations is presented in the following section, in conjunction with the parameter adaptation.

6.5 Parameter Adaptation

The orthogonal projection vector $\left(\mathbf{J}\,\boldsymbol{\phi}_{app}\right)$ and the corresponding error signal ϵ_j are explored for parameter adaptation. Concurrent speed error estimation and parameter adaptation is not feasible as both employ the orthogonal projection vector. Henceforth, the simplified APP vector without the derivative term ($h = 0$) is used. The block diagram of the APP scheme with parameter adaptation is shown in Fig. 6.15.

6.5.1 Adaptation Feasibility and Design

Among the three parameter errors $\left(\tilde{\lambda}^i_d,\, \tilde{\lambda}^i_q,\, \tilde{R}_s\right)$ in contention, the feasibility of adaptation is determined by evaluating the steady-state value of the error signal ϵ_j for the three parameter errors independently considered, as reported in the following expressions:

$$\epsilon_j\Big|_{s=0} = \left(\mathbf{J}\,\boldsymbol{\phi}_{app}\right)^{\mathrm{T}} \boldsymbol{h}_{\tilde{R}_s}\,\tilde{R}_s\Big|_{s=0} = -\frac{1}{\omega\,|\hat{\boldsymbol{\lambda}}^a_{\hat{dq}}|^2}\left(\hat{\boldsymbol{\lambda}}^a_{\hat{dq}}\right)^{\mathrm{T}} \boldsymbol{i}_{\hat{dq}}\,\tilde{R}_s \tag{6.13}$$

$$\epsilon_j\Big|_{s=0} = \left(\mathbf{J}\,\boldsymbol{\phi}_{app}\right)^{\mathrm{T}} \boldsymbol{H}_{\tilde{\boldsymbol{\lambda}}^i} \begin{bmatrix}\tilde{\lambda}^i_d \\ 0\end{bmatrix}\Bigg|_{s=0} = -\frac{\hat{\lambda}^a_{\hat{q}}}{|\hat{\boldsymbol{\lambda}}^a_{\hat{dq}}|^2}\,\tilde{\lambda}^i_d \tag{6.14}$$

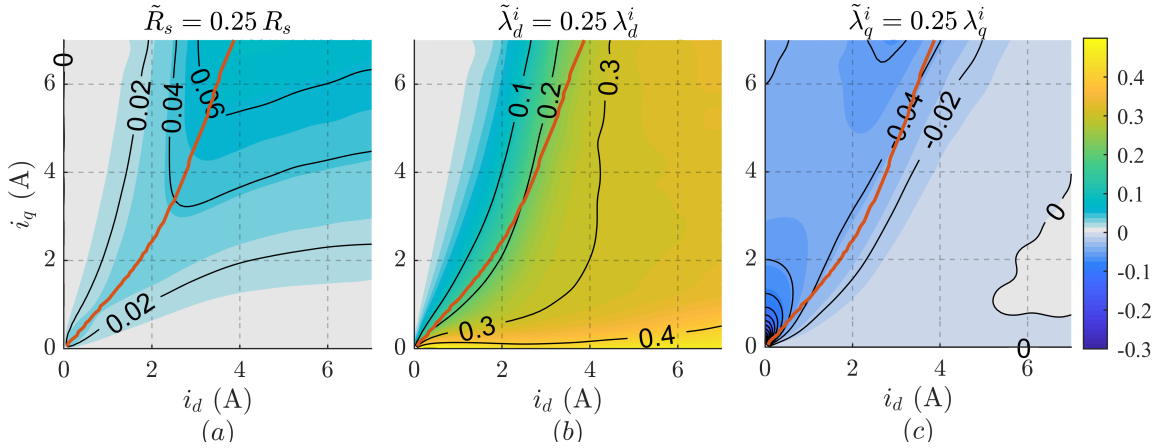

Figure 6.16: Steady-state orthogonal error signal ϵ_j of the orthogonal projection vector $\boldsymbol{\phi}_j$ due to parameter inaccuracies: (a) $\tilde{R}_s = -0.25\,R_s$ at $\omega = 2\pi \cdot 10$ rad/s; (b) $\tilde{\lambda}^i_d = -0.25\,\lambda^i_d$; (c) $\tilde{\lambda}^i_q = -0.25\,\lambda^i_q$. Note that the error signal ϵ_j is dimensionless.

$$\epsilon_j\Big|_{s=0} = \left(\mathbf{J}\,\boldsymbol{\phi}_{app}\right)^{\mathrm{T}} \boldsymbol{H}_{\tilde{\lambda}^i} \begin{bmatrix} 0 \\ \tilde{\lambda}^i_q \end{bmatrix}\Bigg|_{s=0} = \frac{\hat{\lambda}^a_{\hat{d}}}{|\hat{\boldsymbol{\lambda}}^a_{\hat{d}\hat{q}}|^2}\,\tilde{\lambda}^i_q. \tag{6.15}$$

A sufficiently high ϵ_j is essential for reliable adaptation; bigger the error signal, better is the prospect for adaptation. For a fair comparison, the magnitude of error signal ϵ_j is calculated for a -25% parametric error in $\tilde{R}_s = -0.25\,R_s$, $\tilde{\lambda}^i_d = -0.25\,\lambda^i_d$ and $\tilde{\lambda}^i_q = -0.25\,\lambda^i_q$, shown in Figs. 6.16(a), 6.16(b) and 6.16(c) respectively. The d-axis current-model flux error is seen to noticeably dominant by a factor of about 4, indicating a strong prospect for $\tilde{\lambda}^i_d$ adaptation.

6.5.2 Stator Resistance Adaptation

In presence of accurate flux-map LUTs, a stator resistance adaptation can be resorted to track temperature induced variations. The APP scheme is inherently immune to $\tilde{R}_s$ and dead-time errors on the MTPA trajectory as discussed in Section 6.4.1. However, high performance drives can benefit from accurate stator flux and torque estimation that are susceptible to resistance error.

Let ϵ_r and $\boldsymbol{\phi}_r$ denote the resistance error signal and the resistance error projection vector, respectively, such that

$$\epsilon_r\Big|_{s=0} = \tilde{R}_s. \tag{6.16}$$

Following (6.13), the resistance error projection vector satisfying (6.16) is given by

$$\boldsymbol{\phi}_r^{\mathrm{T}} = -\frac{\omega\,|\hat{\boldsymbol{\lambda}}^a_{\hat{d}\hat{q}}|^2}{\left(\hat{\boldsymbol{\lambda}}^a_{\hat{d}\hat{q}}\right)^{\mathrm{T}} \boldsymbol{i}_{\hat{d}\hat{q}}} \left(\mathbf{J}\,\boldsymbol{\phi}_{app}\right)^{\mathrm{T}}. \tag{6.17}$$

The resistance adaption law is defined as

$$\hat{R}_s = k_r \int \epsilon_r \, \mathrm{d}t \tag{6.18}$$

where k_r is an integral gain as depicted in Fig. 6.15. The effective estimated resistance also encompasses the non-ideal dead-time compensation, discussed in Section 3.2.4, as

$$\hat{R}_s = R_s + \frac{1}{i}\frac{4}{\pi} v_{dc} \, f_s \, \tilde{t}_d \tag{6.19}$$

As mentioned before, a minimum current is imposed in SyR machines for fundamental excitation at no load. Thus, the operating point diverges from the MTPA trajectory for small loads. However, it can discerned from Fig. 6.16(a) that such operating points have poor error signal strength, making the resistance error unobservable. Hence, the resistance adaptation is disabled for $|T| < 0.2$ p.u.

Thus, a conflicting situation arises: the resistance adaption is not feasible in the non-MTPA regions at low loads where APP position observer is susceptible. The resulting steady-state position error is unavoidable, as predicted in Fig. 6.13(a). Adaptation is resumed at high loads which primarily benefits accurate stator flux and torque estimation. Moreover, the resistance error signal suffers from poor signal to noise ratio at high speeds and is disabled for $|\omega| > 0.75$ p.u. This is of relative importance, as the impact of the resistance error is inversely proportional with speed and thus, negligible in such speed range.

6.5.3 Current-Model Flux Adaptation

In presence of inaccurate flux-map LUTs, adapting resistance is not advisable due to the dominance of the d-axis current-model flux error on the error signal ϵ_j as seen in Fig. 6.16. For the same reason, the adaptation of q-axis current-model flux is not undertaken. The adaptation of $\tilde{\lambda}_d^i$ is preferred that further helps to alleviate the steady-state position error in Fig. 6.13(b). Alternatively, under accurate flux-map LUTs, q-axis adaptation can be considered for machines with magnets to track the temperature induced variations.

Design of the d-axis Flux Adaptation

Let ϵ_δ and $\boldsymbol{\phi}_\delta$ denote the d-axis current-model flux error signal and error projection vector, respectively, such that

$$\epsilon_\delta\Big|_{s=0} = \tilde{\lambda}_d^i. \tag{6.20}$$

Following (6.14), the current-model flux error projection vector satisfying (6.20) is given by

$$\boldsymbol{\phi}_\delta^{\mathrm{T}} = -\frac{|\hat{\boldsymbol{\lambda}}_{\hat{d}\hat{q}}^a|^2}{\hat{\boldsymbol{\lambda}}_{\hat{q}}^a} \left(\mathbf{J}\,\boldsymbol{\phi}_{app}\right)^{\mathrm{T}}. \tag{6.21}$$

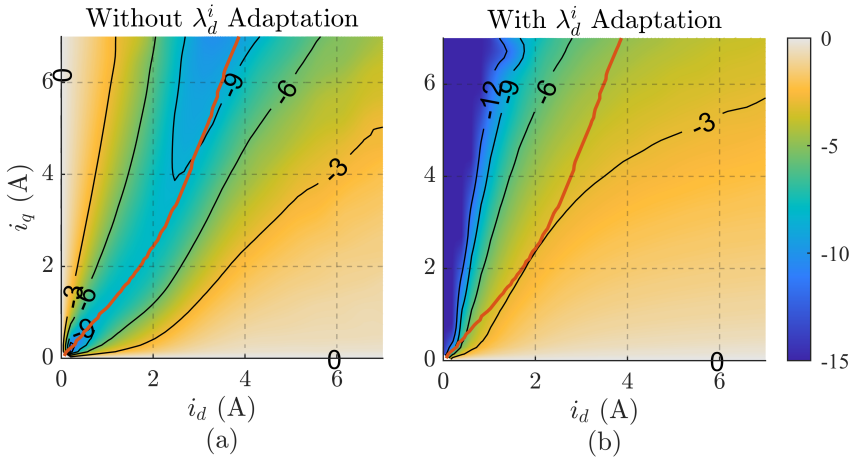

Figure 6.17: Steady-state position error in ° (electrical) at +20% error in both axes, $\tilde{\lambda}_d^i = 0.2\,\lambda_d^i$ and $\tilde{\lambda}_q^i = 0.2\,\lambda_q^i$: (a) Without λ_d^i adaptation (6.24); (b) With λ_d^i adaptation (6.25). Motor: *B*.

The d-axis current-model flux adaption law supplements the flux estimate from LUTs, defined as

$$\delta\lambda_d^i = k_\delta \int \epsilon_\delta \,\mathrm{d}t \qquad \Rightarrow \qquad \hat{\lambda}_{\hat{d}}^i = \hat{\boldsymbol{\Lambda}}_d(\boldsymbol{i}_{\hat{d}q}) + \delta\lambda_d^i \tag{6.22}$$

where k_δ is an integral gain and $\delta\lambda$ is the supplementary term defined in Fig. 6.15 when flux adaptation is chosen.

Sensitivity to Error in q-axis

In designing adaptation for the erroneous d-axis flux-map, it is unreasonable to assume accurate q-axis flux-maps. Hence, the sensitivity to the error in the q-axis flux-map with the d-axis flux adaptation active is determined by evaluating the corresponding steady-state d-axis current-model flux error λ_{d0}^i as

$$\epsilon_\delta = \boldsymbol{\phi}_\delta^{\mathrm{T}}\, \boldsymbol{H}_{\tilde{\boldsymbol{\lambda}}^i}\, \tilde{\boldsymbol{\lambda}}_{dq}^i = 0 \qquad \Rightarrow \qquad \tilde{\lambda}_{d0}^i = \tilde{\lambda}_q^i \cdot \frac{\hat{\lambda}_{\hat{d}}^a}{\hat{\lambda}_{\hat{q}}^a} \tag{6.23}$$

The expression (6.23) expresses the propagation of the q-axis current-model error into the d-axis due to the adaptation law.

From (6.11) and (6.12), the steady-state position error under inaccuracies in d and q-axes flux-map without the current-model flux adaptation is given by

$$\tilde{\theta}_0 = -\tilde{\lambda}_d^i \frac{\hat{\lambda}_{\hat{d}}^a}{|\hat{\boldsymbol{\lambda}}_{\hat{d}q}^a|^2} - \tilde{\lambda}_q^i \frac{\hat{\lambda}_{\hat{q}}^a}{|\hat{\boldsymbol{\lambda}}_{\hat{d}q}^a|^2} \tag{6.24}$$

If the d-axis current-model flux adaptation is enabled, the resulting steady-state position error can be derived by using (6.23) in (6.24) as

$$\tilde{\theta}_0 = -\tilde{\lambda}_q^i \frac{1}{\hat{\lambda}_{\hat{q}}^a}. \tag{6.25}$$

Fig. 6.17 shows the contour of position error with and without d-axis current-model flux adaptation at +20% error in either axes, $\tilde{\lambda}_d^i = 0.2\,\lambda_d^i$ and $\tilde{\lambda}_q^i = 0.2\,\lambda_q^i$; no resistance error is considered. A conspicuous improvement in position error along the MTPA trajectory is discerned in Fig. 6.17(b) due to parameter adaptation, experimentally validated in the succeeding section.

A large position error is noticed in Fig. 6.17(b) for flux-weakening operating points towards the q-axis. The adaptation should be disabled in the vicinity of the q-axis where the strength of $\tilde{\lambda}_d^i$ signal gets progressively weaker (see Fig. 6.16(b)). Thus, this adaptation is purposeful for operation up to nominal speed under imprecise flux-map LUTs.

For machines with magnets, the q-axis flux shows temperature dependence; however, it is suggested to adapt the q-axis current-model [26] only if the d-axis flux-map is reasonably accurate.

6.5.4 Stability Analysis

APP Position Observer with Resistance Adaptation

Using (3.33), the combined dynamics of the flux and the position observers with stator resistance adaptation is given by

$$s\,\boldsymbol{y}_r = \boldsymbol{A}_r\,\boldsymbol{y}_r \tag{6.26}$$

$$\boldsymbol{A}_r = \begin{bmatrix} -(\boldsymbol{G} + \omega\,\mathbf{J}) & \boldsymbol{G}\,\hat{\boldsymbol{\lambda}}_{\hat{d}\hat{q}}^a & \mathbf{0} & -\boldsymbol{i}_{\hat{d}\hat{q}} \\ k_p\,\boldsymbol{\phi}_{app}^{\mathrm{T}} & -k_p\,\boldsymbol{\phi}_{app}^{\mathrm{T}}\,\hat{\boldsymbol{\lambda}}_{\hat{d}\hat{q}}^a & 1 & 0 \\ k_i\,\boldsymbol{\phi}_{app}^{\mathrm{T}} & -k_i\,\boldsymbol{\phi}_{app}^{\mathrm{T}}\,\hat{\boldsymbol{\lambda}}_{\hat{d}\hat{q}}^a & 0 & 0 \\ k_r\,\boldsymbol{\phi}_r^{\mathrm{T}} & -k_r\,\boldsymbol{\phi}_r^{\mathrm{T}}\,\hat{\boldsymbol{\lambda}}_{\hat{d}\hat{q}}^a & 0 & 0 \end{bmatrix}$$

where $\boldsymbol{y}_r = \begin{bmatrix} \left(\tilde{\boldsymbol{\lambda}}_{\hat{d}\hat{q}}\right)^{\mathrm{T}} & \tilde{\theta} & \tilde{\omega}_i & \tilde{R}_s \end{bmatrix}^{\mathrm{T}}$.

Fig. 6.18(a) shows the movement of poles for $\omega = 0.2 \ldots 2$ p.u. The movement of the resistance adaptation pole (yellow line), although dependent on operating point, is not as pronounced as the PLL and the flux observer poles. Stability at $T = 1$ p.u. is ascertained.

It was noted that the control system becomes unstable for large values of k_r (eg. $2\pi \cdot 10$ rad/s) at low speeds. Since temperature is slow time-varying, a high k_r is unwarranted; the following experimental results use $k_r = 2\pi \cdot 0.5$ rad/s.

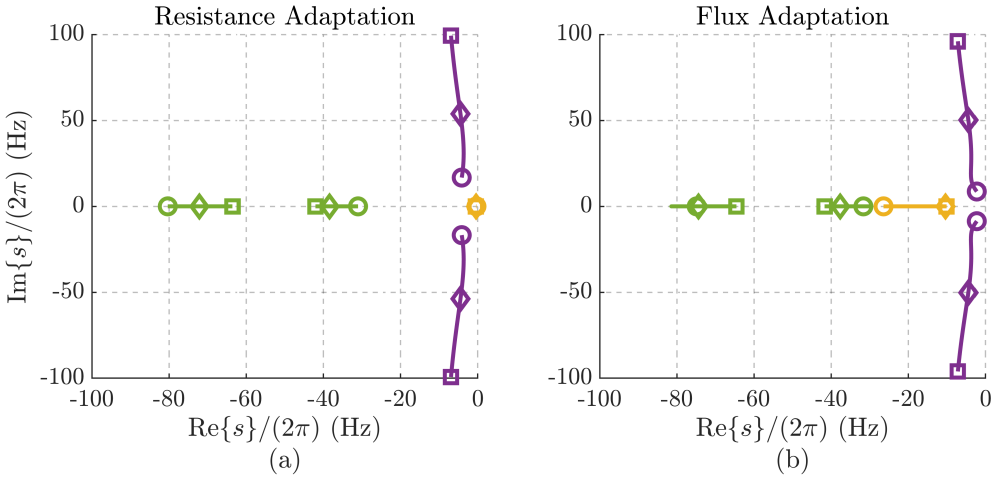

Figure 6.18: Locus of poles position and flux observer for $\omega = 0.2 \ldots 2$ p.u. at $T = 1$ p.u. where the markers $\circ$, $\diamond$ and $\square$ denote the speeds 0.2, 1 and 2 p.u., respectively: (a) With resistance adaptation; (b) With d-axis current-model flux adaptation. Color code: PLL poles are denoted in green, flux observer in blue, resistance/flux observer in yellow. Parameters: $g = 2\pi \cdot 10$ rad/s, $\Omega_\omega = 2\pi \cdot 50$ rad/s, $k_r = 2\pi \cdot 0.5$ rad/s, $k_\delta = 2\pi \cdot 10$ rad/s. Motor: B.

APP Position Observer with Flux Adaptation

Using (3.33), the combined dynamics of the flux and the position observers with flux adaptation is expressed as

$$s\boldsymbol{y}_\delta = \boldsymbol{A}_\delta \, \boldsymbol{y}_\delta \tag{6.27}$$

$$\boldsymbol{A}_\delta = \begin{bmatrix} -(\boldsymbol{G} + \omega \, \mathbf{J}) & \boldsymbol{G} \, \hat{\boldsymbol{\lambda}}^a_{\hat{d}\hat{q}} & \mathbf{0} & \boldsymbol{G} \begin{bmatrix} 1 & 0 \end{bmatrix}^{\mathrm{T}} \\ k_p \, \boldsymbol{\phi}^{\mathrm{T}}_{app} & -k_p \, \boldsymbol{\phi}^{\mathrm{T}}_{app} \, \hat{\boldsymbol{\lambda}}^a_{\hat{d}\hat{q}} & 1 & -k_p \, \boldsymbol{\phi}^{\mathrm{T}}_{app} \begin{bmatrix} 1 & 0 \end{bmatrix}^{\mathrm{T}} \\ k_i \, \boldsymbol{\phi}^{\mathrm{T}}_{app} & -k_i \, \boldsymbol{\phi}^{\mathrm{T}}_{app} \, \hat{\boldsymbol{\lambda}}^a_{\hat{d}\hat{q}} & 0 & -k_i \, \boldsymbol{\phi}^{\mathrm{T}}_{app} \begin{bmatrix} 1 & 0 \end{bmatrix}^{\mathrm{T}} \\ k_\delta \, \boldsymbol{\phi}^{\mathrm{T}}_{\delta} & -k_\delta \, \boldsymbol{\phi}^{\mathrm{T}}_{\delta} \, \hat{\boldsymbol{\lambda}}^a_{\hat{d}\hat{q}} & 0 & -k_\delta \, \boldsymbol{\phi}^{\mathrm{T}}_{\delta} \begin{bmatrix} 1 & 0 \end{bmatrix}^{\mathrm{T}} \end{bmatrix}$$

where $\boldsymbol{y}_\delta = \begin{bmatrix} \left(\tilde{\boldsymbol{\lambda}}_{\hat{d}\hat{q}}\right)^{\mathrm{T}} & \tilde{\theta} & \tilde{\omega}_i & \tilde{\lambda}^i_d \end{bmatrix}^{\mathrm{T}}$.

Fig. 6.18(b) shows the movement of poles for $\omega = 0.2 \ldots 2$ p.u. at $T = 1$ p.u. Similar to the former case, the poles are stable and seen to converge to their designated value at high speeds. Unlike the gain k_r, the system is stable for all values of k_δ; the following experimental results use $k_\delta = 2\pi \cdot 10$ rad/s.

6.5.5 Experimental Results

Parameters: sampling frequency = 10 kHz, flux observer gain $g = 2\pi \cdot 10$ rad/s, PLL poles $\Omega_\omega = 2\pi \cdot 25$ rad/s, speed controller poles $s = -2\pi \cdot 1$ rad/s, minimum

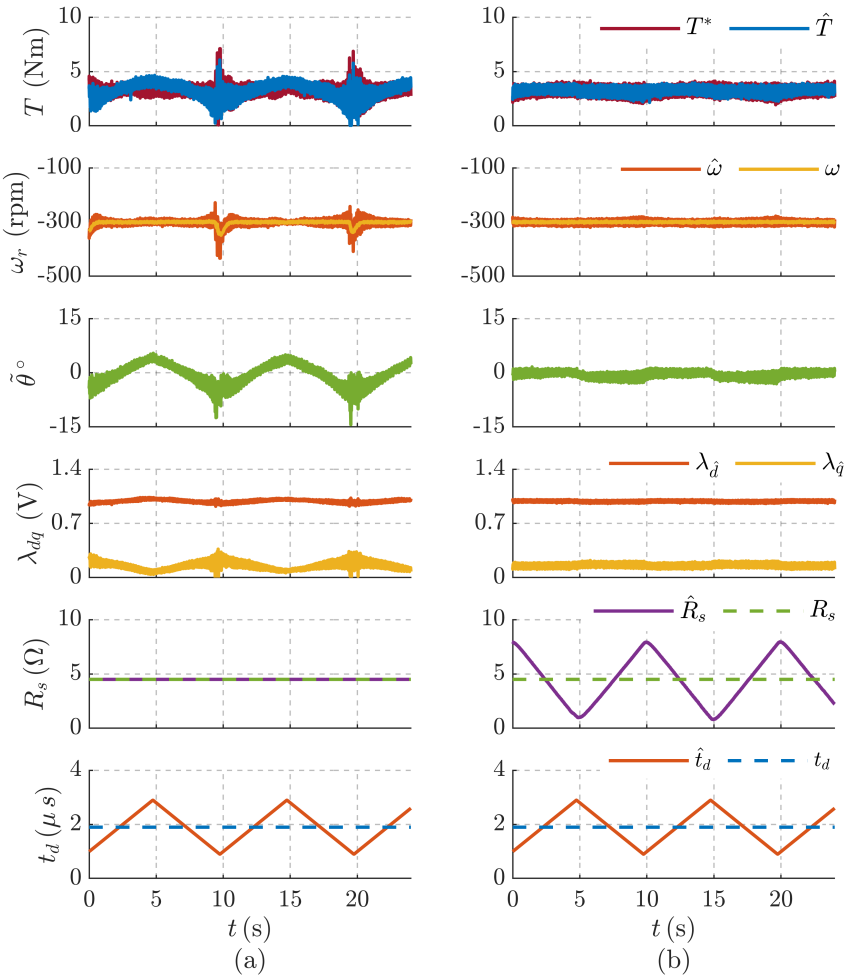

Figure 6.19: Variations on dead-time compensation ($\pm 1\mu s$) to emulate $\tilde{R}_s$ at $T_L = 0.5$ p.u. and $\omega = -0.2$ p.u: (a) Without R_s adaptation; (b) With R_s adaptation. Motor: *B*.

current $i_d^{min} = 0.6$ p.u. (2A), resistance adaptation gain $k_r = 2\pi \cdot 0.5$ rad/s and d-axis flux adaptation again $k_\delta = 2\pi \cdot 10$ rad/s.

Stator Resistance Adaptation

The competency of resistance adaption is studied by imposing deliberate variations on the dead-time compensation which is equivalent to physical variations in resistance. A compensated dead-time variation of $\tilde{t}_d = \pm 1\mu$s is equivalent to $\pm 3\ \Omega$ at $T_L = 0.5$ p.u. (non-MTPA); the equivalence is a function of peak current and changes with load as expressed in (3.18).

Figs. 6.19(a) and 6.19(b) illustrate the effect of perturbation in compensated

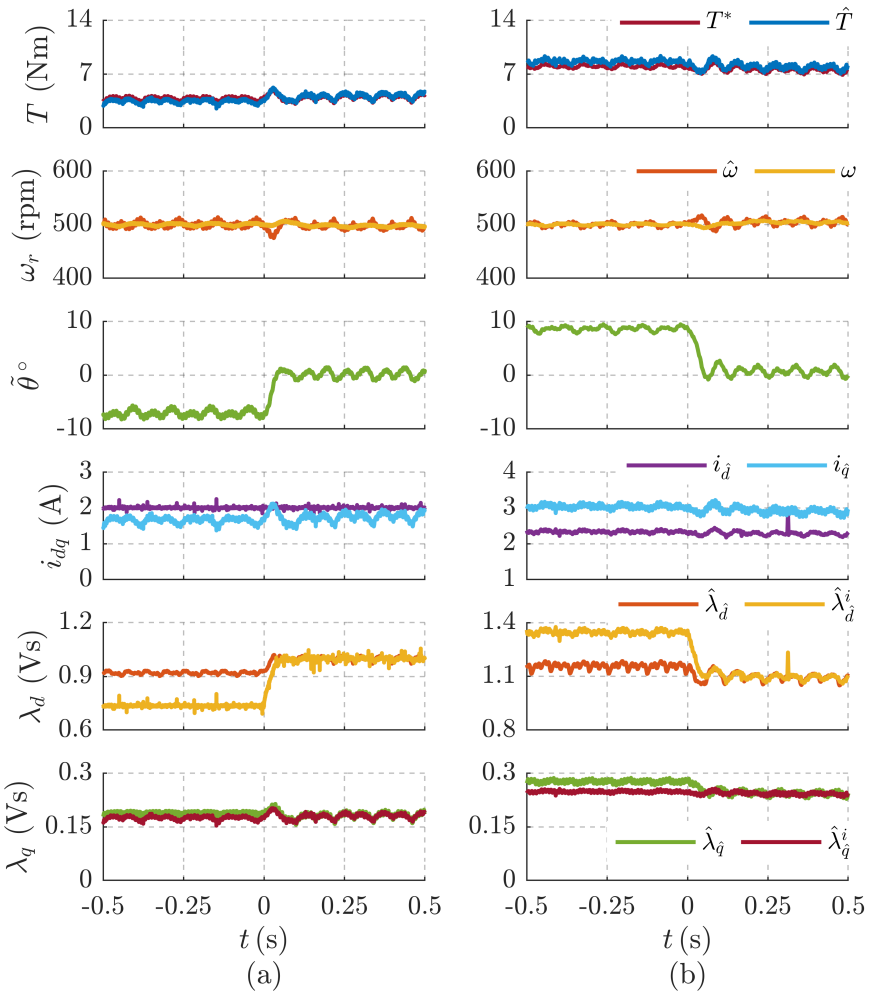

Figure 6.20: Validation of d-axis current-model flux adaptation at $\tilde{\lambda}^i_q = 0.$, enabled at $t = 0$ s: (a) +25% error $\tilde{\lambda}^i_d = 0.25\,\lambda^i_d$ at $T_L = 0.5$ p.u; (b) -25% error $\tilde{\lambda}^i_d = -0.25\,\lambda^i_d$ at $T_L = 1$ p.u. Motor: *B*.

dead-time without and with resistance adaption, respectively. In Fig. 6.19(a), variations in position error, observed flux and estimated torque exists proportional to the induced perturbations in dead-time. With the adaptation enabled in Fig. 6.19(b), the $\hat{R}_s$ tracks the changes in dead-time and thereby alleviates the impact on observed position, stator flux and torque.

d-axis Current-Model Flux Adaptation

A series of tests are conducted to validate the proposed flux adaptation scheme. In Fig. 6.20(a), a +25% error in d-axis flux-maps LUT ($\tilde{\lambda}^i_d = 0.25\,\lambda^i_d$) is imposed

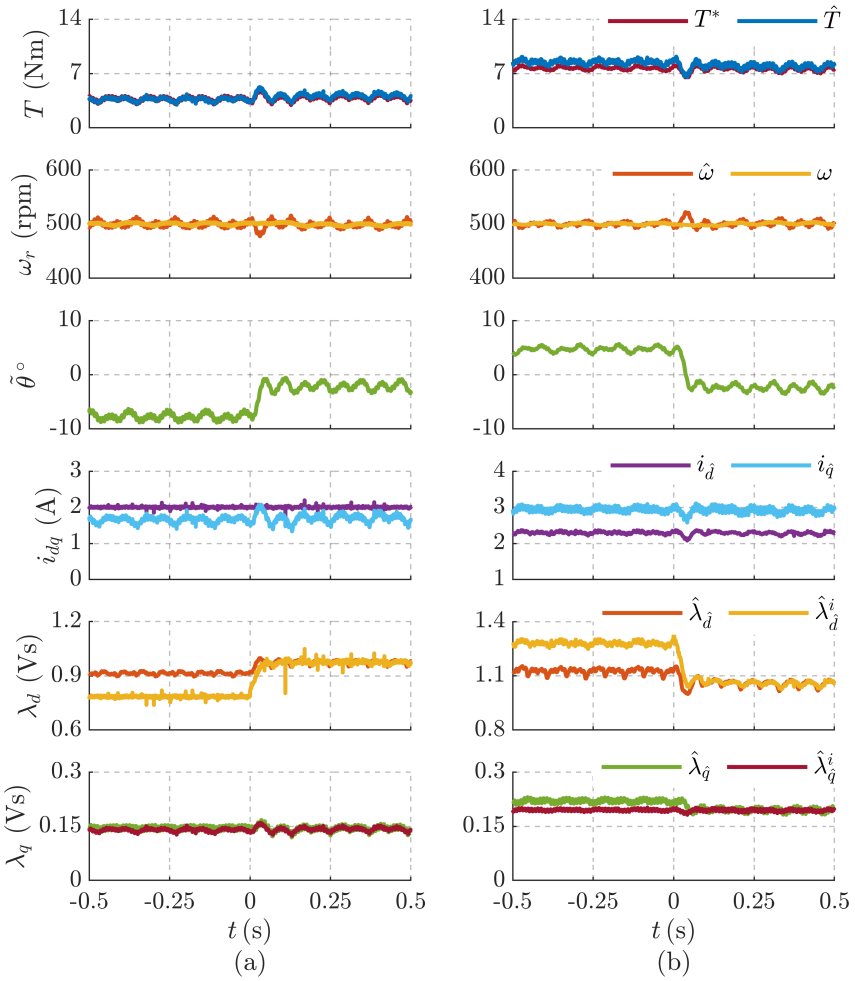

Figure 6.21: Validation of d-axis current-model flux adaptation at $\tilde{\lambda}^i_q = 0.2\,\lambda^i_q$, enabled at $t = 0$ s: (a) +20% error $\tilde{\lambda}^i_d = 0.2\,\lambda^i_d$ at $T_L = 0.5$ p.u; (b) -20% error $\tilde{\lambda}^i_d = -0.2\,\lambda^i_d$ at $T_L = 1$ p.u. Motor: *B*.

at $T_L = 0.5$ p.u. while in Fig. 6.20(b), a -25% error ($\tilde{\lambda}^i_d = -0.25\,\lambda^i_d$) is imposed at $T_L = 1$ p.u. Accurate q-axis flux-map is considered. For $t < 0$ s without adaptation, the steady-state position error in Fig. 6.20(a) is approximately $-8°$ (electrical), corroborating the analysis in Fig. 6.13. The inductance adaptation is enabled at time $t = 0$ s upon which the position error reduces to zero as estimated $\hat{\lambda}^i_d$ converges to λ_d.

The performance under parametric error in both d and q-axes flux-maps is analyzed in Fig. 6.21. An error of +20 % is imposed ($\tilde{\lambda}^i_d = 0.2\,\lambda^i_d$ and $\tilde{\lambda}^i_q = 0.2\,\lambda^i_q$) at $T_L = 0.5$ p.u. in Fig. 6.21(a) while an error of -20% in d and +20 in q ($\tilde{\lambda}^i_d = -0.2\,\lambda^i_d$

and $\tilde{\lambda}_q^i = 0.2\,\lambda_q^i$) is imposed in Fig. 6.21(b). For $t < 0$ s without adaptation, the steady-state position error in Fig. 6.21(a) is approximately $-9°$; it is lower in Fig. 6.21(b), about $5°$, since the flux-map errors have opposing signs. As the adaptation is enabled at $t = 0$ s, a small residue in steady-state position error of around $-3°$, remains due to the error in q-axis flux-maps ($\tilde{\lambda}_q^i$), corroborating the analysis in Fig. 6.17.

6.6 Summary of the Chapter Contributions

The main contributions in the design of APP scheme in Sections 6.2 and 6.3, published in [23][24], are listed as follows:

- The new adaptive projection vector for position error estimation (APP) position observer sorts the stability problems of the state-of-art fundamental-wave sensorless techniques.
- Differing from the AUX scheme, the APP projection vector is developed from the dynamics of the flux observer; both schemes are stable at all operating points.
- Unlike the former AUX scheme, the proposed APP technique has the capability to estimate the speed error in addition to and independent of the position error, using two orthogonal projection vectors. A LPF derivative term is deemed essential for speed estimation, whereas it can be omitted if only the position error estimation is sufficient.

The major findings of the parameter adaptation in Sections 6.4 and 6.5, published in [11][12], are enumerated as follows:

- The sensitivity to various parametric errors on the steady-state position error of the APP scheme is analytically examined, revealing dominance of d-axis current-model flux error.
- The APP position observer is shown to possess immunity to resistance error for those operating points respecting MTPA law. The immunity also extends to the voltage error due to non-ideal compensation of inverters as the fundamental component of voltage error is in phase with the stator current. This is a unique feature to APP position observer and the finding on resistance immunity property is patented.
- In the interest of reliability, the projection vector orthogonal to APP is utilized for parameter adaptation. A stator resistance adaption is developed to track the temperature induced variations that primarily aids in torque and flux

estimation. Alternatively, a d-axis flux adaptation is proposed for operations under parametric error in flux-map LUTs, resulting in a reduced position error.

The observers with resistance/inductance adaptation are subjected to stability analysis. The design and analysis are supported by experimental validation on a 1.1 kW SyR motor test-bench.

Chapter 7

Accurate Torque Control with APP-based Adaptive MTPA Tracking

A new model-based torque control with adaptive MTPA tracking and a novel current-model flux adaptation is developed within the APP sensorless framework; the findings are published in [48].

7.1 Introduction

A control aspect hampered by parameter inaccuracy is the torque estimation and control. Under parameter errors, the torque estimation is enhanced using inductance adaptation in extended back-emf based sensorless control of an IPM synchronous motor in [49]. However, due to the coupling of position observer with inductance adaption, a small residual error in torque estimation remains.

A new torque control technique is proposed in Section 7.2 where the optimal current reference generation is devised as a function of discrepancy between commanded and estimated torque using the small-signal model of the machine. Moreover, the MTPA tracking is guaranteed by aligning the stator current to the auxiliary-flux vector.

In the former chapter in Section 6.5, the current-model flux adaptation along d-axis was proposed which, however, was susceptible to flux-map errors in q-axis. Thus, a new current-model flux adaptation law is designed in Section 7.3 that adapts in the direction orthogonal to the auxiliary-flux vector for mitigating torque estimation error caused by parameter inaccuracies, within the APP sensorless framework. Section 7.4 discusses the stability analysis followed by the experimental validation in Section 7.5. The findings and the major contributions of this chapter are summarized in Section 7.6.

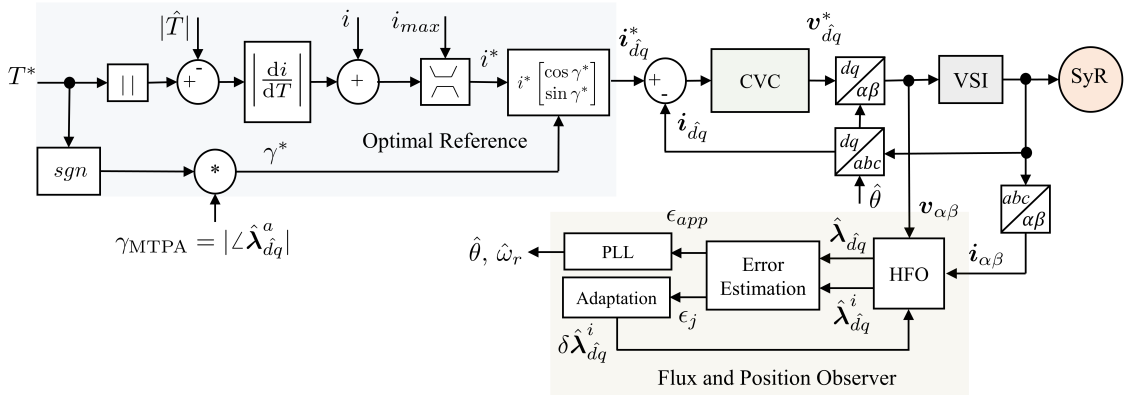

Figure 7.1: Torque control system overview illustrating the model-based optimal current reference generation, hybrid flux observer and position observer with flux adaptation.

7.2 Small-Signal Model-Based Torque Control

The block diagram of the small-signal model-based torque control scheme with MTPA optimal tracking is shown in Fig. 7.1. The MTPA condition (2.6) as a cross-product of the auxiliary-flux and the current vector is recalled in Fig. 7.2(a), i.e, $\gamma_{\mathrm{MTPA}} = \angle\hat{\boldsymbol{\lambda}}^a_{dq}$.

7.2.1 Optimal Current Reference Computation

For the commanded torque reference T^*, the current reference magnitude i^* is analytically derived as

$$i^* = i + \left|\frac{\mathrm{d}i}{\mathrm{d}T}\right|_\gamma \cdot \Big(|T^*| - |\hat{T}|\Big) \tag{7.1}$$

where the estimated torque $\hat{T}$ is computed with the observed flux in the torque equation (3.2). The derivative of torque w.r.t current amplitude for a given current angle can be expressed in the dq reference frame as

$$\left.\frac{\mathrm{d}T}{\mathrm{d}i}\right|_\gamma = \frac{3p}{2}\left(\frac{\boldsymbol{i}^{\mathrm{T}}_{dq}}{i}\,\mathbf{J}\,\boldsymbol{\lambda}_{dq} + \boldsymbol{i}^{\mathrm{T}}_{dq}\,\mathbf{J}\,\boldsymbol{L}_\partial\,\frac{\boldsymbol{i}_{dq}}{i}\right). \tag{7.2}$$

where $i = |\boldsymbol{i}_{dq}|$ is the stator current amplitude. Upon manipulation,

$$\left.\frac{\mathrm{d}T}{\mathrm{d}i}\right|_\gamma = \frac{3p}{2}\,\frac{\boldsymbol{i}^{\mathrm{T}}_{dq}}{i}\,\mathbf{J}\left(\boldsymbol{\lambda}_{dq} + \boldsymbol{L}_\partial\,\boldsymbol{i}_{dq}\right). \tag{7.3}$$

The contours of (7.3) for SyR motor A is shown in Fig. 7.2(b). These are representative of the torque factor (Nm/A), being maximum along the MTPA trajectory

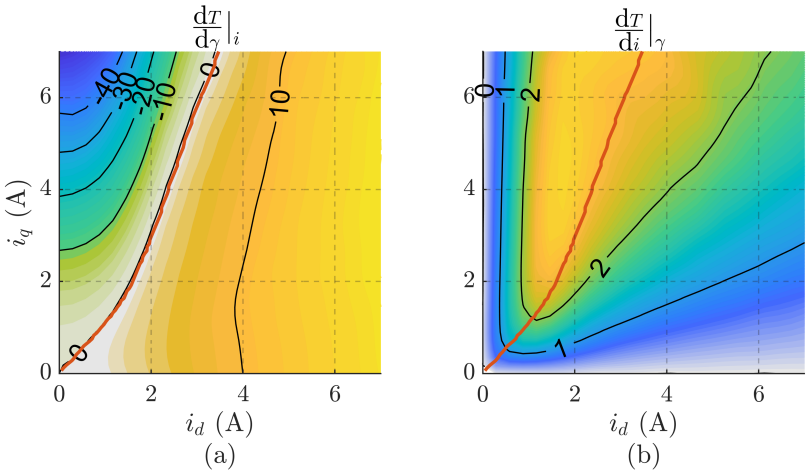

Figure 7.2: (a) Contour of derivative of torque w.r.t current angle in (2.6) for MTPA adaptation; (b) Contour of derivative of torque w.r.t current amplitude in (7.3) for reference torque tracking. Red curve is the MTPA trajectory. Motor: *A*.

shown in red. Note that care must be taken at very low loads as the quantity in (7.3) approaches zero at either axes as seen in Fig. 7.2(b): otherwise said, the SyR machine cannot produce torque without current excitation in both the axes.

The inverse of the quantity (7.3) can be real-time computed using the measured current angle, the observed flux and the incremental inductances retrieved from flux-map, all in estimated coordinates.

Finally, the optimal reference current is computed as

$$\boldsymbol{i}^*_{\hat{d}\hat{q}} = i^* \begin{bmatrix} \cos\gamma^* \\ \sin\gamma^* \end{bmatrix} \tag{7.4}$$

where the reference current angle magnitude is determined by the MTPA criterion, $|\gamma^*| = |\angle \hat{\boldsymbol{\lambda}}^a_{\hat{d}\hat{q}}|$ and it takes the sign of T^*, as shown in Fig. 7.1.

Thus, the proposed scheme guarantees accurate torque control and the respect of the MTPA law without using dedicated current reference look-up-tables, so long as the flux-map LUTs and the estimated torque are accurate. In the following, the torque error related to parameter errors is identified and suitably compensated.

7.2.2 Torque Estimation Error

The parameter dependent position error (3.29) and the direct effect of parameter errors contribute to the torque estimation error. This directly translates to the error in torque output w.r.t commanded torque through (7.1). The steady-state error of the estimated electromagnetic torque $\tilde{T}_0$ is given by

$$\tilde{T}_0 = \frac{3p}{2}\, \boldsymbol{i}^{\mathrm{T}}_{\hat{d}\hat{q}}\, \mathbf{J}\, \tilde{\boldsymbol{\lambda}}_{\hat{d}\hat{q}}. \tag{7.5}$$

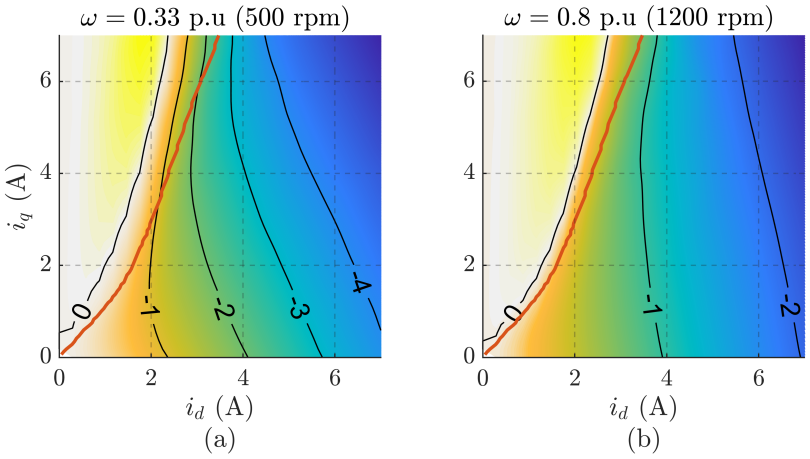

Figure 7.3: Steady-state torque estimation error $\tilde{T}_0$ in Nm at +30% error in d-axis, $\tilde{\lambda}_d^i = 0.3\,\lambda_d$: (a) $\omega = 0.33$ p.u. (500 rpm); (b) $\omega = 0.8$ p.u. (1200 rpm). In red is the MTPA trajectory. Rated torque $T_n = 7.1$ Nm; $g = 2\pi \cdot 10$ rad/s. Motor: A.

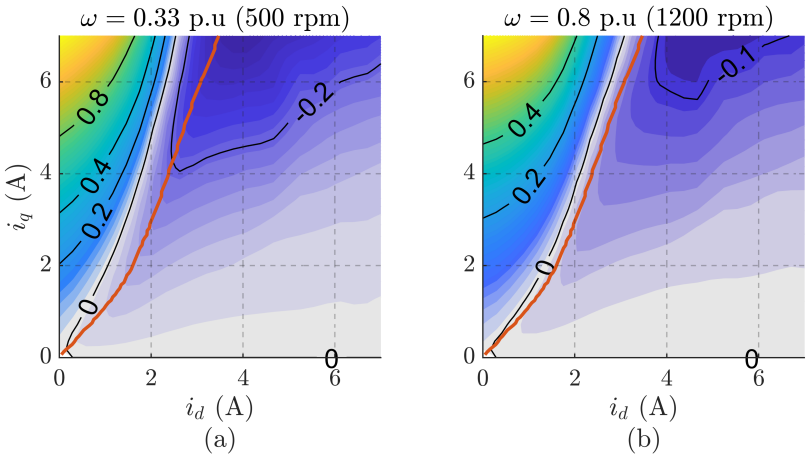

Figure 7.4: Steady-state torque estimation error $\tilde{T}_0$ in Nm at +30% error in q-axis, $\tilde{\lambda}_q^i = 0.3\,\lambda_q$: (a) $\omega = 0.33$ p.u. (500 rpm); (b) $\omega = 0.8$ p.u. (1200 rpm). In red is the MTPA trajectory. Rated torque $T_n = 7.1$ Nm; $g = 2\pi \cdot 10$ rad/s. Motor: A.

Using the steady-state flux estimation error, $s = 0$ in (3.23), the torque estimation error becomes

$$\tilde{T}_0 = \frac{3p}{2}\, \boldsymbol{i}_{\hat{d}q}^{\mathrm{T}}\, \mathbf{J}\, (\boldsymbol{G} + \omega \mathbf{J})^{-1} \left[\boldsymbol{G}\, (\hat{\boldsymbol{\lambda}}_{\hat{d}q}^{a}\, \tilde{\theta}_0 + \tilde{\boldsymbol{\lambda}}_{\hat{d}q}^{i}) - \tilde{R}_s \boldsymbol{i}_{\hat{d}q} \right]. \tag{7.6}$$

Substituting the steady-state position error (6.9) into (7.6) and considering accurate stator resistance, the terms in phase with the auxiliary-flux vector cancel out and the torque estimation error simplifies to

$$\tilde{T}_0 = \frac{3p}{2}\, \boldsymbol{i}_{\hat{d}q}^{\mathrm{T}}\, \mathbf{J}\, (\boldsymbol{G} + \omega \mathbf{J})^{-1}\, \boldsymbol{G}\, \mathbf{J}\, \hat{\boldsymbol{u}}^{a} \cdot \left(\mathbf{J}\, \hat{\boldsymbol{u}}^{a} \right)^{\mathrm{T}} \tilde{\boldsymbol{\lambda}}_{\hat{d}q}^{i} \tag{7.7}$$

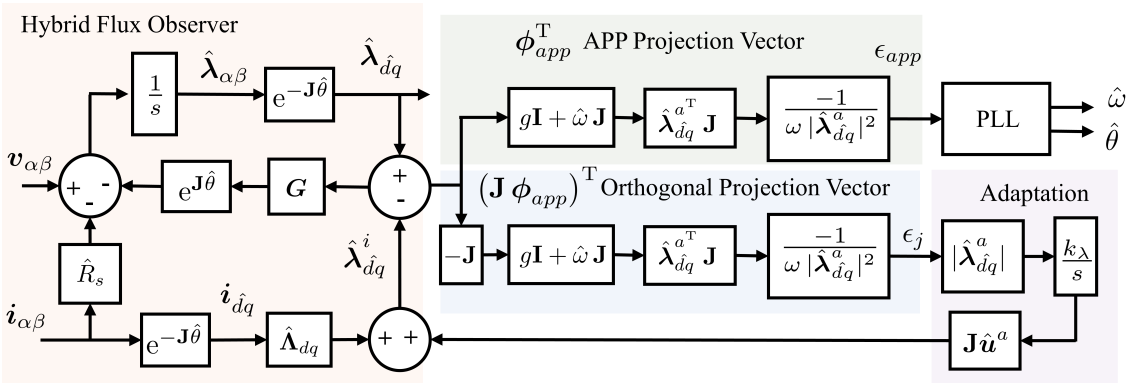

Figure 7.5: Hybrid flux observer in stator reference frame with the APP position observer augmented with flux adaptation for accurate torque estimation.

where $\hat{\boldsymbol{u}}^a$ is an unit vector along the auxiliary-flux vector as

$$\hat{\boldsymbol{u}}^a = \frac{\hat{\boldsymbol{\lambda}}^a_{\hat{d}\hat{q}}}{|\hat{\boldsymbol{\lambda}}^a_{\hat{d}\hat{q}}|}. \tag{7.8}$$

The expression (7.7) states that the torque estimation error is a function of the operating speed and is proportional to the current-model flux error orthogonal to auxiliary-flux vector, i.e., $\mathbf{J}\,\hat{\boldsymbol{u}}^a$.

The steady-state torque estimation error contour (7.7) for +30% errors in the d-axis flux-map ($\tilde{\lambda}^i_d = 0.3\,\lambda_d$) at speeds $\omega = 0.33$ p.u. and $\omega = 0.8$ p.u.. is shown in Figs. 7.3(a) and 7.3(b), respectively. The same plots are reproduced for +30% errors in the q-axis flux-map ($\tilde{\lambda}^i_q = 0.3\,\lambda_q$) in Fig. 7.4. It is observed that the torque error is more sensitive to the d-axis parameter error and that the estimation accuracy degrades with decreasing speed.

7.3 Current-Model Flux Adaptation

The block diagram of the proposed current-model flux adaptation supplemented to APP position observer is shown in Fig. 7.5.

7.3.1 Adaptation Design

In the former sections, the feasibility of the orthogonal projection vector $\mathbf{J}\,\boldsymbol{\phi}_{app}$ for stator resistance and the d-axis current-model flux adaptation were investigated. As alluded to in Section 6.5.3, adapting a single parameter (eg. d-axis flux) in the presence of flux-map error in both d and q-axes could negatively influence the position observer. Hence, a new adaptation law is investigated in this section targeting accurate torque estimation under parameters error.

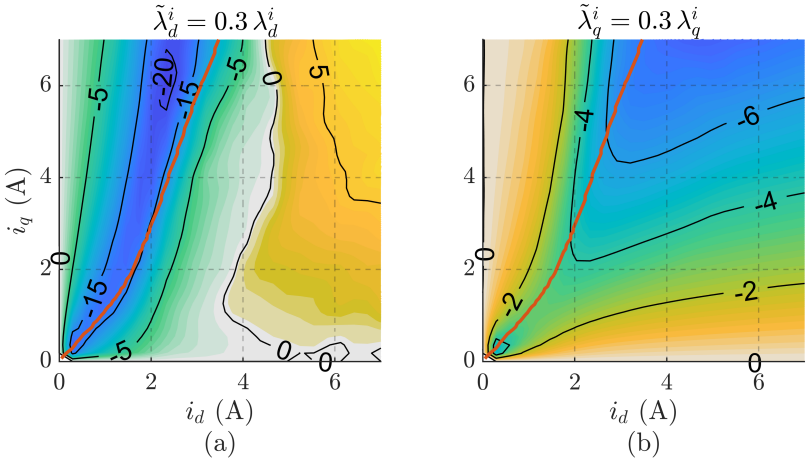

Figure 7.6: Steady-state position error $\tilde{\theta}_0$ in degrees (electrical): (a) +30% error in d-axis, $\tilde{\lambda}_d^i = 0.3\,\lambda_d^i$; (b) +30 % error in q-axis, $\tilde{\lambda}_q^i = 0.3\,\lambda_q^i$. In red is the MTPA trajectory. Motor: A.

The relation of the orthogonal error signal ϵ_j to the current-model flux error $\tilde{\boldsymbol{\lambda}}_{\hat{dq}}^i$ is established using (3.28) as

$$\epsilon_j\big|_{s=0} = \Big(\mathbf{J}\,\boldsymbol{\phi}_{app}\Big)^{\mathrm{T}}\,\boldsymbol{H}_{\tilde{\lambda}^i}\,\tilde{\boldsymbol{\lambda}}_{\hat{dq}}^i\big|_{s=0} = \frac{1}{|\hat{\boldsymbol{\lambda}}_{\hat{dq}}^a|}\Big(\mathbf{J}\,\hat{\boldsymbol{u}}^a\Big)^{\mathrm{T}}\,\tilde{\boldsymbol{\lambda}}_{\hat{dq}}^i. \tag{7.9}$$

The expression (7.9) implies that the error signal ϵ_j is proportional to the current-model flux error along the vector $\mathbf{J}\,\hat{\boldsymbol{\lambda}}_{\hat{dq}}^a$. Thus, a flux adaptation is designed along this vector.

Let ϵ_λ denote the error signal that is equal to the current-model flux error along $\mathbf{J}\,\hat{\boldsymbol{u}}^a$; then, from (7.9), it follows that the equivalent projection vector $\boldsymbol{\phi}_\lambda$ is

$$\epsilon_\lambda\Big|_{s=0} = \Big(\mathbf{J}\,\hat{\boldsymbol{u}}^a\Big)^{\mathrm{T}}\,\tilde{\boldsymbol{\lambda}}_{\hat{dq}}^i \quad \Rightarrow \quad \boldsymbol{\phi}_\lambda = |\hat{\boldsymbol{\lambda}}_{\hat{dq}}^a|\,\Big(\mathbf{J}\,\boldsymbol{\phi}_{app}\Big). \tag{7.10}$$

Finally, the adaptation law is formulated as

$$\hat{\boldsymbol{\lambda}}_{\hat{dq}}^i = \hat{\boldsymbol{\Lambda}}_{dq}(\boldsymbol{i}_{\hat{dq}}) + \mathbf{J}\,\hat{\boldsymbol{u}}^a \cdot k_\lambda \int \epsilon_\lambda\,\mathrm{d}t \tag{7.11}$$

where k_λ is the integral gain as depicted in Fig. 7.5.

In steady-state conditions, the adaptation (7.11) mitigates the current-model flux error along the vector $\mathbf{J}\,\hat{\boldsymbol{u}}^a$. Consequently, the torque estimation error in (7.7) converges to zero and accurate torque control becomes realizable. It is worth pointing out that the steady-state position error (6.9) shown in Fig. 7.6 remains unaffected by the flux adaptation. It can also be shown that the flux estimation error in (3.23) converges to zero under adaptation.

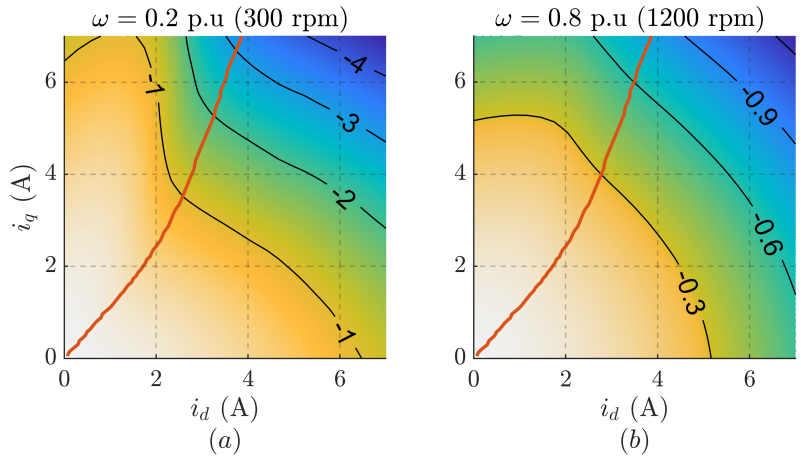

Figure 7.7: Steady-state torque estimation error $\tilde{T}_0$ in Nm at $\tilde{R}_s = 1\Omega$ (0.16 p.u.): (a) $\omega = 0.2$ p.u. (300 rpm); (b) $\omega = 0.8$ p.u. (1200 rpm). In red is the MTPA trajectory. Rated torque $T_n = 7.1$ Nm; $g = 2\pi \cdot 10$ rad/s. Motor: A.

7.3.2 Susceptibility to Resistance Variations

In the presence of resistance error, the steady-state errors in stator flux and torque estimation are inevitable. The flux adaptation converges to an inaccurate value that is given by

$$\begin{aligned} \epsilon_\lambda &= \boldsymbol{\phi}_\lambda^{\mathrm{T}}\, \boldsymbol{H}_{\tilde{\boldsymbol{\lambda}}^i}\, \tilde{\boldsymbol{\lambda}}^{i}_{\hat{dq}0} + \boldsymbol{\phi}_\lambda^{\mathrm{T}}\, \boldsymbol{h}_{\tilde{R}}\, \tilde{R}_s = 0 \\ &\Rightarrow \left(\mathbf{J}\, \hat{\boldsymbol{u}}^a\right)^{\mathrm{T}} \cdot \tilde{\boldsymbol{\lambda}}^{i}_{\hat{dq}0} = \tilde{R}_s \cdot \frac{1}{\omega} \left(\hat{\boldsymbol{u}}^a\right)^{\mathrm{T}} \boldsymbol{i}_{\hat{dq}}. \end{aligned} \tag{7.12}$$

Thus, the resistance error introduces a steady-state current-model flux error orthogonal to the auxiliary-flux vector. Owing to the inverse relation with the angular speed, the influence of stator resistance diminishes at high speeds.

Finally, using (7.12) in (7.7), the steady-state torque estimation error due to the resistance error is given by

$$\tilde{T}_0 = \frac{3p}{2}\, \boldsymbol{i}_{\hat{dq}}^{\mathrm{T}}\, \mathbf{J}\, (\boldsymbol{G} + \omega \mathbf{J})^{-1} \left[\boldsymbol{G}\, \mathbf{J}\, \hat{\boldsymbol{u}}^a \cdot \frac{\left(\hat{\boldsymbol{u}}^a\right)^{\mathrm{T}} \boldsymbol{i}_{\hat{dq}}}{\omega} - \boldsymbol{i}_{\hat{dq}} \right] \cdot \tilde{R}_s \tag{7.13}$$

The steady-state torque estimation error contour for $\tilde{R}_s = 1\Omega$ (0.16 p.u.) at $\omega = 0.2$ p.u. (300 rpm) and $\omega = 0.8$ p.u. (1200 rpm) is shown in Figs. 7.7(a) and 7.7(b), respectively. As expected, the torque estimation error due to imprecise resistance is observed to increase with the stator current magnitude and decrease with the angular speed.

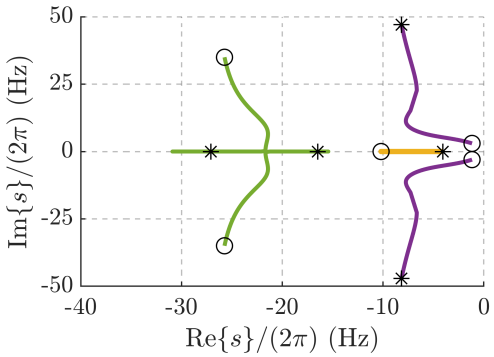

Figure 7.8: Locus of poles of the position observer with flux adaptation for $\omega = 0.1 \ldots 1$ p.u. at rated $T = 7.1$ Nm (MTPA) where the markers $\circ$ and $*$ denote the speeds 0.1 and 1 p.u., respectively. Color code: PLL poles are denoted in green, flux observer in purple, current-model flux adaptation in yellow. Motor: *A*.

7.4 Stability Analysis with Flux Adaptation

It follows from (7.11) that the current-model flux error dynamics with adaptation along $\mathbf{J}\,\hat{\boldsymbol{u}}^a$ become

$$\left(\mathbf{J}\hat{\boldsymbol{u}}^a\right)^{\mathrm{T}} s\tilde{\boldsymbol{\lambda}}^i_{\hat{dq}} = -k_\lambda\,\epsilon_\lambda. \tag{7.14}$$

Using the flux estimation error dynamics (3.23) and the error signal dynamics (3.27), the small signal stability is analyzed as

$$s\,\boldsymbol{y}_\lambda = \boldsymbol{A}_\lambda\,\boldsymbol{y}_\lambda \tag{7.15}$$

where $\boldsymbol{y}_\lambda = \left[\left(\tilde{\boldsymbol{\lambda}}_{\hat{dq}}\right)^{\mathrm{T}} \quad \tilde{\theta} \quad \tilde{\omega}_i \quad \left(\mathbf{J}\hat{\boldsymbol{u}}^a\right)^{\mathrm{T}}\tilde{\boldsymbol{\lambda}}^i_{\hat{dq}}\right]^{\mathrm{T}}$ and $\boldsymbol{A}_\lambda =$

$$\begin{bmatrix} -(\boldsymbol{G}+\omega\,\mathbf{J}) & \boldsymbol{G}\,\hat{\boldsymbol{\lambda}}^a_{\hat{dq}} & \mathbf{0} & \boldsymbol{G}\,\mathbf{J}\,\hat{\boldsymbol{u}}^a \\ k_p\,\boldsymbol{\phi}^{\mathrm{T}}_{app} & -k_p\,\boldsymbol{\phi}^{\mathrm{T}}_{app}\,\hat{\boldsymbol{\lambda}}^a_{\hat{dq}} & 1 & -k_p\,\boldsymbol{\phi}^{\mathrm{T}}_{app}\,\mathbf{J}\,\hat{\boldsymbol{u}}^a \\ k_i\,\boldsymbol{\phi}^{\mathrm{T}}_{app} & -k_i\,\boldsymbol{\phi}^{\mathrm{T}}_{app}\,\hat{\boldsymbol{\lambda}}^a_{\hat{dq}} & 0 & -k_i\,\boldsymbol{\phi}^{\mathrm{T}}_{app}\,\mathbf{J}\,\hat{\boldsymbol{u}}^a \\ k_\lambda\,\boldsymbol{\phi}^{\mathrm{T}}_{\lambda} & -k_\lambda\,\boldsymbol{\phi}^{\mathrm{T}}_{\lambda}\,\hat{\boldsymbol{\lambda}}^a_{\hat{dq}} & 0 & -k_\lambda\,\boldsymbol{\phi}^{\mathrm{T}}_{\lambda}\,\mathbf{J}\,\hat{\boldsymbol{u}}^a \end{bmatrix}. \tag{7.16}$$

The gains of the PLL are chosen for a critically damped response (3.25) with the poles at $s = -\Omega_\omega = -2\pi \cdot 25$ rad/s. The flux observer gain is set to 0.2 p.u. of rated speed as $g = 2\pi \cdot 10$ rad/s. The gain of current-model flux adaptation is $k_\lambda = 2\pi \cdot 4$ rad/s.

Fig. 7.8 shows the eigenvalues of (3.33) for $\omega = 0.1 \ldots 1$ p.u. at rated torque $T = 7.1$ Nm on MTPA trajectory. The closed loop poles of the combined dynamics of the proposed control system are observed to be stable.

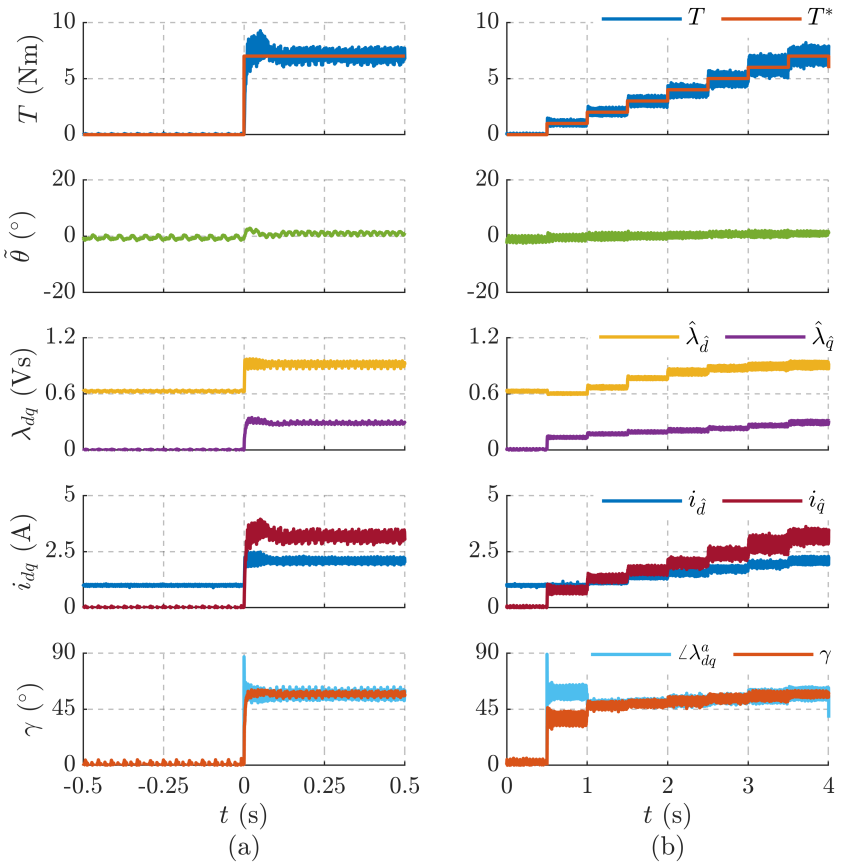

Figure 7.9: Optimal torque control of the proposed scheme at rated speed $\omega = 1$ p.u. (1500 rpm): (a) Rated torque step $T^* = 0 \rightarrow 7.1$ Nm at $t = 0$ s; (b) Incremental torque reference. Motor: A.

7.5 Experimental Results

The proposed torque control scheme with current-model flux adaptation is validated experimentally with SyR motor A. The SyR machine operates in the torque control mode and the auxiliary drive in the speed control mode. A minimum stator current $i_{min} = 1$ A is imposed for fundamental excitation at no load.

MTPA Torque Control

The proposed torque control scheme is validated at rated speed with a rated torque step $T^* = 0 \rightarrow 7.1$ Nm at $t = 0$ s in Fig. 7.9(a). The control is stable with small transient position error ($< 5°$) and is observed to track the torque step reference seamlessly.

In the second test, torque reference is commanded in small incremental steps at the rated speed, shown in Fig. 7.9(b). For small loads ($t < 1$ s), the MTPA

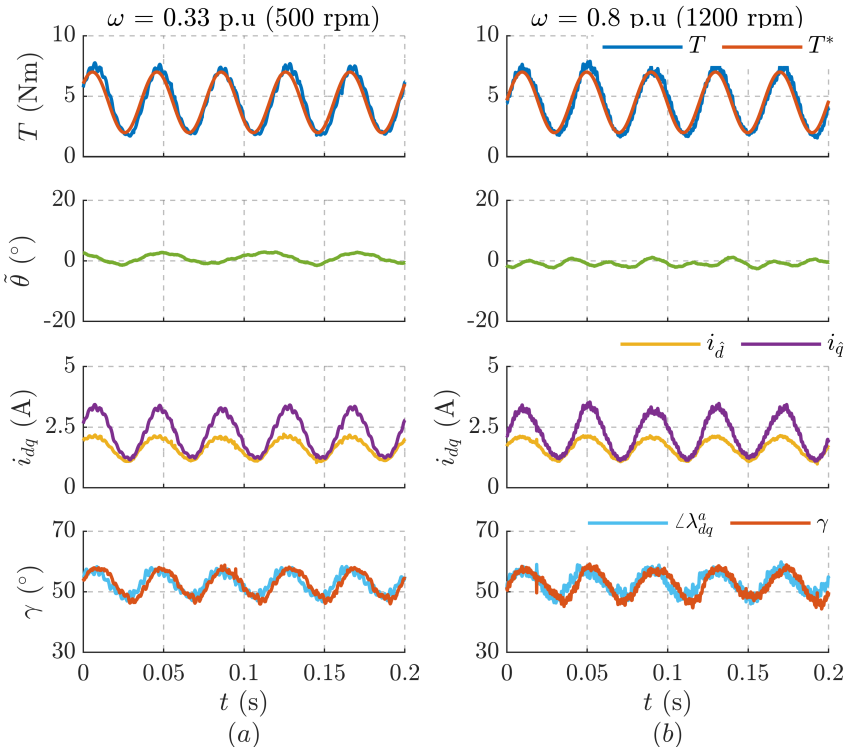

Figure 7.10: Dynamic MTPA adaptation with sinusoidal torque reference (25 Hz). Operating speed: (a) $\omega = 0.33$ p.u. (500 rpm); (b) $\omega = 0.8$ p.u. (1200 rpm). Motor: A.

law is not respected due to the imposition of minimum stator current, as said. For higher loads ($t > 1$ s), the current angle is shown to be coincident with the phase of auxiliary-flux vector, implying MTPA operation.

The dynamic capability of the proposed torque control to track MTPA is evaluated with a sinusoidal torque reference at 25 Hz in Fig. 7.10 at two different speeds; the current angle is observed to track the phase of auxiliary-flux vector. The use of analytical formulation to attain the MTPA state without an additional regulator facilitates the dynamic tracking of MTPA.

Operation under Parameter Errors

The susceptibility of torque controller and position observer in the presence of parameter error in d-axis without flux adaptation is demonstrated in Fig. 7.11. A varying error from +30% ($\hat{\lambda}_d^i = 0.7\,\lambda_d$) to -30% ($\hat{\lambda}_d^i = 1.3\,\lambda_d$) is imposed in steps of -10% increment at rated torque reference $T^* = 7.1$ Nm and two rotor speeds values $\omega = 0.33$ p.u. (500 rpm) and $\omega = 0.8$ p.u. (1200 rpm) in Figs. 7.11(a) and 7.11(b), respectively. Higher speeds are not feasible at rated torque due to voltage limitation as the control diverges from the optimal MTPA point under parameter

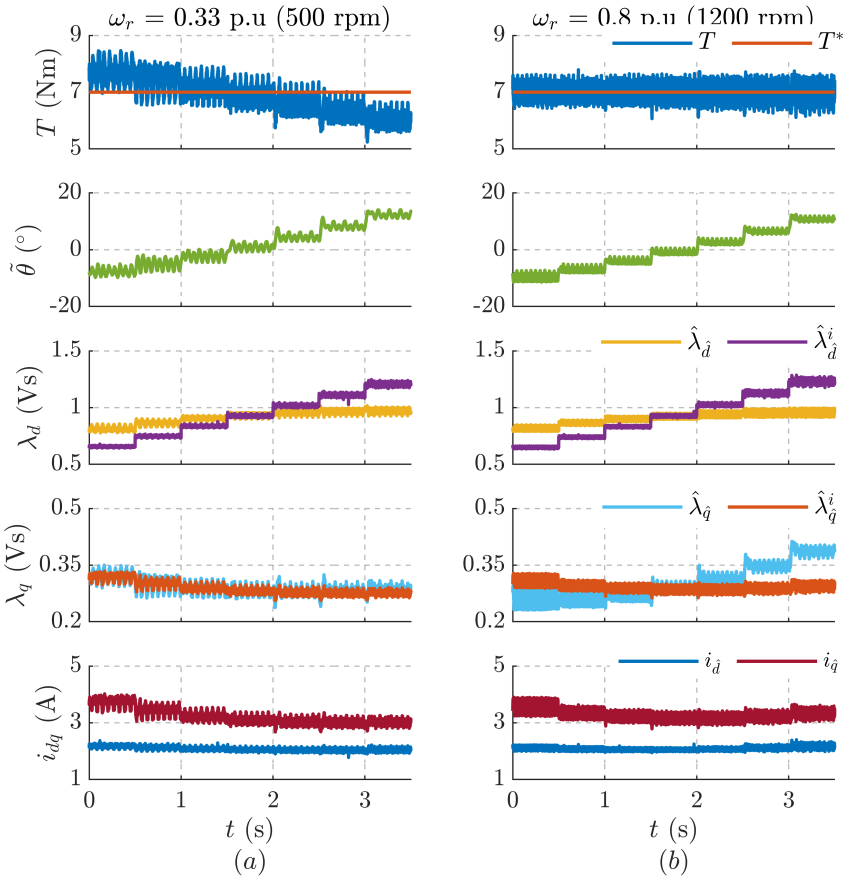

Figure 7.11: Torque control at $T^* = 7.1$ Nm under parameter error in d-axis varying from +30% ($\hat{\lambda}^i_d = 0.7\,\lambda_d$) to -30% ($\hat{\lambda}^i_d = 1.3\,\lambda_d$) in steps of -10% increment every 0.5 s. Operating speed: (a) $\omega = 0.33$ p.u. (500 rpm); (b) $\omega = 0.8$ p.u. (1200 rpm). Motor: A.

error.

The maximum position error is observed to be $\tilde{\theta}_0 \approx 15°$, drawing correlation to the steady-state position error (6.9) in Fig. 7.6(a). It can be discerned from Fig. 7.11 that the position error is independent of operating speed. On contrary, the torque estimation error is more prominent at low speed in Fig. 7.11(a) where, at $t < 0.5$ s, it is approximately -0.75 Nm (-10%) for +30% d-axis flux error, in accordance with the analytical evaluation in Fig. 7.3(a). The torque error is diminished at high speed in Fig. 7.11(b), as evaluated in Fig. 7.3(b).

A similar test is conducted for varying errors in the q-axis flux-map in Fig. 7.12. The speed-independent steady-state position error is observed to be $\tilde{\theta}_0 < 5°$, supporting the analysis in Fig. 7.6(b). The torque estimation shows more resilience towards parameter error in q-axis, in accordance with Fig. 7.4.

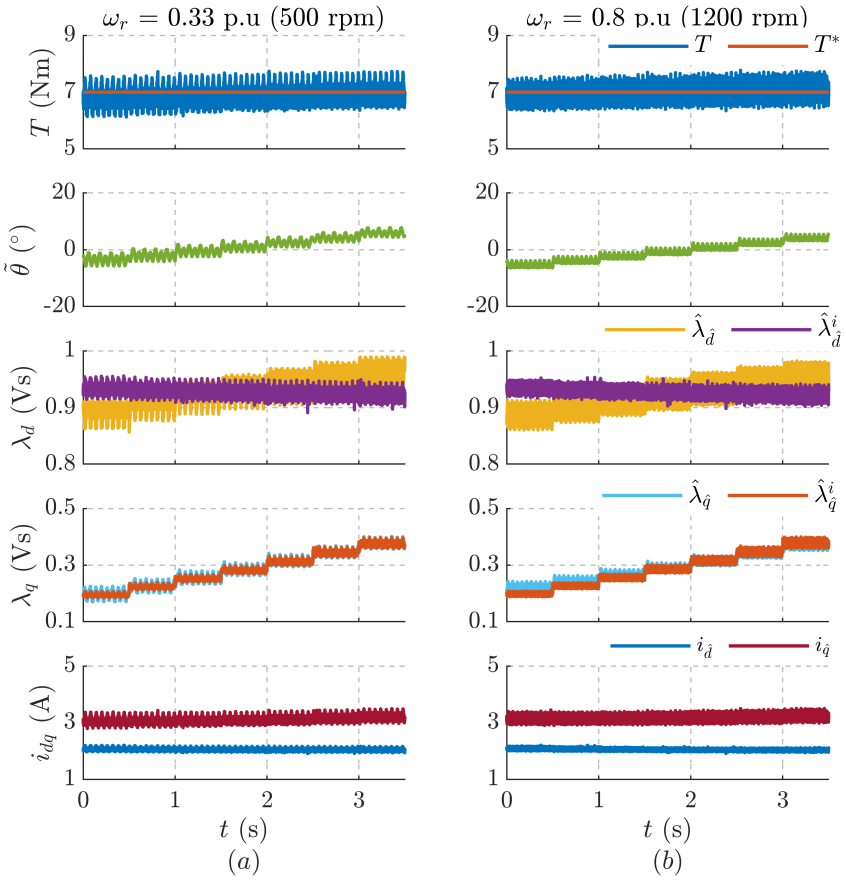

Figure 7.12: Torque control at $T^* = 7.1$ Nm under parameter error in q-axis varying from +30% ($\hat{\lambda}^i_q = 0.7\,\lambda_q$) to -30% ($\hat{\lambda}^i_q = 1.3\,\lambda_q$) in steps of -10% increment every 0.5 s. Operating speed: (a) $\omega = 0.33$ p.u. (500 rpm); (b) $\omega = 0.8$ p.u. (1200 rpm). Motor: A.

Current-Model Flux Adaptation

The efficacy of the current-model flux adaptation is demonstrated at $\omega = 0.33$ p.u. (500 rpm) and at 40% overload in torque $T^* = 1.4$ p.u. (10 Nm) with a varying error in the d-axis flux-map from zero to -50% ($\hat{\lambda}^i_d = 1.5\,\lambda_d$) in steps of -10% increment every 0.5 s, as shown in Fig. 7.13. The operating and parameter error conditions are more severe than the ones considered so far. The performance of the control without and with the flux adaptation is juxtaposed in Figs. 7.13(a) and 7.13(b), respectively. A maximum torque error of +24% is observed in Fig. 7.13(a) while in Fig. 7.13(b), accurate torque control is obtained despite the high position error.

The dynamics of the current-model flux adaptation is illustrated in Fig. 7.14 in the same operating conditions ($T^* = 1.4$ p.u. and $\omega = 0.33$ p.u.) where the adaptation is enabled at $t = 0$ s. The Fig. 7.14(a) considers a -30% flux-map error

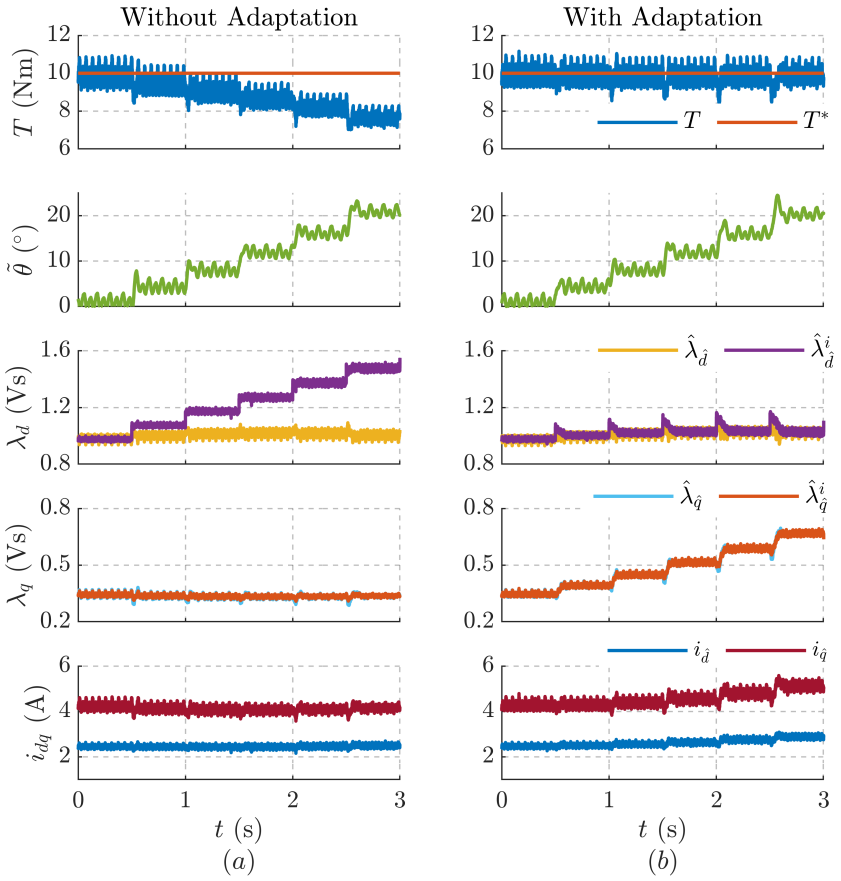

Figure 7.13: Torque control at $T^* = 1.4$ p.u. (10 Nm) and $\omega = 0.33$ p.u. (500 rpm) under parameter error in d-axis varying from 0% to -50% ($\hat{\lambda}_d^i = 1.5\,\lambda_d$) in steps of -10% increment every 0.5 s: (a) Without flux adaptation; (b) With flux adaptation. Motor: *A*.

in either axes while Fig. 7.14 has -30% error in d-axis and +30% error in q-axis. For $t < 0$ s, the torque error is approximately 15% in both the figures as it is dominated by the d-axis error. Conversely, the q-axis flux-map error has a substantial influence on the position error; hence, a high error $\tilde{\theta} \approx 19°$ is discerned in Fig. 7.14(a) while it is reduced in Fig.7.14(b) where the flux-map errors carry opposite signs (see Fig. 7.6).

Once the adaptation is enabled at $t = 0$ s, the observed and current-model flux quantities converge and accurate torque is realized. It is worth highlighting that the steady-state position error remains unaltered by the flux adaptation due to the orthogonality of projection vectors. Moreover, the stator flux and currents in estimated reference frame settle at different values in the two figures due to the steady-state different position errors.

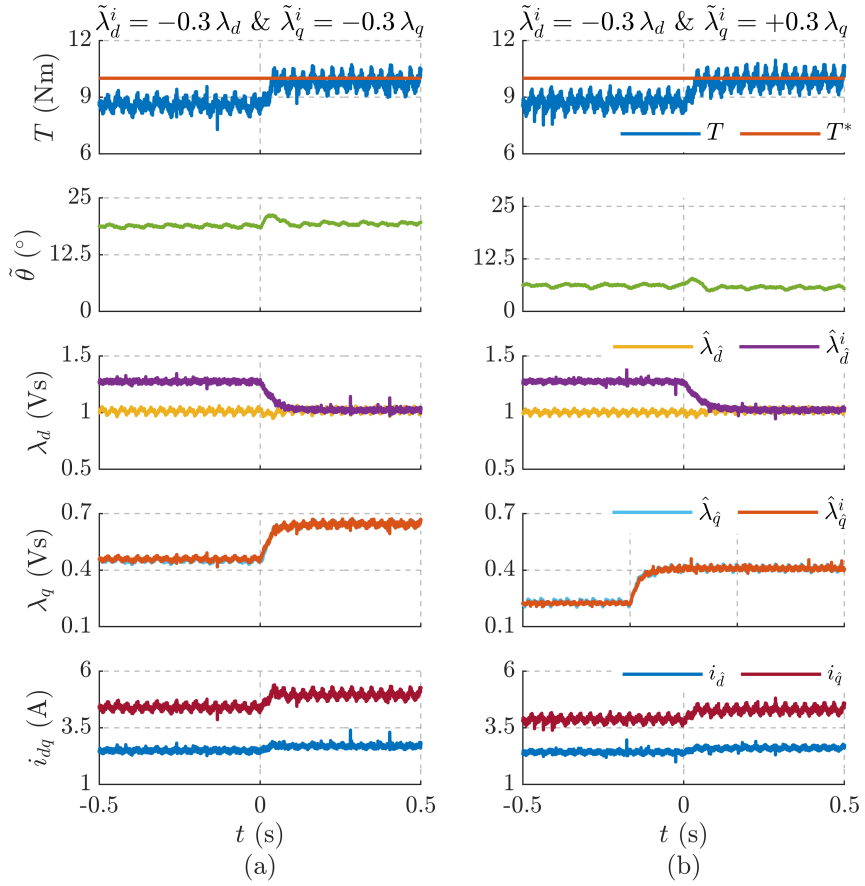

Figure 7.14: Flux adaptation enabled at $t = 0$ s in the torque control at $T^* = 1.4$ p.u (10 Nm) and $\omega = 0.33$ p.u. (500 rpm) under parameter errors in both axes: (a) -30% in d-axis ($\hat{\lambda}_d^i = 1.3\,\lambda_d$) and -30% in q-axis ($\hat{\lambda}_q^i = 1.3\,\lambda_q$); (b) -30% error in d-axis and +30% error in q-axis ($\hat{\lambda}_q^i = 0.7\,\lambda_q$). Motor: A.

Susceptibility to Stator Resistance

The susceptibility of the proposed torque control scheme to a stator resistance perturbation of $\tilde{R}_s = \pm 1\Omega$ (0.16 p.u.) is evaluated at speeds $\omega = 0.2$ p.u. (300 rpm) and $\omega = 0.8$ p.u. (1200 rpm) in Figs. 7.15(a) and 7.15(b), respectively. In accordance to the analytical estimate in Fig. 7.7, the maximum torque error is approximately 0.8 Nm at 300 rpm and less than 0.2 Nm at 1200 rpm. It is worth pointing out that the position error is null despite the variations in stator flux and torque, attesting to the resistance immunity property of the APP scheme.

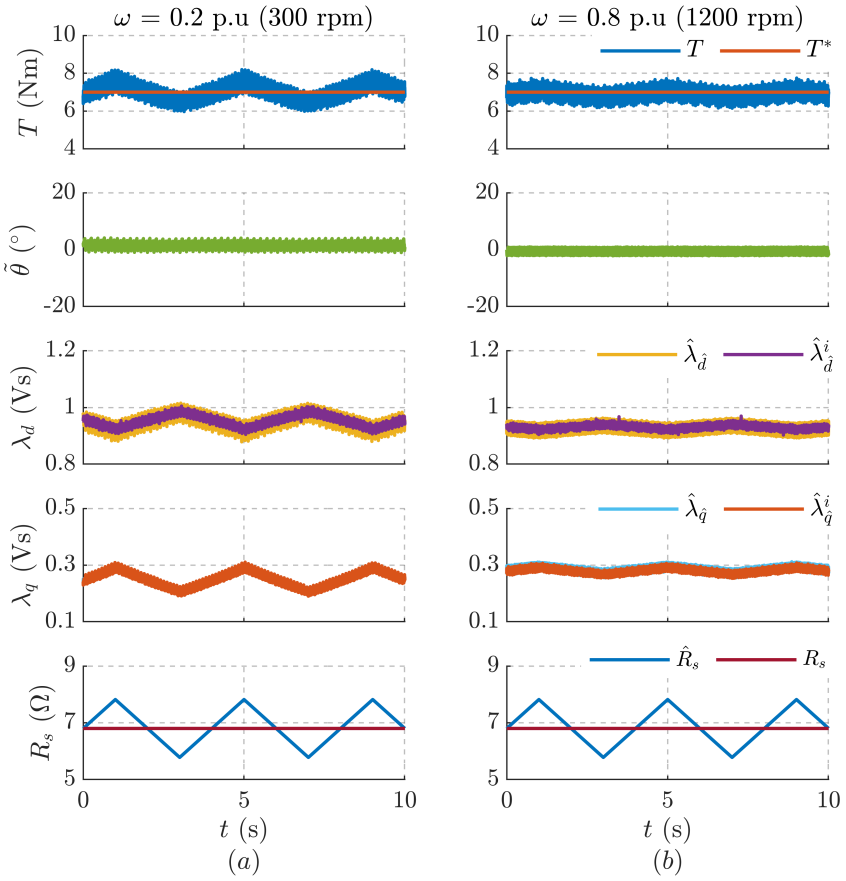

Figure 7.15: Susceptibility of the proposed torque control to a stator resistance perturbation of $\tilde{R}_s = \pm 1\Omega$ (0.16 p.u.) at rated torque: (a) $\omega = 0.2$ p.u. (300 rpm); (b) $\omega = 0.8$ p.u. (1200 rpm). Motor: *A*.

7.6 Summary of the Chapter Contributions

The main contributions of the accurate torque control with flux adaptation are listed as follows:

- An optimal current reference generation respecting MTPA criterion is devised as a function of discrepancy between commanded and estimated torque using the small-signal model of the machine.
- An analytical expression for torque estimation error is derived as a function of parameter errors and steady-state position error. It is subsequently formulated for the APP sensorless scheme.
- A projection vector that is orthogonal to APP is employed for current-model flux adaptation, ensuring decoupling and non-interference with the position

observer. The proposed adaptation law is shown to alleviate the error in torque estimation. Thus, accurate torque control becomes realizable in presence of flux-map errors.

The stability analysis of the position observer with flux adaptation is studied and the performance of the proposed torque control sensorless scheme with flux adaptation is experimentally validated on a 1.1 kW SyR machine test bench.

Chapter 8

High-Frequency Excitation Schemes

A new injection-less sensorless technique using finite-control-set model-predictive-control is disclosed in [50] and further extended to full-speed with the APP position observer augmented for high speeds, published in [51]. A square-wave voltage injection based position estimation augmented with auxiliary-flux position observer is published in [47].

8.1 Introduction

Sensorless techniques relying on fundamental-wave excitation falter at low speeds due to the poor signal-to-noise ratio in the back-emf based flux estimation and back-emf non-observability at zero speed. Thus arises the need to design position estimation techniques tailored for the low speeds region.

For some applications like pumps, fans and compressors where a sustained operation at low speeds is not required, an open-loop start with a voltage reference in a slow ramped synchronous rotating reference frame [52], referred as *V/f* control, can be pursued for simplicity. Alternatively, an open rotating current reference, referred as *I/f* control, is proposed [53]–[56] for the ease of control and robustness in synchronous machines.

The closed-loop low speed sensorless techniques rely on the incremental magnetic anisotropy of the machine that is exploited with various high-frequency excitation techniques. Besides accurate and high performance position estimation, they are capable of withstanding torque disturbances at zero speed standstill condition. Based on the type of high-frequency excitation, they can be classified into two categories [57]: *(i)* Continuous excitation schemes; *(ii)* Discontinuous excitation schemes.

This chapter is organized as follows: Sections 8.2 and 8.3 present the review

of the continuous and the discontinuous schemes, respectively. The feasible region of operation for low speed sensorless control is assessed through the incremental saliency analysis in Section 8.4. A new projection vector framework for high-frequency excitation schemes is developed in Section 8.5, based on which the discontinuous and the continuous excitation schemes are validated in Sections 8.6 and 8.7, respectively. A new injection-less sensorless control using finite-control-set model-predictive-control (FCS-MPC) is designed to be augmented with the APP position observer in Section 8.6 while a square-wave pulsating voltage injection is augmented with AUX position observer in Section 8.7, representing two alternative full-speed sensorless solutions.

8.2 Review of Continuous Excitation Schemes

This chapter presents a review on the periodic high-frequency signal injection schemes where the position information is embedded in the magnitude/phase of the resulting high-frequency response. Among the two high-frequency signal injection possibilities (voltage and current), an identical performance can be obtained with a well-designed control system in either case. However, for the ease of implementation with the voltage source inverters, it is more prevalent to inject high-frequency voltage signals as the current injection demands either a high bandwidth fundamental current tracking loop or a supplementary parallel-operating (resonant) current regulators [58], [59].

8.2.1 Pulsating Signal Injection

The high-frequency terms are denoted by the subscript h. Let the injected sinusoidal voltage magnitude and frequency along estimated $\hat{d}$-axis be denoted as V_h and ω_h, respectively, i.e,

$$\boldsymbol{v}_{\hat{d}qh} = V_h \begin{bmatrix} \cos(\omega_h \mathrm{t}) \\ 0 \end{bmatrix}. \tag{8.1}$$

The high-frequency stator voltage equation is given by

$$s\,\boldsymbol{\lambda}_{\hat{d}qh} = \boldsymbol{v}_{\hat{d}qh} - R_s\,\boldsymbol{i}_{\hat{d}qh} - \omega \mathbf{J}\,\boldsymbol{\lambda}_{\hat{d}qh}. \tag{8.2}$$

In (8.2), the resistance and the back-emf terms are generally neglected as they are relatively insignificant in the high-frequency domain at low speeds. Thus, the resulting high-frequency flux components are

$$\boldsymbol{\lambda}_{\hat{d}qh} \approx \frac{V_h}{\omega_h} \begin{bmatrix} \sin(\omega_h t) \\ 0 \end{bmatrix}. \tag{8.3}$$

If the signal injection-based sensorless control is also persevered at higher speeds, then the high-frequency back-emf term can no longer be neglected. To this end, the back-emf in q-axis can be compensated with an elliptical injection [60], [61] as

$$\boldsymbol{v}_{\hat{dq}h} = V_h \begin{bmatrix} \cos(\omega_h t) \\ \frac{\omega}{\omega_h} \sin(\omega_h t) \end{bmatrix}. \tag{8.4}$$

Given the acoustic noise and the reduced voltage for torque production, there is little incentive to extend the signal injection schemes beyond the low speeds region where the fundamental-wave excitation schemes are reliable.

An alternative to (8.2) is the high-frequency pulsating voltage injection along q-axis but is out of favor due to the increased torque ripples [62]. With respect to minimizing torque ripples, pulsating injection along the constant torque locus have been reported [63]–[65].

A pulsating injection in stationary reference frame is investigated in [66], [67] with no discernible benefits over the conventional synchronous frame injection. The pulsating current injection is explored in [59], concluding in the favor of voltage injection.

Current Demodulation

The earliest works on the pulsating voltage injection and current demodulation in rotor reference frame dates back more than two decades [60] and have been extensively studied since.

The resulting high-frequency current response to the pulsating voltage (8.2) can be expressed using (3.5) as

$$\boldsymbol{i}_{\hat{dq}h} = \mathrm{e}^{\mathbf{J}\tilde{\theta}}\, \boldsymbol{L}_{\partial}^{-1}\, \mathrm{e}^{-\mathbf{J}\tilde{\theta}}\, \boldsymbol{\lambda}_{\hat{dq}h}. \tag{8.5}$$

Using (8.3), the expression for $\boldsymbol{i}_{\hat{dq}h}$ simplifies to

$$\boldsymbol{i}_{\hat{dq}h} = \frac{V_h \sin(\omega_h t)}{\omega_h \left(l_d l_q - l_{dq}^2\right)} \begin{bmatrix} l_\Sigma - l_\Delta \cos(2\tilde{\theta}) + l_{dq} \sin(2\tilde{\theta}) \\ -l_\Delta \sin(2\tilde{\theta}) - l_{dq} \cos(2\tilde{\theta}) \end{bmatrix} \tag{8.6}$$

where $l_\Sigma = \frac{l_d + l_q}{2}$ and $l_\Delta = \frac{l_d - l_q}{2}$. Linearizing (8.6), the q-axis high-frequency current is given by

$$i_{\hat{q}h} = -\frac{V_h \sin(\omega_h t)}{\omega_h} \left(\frac{l_\Delta}{l_d l_q - l_{dq}^2} 2\tilde{\theta} + \frac{l_{dq}}{l_d l_q - l_{dq}^2} \right). \tag{8.7}$$

It can be discerned that the q-axis current $i_{\hat{q}h}$ is composed of a position error bearing term as well as a cross-saturation inductance bearing term. The high-frequency component $i_{\hat{q}h}$ is extracted from $i_{\hat{q}}$ through a bandpass filter and is demodulated with a heterodyne process to obtain the position error signal ϵ_h as

$$\epsilon_h = -\frac{\omega_h}{2V_h} \frac{l_d l_q - l_{dq}^2}{l_\Delta} \operatorname{LPF}\Big[i_{\hat{q}h} \cdot 2 \sin(\omega_h t) \Big]. \tag{8.8}$$

Equating $\epsilon_h = 0$ reveals the cross-saturation induced steady state position error $\tilde{\theta}_{dq}$ given by [10], [68]

$$\tilde{\theta}_{dq} = \frac{1}{2}\tan^{-1}\frac{-l_{dq}}{l_\Delta}. \tag{8.9}$$

The highlights of this scheme are summarized as follows:

- Limited dependency on motor parameters since the inductances only appear as a scaling factor in (8.6). Hence, inaccuracy in inductance merely shifts the poles of the position observer.
- Suffers from cross-saturation error which is more magnified at high loads ($\tilde{\theta}_{dq} \approx 20^\circ$ at $T = 2$ p.u. [69]). Many of the earlier works overlook the impact of the cross-saturation term [44], [60], [70]–[74]. Offline measurements-based compensation for cross-saturation is reported in [62]. To account for the cross-saturation error, [67], [75] proposed a feed-forward correction term as a function of load current; [76], [77] introduced a coupling factor in the error function based on the prior measurements. Compensation techniques for improved stability at high loads are explored in [78]–[80].
- The LPF in heterodyne signal processing stage in (8.8) imposes limitation on the maximum achievable bandwidth of the position observer [68]. Typically, the closed-loop bandwidth of the position tracking loop is set to three times lower than the cutoff frequency of the LPF [77]. Besides, an additional filter to remove the high-frequency current component for fundamental current regulation could affect the dynamics of the inner current loop in current-vector-control.

Current-Model Flux Demodulation

The cross-saturation effects can be alleviated by designing the position error signal from the q-axis current-model flux estimate $\lambda^i_{\hat{q}}$ instead of the q-axis current $i_{\hat{q}}$ [31], [69]. The high-frequency current-model flux estimate can be expressed as

$$\boldsymbol{\lambda}^i_{\hat{d}qh} = \boldsymbol{L}_\partial \cdot \boldsymbol{i}_{\hat{d}qh} = \boldsymbol{L}_\partial \cdot \mathrm{e}^{\mathbf{J}\tilde{\theta}}\, \boldsymbol{L}_\partial^{-1}\, \mathrm{e}^{-\mathbf{J}\tilde{\theta}}\, \boldsymbol{\lambda}_{\hat{d}qh}. \tag{8.10}$$

Using (8.6), the q-axis term $\lambda^i_{\hat{q}h}$ is derived as

$$\lambda^i_{\hat{q}h} = \frac{V_h\,\sin(\omega_h t)}{\omega_h\Big(l_d l_q - l_{dq}^2\Big)}\Big[l_{dq}\, l_\Sigma\,(1-\cos(2\tilde{\theta})) - (l_q\, l_\Delta - l_{dq}^2)\sin(2\tilde{\theta})\Big]. \tag{8.11}$$

Linearizing (8.11) for small position error leads to

$$\lambda^i_{\hat{q}h} = -\frac{V_h\,\sin(\omega_h t)}{\omega_h}\,\frac{l_q\, l_\Delta - l_{dq}^2}{l_d l_q - l_{dq}^2}\,2\tilde{\theta}. \tag{8.12}$$

Unlike (8.7), the q-axis high-frequency current-model flux estimate (8.12) is observed to have a direct correlation to the position error without deviation induced by cross-saturation. Thus, the corresponding error signal ϵ_h is obtained from (8.12) through a heterodyne process as

$$\epsilon_h = -\frac{\omega_h}{2V_h}\,\frac{l_d l_q - l_{dq}^2}{l_q\, l_\Delta - l_{dq}^2}\,\mathrm{LPF}\Big[\lambda_{\hat{q}h}^{i}\cdot 2\sin(\omega_h t)\Big]. \tag{8.13}$$

The highlights of this scheme are summarized as follows:

- Mitigates the cross-saturation error while retaining the simplicity and structure of the current modulation technique [31], [69].
- The effectiveness of this technique is coupled to the accuracy of the flux-maps LUTs and consequently is sensitive to parameter errors unlike the former technique.
- Just as the current demodulation, the LPF in the heterodyne signal processing stage (8.13) imposes limitation on the maximum achievable bandwidth of the position observer [68].

8.2.2 Rotating Signal Injection

The rotating voltage injection is a classical technique [81], [82] where the position spatial information is retrieved from the negative sequence current response. Multiple frequency injection for secondary saliences in concentrated windings is proposed in [83]. A rotating current injection with a dedicated high-frequency controller is developed for an extended-emf framework in [84].

A rotating voltage injection of magnitude V_h and frequency ω_h in the stationary reference frame is denoted by

$$\boldsymbol{v}_{\alpha\beta h} = V_h \begin{bmatrix} -\sin(\omega_h \mathrm{t}) \\ \cos(\omega_h \mathrm{t}) \end{bmatrix}. \tag{8.14}$$

Neglecting the stator resistance and the back-emf terms, the rotating high-frequency flux has a 90° phase lag to the injection voltage as

$$\boldsymbol{\lambda}_{\alpha\beta h} \approx \frac{V_h}{\omega_h} \begin{bmatrix} \cos(\omega_h \mathrm{t}) \\ \sin(\omega_h \mathrm{t}) \end{bmatrix}. \tag{8.15}$$

From (8.5) and (8.15), the rotating high-frequency current in the stationary reference frame is given by

$$\boldsymbol{i}_{\alpha\beta h} = \mathrm{e}^{\mathbf{J}\theta}\,\boldsymbol{L}_\partial^{-1}\,\mathrm{e}^{-\mathbf{J}\theta}\,\boldsymbol{\lambda}_{\alpha\beta h} = \frac{V_h}{\omega_h}\,\mathrm{e}^{\mathbf{J}\theta}\,\boldsymbol{L}_\partial^{-1}\,\mathrm{e}^{-\mathbf{J}\theta} \begin{bmatrix} \cos(\omega_h \mathrm{t}) \\ \sin(\omega_h \mathrm{t}) \end{bmatrix}. \tag{8.16}$$

The high-frequency current can be decomposed into positive and negative sequence components as .

$$\boldsymbol{i}_{\alpha\beta h} = \frac{V_h}{\omega_h\left(l_d l_q - l_{dq}^2\right)} \left(l_\Sigma \cdot \begin{bmatrix} \cos(\omega_h \mathrm{t}) \\ \sin(\omega_h \mathrm{t}) \end{bmatrix} - \sqrt{l_\Delta^2 + l_{dq}^2} \cdot \mathrm{e}^{2\mathbf{J}\,(\theta - \tilde{\theta}_{dq})} \begin{bmatrix} \cos(\omega_h \mathrm{t}) \\ \sin(-\omega_h \mathrm{t}) \end{bmatrix} \right) \quad (8.17)$$

where $\tilde{\theta}_{dq}$ is the cross-saturation error defined in (8.9).

The phase of the negative sequence component is observed to carry the position information although it is displaced by the cross-saturation error. A standard demodulation scheme [34] has the PLL tracking the negative sequence current component, with the fundamental and positive sequence components attenuated by a LPF.

The highlights of this scheme are summarized as follows:

- Akin to the pulsating current demodulating technique, this has low dependency on motor parameters and is not sensitive to parameter errors. The discrepancy in inductances only affect the bandwidth of the position observer.
- By tracking the phase of negative sequence component in (8.17), the estimated position is effectively along $\theta - \tilde{\theta}_{dq}$ which suffers from the cross-saturation error. The impact of cross-saturation on rotating injection is discussed in [10], [85].
- In addition to the higher torque ripples incurred by the rotating voltage injection scheme, it is also computationally expensive relative to the pulsating voltage injection. Similar to the preceding schemes, the LPF in signal processing stage limits the bandwidth of position observer to a fraction of the LPF cutoff frequency.

8.2.3 Square-Wave Voltage Injection

A noteworthy technique is the position estimation with a square-wave voltage injection near the switching frequency which reaps benefits in simplifying the signal processing stage. It has a large spectral separation between the injection and the fundamental frequency, reducing the interference with current regulator (in the case of current-vector-control) and can be either a rotating or a pulsating signal injection.

The rotating voltage injection at one-third the switching frequency, which is the maximum attainable frequency at synchronous sampling, is developed in [35]. Dual sampling permits rotating injection at two-third the switching frequency as shown in [86]. Rotating injection at one-fourth the switching frequency is explored in [87], [88].

Pulsating square voltage injection at half the switching frequency (the maximum permissible frequency at single synchronous sampling) is proposed in [68], [89] while injection at switching frequency with dual sampling is proposed in [90]. The effect of voltage errors from non-ideal inverter compensation on square voltage injection is studied in [91]; [92] concludes that injection at half the switching frequency shows better immunity to inverter errors than injection at the switching frequency. To increase the amplitude of current response, the frequency of square-wave injection was reduced to one-fourth of switching frequency in [93].

Dealing with the method in [68], let superscript k denote the discrete domain representation of the k^{th} sampling instant, V_h be the magnitude of injected voltage in $\hat{d}$ axis at half the switching frequency. Then the injected voltage is

$$v_{\hat{d}h}^{k} = V_h \cos(\pi k) = \begin{cases} +V_h, & \text{if } k == 2n \\ -V_h, & \text{if } k == 2n+1 \end{cases} \tag{8.18}$$

where n is an integer. Note that due to the computational delay, the voltage reference at $k-1$ is the voltage applied at k, i.e., ${\boldsymbol{v}_{dq}^{*}}^{k-1} = \boldsymbol{v}_{dq}^{k}$.

Let the discrete time derivative function be represented the operator Δ as

$$\Delta x^k = \frac{1}{T_s}(x^k - x^{k-1}) \tag{8.19}$$

where T_s is the sampling interval. Then, the high-frequency components of flux and current are given by

$$\Delta\boldsymbol{\lambda}_{\hat{d}q}^{k} \approx V_h \begin{bmatrix} \cos\Big(\pi(k-1)\Big) \\ 0 \end{bmatrix} \quad \Rightarrow \quad \Delta\boldsymbol{i}_{\hat{d}q}^{k} = V_h \, \mathrm{e}^{\mathbf{J}\tilde{\theta}} \, \boldsymbol{L}_{\partial}^{-1} \, \mathrm{e}^{-\mathbf{J}\tilde{\theta}} \begin{bmatrix} \cos\Big(\pi(k-1)\Big) \\ 0 \end{bmatrix} \tag{8.20}$$

Using (8.5), the discrete high-frequency currents are obtained as

$$\Delta\boldsymbol{i}_{\hat{d}q}^{k} = \frac{V_h \cos\Big(\pi(k-1)\Big)}{l_d l_q - l_{dq}^2} \begin{bmatrix} l_\Sigma - l_\Delta \cos(2\tilde{\theta}) + l_{dq} \sin(2\tilde{\theta}) \\ -l_\Delta \sin(2\tilde{\theta}) - l_{dq} \cos(2\tilde{\theta}) \end{bmatrix} \tag{8.21}$$

Linearizing the q component of (8.21), the error signal with square-wave demodulation is found:

$$\epsilon_h = -\frac{\cos\Big(\pi(k-1)\Big)}{2V_h} \, \frac{l_d l_q - l_{dq}^2}{l_\Delta} \, \frac{i_{\hat{q}}^{k} - i_{\hat{q}}^{k-1}}{T_s}. \tag{8.22}$$

This is equivalent to the error signal (8.8) obtained with sinusoidal injection and current demodulation.

In a similar fashion, it can be shown that the current-model flux demodulation leads to an error signal equivalent to (8.13) as

$$\epsilon_h = -\frac{\cos\Big(\pi(k-1)\Big)}{2V_h}\,\frac{l_d l_q - l_{dq}^2}{l_q\, l_\Delta - l_{dq}^2}\,\frac{\Big(\lambda_{\hat{q}}^i\Big)^k - \Big(\lambda_{\hat{q}}^i\Big)^{k-1}}{T_s}. \tag{8.23}$$

As the pulsating square-wave injection is a subset of the alternating signal injection, the current derived error signal (8.22) is prone to cross-saturation position error, whereas the flux estimate derived error signal (8.23) is not. The highlights of this scheme are summarized as follows:

- The primary benefit of the square-wave pulsating injection at half the switching frequency lies in simplifying the signal processing stage where the LPF is no longer necessary. Thus, besides the computation ease, the realization of higher position observer bandwidth becomes feasible as it no longer restricted by the LPF.
- Current and current-model flux demodulation schemes can be adapted to the square-wave injection method. The aforementioned merits and demerits of the either demodulation schemes applies.
- With increase in the injection frequency, the excited current response diminishes for the same voltage magnitude V_h. Hence, for large inductance machines, sufficiently high voltage is necessary to ensure that the high-frequency current, $\Delta \boldsymbol{i}_{\hat{dq}}^k$, is compatible with the resolution of the current sensors. In turn, this method could demand a larger high-frequency voltage magnitude compared to standard pulsating injection in certain machines.

8.2.4 Convergence Analysis

This section aims to analysis the ability of the sensorless scheme to converge to a stable steady-state operating point upon perturbed with a position error. Hitherto, a small position error was considered for linearization purposes where $\boldsymbol{L}_\partial^i(\boldsymbol{i}_{\hat{dq}}) = \boldsymbol{L}_\partial(\boldsymbol{i}_{dq})$ holds. However, for convergence analysis, the current-model incremental inductance is explicitly defined.

The convergence analysis is investigated for the pulsating voltage injection with current and current-model flux demodulation schemes.

Current Demodulation

From (8.6) and (8.8), the position error signal can be expressed in terms of the position error as

$$\epsilon_h = \frac{l_d^i\, l_q^i - (l_{dq}^i)^2}{2\, l_\Delta^i}\left(\frac{l_\Delta}{l_d\, l_q - l_{dq}^2}\,\sin(2\tilde{\theta}) + \frac{l_{dq}}{l_d\, l_q - l_{dq}^2}\,\cos(2\tilde{\theta})\right) \tag{8.24}$$

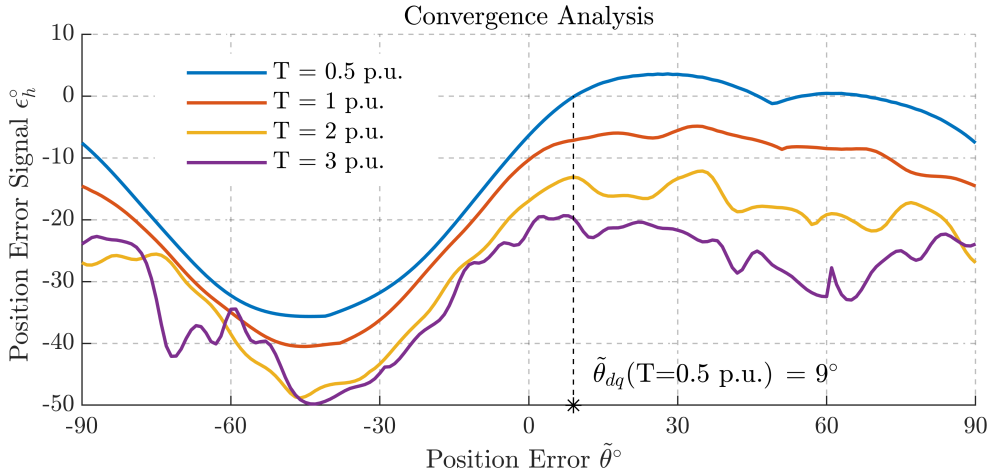

Figure 8.1: Convergence analysis for stator current demodulation scheme where the position error signal (8.24) has no zero-up crossing at high loads on MTPA. Motor: *A*.

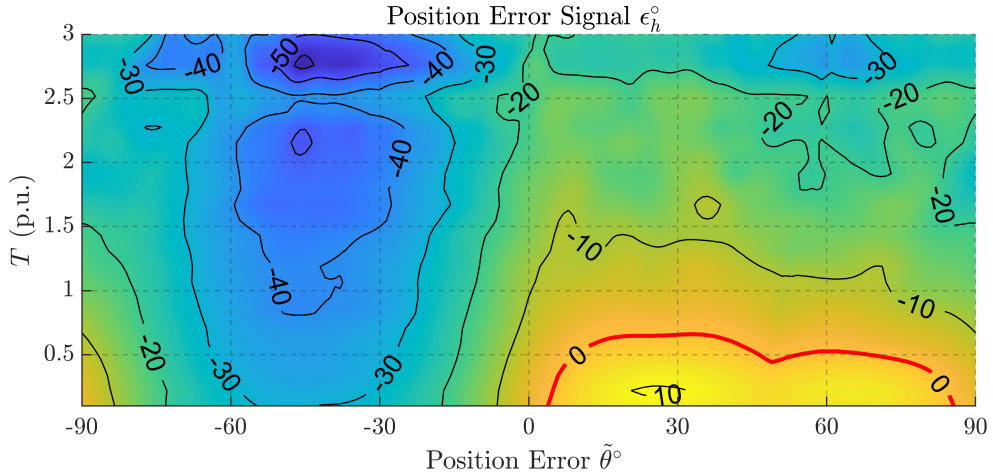

Figure 8.2: Comprehensive convergence analysis of the stator current demodulation scheme using position error signal (8.24) contour for the MTPA torque reference points. Motor: *A*.

where the current-model incremental inductance terms (denoted by subscript i) corresponds to the estimated reference frame $\boldsymbol{L}^i_\partial(\boldsymbol{i}_{\hat{dq}})$ while the real inductance refers to the real rotor reference frame $\boldsymbol{L}_\partial(\boldsymbol{i}_{dq})$.

Fig. 8.1 shows the position error signal (8.24) as a function of position error for four torque references on MTPA. The zero-up crossing is a stable operating point. At $T = 0.5$ p.u., the convergence angle is the cross-saturation error computed from (8.9). For higher loads, no convergence point is discerned, implying the inapplicability of this technique at these operating points. Fig. 8.2 shows a comprehensive position error signal contour to illustrate the absence of zero-up crossing points at higher loads.

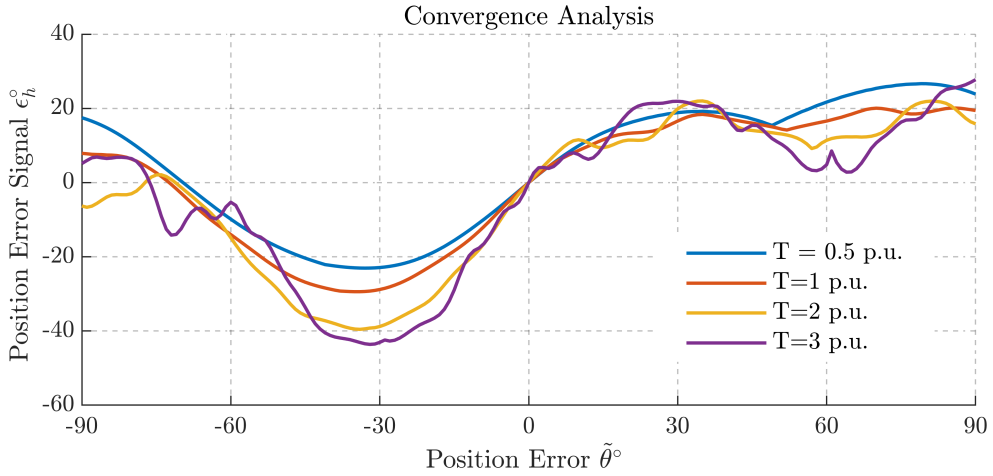

Figure 8.3: Convergence analysis for current-model flux demodulation scheme where the position error signal (8.25) has zero-up crossing at zero position error for all torque. Motor: *A*.

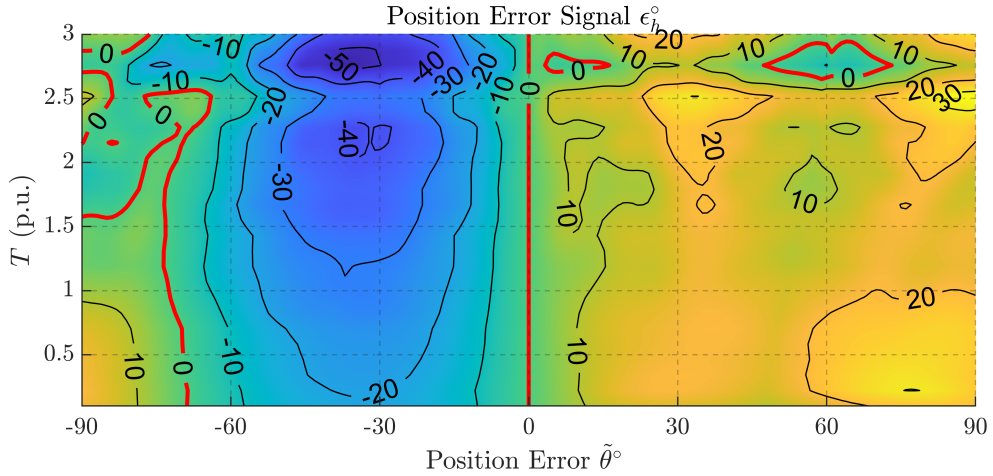

Figure 8.4: Comprehensive convergence analysis of the current-current demodulation scheme using position error signal (8.25) contour for the MTPA torque reference points. Motor: *A*.

To circumvent the instability, [78]–[80] proposed a tilted reference frame voltage injection and a compensation signal to shift the convergence point to zero position error with an adequate convergence margin (angular span between two zero-up crossings).

Current-Model Flux Demodulation

The position error signal for the current-model flux demodulation scheme (8.13) can be expressed as a function of position error using (8.11) without linearizing as

$$\epsilon_h = \frac{1}{2}\frac{l_d^i\, l_q^i - (l_{dq}^i)^2}{l_q^i\, l_\Delta^i - (l_{dq}^i)^2}\left(\frac{l_q\, l_\Delta - l_{dq}^2}{l_d\, l_q - l_{dq}^2}\,\sin(2\tilde{\theta}) - \frac{l_{dq}\, l_\Sigma}{l_d\, l_q - l_{dq}^2}\left(1-\cos(2\tilde{\theta})\right)\right). \tag{8.25}$$

Fig. 8.3 shows the evolution of the position error signal for four torque levels; unlike Fig. 8.1, the zero-up crossing of the position error signal coincides with the zero position error, implying correct convergence. Moreover, a healthy convergence margin is observed. The stability at all loads is verified with the contour plot of the position error signal in Fig. 8.4.

8.3 Review of Discontinuous Excitation Schemes

For simplicity, those low speeds position estimation schemes that do not use a continuous periodic signal injection are classified under envelope of discontinuous excitation schemes. This includes modified PWM modulation and current derivative based methods.

A widely referenced technique is Indirect Flux detection by Online Reactance Measurement (INFORM) [94]–[96] which relies on the current slope response to a discrete voltage vector. One established INFORM implementation exploits modified PWM patterns and current over-sampling [97], [98].

In [99], the 3-phase PWM carrier waves are phase shifted to generate a rotating voltage at the switching frequency. The scheme reported in [100] suspends the control routine for half the control period to impose a pulsating voltage injection. A scheme based on additional sensors for di/dt measurement is proposed in [101], [102] which is not favorable due to the additional hardware requirements. Intermittent test voltage vector injection is proposed in [100], [103]. Mathematics of most of these schemes closely resemble the INFORM technique with the need for multiple sampling.

Alternatively, finite control set model predictive control (FCS-MPC) assists current derivatives/ripples-based approach as the full dc-link voltage appears across the motor terminals in a control period due to the absence of modulators. An optimization solver is used in [104] for MPC based position estimation which has a demerit of high steady-state error ($> 10°$) under load due to neglected effects of saturation. Predictive torque control is used in [105], where the position error signal is computed in the stationary reference frame; the position error is observed to be quite large in the bounds of $\pm 20°$. Additional angle compensation curve is used to compensate for cross-saturation effects. Position estimation in stationary reference frame with MPC is proposed in [106] which, besides being computationally elaborate, overlooks the impact of saturation and cross-saturation.

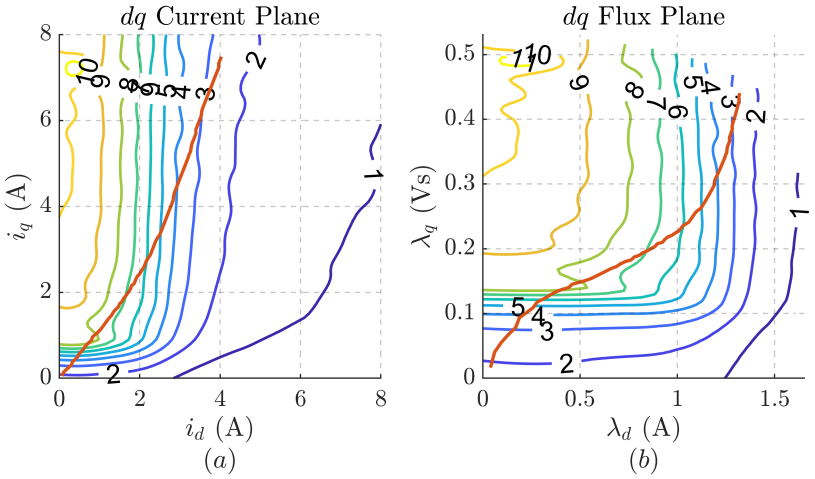

Figure 8.5: Incremental saliency l_d/l_q analysis for feasibility study of low speeds sensorless control: (a) in i_{dq} current plane; (b) in λ_{dq} flux plane. Red curve is the MTPA trajectory. Motor: *B*.

8.4 Incremental Saliency Analysis and Control Feasibility

The high-frequency excitation schemes extract the position information from the local magnetic anisotropy in the vicinity of the operating point. Incremental saliency, defined as the ratio of incremental inductances l_d/l_q, is a key indicator to access the feasibility of the low speed sensorless schemes at an operating point. Poor incremental saliency implies a weak local saliency that portends the inability of operation under sensorless condition. The critical areas of operation are at high loads, where saturation reduces the incremental saliency, and at zero torque, where the SyR machine is non salient if unexcited.

Fig. 8.5 shows the incremental saliency of SyR motor *B* in both *dq* current and *dq* flux linkage planes. At very high loads, the saturation of *d*-axis weakens the incremental saliency on the MTPA trajectory, suggesting the challenges of overload operations at low speeds. At no load, the incremental saliency vanishes around the origin of the *dq* plane for SyR motors due to the unsaturated ribs in the *q*-axis. It is therefore common to impose a minimum current in *d*-axis, $i_{d,min}$, as done for the fundamental excitation at no-load. A proper amount of *d*-axis excitation saturates the rotor ribs in the *q*-axis thanks to cross-saturation effect. However, if the imposed $i_{d,min}$ is excessively large, the saturation of the *d*-axis diminishes the incremental saliency again and can even possibly result in saliency reversal (for $i_{d,min} > 3$ A, $l_d/l_q < 1$ in Fig. 8.5(a)) [69]. Alternatively, the minimum excitation can be imposed to the *q*-axis to ensure saliency as discussed in the next section; note that minimum *q*-axis excitation is not compatible with the active-flux position observer. Hence, low speed sensorless drives should be wary of poor saliency regions

for stable operation. In conclusion:

- The $i_{d,min}$ in SyR machines is purposely designed for the low speed region, requiring knowledge of the flux-map LUTs of the machine under test.
- Minimum excitation in q-axis is favorable for low speeds region; however, it may not necessarily provide sufficient fundamental excitation.
- Automatic calibration of minimum excitation will be the scope of future works.

8.5 High-Frequency Projection Vector Framework

In the spirit of extending the projection vector framework in Section 3.4.2 beyond the fundamental-wave excitation schemes, a generalized high-frequency projection vector framework is designed where the position error signal ϵ_h is defined as the projection of difference between voltage and current-model high-frequency flux estimates on the projection vector $\boldsymbol{\phi}_h$, expressed as

$$\epsilon_h = \boldsymbol{\phi}_h^{\mathrm{T}} \left(s\, \boldsymbol{\lambda}_{\hat{dq}} - \boldsymbol{L}_\partial \cdot s\, \boldsymbol{i}_{\hat{dq}} \right) \tag{8.26}$$

where the derivatives represent the high-frequency terms. The projection vector $\boldsymbol{\phi}_h$ has the dimension of V^{-1}. To establish the relation between the position error signal ϵ_h in (8.26) and the position error $\tilde{\theta}$, the term $s\, \boldsymbol{i}_{\hat{dq}}$ is examined as

$$\begin{aligned} s\, \boldsymbol{i}_{\hat{dq}} &= s \left(\mathrm{e}^{\mathbf{J}\tilde{\theta}} \boldsymbol{i}_{dq} \right) = s\, \tilde{\theta} \cdot \mathbf{J}\, \mathrm{e}^{\mathbf{J}\tilde{\theta}}\, \boldsymbol{i}_{dq} + \mathrm{e}^{\mathbf{J}\tilde{\theta}} \cdot s\, \boldsymbol{i}_{dq} \\ &= \mathrm{e}^{\mathbf{J}\tilde{\theta}}\, \boldsymbol{L}_\partial^{-1}\, \mathrm{e}^{-\mathbf{J}\tilde{\theta}} \cdot s\, \boldsymbol{\lambda}_{\hat{dq}} + s\, \tilde{\theta} \cdot \mathrm{e}^{\mathbf{J}\tilde{\theta}} \Big(\mathbf{J}\, \boldsymbol{L}^{-1} - \boldsymbol{L}_\partial^{-1} \mathbf{J} \Big)\, \mathrm{e}^{-\mathbf{J}\tilde{\theta}}\, \boldsymbol{\lambda}_{\hat{dq}} \end{aligned} \tag{8.27}$$

The derivative of the position error is neglected, i.e., $s\, \tilde{\theta} = 0$, considering that the mechanical dynamics is much slower than the current and flux linkage dynamics. Linearizing (8.27) for small values of $\tilde{\theta}$ gives

$$s\, \boldsymbol{i}_{\hat{dq}} \approx \boldsymbol{L}_\partial^{-1} \cdot s\, \boldsymbol{\lambda}_{\hat{dq}} + \tilde{\theta} \left(\mathbf{J}\, \boldsymbol{L}_\partial^{-1} - \boldsymbol{L}_\partial^{-1} \mathbf{J} \right) \cdot s\, \boldsymbol{\lambda}_{\hat{dq}} \tag{8.28}$$

Substituting (8.28) in (8.26), the high-frequency position error signal simplifies to

$$\epsilon_h = \boldsymbol{\phi}_h^{\mathrm{T}} \cdot \tilde{\theta} \left(\mathbf{J} - \boldsymbol{L}_\partial\, \mathbf{J}\, \boldsymbol{L}_\partial^{-1} \right) \cdot s\, \boldsymbol{\lambda}_{\hat{dq}} \tag{8.29}$$

where

$$\mathbf{J} - \boldsymbol{L}_\partial\, \mathbf{J}\, \boldsymbol{L}_\partial^{-1} = \frac{2}{l_d\, l_q - l_{dq}^2} \begin{bmatrix} -l_{dq}\, l_\Sigma & l_d\, l_\Delta + l_{dq}^2 \\ l_q\, l_\Delta - l_{dq}^2 & l_{dq}\, l_\Sigma \end{bmatrix}. \tag{8.30}$$

It can be inferred from (8.29) that the error signal ϵ_h is always a function of the position error $\tilde{\theta}$, irrespective of the projection vector $\boldsymbol{\phi}_h$. In the next sections, the projection vector approach will be used to formulate two new sensorless observers, one based on FCS-MPC and other using square-wave pulsating injection.

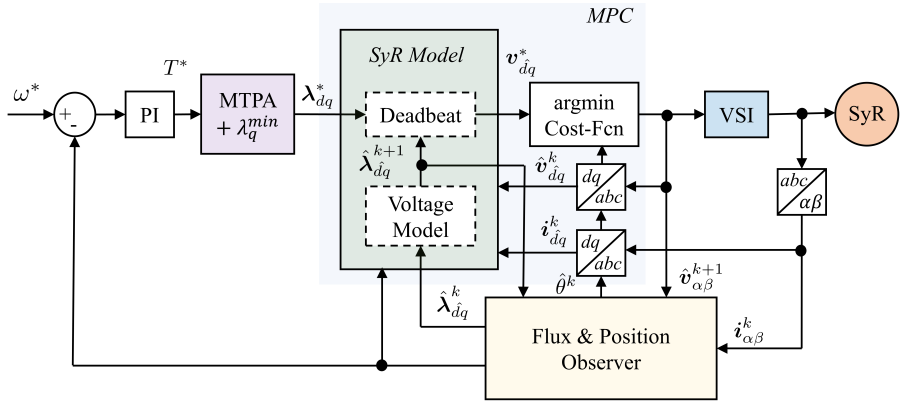

Figure 8.6: Overview of the finite-control-set model-predictive-control based sensorless control scheme with a deadbeat voltage reference in the cost function.

8.6 Projection Vector based Injection-less FCS-MPC scheme

A discontinuous excitation scheme for low speeds sensorless control without periodic signal injection is proposed using a finite-control-set model-predictive-control [50], [51]. The block diagram of the scheme is shown in Fig. 8.6. The background of FCS-MPC is briefed reviewed before discussing the position estimation technique.

8.6.1 Finite-Control-Set Model Predictive Control

The key equations pertaining to a deadbeat type FCS-MPC in estimated synchronous rotor reference frame $\hat{dq}$ are presented in (8.31)-(8.33). Controlled variables are the flux linkage components $\lambda_{\hat{d}}$ and $\lambda_{\hat{q}}$ for the ease of computing the dead-beat voltage.

To account for the unit digital delay, the observed state variable $\hat{\boldsymbol{\lambda}}^k_{\hat{d}\hat{q}}$ is estimated for the $k+1^{th}$ sampling instant as

$$\hat{\boldsymbol{\lambda}}^{k+1}_{\hat{d}\hat{q}} = \hat{\boldsymbol{\lambda}}^{k}_{\hat{d}\hat{q}} + T_s\Big(\boldsymbol{v}^k_{\hat{d}\hat{q}} - R_s\boldsymbol{i}^k_{\hat{d}\hat{q}} - \hat{\omega}\mathbf{J}\,\hat{\boldsymbol{\lambda}}^k_{\hat{d}\hat{q}}\Big) \tag{8.31}$$

where T_s is the sampling interval. This corresponds to the voltage model block in Fig. 8.6. The voltage $\boldsymbol{v}^k_{\hat{d}\hat{q}}$ in (8.31) is estimated according to the duty-cycle commands, incorporating the dead-time compensation.

The deadbeat reference voltage $\boldsymbol{v}^*_{\hat{d}\hat{q}}$ that drives the error to zero at the next control cycle is given by

$$\boldsymbol{v}^*_{\hat{d}\hat{q}} = R_s\,\boldsymbol{i}^k_{\hat{d}\hat{q}} + \frac{\boldsymbol{\lambda}^*_{\hat{d}\hat{q}} - \hat{\boldsymbol{\lambda}}^{k+1}_{\hat{d}\hat{q}}}{T_s} + \hat{\omega}\,\mathbf{J}\,\hat{\boldsymbol{\lambda}}^{k+1}_{\hat{d}\hat{q}} \tag{8.32}$$

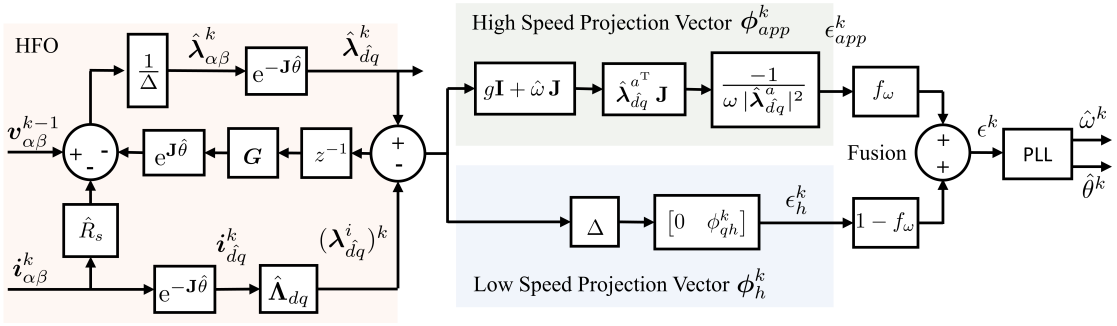

Figure 8.7: Block diagram of the proposed injection-less sensorless technique highlighting the hybrid flux observer with low and high speed projection vectors relying on high-frequency and fundamental excitation respectively, fusion mechanism and PLL.

where $\boldsymbol{\lambda}^*_{dq}$ is the reference flux that corresponds to the commanded reference torque T^* from the speed control loop. The $T^* \rightarrow \boldsymbol{\lambda}^*_{dq}$ relationship is obtained by superimposing a minimum $\lambda_{q,min}$ over the MTPA trajectory. Besides proving the fundamental excitation at no-load, the imposition of $\lambda_{q,min}$ ensures sufficient incremental saliency at low speeds operation (see Fig. 8.5(b)). The resistive term in (8.32) is relatively insignificant and hence, the current quantities are not estimated for $k+1$ in the interest of computational optimization.

The cost function to determine the voltage vector that is at the shortest Euclidean distance from the reference voltage (8.32) is given by

$$f(\boldsymbol{v}^{k+1}_{\hat{dq},j}) = |\boldsymbol{v}^*_{\hat{dq}} - \boldsymbol{v}^{k+1}_{\hat{dq},j}| \tag{8.33a}$$

$$\boldsymbol{v}^{k+1}_{\hat{dq}} = \underset{j=0,1..7}{\operatorname{argmin}}\, f(\boldsymbol{v}^{k+1}_{\hat{dq},j}) \tag{8.33b}$$

where the notation $\boldsymbol{v}_{\hat{dq},j}$ represents the six active vectors ($j = 1 \ldots 6$) and two zero vectors ($j = 0,7$) of a two-level voltage source inverter in the estimated rotor reference frame.

8.6.2 Position Error Estimation

Owing to the nature of finite-control-set MPC, discrete voltage vectors are applied. The proposed sensorless scheme is based on the instantaneous machine response upon excitation with an active voltage vector. The block diagram of the flux and position observer is shown in Fig. 8.7 where the APP scheme branch (green rectangle) serves for position estimation at high speeds.

Projection Vector Design

The discretized form of the high-frequency projection vector position error function (8.26) is expressed with the discrete derivative operator Δ defined in (8.19)

as

$$\epsilon_h^k = \left(\boldsymbol{\phi}_h^k\right)^{\mathrm{T}} (\Delta\boldsymbol{\lambda}_{\hat{dq}}^k - \boldsymbol{L}_\partial \cdot \Delta\boldsymbol{i}_{\hat{dq}}^k). \tag{8.34}$$

The term $\Delta\boldsymbol{\lambda}_{\hat{dq}}^k$ is computed from the HFO while $\Delta\boldsymbol{i}_{\hat{dq}}^k$ is determined from the measurements. Inspecting the susceptibility of the error function (8.34) to measurement noise, owing to the smaller inductance in q-axis, the current ripple Δi_q is generally higher than Δi_d and consequently, less susceptible to measurement noise and current sensor resolution. Furthermore, the noise is amplified in $l_d\,\Delta i_d$ more than $l_q\,\Delta i_q$ since $l_d > l_q$. Hence, a projection vector along q-axis is preferred as

$$\boldsymbol{\phi}_h^k = \begin{bmatrix} 0 & \phi_{qh}^k \end{bmatrix}^{\mathrm{T}}. \tag{8.35}$$

The gain ϕ_{qh}^k should be chosen such that $\epsilon_h = \tilde{\theta}$. It follows from (8.29) and (8.30) that ϕ_{qh} is given by

$$\left(\phi_{qh}^k\right)^{-1} = \frac{2}{l_d\,l_q - l_{dq}^2}\Big(\left(l_q\,l_\Delta - l_{dq}^2\right)\Delta\lambda_{\hat{d}}^k + \left(l_{dq}\,l_\Sigma\right)\Delta\lambda_{\hat{q}}^k\Big). \tag{8.36}$$

At low speeds, the magnitude of the active voltage vector is much greater than the resistance and back-emf voltage terms. Hence, for computational simplicity, the low speed approximation $\Delta\boldsymbol{\lambda}_{\hat{dq}}^k \approx \boldsymbol{v}_{\hat{dq}}^{k-1}$ is adopted, leading to

$$\left(\phi_{qh}^k\right)^{-1} \approx \frac{2}{l_d\,l_q - l_{dq}^2}\Big(\left(l_q\,l_\Delta - l_{dq}^2\right)v_{\hat{d}}^{k-1} + \left(l_{dq}\,l_\Sigma\right)v_{\hat{q}}^{k-1}\Big). \tag{8.37}$$

Implementation Constraints

At low speeds, the MPC cost function minimization tends to impose a string of zero voltage vectors in steady-state condition. This impedes the sensorless performance as the machine remains unexcited for a short span of time where the position is unobservable. Moreover, the quantity $(\phi_{qh})^{-1}$ (8.36) represents the strength of the position error signal and must be large enough for a reliable position estimation. To meet these requirements, two thresholds are defined:

- ϕ_{min}^{-1} is the minimum value of $|(\phi_{qh}^k)^{-1}|$ to be deemed reliable.
- N_{max} is the maximum permissible number of consecutive voltage vectors to have failed the threshold ϕ_{min}^{-1}.

The cost function is modified such that a hard constraint C is enabled once the threshold N_{max} is reached as

$$f(\boldsymbol{v}_{\hat{dq},j}^{k+1}) = |\boldsymbol{v}_{\hat{dq}}^* - \boldsymbol{v}_{\hat{dq},j}^{k+1}| + \left(n > N_{max}\right)C_j \tag{8.38}$$

where n is the count of consecutive instances of $|{\phi_{qh}^{k}}^{-1}| < \phi_{min}^{-1}$. When the limit N_{max} is exceeded, the hard constraint C_j functions to ensure that only those active voltage vectors $\boldsymbol{v}_{\hat{dq},j}^{k+1}$ that satisfy ϕ_{min}^{-1} are eligible for the next sampling instant. This is accomplished by computing the term $\phi_{qh,j}^{-1}$ for each of the six active vectors ($j = 1 \dots 6$) excluding the zero vectors and assigning a large penalty for the j^{th} vector if $|\phi_{qh,j}^{-1}| < \phi_{min}^{-1}$ as

$$C_j = \left(|\phi_{qh,j}^{-1}| \leq \phi_{min}^{-1} \right) \cdot \infty + \left(|\phi_{qh,j}^{-1}| > \phi_{min}^{-1} \right) \cdot 0 \tag{8.39}$$

For the applied voltage vectors having $|{\phi_{qh}^{k}}^{-1}| < \phi_{min}^{-1}$, the evaluation of error function is suspended with $\epsilon_h^k = 0$.

Tuning Guidelines

For a precise position estimation at low speeds, it is desired that the error function is evaluated at the least once every mechanical degree. Considering the upper speed limit for the high-frequency excitation scheme to be the flux observer cross-over frequency g rad/s (0.2 p.u.) results in $N_{max} = 5$ at the switching frequency of 10 kHz. Beyond g, the dominance of high speed model comes into effect.

From the experimental trails, the threshold $\phi_{min}^{-1} = 60$ V that is around 12% of dc-link voltage is determined.

8.6.3 Fusion of Low- and high-speed Sensorless Models

As alluded to before, this FCS-MPC based injection-less technique is augmented to APP scheme for position estimation at high speeds. The position observer is designed to transition from low to high speed model around the cross-over frequency g rad/s, akin to the flux observer. To refrain from sharp discontinuous transition and chattering, the two position estimation models are fused together with a linear speed dependent fusion coefficient f_ω, expressed as

$$\epsilon^k = f_\omega \cdot \epsilon_{app}^k + \left(1 - f_\omega\right) \cdot \epsilon_h^k \tag{8.40a}$$

$$f_\omega = \begin{cases} 0, & \text{if } |\hat{\omega}^k| < g - \omega_g \\ 1, & \text{if } |\hat{\omega}^k| > g + \omega_g \\ \frac{|\hat{\omega}^k| + \omega_g - g}{2\omega_g}, & \text{otherwise} \end{cases} \tag{8.40b}$$

where the term ω_g signifies the span of transition on either sides of cross-over frequency g. The fusion coefficient f_ω is designed to ensure smooth transition over the span of speeds $g - \omega_g$ to $g + \omega_g$.

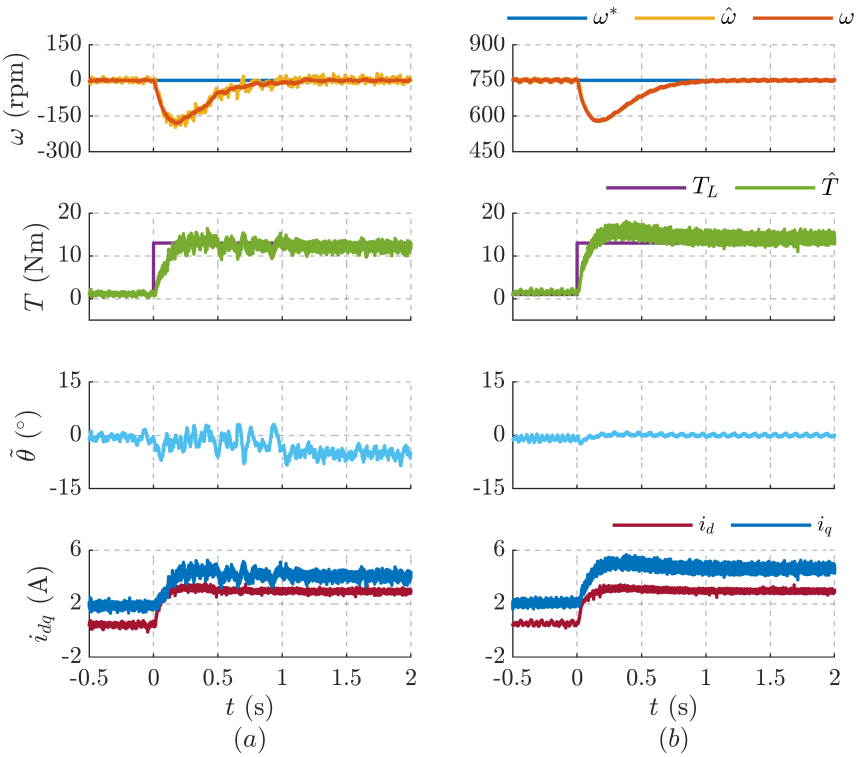

Figure 8.8: Torque step of $0 \rightarrow 2$ p.u. to test for dynamic stiffness with speed controller poles at $2\pi \cdot 1$ rad/s: (a) Low speed model at standstill condition $\omega^* = 0$; (b) High speed model at $\omega^* = 0.5$ p.u. (750 rpm). Motor: *B*.

8.6.4 Experimental Results

The proposed injection-less sensorless scheme is validated experimentally with the SyR motor *B* at a sampling frequency of 10 kHz.

The flux observer gain is set to $g = 2\pi \cdot 10$ rad/s (300 rpm). The transition span of the fusion model is set to $\omega_g = 2\pi \cdot 2$ rad/s. The position observer poles are placed at $\Omega_\omega = 2\pi \cdot 25$ rad/s; the estimated speed is low-pass filtered at $2\pi \cdot 25$ rad/s. The poles of PI speed controller of the SyR machine are placed for a critically damped response at $2\pi \cdot 1$ rad/s. A minimum flux $\lambda_q^{min} = 0.2$ Vs is imposed for saliency and fundamental excitation at no-load. Unless mentioned otherwise, the following results adhere to aforementioned parameters.

Test for Dynamic Stiffness

A challenging scenario for a low speed sensorless control is to sustain a rated torque step at standstill. In Fig. 8.8(a), a heavy transient of twice the rated torque is imposed at standstill condition. The position error is stable with an error $< 5°$ at steady-state. The small error at standstill is likely due to secondary saliences as

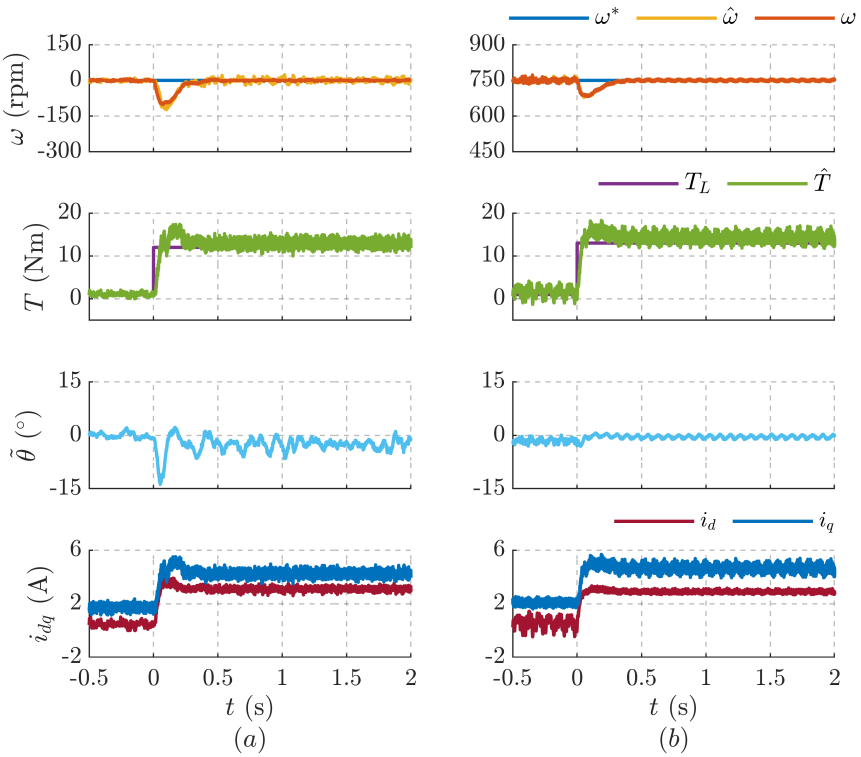

Figure 8.9: Torque step of 0 → 2 p.u. to test for dynamic stiffness with speed controller poles at $2\pi \cdot 2.5$ rad/s: (a) Low speed model at standstill condition $\omega^* = 0$; (b) High speed model at ω^* = 0.5 p.u. (750 rpm). Motor: *B*.

the flux-map LUTs is an average model computed from constant speed test [22]. The APP-based high speed model is subjected to a similar test in Fig. 8.8(b) at 750 rpm (0.5 p.u); negligible position error is observed. Besides, the two tests show similar sag in angular speed of around 150 rpm during transients.

The tests in Fig. 8.8 are repeated for a higher bandwidth speed controller whose the poles are shifted from $2\pi \cdot 1$ rad/s to $2\pi \cdot 2.5$ rad/s, shown in Fig. 8.9. To curtail the high-frequency noise, the position observer poles are lowered from $2\pi \cdot 25$ rad/s to $2\pi \cdot 15$ rad/s which corresponds to a bandwidth of 37 Hz. Same scales are retained for ease of comparison. Peak transient position error is around 15°. The sag in speed is observed to decrease by a factor of 2 to about 75 rpm while the settling time is improved by a factor of 3.

Speed Transients

To demonstrate the speed loop dynamic performance and the effectiveness of the low to high speed transition, a step change in speed reference is imposed from 0 → 1500 rpm (1 p.u) and subsequently, speed reversal from 1500 →-1500 rpm are reported in Fig. 8.10.

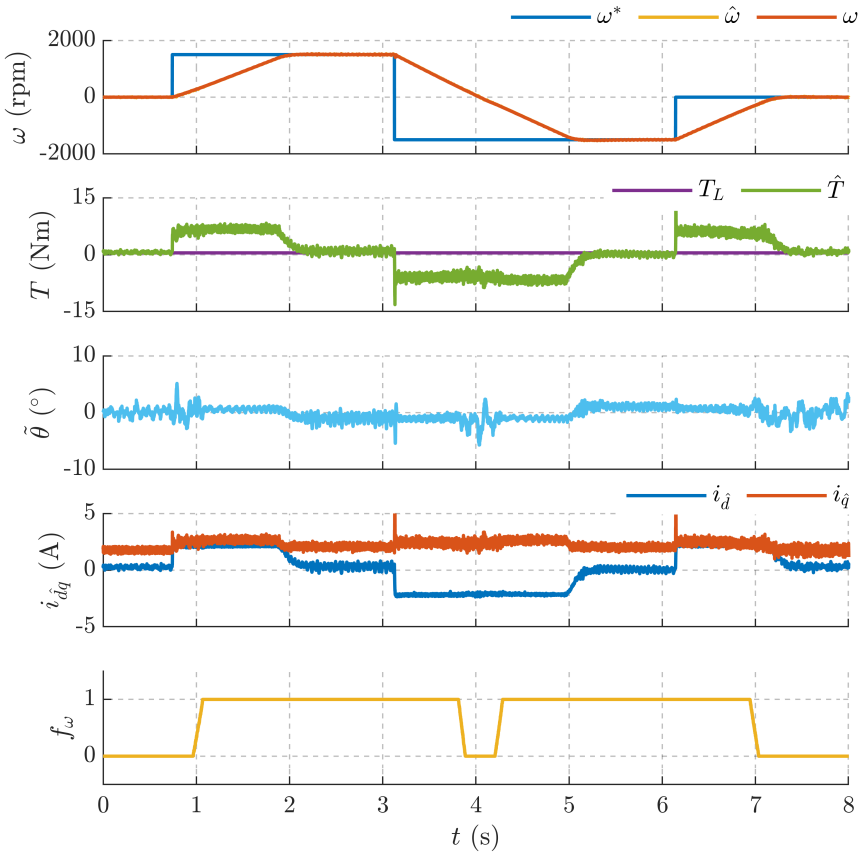

Figure 8.10: Dynamic performance evaluation with rated speed step and speed reversal commanded at no load. Motor: *B*.

Negligible transient and steady-state position error is observed. The fusion coefficient f_ω signifies relative dominance of the two models and the control is observed to move seamlessly from one model to the other.

Fusion

To illustrate the dynamic performance in the fusion window, a torque step in load of 1 p.u. is applied in Fig. 8.11(a). The operating speed of machine is the upper-bound of fusion window, $g + \omega_g$. At $t = 0$ s, the control abruptly transitions to the low speed model as pointed out by the fusion coefficient f_ω. Stability is seamlessly retained.

In another test, a slow speed ramp is applied at a load torque of 0.5 p.u. in Fig. 8.11(b) to illustrate the smooth transitioning between the models. The position error in Fig. 8.11(b) reflects the transition where the high-frequency noise is largely suppressed after $t = 3$ s once the fundamental-wave excitation based estimation

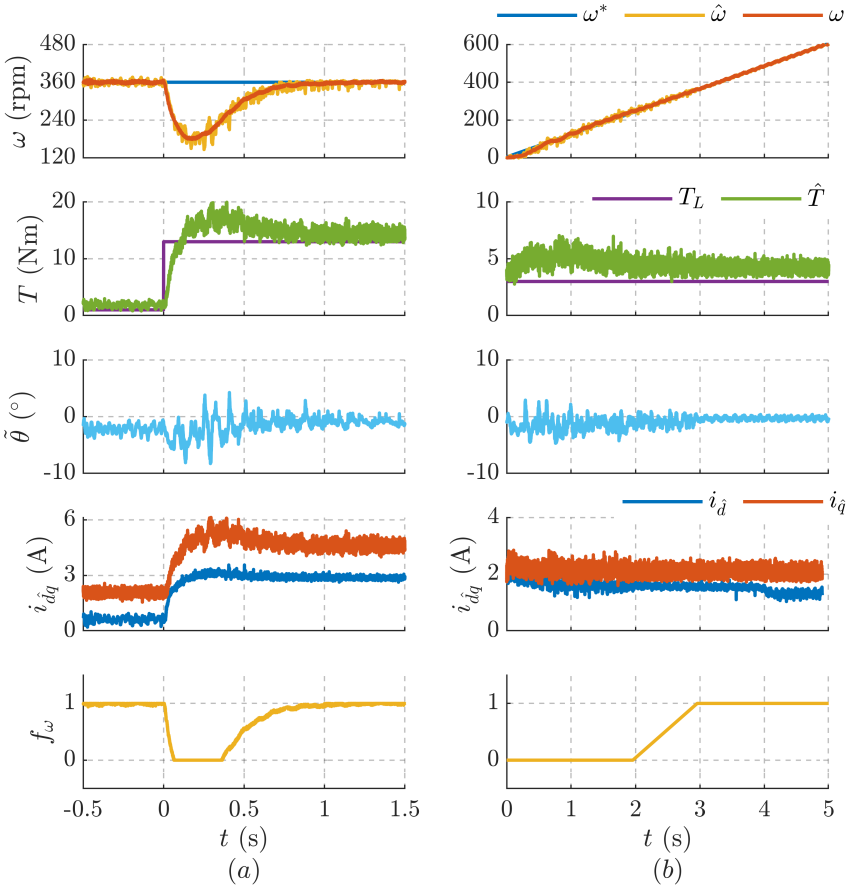

Figure 8.11: Analysis of fusion: (a) Torque step at upper-bound speed of fusion window, $g+\omega_g$, to demonstrate transient performance; (b) Slow speed ramp to highlight the smoothness of transition. Motor: *B*.

gains dominance.

Speed Control Bandwidth Analysis

Finally, the speed control dynamic response is comparatively tested in the low and high speed regions. To evaluate objectively the speed control bandwidth, a sinusoidal speed reference is imposed at standstill to validate the low speed sensorless model, as reported in Fig. 8.12(a). At a disturbance frequency of 1.5 Hz, the estimated speed is phase shifted by 45° from the reference speed. Similar behavior is observed at 750 rpm when the high speed model prevails, as shown in Fig. 8.12(b). In either case, the position error is negligible.

A second test regards sinusoidal disturbances in load torque injected at standstill conditions, reported in Fig. 8.13(a). At 1.5 Hz, the estimated torque lags the load torque by an angle of 45°. On repeating the test at 750 rpm for the high speed

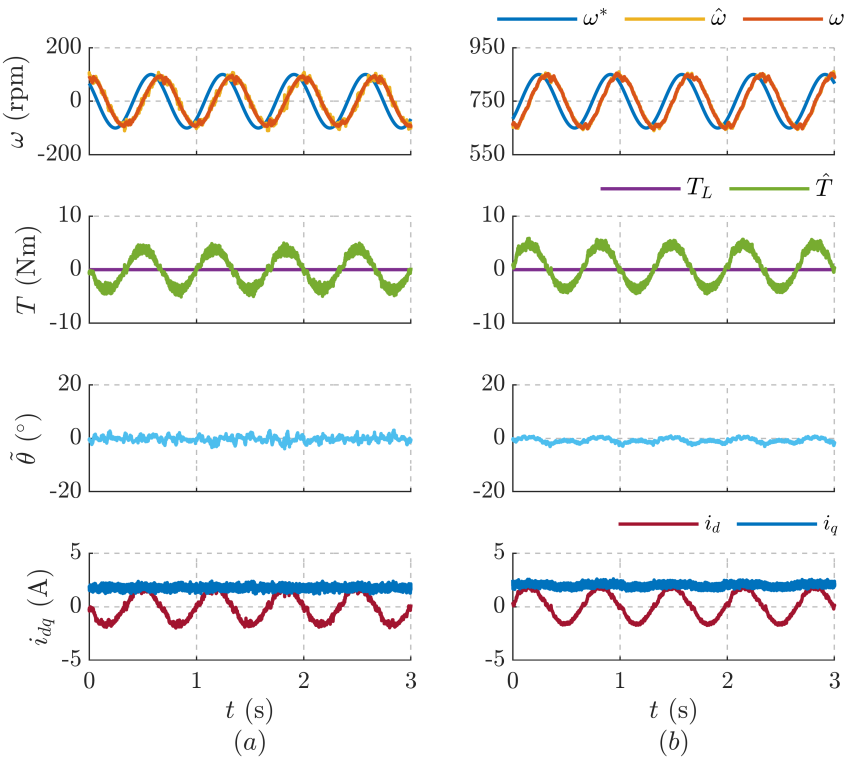

Figure 8.12: Sinusoidal speed reference disturbances at 1.5 Hz: (a) Low speed model at standstill condition mean $\omega^* = 0$; (b) High speed model at mean $\omega^* = 0.5$ p.u. (750 rpm). Motor: *B*.

model in Fig. 8.13(b), identical behavior is discerned. The position error remains negligible.

These tests conclude that the control is capable of tracking disturbances either in load torque or in reference speed up to 1.5 Hz for the speed controller with poles at $2\pi \cdot 1$ rad/s. Shifting the poles to $2\pi \cdot 2.5$ rad/s increases the tracking frequency to 3 Hz as demonstrated in Fig. 8.14 where disturbances in load torque is injected at standstill and half-rated speed, analogous to the test in Fig. 8.13. Should higher bandwidth be desired, the gains of speed controller can be increased at the cost of increase in torque ripples due to the discrete nature of FCS-MPC.

8.7 Position Estimation with Square-Wave Voltage Injection

Using the high-frequency projection vector framework in Section 8.5, the position observer with pulsating square-wave voltage injection in along *d*-axis is designed. It is analogous to the flux demodulation scheme discussed in Section 8.2.1.

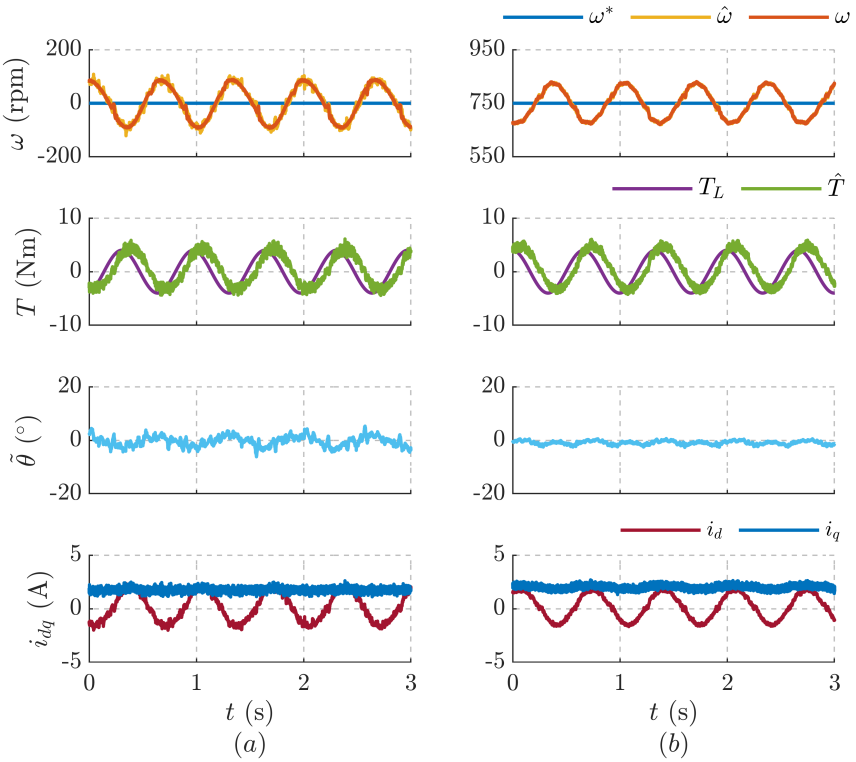

Figure 8.13: Sinusoidal load torque disturbances at 1.5 Hz with speed controller poles at $2\pi \cdot 1$ rad/s: (a) Low speed model at standstill condition $\omega^* = 0$; (b) High speed model at $\omega^* = 0.5$ p.u. (750 rpm). Motor: *B*.

This high-frequency technique is augmented with AUX scheme for high speeds position estimation. The current-vector-control (CVC) with MTPA LUTs is used though the sensorless scheme is just as valid for other control techniques with modulator. The block diagram of the flux and position observer of the full speed scheme is shown in Fig. 8.15.

8.7.1 Projection Vector Design

For the square-wave voltage of nature (8.18), the generalized position error signal (8.26) becomes

$$\epsilon_h^k = \left(\boldsymbol{\phi}_h^k\right)^{\mathrm{T}} \left(\begin{bmatrix} V_h \cos\left(\pi(k-1)\right) \\ 0 \end{bmatrix} - \boldsymbol{L}_\partial \cdot \Delta \boldsymbol{i}_{\hat{dq}}^k \right) \tag{8.41}$$

It follows from (8.29) and (8.30) that the position error signal (8.41) can be expressed as

$$\epsilon_h^k = \left(\boldsymbol{\phi}_h^k\right)^{\mathrm{T}} \frac{2}{l_d l_q - l_{dq}^2} \begin{bmatrix} -l_{dq}\, l_\Sigma \\ l_q\, l_\Delta - l_{dq}^2 \end{bmatrix} V_h \cos\left(\pi(k-1)\right) \cdot \tilde{\theta} \tag{8.42}$$

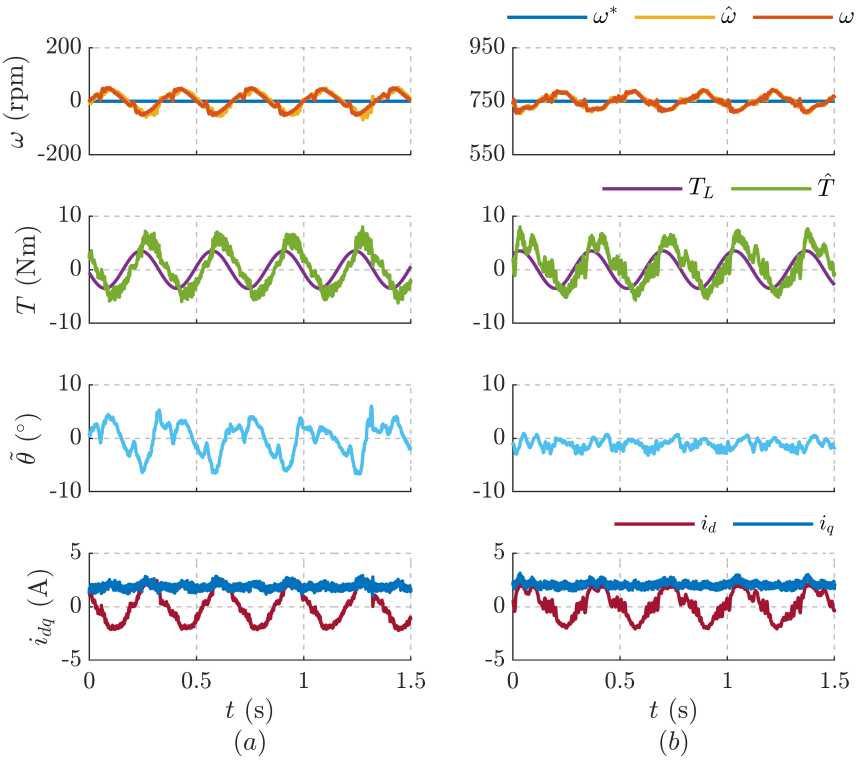

Figure 8.14: Sinusoidal load torque disturbances at 3 Hz with speed controller poles at $2\pi \cdot 2.5$ rad/s: (a) Low speed model at standstill condition $\omega^* = 0$; (b) High speed model at $\omega^* = 0.5$ p.u. (750 rpm). Motor: *B*.

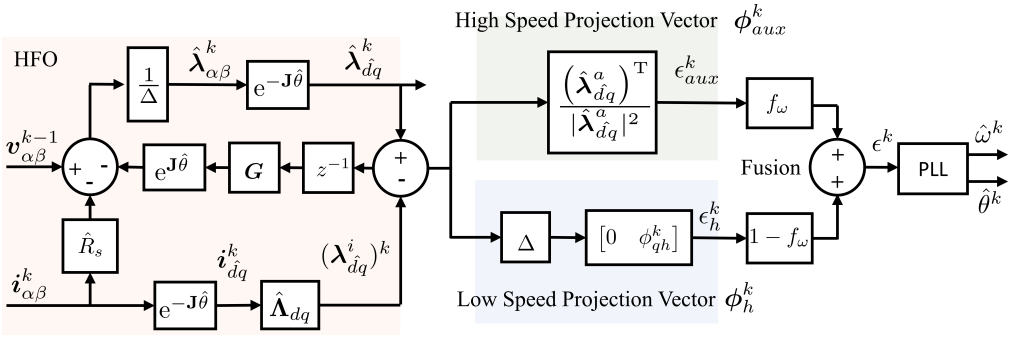

Figure 8.15: Block diagram of the flux and position observer of the full speed scheme: square-wave voltage injection with current-model flux demodulation at low speeds and AUX position observer at high speeds.

The d-axis error signal in (8.42), being proportional to the cross-saturation term l_{dq}, is diminished in magnitude and unobservable at no load. Hence, the q-axis error signal is preferred for reliability whose the corresponding projection vector is

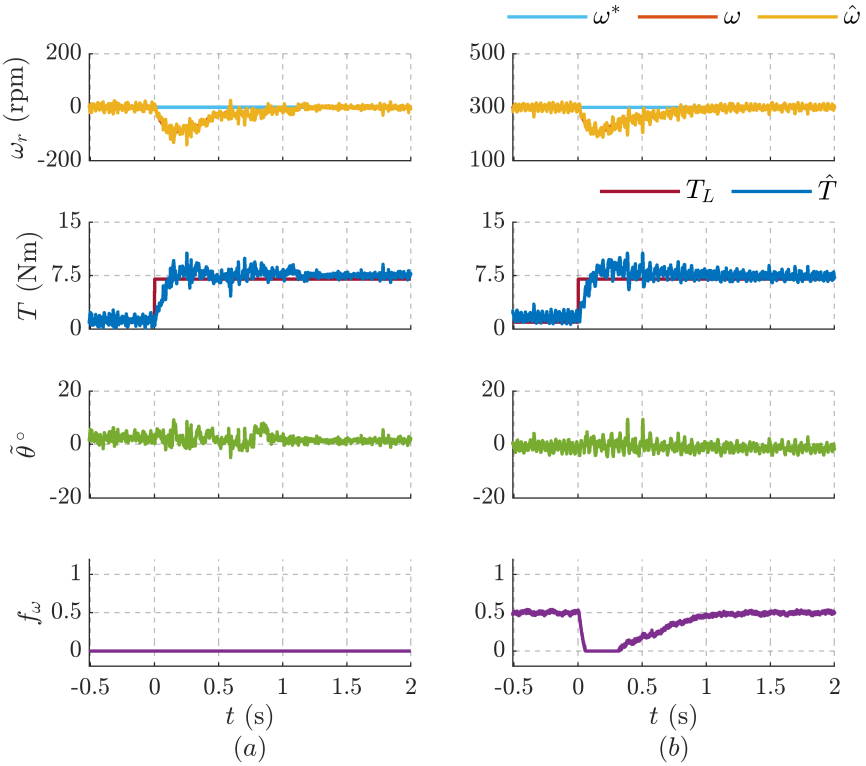

Figure 8.16: Test for dynamic stiffness with rated load torque step $T_L = 0 \rightarrow 7.1$ Nm at $t = 0$ s: (a) Standstill $\omega = 0$; (b) Mid-fusion speed $\omega = 2\pi \cdot 10$ rad/s (0.2 p.u.). Motor: A.

given by

$$\boldsymbol{\phi}_h^k = \begin{bmatrix} 0 & \phi_{qh}^k \end{bmatrix}^{\mathrm{T}} \tag{8.43a}$$

$$\phi_{qh}^k = \frac{\cos\Big(\pi(k-1)\Big)}{2V_h} \frac{l_d l_q - l_{dq}^2}{l_q\, l_\Delta - l_{dq}^2}. \tag{8.43b}$$

The projection vector (8.43) is a subset of the FCS-MPC based projection vector (8.37) when the q-axis high-frequency voltage injection is null. Hence, the same notations are retained.

As alluded to before, the square-wave voltage injection method benefits from a simplified signal processing stage. This scheme is supplemented to the AUX position observer with the linear speed-dependent fusion (8.40a) discussed in Section 8.6.3.

8.7.2 Experimental Results

The proposed sensorless scheme is validated experimentally with SyR motor A at a sampling frequency of 5 kHz. The SyR machine is sensorless speed controlled

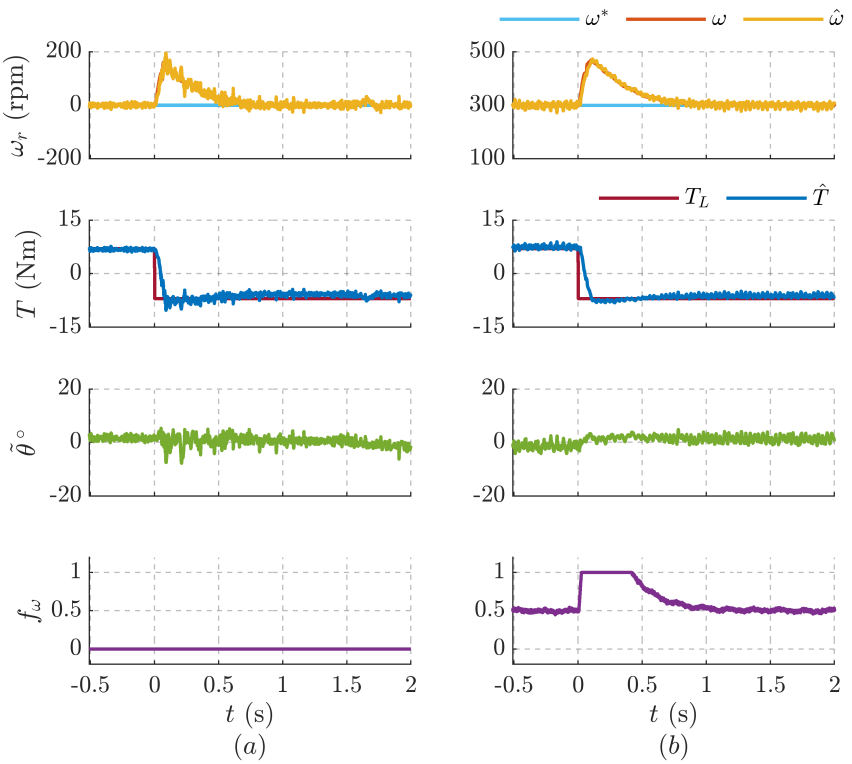

Figure 8.17: Load torque reversal test $T_L = 0 \rightarrow 7.1$ Nm at $t = 0$ s: (a) Standstill $\omega = 0$; (b) Mid-fusion speed $\omega = 2\pi \cdot 10$ rad/s (0.2 p.u). Motor: A.

while the load torque is imposed by an auxiliary drive.

The PLL gains are tuned for $\Omega_\omega = 2\,\pi \cdot 25$ rad/s. The flux observer gain is $g = 2\,\pi \cdot 10$ rad/s. The span of fusion window is $\omega_g = 2\pi \cdot 2$ rad/s. The speed PI controller is tuned for critical damping at $s = -2\pi \cdot 1$ rad/s. A minimum current $i_d^{min} = 1$ A is imposed for ensuring saturation of ribs at low speeds and minimum fundamental excitation at high speeds.

Dynamic Stiffness

The test for dynamic stiffness of the low speed model is performed at standstill with a rated step in load torque in Fig. 8.16(a) and a rated reversal in load torque in Fig. 8.17(a). In either case, the position error is observed to be negligible and the speed sag to be around 100 rpm for step torque and 200 rpm for torque reversal test.

Fusion Evaluation

The competence of fusion is evaluated with a test for dynamic stiffness at the mid-fusion speed, $\omega = g = 2\pi \cdot 10$ rad/s, with rated torque step and rated torque

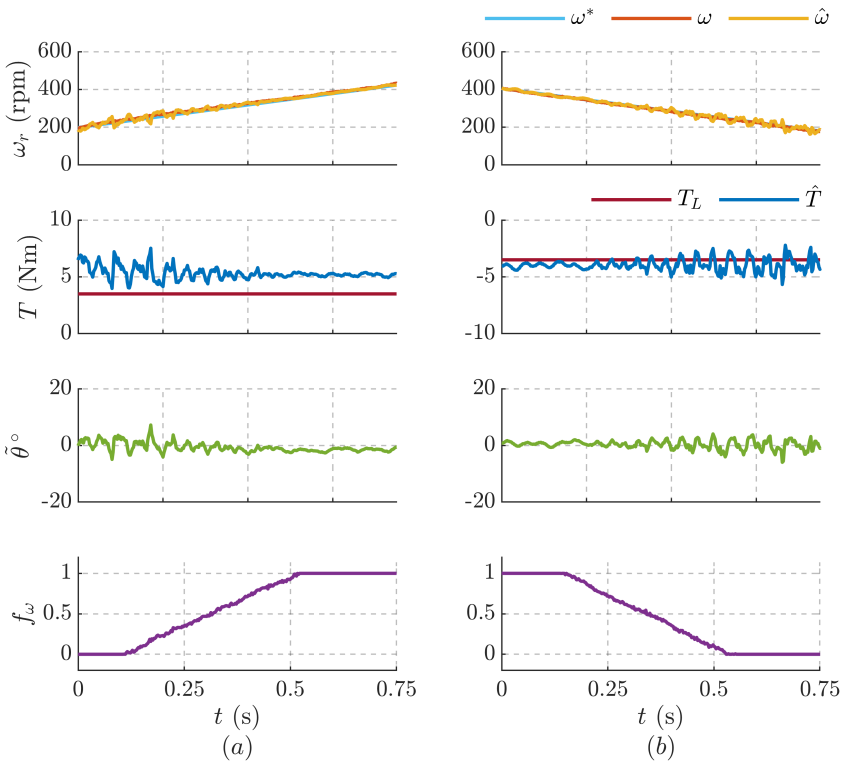

Figure 8.18: A slow ramp speed reference to illustrate the smooth fusion between the two models at $T_L = 3.5$ Nm (0.5 p.u). Motor: A.

reversal in Fig. 8.16(b) and 8.17(b), respectively. Also shown is the fusion coefficient f_ω to illustrate the relative dominance of the two models. The position error is observed to be negligible. It is juxtaposed with the tests at standstill condition to show the similarity in speed sag at either speeds.

To further demonstrate the smooth transition, an accelerating and decelerating slow speed ramp reference is imposed at half rated torque in Fig. 8.18(a) and 8.18(b), respectively. It can be observed that the noise in position error diminished as the control transitions towards the high speed model. No discontinuity is discerned.

Transient Performance

The transient performance is evaluated with an accelerating and decelerating speed ramp reference, rate limited at 5000 rpm/s, at no load in Fig. 8.19(a) and 8.19(b), respectively. A 50% overload in torque is permitted. It can be observed that the position error during transients is $< 5°$.

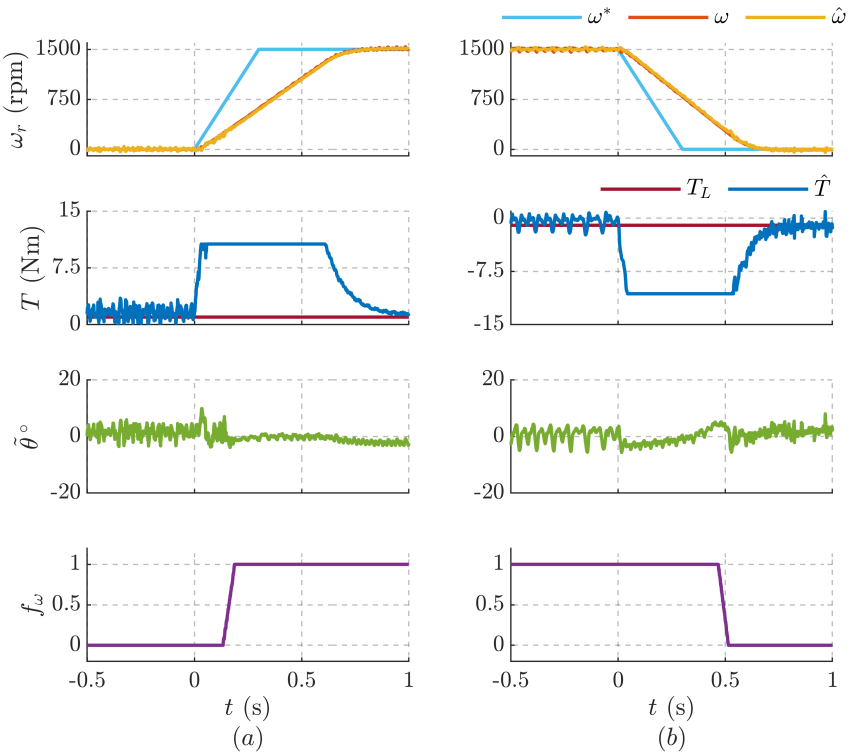

Figure 8.19: Transient performance evaluation with speed ramp reference rate limited at 5000 rpm/s: (a) $\omega^* = 0 \rightarrow 1500$ rpm at $t = 0$ s; (b) $\omega^* = 1500 \rightarrow 0$ rpm at $t = 0$ s. A 50% overload in torque is permitted. Motor: *A*.

8.8 Summary of the Chapter Contributions

The major contributions and findings of the discontinuous excitation scheme published in [50], [51] are listed as follows:

- Akin to the fundamental model, a general high-frequency projection vector framework is developed to aid in the design of sensorless position estimation at zero to low speeds region. It is applicable to both continuous excitation and discontinuous excitation schemes.
- An injection-less sensorless scheme is developed that extracts position estimation from the switching actuation of the FCS-MPC, inherently accounting for saturation and cross-saturation effects. Besides avoiding the monotonous acoustic noise that accompanies the periodic high-frequency injection, the availability of full dc-link voltage for torque production aids in transient performance.
- This discontinuous excitation scheme is integrated with APP scheme for high speeds region with a linear speed-dependent fusion coefficient for smooth

transition. Experimental validation shows good dynamic performance during transients with seamless transition between the two models, including identical dynamic performance independently of the speed region.

The main contributions of the continuous excitation scheme published in [47] are as follows:

- Analogous to the active-flux position observer, a high-frequency projection vector along q-axis for a square-wave voltage injection in d-axis is investigated.
- It is augmented with auxiliary-flux position observer for high speeds with a speed-dependent fusion for a seamless transition between the two models.

The two high-frequency excitation schemes are mathematically identical, relying the q-axis high-frequency flux and show similar performance. The choice between them is based on factors such as machine inductances, switching frequency and control strategy (presence of modulator).

Chapter 9

Self-Commissioning Techniques for SyR Machines

This chapter presents two self-commissioning techniques for the magnetic model identification (MMI) of synchronous reluctance machines with and without the position transducer. The findings of the commissioning technique with encoder at free shaft is published in [107] while the sensorless technique at standstill condition is published in [108].

9.1 Introduction

The popularity of SyR motors for several variable speed applications can be attributed to their high efficiency, robustness, manufacturing simplicity, competitive cost and continuous torque per volume ratio. For SyR motors, the most complicated parameter to be estimated is often the current-to-flux linkage relationship, also called flux-map, which is nonlinear due to both self-axis saturation and cross-coupling effect. The optimal operation for minimizing stator resistance losses lies on the MTPA curve, which is flux-map dependent. In addition, the optimal control references in the flux-weakening and the MTPV limits are also dependent on the flux-map, which are typically stored a offline preprocessed LUTs. This is common for many control schemes: current vector control in [109] and direct flux vector control in [69], [110]. Therefore, the need for complete flux-map of a SyR machine is recognized.

The standard methods for identifying the machine magnetic model [111] require to test the machine in a dedicated laboratory environment. A constant speed test is reported in [22] where the dq current plane is systematically explored and mapped with alternating motoring and braking operation. The evaluation of saturation and cross-saturation in IPMSM under locked rotor condition is reported in [112]. Several automatic procedures without additional auxiliary drive are developed [113]–[117];

an AC signal injection with DC bias is proposed in [113] to build the flux-map from incremental inductance at standstill condition. Dual hysteresis current controllers for rapid torque reversal at standstill is proposed in [118] where the saturation approximating function is computed with multiple linear regression. An alternating acceleration and deceleration test at free-shaft to identify the magnetic model is proposed in [115].

It is worth pointing out that, for sensorless drives, the commissioning stage must also be performed without position transducers. In addition, some applications may require to evaluate the machine parameters without moving the rotor at standstill condition. These constraints are satisfied in the reported works [114], [118]–[121], where the complete flux-map is identified by exciting the machine with a proper sequence of bipolar voltage pulses.

A new sensorless self-commissioning at standstill is investigated in Section 9.2 that is capable of rotor self-locking. A magnetic model identification technique at free-shaft with alternating acceleration-deceleration is presented in Section 9.3 using the position transducer. Finally, Section 9.4 summarizes the chapter contributions.

9.2 Sensorless Self-Commissioning with Rotor Self-Locking Mechanism

A new rotor self-locking mechanism [108] is developed for self-commissioning of SyR machines at sensorless and standstill condition. The control dq reference frame is aligned with the initial rotor position, detected by a standard saliency based algorithm; alternatively, it can be imposed with parking technique. The magnetic model of d-axis without cross-saturation ($i_q = 0$) is identified with a hysteresis square-wave voltage injection, referred as test-i. A similar exploration of the q-axis with hysteresis square-wave voltage injection at $i_d = 0$ is referred as test-ii. Then, to map the cross-saturation, the dq current plane is explored in test-iii. A weak PI regulator in d-axis imposes an average i_d while the q-axis is controlled with a hysteresis square-wave injection to ensure that the torque transients are fast enough to retain the rotor at standstill. By manipulating the PI reference i_d^* and the hysteresis limit $i_{q,max}$, the dq plane is systematically explored. The imposed dc current i_d in fixed control reference frame produces a counteracting torque if the rotor displaces from the initial position; thus, respect to the previous methods [120], it increases stability and the permissible area of inspection. The cross-saturation phenomenon is identified from the high-frequency components in i_d that are induced by the q-axis hysteresis control.

The tests i and ii to identify self-saturation with hysteresis control are the same as tests #1 and #2 of [120]. To model cross-saturation effects, the test #3 in [120] excites both the d and q-axes simultaneously with hysteresis control; it is supplemented with a sensorless position scheme to track the rotor movement. In

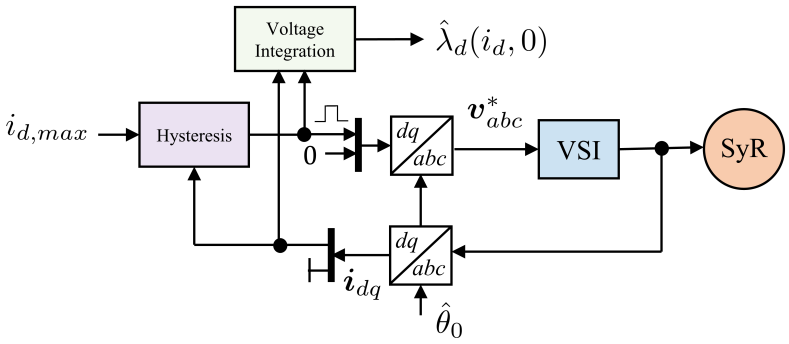

Figure 9.1: Block diagram for self-saturation identification of $\lambda_d(i_d,0)$: test-i

this new method, the test-iii aims to replace the test #3 for a more systematic exploration of the dq current plane with a self-locking to firmly hold the rotor at standstill.

9.2.1 Proposed Self-Commissioning Technique

In this work, the rotor is parked to align the d-axis with phase a. Alternatively, the initial position can be identified by injecting an high-frequency rotating voltage and capturing the minor axis of the resulting elliptical current trajectory.

Let $\hat{\theta}_0$ be the initial electrical angle of the rotor. In the succeeding text, dq denotes a fixed reference frame along $\hat{\theta}_0$. If the rotor deviates from the initial position, the error in electrical angle is given by $\tilde{\theta} = \theta - \hat{\theta}_0$.

Test-i & Test-ii: identification of self-saturation

The self-saturation curves $\hat{\lambda}_d(i_d,0)$ and $\hat{\lambda}_q(0,i_q)$ are identified through tests i and ii respectively. In test-i, the d-axis is excited with a square-wave voltage controlled by an hysteresis mechanism, reversing the polarity of v_d whenever i_d exceeds a threshold value $i_{d,max}$. Meanwhile, v_q^* is set to zero, as shown in Fig. 9.1. Since the torque produced is zero, the current limit can be extended up to the machine thermal ratings without rotor movement. The stator flux is obtained from the voltage equation (3.1), expressed as

$$\hat{\lambda}_d(i_d,0) = \int (\hat{v}_d - \hat{R}_s\, i_d)\mathrm{d}t \tag{9.1}$$

where the applied voltage is estimated from the measured dc-link and the three phase duty cycles, accounting for the inverter dead-time compensation.

In test-ii, the self-saturation of q-axis is identified in a similar fashion as test-i where the square-wave voltage pulses are applied in q-axis with hysteresis limit of

$i_{q,max}$ and $v_d = 0$. The flux is obtained by direct integration as

$$\hat{\lambda}_q(0, i_q) = \int (\hat{v}_q - \hat{R}_s\, i_q)\mathrm{d}t. \tag{9.3}$$

Unlike test-i, the hysteresis on q-axis is quasi-stable and the maximum attainable $i_{q,max}$ is often determined by factors such as static friction and shaft inertia. Technique to extend the measurement area in the q-axis using signal injection is reported in [120].

Cross-saturation Model of the SyR Machine

Besides saturation along self-axis, it is known that SyR machine exhibits cross-saturation characteristics, expressed as

$$\lambda_d(i_d, i_q) = \lambda_d(i_d,0) + \int_0^{i_q} l_{dq}(i_d, x)\,\mathrm{d}x \tag{9.4a}$$

$$\lambda_q(i_d, i_q) = \lambda_q(0, i_q) + \int_0^{i_d} l_{dq}(x, i_q)\,\mathrm{d}x \tag{9.4b}$$

where the incremental cross-saturation inductance l_{dq} is a function of the operating point i_d, i_q and is defined as

$$l_{dq}(i_d, i_q) = \frac{\partial \lambda_d}{\partial i_q} = \frac{\partial \lambda_q}{\partial i_d}. \tag{9.5}$$

Test-*iii*: identification of cross-saturation

To explore the dq current plane, the proposed technique exploits the propensity of rotor to align itself along the current vector (parking technique). To this end, if a sufficiently large i_d is imposed along $\hat{d}$ (fixed reference frame along $\hat{\theta}_0$), it acts as a natural locking mechanism and inhibits the rotor motion. This is realized with a PI controller on d-axis and a hysteresis current control on the q-axis as illustrated in Fig. 9.2, referred to as test-*iii*. In contrast to the techniques using dual hysteresis control on d and q-axes simultaneously, the proposed scheme has a larger hysteresis voltage bandwidth since the d-axis consumes minimal voltage (resistive drop); consequently, faster torque reversals can be achieved. However, very high-frequency leads to increase in iron losses and reduction in the acquired number of data points per cycle.

The high-frequency oscillation of the q-axis permeates into the d-axis current through the cross-saturation term as

$$\frac{\mathrm{d}i_d}{\mathrm{d}t} = \frac{1}{l_d l_q - l_{dq}^2}\left(l_q \frac{\mathrm{d}\lambda_d}{\mathrm{d}t} - l_{dq} \frac{\mathrm{d}\lambda_q}{\mathrm{d}t}\right). \tag{9.6}$$

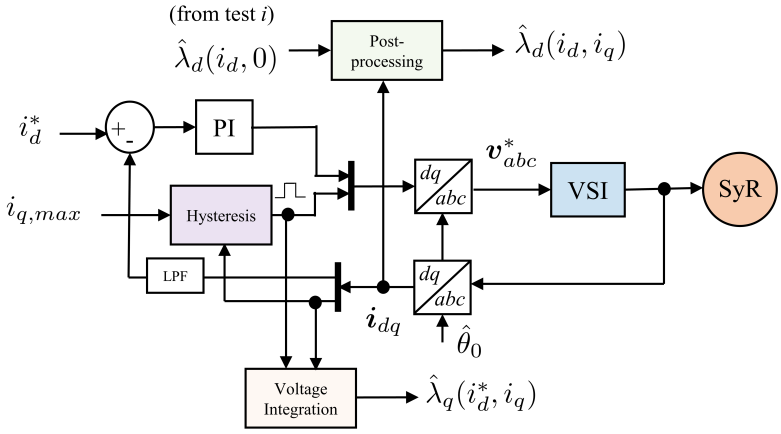

Figure 9.2: Block diagram for cross-saturation identification of $\lambda_{dq}(i_d, i_q)$: test-*iii*

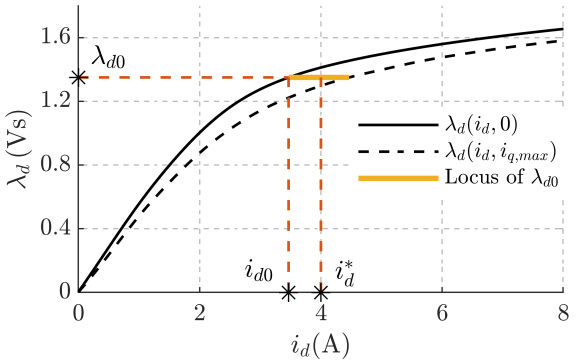

Figure 9.3: Principle of the proposed cross-saturation identification in test-*iii*. In yellow is the constant λ_d locus for oscillating i_d with mean i_d^*.

If the d-axis PI controller is designed such that the high-frequency oscillation in i_d induced by the q-axis is out of its bandwidth, then a constant flux is established as the voltage v_d^* is devoid of high-frequency terms. For the reasons of symmetry, the oscillations in i_d is at twice the hysteresis frequency. It is conceptually depicted in Fig. 9.3 where the i_d oscillates around the mean value i_d^*, tracing the locus of a constant λ_d. This oscillation is in tandem with i_q which is hysteresis controlled with a current limit of $i_{q,max}$. The minimum value of i_d coincides with the zero-crossing of i_q, denoted by i_{d0} in Fig. 9.3. The self-saturation curve (in sold line), $\lambda_d(i_d,0)$, is available from test-i; hence, with i_{d0} extracted from the measured current, the flux $\lambda_{d0} = \lambda_d(i_{d0},0)$ and subsequently, the locus of constant λ_d are determined.

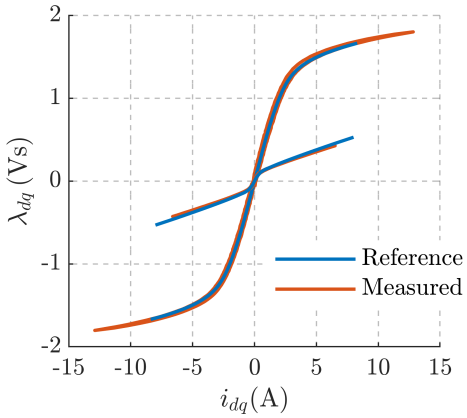

Figure 9.4: Self-saturation identification of $\hat{\lambda}_d(i_d,0)$ and $\hat{\lambda}_q(0,i_q)$ in tests i and ii respectively; shows good correlation with reference flux-map. Motor: *B*.

9.2.2 Data Processing and Results

The proposed sensorless scheme is validated experimentally with SyR motor B at a sampling frequency of 10 kHz. The tests are performed under free shaft condition without a load to minimize shaft inertia.

Data manipulation for self-saturation (test-i + test-ii)

The current limit $i_{d,max}$ in test-i is only restricted by the thermal ratings of the machine; for a short time, large currents can be acceptable. For the result shown in Fig. 9.4, the limits are set to $i_{d,max} = 12$ A (3.7 p.u.) and $v_d^* = \pm 220$ V. A good correlation between the measured and reference curves is observed. The reference flux-map are experimentally obtained from the constant speed test [22].

As alluded to earlier, the $i_{q,max}$ in test-ii is quasi-stable for very high current values. Hence, it is curtailed to twice the rated peak current in Fig. 9.4 as $i_{q,max} = 6.5$ A (2 p.u.) at $v_q^* = \pm 220$ V. As with test-i, good correlation is observed.

Data manipulation for $\hat{\lambda}_d(i_d, i_q)$ (test-i + test-iii)

For a robust self-locking mechanism in test-iii, a minimum i_d^* is necessary; a lower limit of 0.3 p.u.(1 A) is recommended at free shaft. Since the machine is at standstill, a constant i_d is essentially a dc current in phase a. Hence, attention must be paid to the maximum value of i_d^* to respect thermal ratings of the machine; it is set to 2 p.u.(6.5A). The step size of i_d^* is 0.1 A; an external fan is used for cooling although the entire test only lasts a couple of minutes. The hysteresis limits are set to $i_{q,max} = 6.5$ A at $v_q = \pm 220$ V. The PI controller is designed for a bandwidth of $\approx 2\pi \cdot 10$ rad/s; it can be calibrated with a rough estimate of inductance from the self-saturation test. To further preserve the high-frequency oscillations in i_d, a low

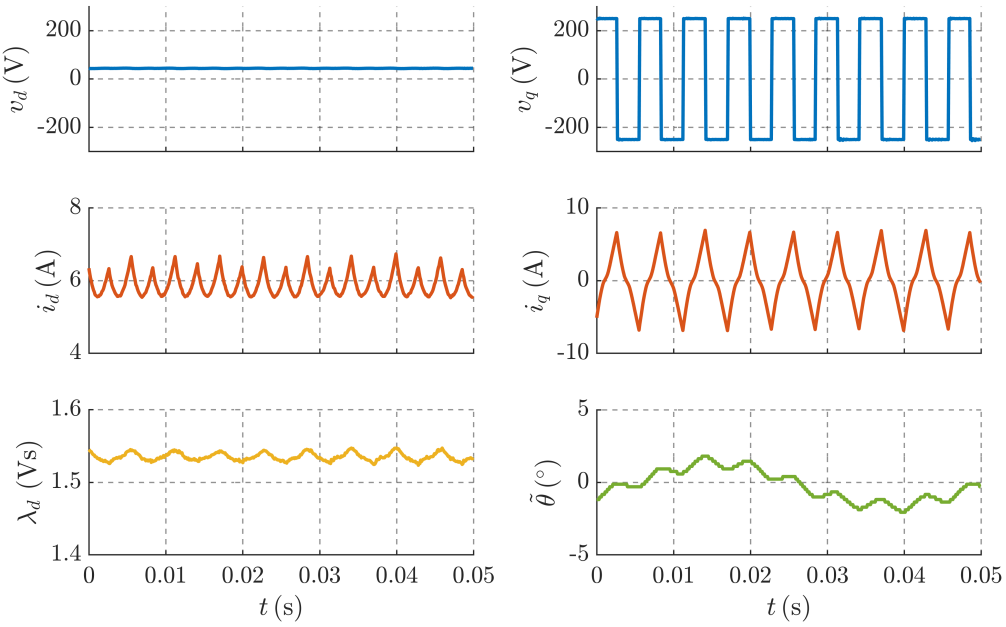

Figure 9.5: Test-*iii* data recording at $i_d^* = 6$ A and $i_{q,max} = 6.5$ A; illustrates high-frequency oscillations in i_d, relatively constant v_d and λ_d, and confined rotor movement $|\tilde{\theta}| < 2°$ electrical. Motor: *B*.

pass filter with cutoff frequency of 15 Hz is used at the feedback of d-axis current control loop as shown in Fig. 9.2.

Fig. 9.5 shows the time plots of the data acquired at $i_d^* = 6$ A (1.85 p.u.) and $i_{q,max} = 6.5$ A (2 p.u.) in the test-*iii*. It illustrates the high-frequency components of i_d at twice the hysteresis frequency. Moreover, it can be observed that the weak PI controller generates a relatively constant v_d and thereby, reasoning the assumption of constant λ_d. It is worth pointing out that the rotor movement is restricted to $|\tilde{\theta}| < 2°$ electrical, validating the self-locking mechanism. The position error wave in Fig. 9.5 gives evidence of the natural realignment caused by the constant i_d.

Fig. 9.6(a) shows the data acquired in the test-*iii* for selected values of i_d^*. The high-frequency oscillations in i_d are superimposed over the reference flux-map to draw parallels to Fig. 9.3 and to illustrate the relatively constant λ_d. Fig. 9.6(b) shows the corresponding current trajectories whose increasing convex nature with higher i_d^* is a testament to the cross-saturation phenomenon.

The results obtained for each i_d^* value are interpolated with a quadratic polynomial function (dotted lines in Fig. 9.6(b)) whose equation is given by

$$i_d(\lambda_d, |i_q|) = i_{d0}(\lambda_d) + a_1(\lambda_d) \cdot |i_q| + a_2(\lambda_d) \cdot |i_q|^2 \tag{9.7}$$

where i_{d0} is the self-saturation term depicted in Fig. 9.3, and a_1 and a_2 are the first and second order coefficients. The absolute value of $|i_q|$ is used due to symmetry.

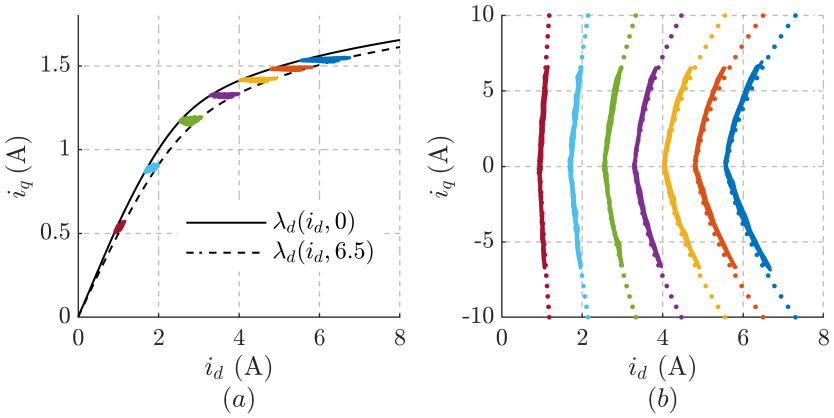

Figure 9.6: (a) Test-*iii* for cross-saturation identification. Data acquired for different i_d^* at $i_{q,max} = 6.5$ A. High frequency oscillations of i_d projected over the reference flux-map to illustrate constant λ_d; (b) Current trajectories on constant λ_d locus traced during test-*iii*. Dotted lines denote the quadratic polynomial fitting (9.7). Note that identical color codes are used in the two figures for ease of comparison. Motor: *B*.

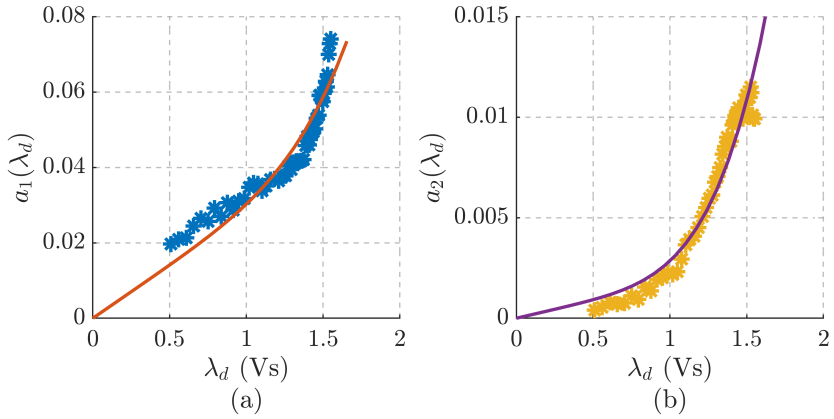

Figure 9.7: Coefficients of constant λ_d locus and the best-fit polynomial (9.8): (a) $a_1(\lambda_d)$; (b) $a_2(\lambda_d)$. Motor: *B*.

This expression (9.7) represents locus of the constant *d*-axis flux λ_d; the value of λ_d is interpolated from the results of self-saturation test-*i* using i_{d0} as $\hat{\lambda}_d(i_{d0},0)$. Fig. 9.7 represents the coefficients in (9.7) as a function of λ_d. Each data point in Fig. 9.7 represents a unique measurement set for various i_d^*. It can be observed that the data points are absent for low magnitudes of flux due to the imposed minimum i_d^* for rotor locking. In order to extrapolate, a higher order polynomial fitting is found accommodating, as

$$\begin{aligned} a_1(\lambda_d) &= a_{11} \cdot \lambda_d + a_{15} \cdot \lambda_d^5 \\ a_2(\lambda_d) &= a_{21} \cdot \lambda_d + a_{25} \cdot \lambda_d^5 \end{aligned} \tag{9.8}$$

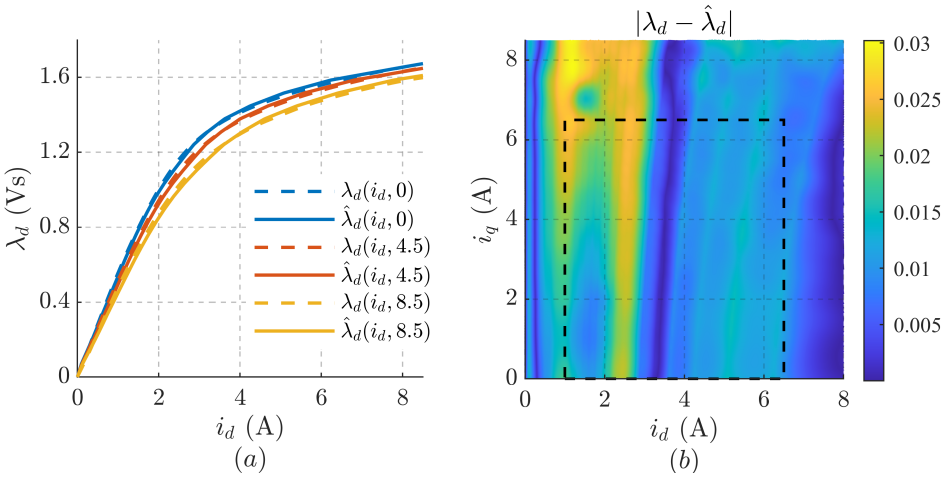

Figure 9.8: (a) Comparison of self-commissioning vs. reference flux-map for d-axis; (b) Error contour of d-axis flux-map identification. Dotted black box denotes the region of exploration. Motor: *B*.

where the four constants (a_{11}, a_{15}, a_{21} & a_{25}) are estimated with the combination of tests i and iii and in turn, the complete map of $i_d(\lambda_d, |i_q|)$ becomes realizable. Upon manipulation, the direct flux map $\lambda_d(i_d, i_q)$ is obtained.

Fig. 9.8(a) shows the identified flux curves with the proposed self-commissioning technique where a good correlation with reference curves is observed. Despite the limited exploration of q-axis with maximum $i_{q,max} = 6.5$ A (2 p.u.), the estimated d-axis flux at regions beyond the exploration ($\hat{\lambda}_d(i_d$,8.5)) shows good correspondence with the reference, validating the extrapolation coefficients. A comprehensive comparison is reported in Fig. 9.8(b) by computing the flux error contour in dq current plane; the error is confined to less than 0.03 Vs (3% of rated flux), predominantly in vicinity of the knee-point. The region of exploration is denoted by a black box to highlight the potential of proposed technique to extrapolate with good accuracy.

Data manipulation for $\hat{\lambda}_q(i_d, i_q)$ (test-ii + test-iii)

The data processing for q-axis flux-map is largely simplified due to the application of hysteresis control. Akin to the self-saturation identification in test-ii, direct integration of hysteresis voltage is also applicable for test-iii as

$$\hat{\lambda}_q(i_d^*, i_q) = \int (\hat{v}_q - R_s\, i_q)\mathrm{d}t \tag{9.9}$$

For simplicity, the i_d is approximated to the reference value, i_d^*. Thus, it is a straightforward estimation of the flux curves $\hat{\lambda}_q(i_d^*, i_q)$ for points within the region of exploration. To compute flux beyond the explored region, the dq current plane is segmented into three regions as shown in Fig. 9.9. Upon saturation, the q-axis

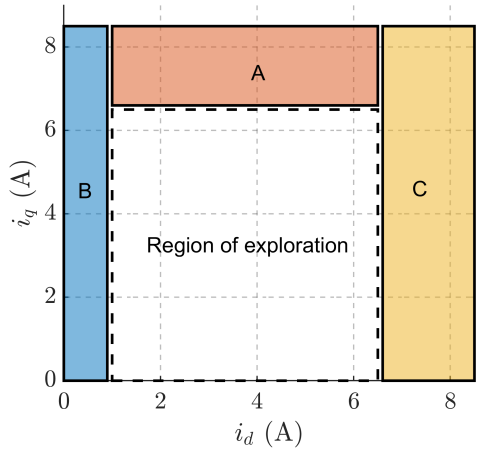

Figure 9.9: Segmented regions (A,B and C) for flux estimation beyond the region of exploration.

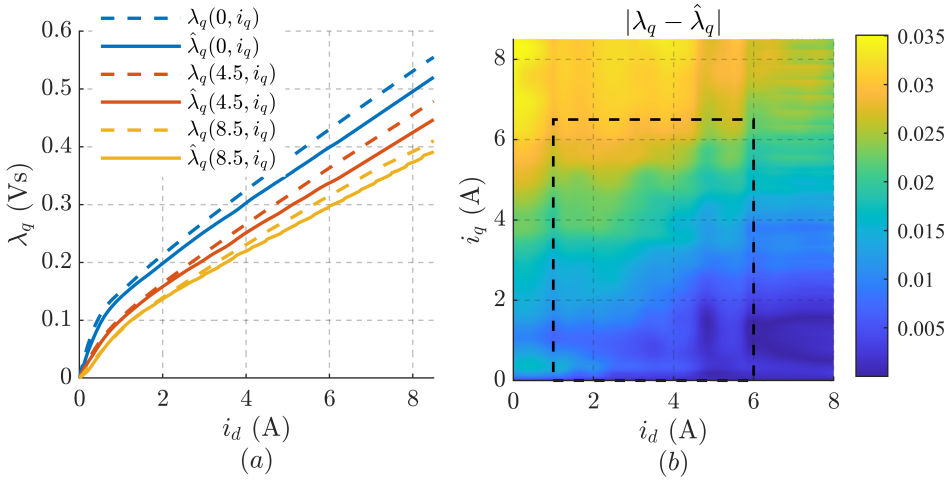

Figure 9.10: (a) Comparison of self-commissioning vs. reference flux-map for q-axis; (b) Error contour of q-axis flux-map identification. Dotted black box denotes the region of exploration. Motor: *B*.

exhibits a largely constant incremental inductance; this property is exploited in region A where the flux curves are linearly extrapolated by computing the saturated inductance. Region B is bounded by the curve from the self-saturation test-*ii* to the left and the cross-saturation test-*iii* to the right. Hence, a simple linear interpolation is carried out. In the case of region C, the reciprocity property (9.5) of cross-saturation inductance l_{dq} is exploited. For each operating point, the term $l_{dq}(i_d, i_q)$ is computed from the d-axis flux-map. Then, with the boundary of explored region as the starting point, the q-axis flux $\hat{\lambda}_q$ is estimated progressively to the right using (9.4b).

The identified q-axis curves with the proposed self-commissioning technique are

shown in Fig. 9.10 where a discrepancy with reference maps is seen. The absolute error is approximately 5% at the rated peak current and increases at overload. This error can be attributed to iron losses owing to the high hysteresis frequency in the range of 175 Hz. Fig. 9.10(b) provides the comprehensive error contour where the maximum error is about 0.03 Vs ($< 3\%$ of the rated flux). Thus, while d-axis estimation error is less than 3%, the q-axis is overestimated by 6-7%. Improvements in this direction will be the scope of future work.

9.3 Kinetic-Rotor Magnetic Model Identification with Online Adaptation

Akin to [115], this new identification scheme [107] involves self-acceleration and deceleration at free-shaft to identify the magnetic model via adaptation in real-time. The identification scheme systematically explores the dq current plane with a bipolar reference q-axis current i_q^* for torque reversals. The speed regulation is achieved by varying the duty-cycle of the bipolar i_q through a low-frequency pulse-width-modulation (LF-PWM) structure, as shown in Fig. 9.11. Respect to former the sensorless technique in Section 9.2, this new method characterizes the cross-saturation phenomenon with precision, although with the help of an encoder. The inability of [115] to characterize the self-saturation curves due to the zero torque areas is overcome in this new technique. Besides a position encoder, neither a dedicated rig nor any additional hardware is necessary. As many SyR machines in the market are not innately accompanied with a position encoder, the proposed technique is also applicable as an end-of-line MMI, where the motor under test is coupled to an external encoder and identified within a few minutes, without the need of a prime mover or data recorders.

The projection vector framework introduced in Chapter 3 is the context of sensorless control for position estimation using the flux-map LUTs. It is inversely applied here where the flux-map is retrieved in the presence of an encoder. Based on the projection vector framework, an online stator flux and resistance adaptation is developed.

9.3.1 Proposed Control Scheme for MMI

Self-Saturation Curves Identification at Standstill

In the first stage (test-d), the magnetic model of d-axis without cross-saturation ($i_q = 0$) is identified with a hysteresis square-wave voltage injection, just as test-i in Section 9.2.1. Similar exploration of q-axis (test-q) with hysteresis square-wave voltage injection at $i_d = 0$ is performed, just as test-ii in Section 9.2.1. Respect to the sensorless implementation in the former section, the presence of encoder

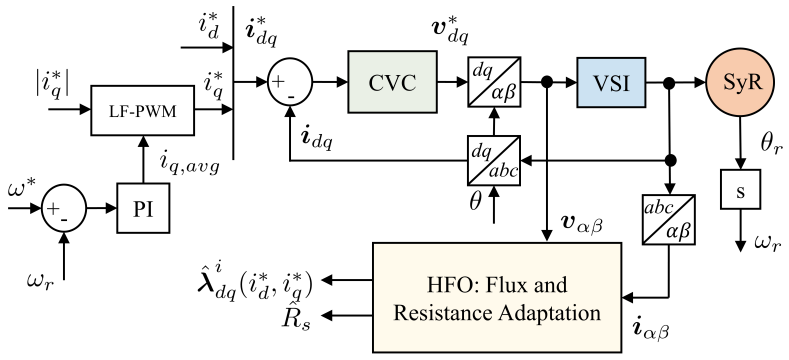

Figure 9.11: Proposed MMI scheme: block diagram of current vector control (CVC) technique with low frequency pulse-width-modulation (LF-PWM) for q-axis current reference and online adaptation with hybrid flux observer (HFO).

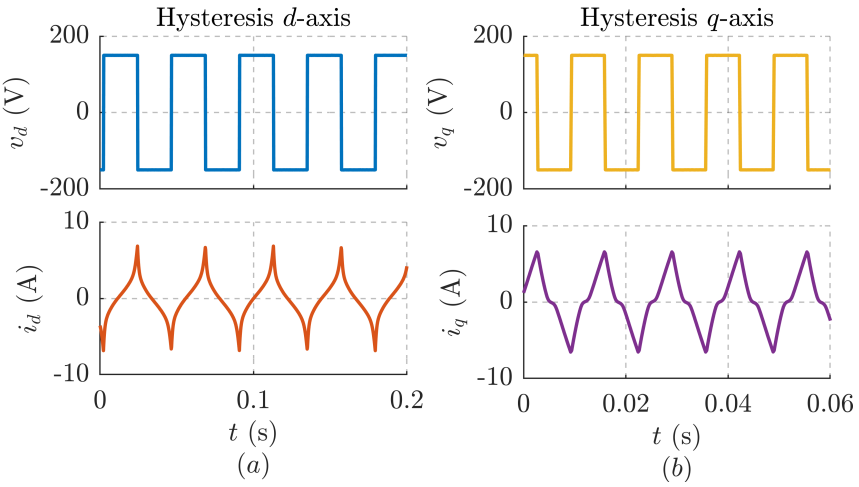

Figure 9.12: Time plots of hysteresis controller for self-saturation identification: (a) d-axis excitation; (b) q-axis excitation. Motor B.

permits extensive exploration of q-axis without problems of stability at high values of i_q.

The time-plots of the self-saturation identification test is shown in Fig. 9.12. Due to the smaller inductance along q-axis, a higher hysteresis frequency is observed. The square-wave voltage magnitude is set to 150 V (0.46 p.u.) and the current is limited to twice the rated value, $i_d^* = i_q^* = 6.5$ A (2 p.u.). The stator flux is computed from the integration of voltage equation (9.1) and (9.3), shown in Fig. 9.13 where a good correlation with the reference curves is discerned. This initial self-saturation look-up tables (LUTs) are denoted as $\hat{\boldsymbol{\Lambda}}_d$ and $\hat{\boldsymbol{\Lambda}}_q$.

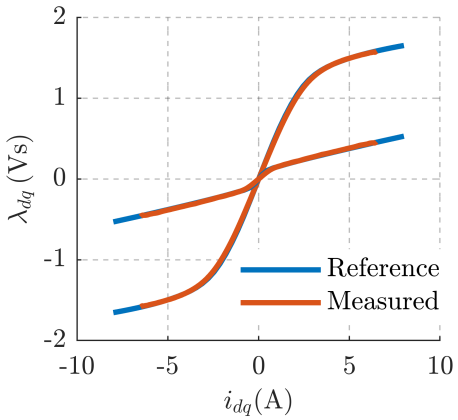

Figure 9.13: Self-saturation identification curves from test-d and test-q with current limit $i_d^* = i_q^* = 6.5$ A (2 p.u.) and superimposed over the reference curves, showing good correlation. Motor *B*.

Cross-Saturation Identification

The block diagram of the control technique for cross-saturation identification at free-shaft is shown in Fig. 9.11 and constitutes an integral contribution of this method. The self-saturation LUTs will be corrected for including the cross-saturation current domain using an hybrid flux observer and a flux adaptation technique mutated from sensorless control, as described later. A closed-loop speed control is implemented with a current-vector-control scheme to impose the reference current $\boldsymbol{i}_{dq}^*$. The parameters from the self-saturation test can be used to tune the CVC regulators. A non-zero $|i_d^*|$ and $|i_q^*|$ couple generates electromagnetic torque and results in rotor movement. To limit the rotor speed, a bipolar reference for q-axis current is used for alternating acceleration and deceleration around the speed set-point, as shown in Fig. 9.14. The speed controller establishes an average speed equal to the reference speed by imposing an average q-axis current reference $i_{q,avg}$.

A low frequency pulse-width-modulation (LF-PWM) is used to calibrate the duty cycle of the bipolar i_q^* reference such that the mean value respects the speed controller commanded $i_{q,avg}$. The frequency of modulation f_q for LF-PWM should be an order higher than the bandwidth of speed controller.

Around nominal speed, iron losses gains significance whereas at very low speeds, flux estimation is unreliable due to the low signal-to-noise (SNR) of the back-emf signal integral. Hence, the mechanical speed span $0.33 < |\omega_r| < 0.66$ p.u. is considered optimal for MMI, represented by the shaded region in Fig. 9.14(a). Ideally, it is desirable to confine the operation within optimal speed span by adapting the LF-PWM modulation frequency f_q as a function of the torque. However, this is not feasible due to the excessive mechanical vibrations for high f_q corresponding to high i_q^* and high torque. Alternatively, the maximum speed and the LF-PWM

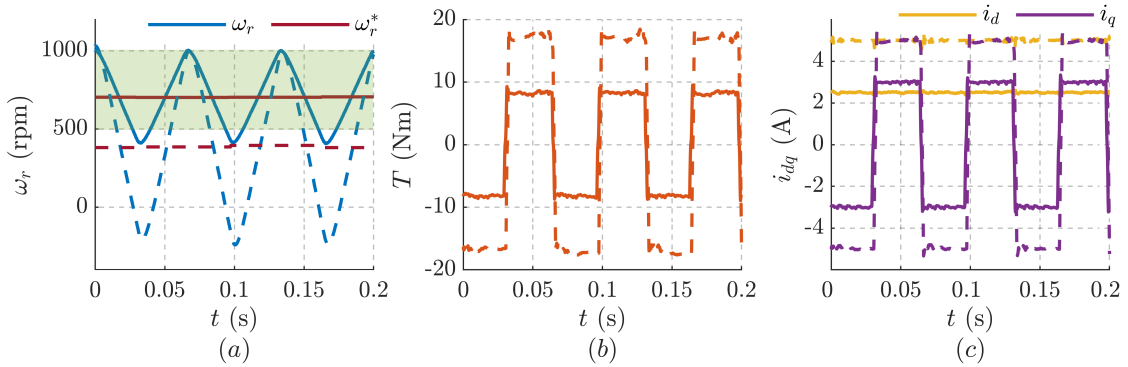

Figure 9.14: Experimental time plots of cross-saturation identification: (a) Mechanical speed where the shaded region represents the optimal speed span for online adaptation; (b) Bipolar torque estimate; (c) Constant d and bipolar q-axis currents. Line Marker: continuous lines denote identification at $i_d^* = 2.5$ & $|i_q^*| = 3$ (A); dotted lines denote identification at $i_d^* = 5$ & $|i_q^*| = 5$ (A). Motor *B*.

frequency f_q are held constant at 0.66 p.u. (1000 rpm) and 15 Hz (experimentally calibrated to avoid mechanical vibrations), respectively, while the lower speed limit (speed-span) varies with the torque, as shown in Fig. 9.14. To this end, the speed reference is determined as

$$\omega^* = (2\pi \cdot 25 \times 0.66) - \omega_{avg} \tag{9.10}$$

where ω_{avg} is the real-time computed mean of maximum and minimum speed in the previous LF-PWM cycle. It must be noted that only the data points within the optimal speed span are engaged in online flux and resistance adaptation, as discussed in the following.

9.3.2 Current-Model Flux Adaptation

The block diagram of the proposed scheme with the hybrid flux observer for online stator flux and resistance adaptation is shown in Fig. 9.15. Let ϵ_d and ϵ_q denote the LUTs-based current-model flux error signals along the projection vectors $\boldsymbol{\phi}_d$ and $\boldsymbol{\phi}_q$ for d and q-axes, respectively, expressed as

$$\boldsymbol{\epsilon}_{dq} = \begin{bmatrix} \epsilon_d \\ \epsilon_q \end{bmatrix} = \begin{bmatrix} \boldsymbol{\phi}_d & \boldsymbol{\phi}_q \end{bmatrix}^{\mathrm{T}} (\hat{\boldsymbol{\lambda}}_{dq} - \hat{\boldsymbol{\lambda}}_{dq}^{i}). \tag{9.11}$$

d-axis Adaptation

Reverting to the projection vector framework in Section 3.4.2, the error signal (3.28) is altered with $\tilde{\theta} = 0$ to indicate the operation with encoder. If the dc-component of the d-axis current-model flux error signal should be equal to the

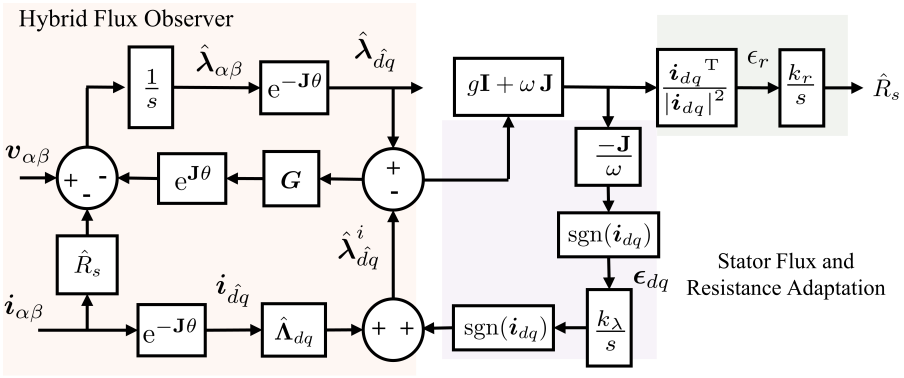

Figure 9.15: Proposed scheme of hybrid flux observer with online current-model flux and stator resistance adaptation for cross-saturation identification.

parameter error, then it follows from (3.28) that the projection vector should be of nature

$$\epsilon_d|_{s=0} = \tilde{\lambda}_d^i \quad \Rightarrow \quad {\phi_d}^{\mathrm{T}} = \frac{1}{\omega}\begin{bmatrix}0 & 1\end{bmatrix}(\boldsymbol{G} + \mathbf{J}\,\omega) \tag{9.12}$$

The d-axis flux adaptation is formulated to reflect the cross-saturation effect on the self-saturation stator flux from test-d as

$$\hat{\lambda}_d^i(i_d, i_q) = \hat{\mathbf{\Lambda}}_d(i_d,0) + \frac{k_\lambda}{s}\,\epsilon_d \tag{9.13}$$

where k_λ is the integral gain. The corresponding $\boldsymbol{i}_{dq}$ point of the $\hat{\mathbf{\Lambda}}_d$ LUTs is populated with the steady-state value of (9.13).

q-axis Adaptation

Despite the bipolar nature of the q-axis current, the error signal ϵ_q is designed to be compatible with the adaptation law by transforming the parameter error to the first-quadrant (motoring) as

$$\epsilon_q|_{s=0} = \tilde{\lambda}_q^i \cdot \mathrm{sgn}(i_q) \quad \Rightarrow \quad {\phi_q}^{\mathrm{T}} = \frac{-1}{\omega}\begin{bmatrix}\mathrm{sgn}(i_q) & 0\end{bmatrix}(\boldsymbol{G} + \mathbf{J}\,\omega). \tag{9.14}$$

Accounting for the polarity, the adaptation law supplements the cross-saturation offset to the self-saturation stator flux from test-q as

$$\hat{\lambda}_q^i(i_d, i_q) = \hat{\mathbf{\Lambda}}_q(0, i_q) + \mathrm{sgn}(i_q) \cdot \frac{k_\lambda}{s}\,\epsilon_q. \tag{9.15}$$

As before, the $\boldsymbol{i}_{dq}$ point of the $\hat{\mathbf{\Lambda}}_q$ LUTs is populated with the steady-state value of (9.15).

Stator Resistance Sensitivity

Under inaccurate resistance, it can be shown from (3.28) that the error signals ϵ_d and ϵ_q are accompanied by the resistance error term as

$$\epsilon_d|_{s=0} = \tilde{\lambda}_d^i + \frac{\tilde{R}_s}{\omega}\, i_q \tag{9.16a}$$

$$\epsilon_q|_{s=0} = \mathrm{sgn}(i_q) \cdot \tilde{\lambda}_q^i - \frac{\tilde{R}_s}{\omega}\, \mathrm{sgn}(i_q) \cdot i_d. \tag{9.16b}$$

However, it can be discerned that the resistance error bearing terms, i_q in (9.16a) and $\mathrm{sgn}(i_q) \cdot i_d$ in (9.16b), are bipolar in nature at the frequency f_q. Hence, the adaptation bandwidth is recommended to be less than one third of the LF-PWM frequency to filter out the bipolar signal, i.e., $k_\lambda < 0.33 \cdot 2\pi f_q$. Thus, the current-model flux adaptation turns out to be independent of resistance error.

9.3.3 Stator Resistance Adaptation

It is worth pointing out that, in addition to the two projection vectors (9.12) and (9.14), a third projection vector for stator resistance adaptation is feasible within the 2-D error domain (dq) because of the bipolar nature of certain signals that are filterable from the error signal projected on such third dimension.

Let ϵ_r denote the resistance error signal. The resistance error projection vector ϕ_r is designed using (3.28) such that the dc-component of the error signal is equal to the resistance error as

$$\epsilon_r|_{s=0} = \tilde{R}_s \quad \Rightarrow \quad \boldsymbol{\phi}_r^{\mathrm{T}} = \frac{\boldsymbol{i}_{dq}^{\mathrm{T}}}{|\boldsymbol{i}_{dq}|^2}\,(\boldsymbol{G} + \mathbf{J}\,\omega). \tag{9.17}$$

The resistance adaptation law is expressed as

$$\hat{R}_s = \frac{k_r}{s}\,\epsilon_r \tag{9.18}$$

where k_r is the integral gain as depicted in Fig. 9.15.

The influence of the current-model parameter errors on resistance adaptation is evaluated as

$$\epsilon_r|_{s=0} = \tilde{R}_s + \frac{\omega}{|\boldsymbol{i}_{dq}|^2}\,(\tilde{\lambda}_d^i\, i_q - \tilde{\lambda}_q^i\, i_d) \tag{9.19}$$

where the current-model error term $(\tilde{\lambda}_d^i\, i_q - \tilde{\lambda}_q^i\, i_d)$ is bipolar in nature. As discussed before, a suitable selection of the adaptation gain to filter out the bipolar signal is $k_r < 0.33 \cdot 2\pi\, f_q$ that helps to decouple the resistance adaptation from the current-model flux errors. Moreover, as discussed in Section 3.2.4, the estimate (9.18) represents the effective stator resistance accounting for the inverter voltage errors.

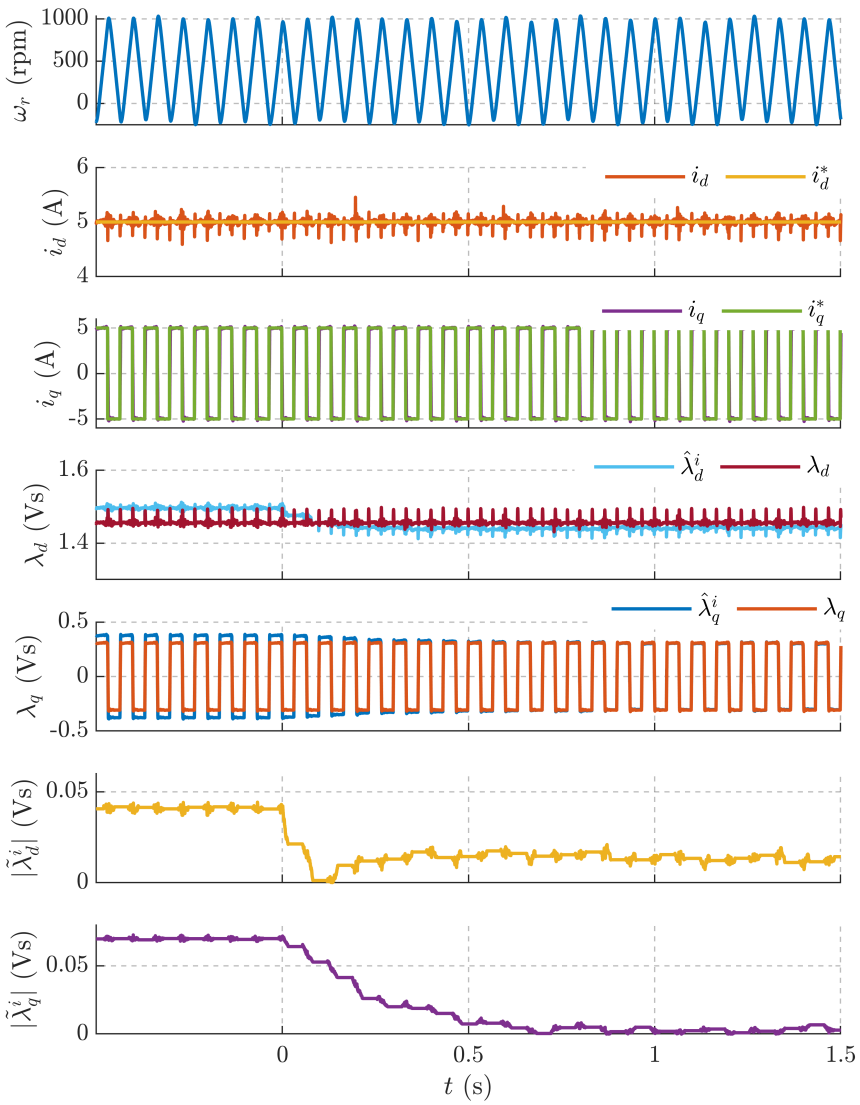

Figure 9.16: Time plots to illustrate the dynamics of current-model flux adaptation at $i_d^* = 5$ A (1.5 p.u.) and $i_q^* = 5$ A (1.5 p.u.). The adaptation is enabled at $t = 0$ s. Motor *B*.

9.3.4 Experimental Validation

The proposed scheme is validated experimentally with SyR motor *B* at a sampling frequency of 10 kHz. The speed controller bandwidth is set to $2\pi \cdot 1$ rad/s. The flux observer gain is $g = 2\pi \cdot 10$ rad/s. The adaptation gains are $k_\lambda = 2\pi \cdot 2.5$ rad/s and $k_r = 2\pi \cdot 0.5$ rad/s

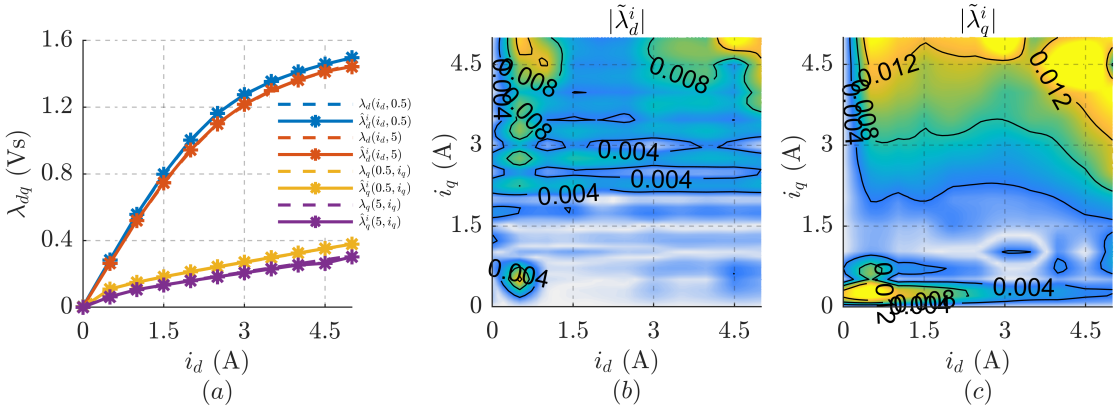

Figure 9.17: Experimental MMI with self and cross-saturation: (a) Identified curves shown against reference flux-map, showing good correlation; (b) Error contour in d-axis in Vs; c) Error contour in q-axis in Vs. Motor *B*.

Dynamics of Current-Model Flux Adaptation

The time-plots of the current-model flux adaptation is shown in Fig. 9.16 for the set-points $i^*_d = 5$ A (1.5 p.u.) and $i^*_q = 5$ A (1.5 p.u.). The speed-swing for these reference points is observed to be approximately 1000 rpm although the adaptation, if enabled, is only active for speeds greater than 0.33 p.u., $\omega_r > 500$ rpm.

The adaptation is enabled at $t = 0$ s. For $t < 0$ s, the current-model flux estimates are derived from the self-saturation identification and hence, an error of $\tilde{\lambda}^i_d = 0.04$ Vs and $\tilde{\lambda}^i_q = 0.07$ Vs exists due to the cross-saturation effect. Once the adaptation is enabled at $t > 0$ s, the errors reduce to $\tilde{\lambda}^i_d = 0.015$ Vs (0.014 p.u.) and $\tilde{\lambda}^i_q = 0.002$ Vs (0.002 p.u.). The settling time is observed to be around 0.75 s. A small error in the d-axis remains which is likely due to the iron losses at high speed.

Systematic MMI with Current-Model Flux Adaptation

The dq current plane is systematically explored for the cross-saturation identification. A minimum torque is necessary for speed regulation; as the motor under test is in free-shaft condition and disconnected from load, a minimum of $i^*_{d,min} = |i^*_{q,min}| = 0.5$ A (0.15 p.u.) on either axes is found sufficient for speed regulation. The maximum current is determined by the inverter limits, subject to the voltage constraint at the maximum speed (1000 rpm); a 50% overload in either axes is found achievable, i.e., $i^*_{d,max} = |i^*_{q,max}| = 5$ A (1.5 p.u.).

The control systematically traverses the dq current plane from $\boldsymbol{i}^*_{dq,min}$ to $\boldsymbol{i}^*_{dq,max}$ in steps of 0.5 A, resulting in a 10×10 grid with 100 data-points. For each set of the references, a small time is elapsed to allow the dynamics of the adaptation to settle down to a steady-state before data acquisition. The total elapsed time per

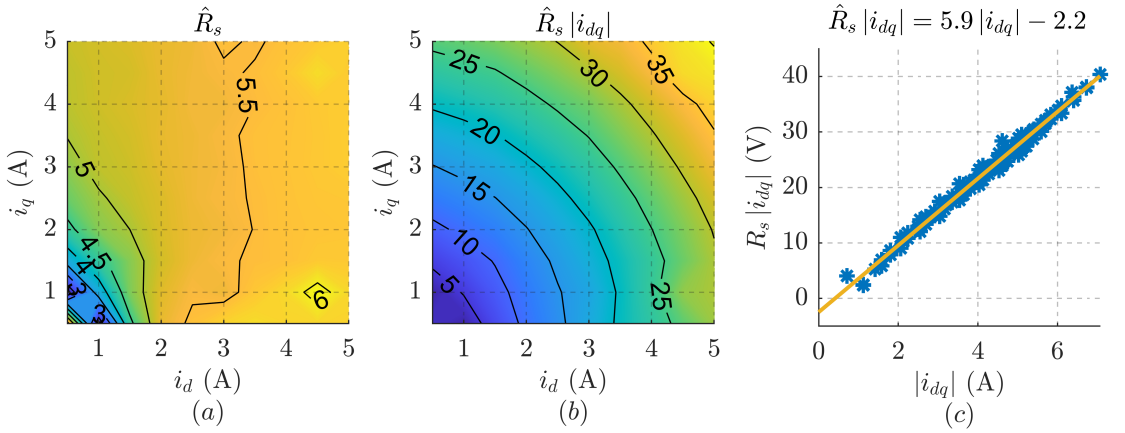

Figure 9.18: Stator resistance adaptation in the experimental MMI: (a) Effective estimate resistance accounting the fundamental dead-time voltage error; (b) Net voltage accounting the resistance drop and the dead-time non-ideal compensation; (c) Characterization of the stator resistance and the inverter dead-time (fundamental component). Motor *B*.

data-point is about 3.5 s and for the complete cross-saturation identification test is around six minutes.

As formerly discussed, the online adaptation is enabled only in the optimal speed-span for speeds greater than 500 rpm. The Fig. 9.17(a) juxtaposes the identified flux curves against the reference curves that show good correlation. The current-model flux error contours of d and q-axes are shown in Fig. 9.17(b) and 9.17(c), respectively. The error increases at high load with the maximum of around 0.015 Vs. The q-axis estimate is inaccurate near the origin due to the sharp saturation of ribs.

Stator Resistance Adaptation

The stator resistance adaption is concurrently active along with the stator flux adaptation of the previous section. The Fig. 9.18(a) shows the contour plot of the effective estimated resistance that inherently accounts for non-idealities in the dead-time compensation as per (3.18). For a better understanding, the net voltage accounting the resistance drop and the dead-time non-ideal compensation is computed in the contour plot Fig. 9.18(b) where a function of the stator current magnitude emerges.

The characterization of the stator resistance and the dead-time error is carried out in Fig. 9.18(c) from which the stator resistance is evaluated to $R_s = 5.9\ \Omega$ and the dead-time error to $\tilde{t}_d = -0.3\ \mu$s. Thus, besides estimation of stator resistance, the proposed adaptation also helps to mitigate non-idealities in the inverter dead-time compensation.

9.4 Summary of the Chapter Contributions

The major contributions of the sensorless standstill commissioning technique of SyR machines [108] in Section 9.2 are:

- The new standstill commissioning technique permits the inspection of a larger dq current area for the identification of the flux-map cross saturation region without a dedicated experimental rig or a mechanical locking.
- This is possible thanks to the increased stability of the new technique by integrating PI and hysteresis controllers to realize a rotor self-locking mechanism that holds the rotor firmly still, as demonstrated experimentally.
- Experimental validation on a 1.1 kW SyR machine test bench shows good correlation with reference flux maps where the estimation error is $< 3\%$ in the d-axis and $< 7\%$ in the q-axis.

The major contributions of self-commissioning technique of SyR machine at free shaft with online adaptation [107] in Section 9.3 are:

1. The new free-shaft MMI improves the state-of-art by using online parameters adaptation within the projection vector mathematical framework first developed for sensorless control.
2. In addition of stator flux adaptation, the stator resistance adaptation is designed to be decoupled and independent.
3. The experimentally identified flux-map shows good correlation with the reference maps and the maximum error is around 0.015 Vs (0.014 p.u.) at high loads, producing negligible error in the interpretation of optimal operation with MTPA and MTPV laws.

Future works aim to explore the applicability of these self-commissioning techniques to motors of different size and PM machines.

Chapter 10

Direct Flux Vector Control (DFVC)

This chapter talks about the new contribution to the direct flux vector control of synchronous machines with a position transducer. The findings of this chapter are under publication [S1-S2].

10.1 Introduction

Synchronous machines, particularly those with interior permanent magnets, possess good flux-weakening capability for extended speed-range [122]–[124]. The large constant-power speed range finds importance in a variety of applications such as traction, industrial applications and home appliances. The optimal control incorporates MTPA and MTPV criteria and abides the current and voltage constraints at all operating points.

The most common current-vector-control (CVC) schemes use PI current regulators in the rotor synchronous dq coordinates. Usually, the combination of torque and operating speed determine the reference current $\boldsymbol{i}^*_{dq}$, fetched from preprocessed LUTs [109], [125], [126]. In other schemes, a voltage feedback regulator is designed to induce flux-weakening at high speeds in [127]–[131]. Alternatively, a gradient descent method is used to track the constant torque locus at high speeds in [132]. As the MTPV control trajectory, if any, is at close proximity to the switch of quadrants in the dq current plane, the CVC is prone to torque reversals even for small errors of the rotor position feedback. This limits the effectiveness of CVC in the very high flux weakening speed range.

Direct torque control (DTC) is a prominent technique adopted for its fast dynamic performance and robustness [133]. The direct of control of stator flux linkage inherently facilitates the flux-weakening operations [134]–[136]. Similar to DTC, the

direct flux vector control (DFVC) has constant switching frequency and straightforward current limitation [110], [137]–[139], thus combining the merits of CVC and DTC. DFVC is implemented in the stator flux oriented reference frame with the stator flux linkage magnitude λ and the quadrature torque producing current i_τ being the controlled variables. The torque producing current loop of DFVC approaches singularity along the MTPV trajectory where i_τ becomes uncontrollable. Hence, an inherent limitation of DFVC is the inability to operate on the MTPV limit [140]. Therefore, a sufficient margin away from MTPV trajectory is necessary for stable operation which restricts exploiting the maximum speed-torque characteristics.

With respect to state-of-art, the dynamic model of DFVC with saturation is developed in Section 10.2. A suitable nonlinear transformation is proposed in Section 10.3 to decouple the torque producing current loop; an online reference generation as opposed to the conventional optimal LUTs is also developed. Section 10.4 presents a new small-signal model based DFVC with load angle as the controlled variable instead of the torque producing loop to alleviate the instability problems.

10.2 Modeling of DFVC Dynamics

Conventionally, two proportional-integral (PI) regulators are used for the control loops. However, the torque producing current loop is nonlinear and therefore, for constant-gain PI stator flux controller, the dynamics becomes a function of the operating point. A nonlinear transformation matrix is proposed in [141] to decouple and achieve uniform bandwidth of the control loops. However, the effect of magnetic saturation on the nonlinear transformation was overlooked. With [141] as the state-of-art, this section aims to model the nonlinear dynamics of DFVC with improved accuracy taking saturation into account.

10.2.1 Stator-Flux-Oriented Control

The stator flux oriented reference frame is denoted by subscript $f\tau$ where the stator flux linkage is aligned along f-axis and τ is the quadrature axis, i.e.,

$$\boldsymbol{\lambda}_{f\tau} = \begin{bmatrix} \lambda \\ 0 \end{bmatrix} = \mathrm{e}^{-\delta \mathbf{J}}\, \boldsymbol{\lambda}_{dq}. \tag{10.1}$$

The Fig. 10.1 illustrates the symbols and notations of the two reference frames.

The voltage equation of a synchronous machine in the stator flux oriented reference frame is expressed as

$$\begin{bmatrix} s\lambda \\ \lambda\, s\delta \end{bmatrix} = \boldsymbol{v}_{f\tau} - R_s\, \boldsymbol{i}_{f\tau} - \omega \mathbf{J}\, \boldsymbol{\lambda}_{f\tau}. \tag{10.2}$$

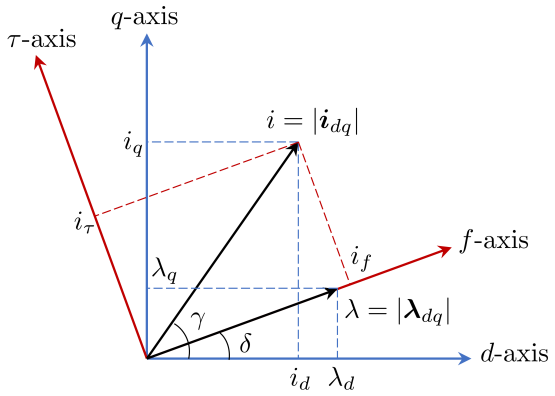

Figure 10.1: Illustration of symbols and notations in dq rotor and $f\tau$ stator flux oriented reference frames.

The electromagnetic torque in the stator flux oriented reference frame simplifies to

$$T = \frac{3p}{2}\,\lambda\, i_\tau \tag{10.3}$$

where the controlled variables stator flux magnitude λ and torque producing current i_τ are evidenced.

10.2.2 Control Dynamics: State-of-Art

This section briefly recounts the state-of-art modeling of control dynamics reported in literature [141][31]. The electromagnetic torque equation (3.2) in dq rotor reference frame can be reformulated using (3.4) as

$$T = \frac{3p}{2}\left(\frac{\lambda^2 \sin(2\delta)}{2}\,\frac{L_d - L_q}{L_d\,L_q} + \lambda\,\cos(\delta)\,\frac{\lambda_m}{L_q}\right). \tag{10.4}$$

Equating (10.3) and (10.4), the torque producing current is

$$i_\tau = \frac{\lambda \sin(2\delta)}{2}\,\frac{L_d - L_q}{L_d\,L_q} + \cos(\delta)\,\frac{\lambda_m}{L_q}. \tag{10.5}$$

Assuming constant apparent inductance in the vicinity of operating point, differentiating (10.5) gives

$$s i_\tau = a' \cdot s\lambda + b' \cdot \lambda\, s\delta \tag{10.6}$$

where the terms a' and b' are

$$\begin{aligned} a' &= \frac{\sin(2\delta)}{2}\,\frac{L_d - L_q}{L_d\,L_q} \\ b' &= \cos(2\delta)\,\frac{L_d - L_q}{L_d\,L_q} - \frac{\sin(\delta)}{L_q}\,\frac{\lambda_m}{\lambda}. \end{aligned} \tag{10.7}$$

The cross-saturation effect is included in the apparent inductances, function of both current components. The shortcoming of this dynamics model is the assumption of constant apparent inductance in the differential equation (10.6). This is inaccurate for machines with nonlinear magnetic model, as addressed in the following section.

10.2.3 Proposed Non-approximated Model

This section aims to build the dynamics model accounting for nonlinearity. The time-derivative of $\boldsymbol{\lambda}_{f\tau}$ in the stator flux reference frame is derived as

$$\begin{aligned} s\boldsymbol{\lambda}_{f\tau} = \begin{bmatrix} s\lambda \\ 0 \end{bmatrix} &= s\left(\mathrm{e}^{-\mathbf{J}\delta}\,\boldsymbol{\lambda}_{dq}\right) \\ &= \mathrm{e}^{-\mathbf{J}\delta}\left[-\mathbf{J}\boldsymbol{\lambda}_{dq}\cdot s\delta + \boldsymbol{L}_{\partial}\cdot s\left(\mathrm{e}^{\mathbf{J}\delta}\,\boldsymbol{i}_{f\tau}\right)\right]. \end{aligned} \tag{10.8}$$

Upon simplification,

$$\begin{bmatrix} s\lambda \\ 0 \end{bmatrix} = \mathrm{e}^{-\mathbf{J}\delta}\left(\boldsymbol{L}_{\partial}\mathbf{J}\,\boldsymbol{i}_{dq} - \mathbf{J}\boldsymbol{\lambda}_{dq}\right)\cdot s\delta + \mathrm{e}^{-\mathbf{J}\delta}\,\boldsymbol{L}_{\partial}\,\mathrm{e}^{\mathbf{J}\delta}\cdot\begin{bmatrix} si_f \\ si_\tau \end{bmatrix}. \tag{10.9}$$

Manipulating (10.9) using the auxiliary-current vector (2.15) and rearranging leads to

$$\begin{bmatrix} si_f \\ si_\tau \end{bmatrix} = \mathrm{e}^{-\mathbf{J}\delta}\,\boldsymbol{L}_{\partial}^{-1}\,\mathrm{e}^{\mathbf{J}\delta}\cdot\begin{bmatrix} s\lambda \\ 0 \end{bmatrix} + \frac{1}{\lambda}\begin{bmatrix} -\boldsymbol{\lambda}_{dq}^{\mathrm{T}}\,\boldsymbol{i}_{dq}^{a} \\ \boldsymbol{\lambda}_{dq}^{\mathrm{T}}\,\mathbf{J}\boldsymbol{i}_{dq}^{a} \end{bmatrix}\cdot s\delta \tag{10.10}$$

It follows from (10.10) that

$$\begin{bmatrix} s\lambda \\ si_\tau \end{bmatrix} = \begin{bmatrix} 1 & 0 \\ a & b \end{bmatrix}\begin{bmatrix} s\lambda \\ \lambda\, s\delta \end{bmatrix} \tag{10.11}$$

where the term a is the cross-coupling gain and the term b is the self-axis gain of the torque producing current loop. They are defined as

$$a = \frac{l_\Delta\,\sin(2\delta) - l_{dq}\,\cos(2\delta)}{l_d l_q - l_{dq}^2} \qquad b = \frac{1}{\lambda^2}\,\boldsymbol{\lambda}_{dq}^{\mathrm{T}}\,\mathbf{J}\boldsymbol{i}_{dq}^{a} \tag{10.12}$$

where $l_\Delta = (l_d - l_q)/2$.

It is worth pointing out that $b = 0$ corresponds to the MTPV law in (2.16). It is of interest to represent the controlled variables (λ, i_τ) in terms of the state variables (λ, δ) in (10.2) as

$$\begin{bmatrix} s\lambda \\ \lambda\, s\delta \end{bmatrix} = \boldsymbol{T}\begin{bmatrix} s\lambda \\ s\, i_\tau \end{bmatrix} \qquad \boldsymbol{T} = \begin{bmatrix} 1 & 0 \\ -a/b & 1/b \end{bmatrix} \tag{10.13}$$

where $\boldsymbol{T}$ is the nonlinear transformation matrix.

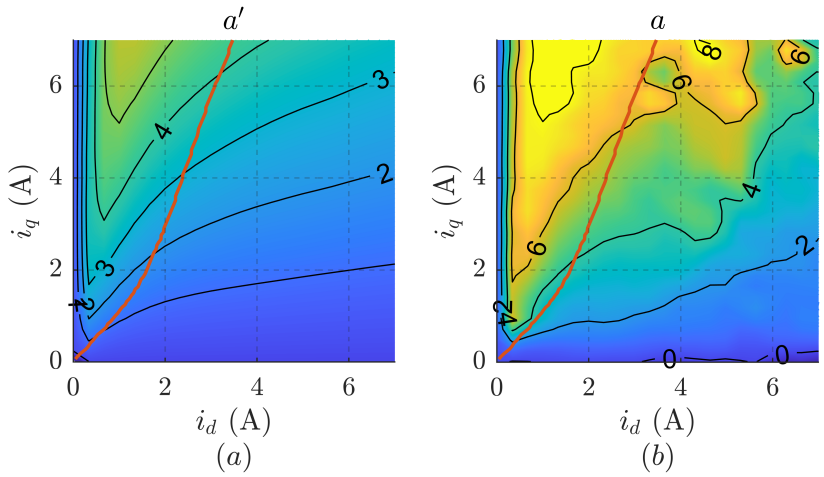

Figure 10.2: Modeling discrepancy in the cross-coupling gain: (a) State-of-the-art a'; (b) Proposed a. Red line is the MTPA trajectory. Motor: A.

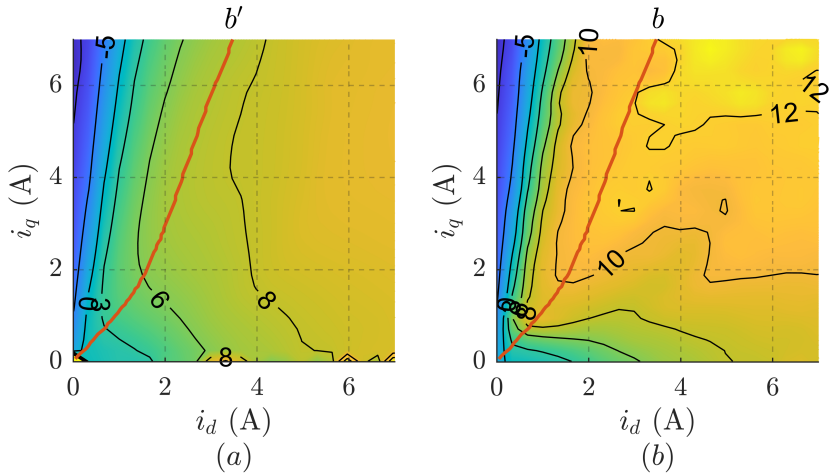

Figure 10.3: Modeling discrepancy in the self-axis gain: (a) State-of-the-art b'; (b) Proposed b. Note that $b = 0$ contour is the MTPV trajectory. Red line is the MTPA trajectory. Motor: A.

The terms a and b are the counterparts of a' and b', respectively. For an objective comparison to highlight the significance of proposed model, the terms a' and a for the SyR motor A are juxtaposed in Fig. 10.2. The state-of-art approach underestimates this term up to a factor of 50%, especially at high load. For the data-point $i_d = 3$ A and $i_q = 6$ A on the MTPA trajectory, the approximated and the non-approximated versions of the cross-coupling gain are $a' = 4$ and $a = 6$.

Likewise, Fig. 10.3 reports the comparison of self-axis gains; the state-of-art approach b' is shown to underestimate b by a factor of approximately 50%.

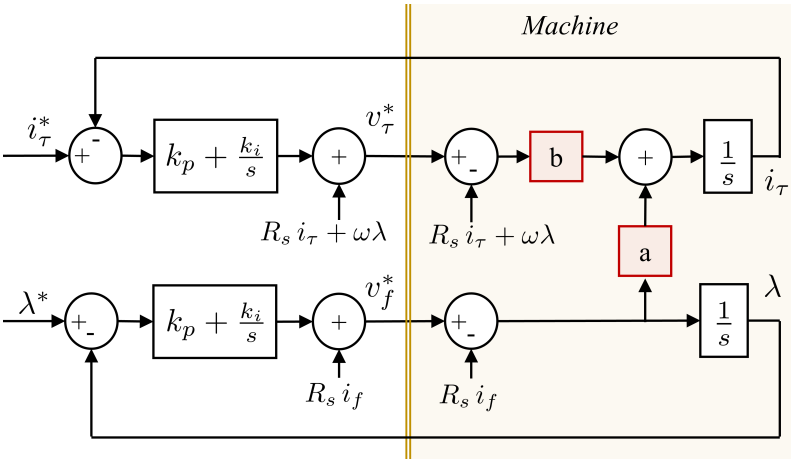

Figure 10.4: Block diagram of the constant-gain PI DFVC control illustrating the closed loop of the linear regulators and the machine model with the cross-coupling gain a and the self-axis gain b in the stator flux oriented reference frame.

10.3 DFVC: Decoupled Model with Adaptive Optimal Reference

This section describes the decoupling of the τ-axis current loop with the nonlinear transformation matrix. The literature on DFVC use offline preprocessed MTPA and MTPV LUTs computed from the flux-map LUTs of the machine under test. Alternatively, MTPA can be tracked online using signal injection [142], [143]. The proposed method tracks the optimal reference in real-time through analytical model of MTPA and MTPV criteria using the auxiliary-flux and auxiliary-current vector concepts, respectively.

10.3.1 Constant-Gain PI DFVC

For a PI stator flux oriented controller, the voltage reference is computed as

$$\boldsymbol{v}_{f\tau}^* = R_s\, \boldsymbol{i}_{f\tau} + \mathbf{J}\, \omega\, \boldsymbol{\lambda}_{f\tau} + \left[\boldsymbol{K}_p + \frac{\boldsymbol{K}_i}{s}\right] \begin{bmatrix} \lambda^* - \hat{\lambda} \\ i_\tau^* - i_\tau \end{bmatrix} \tag{10.14}$$

where the proportional $\boldsymbol{K}_p$ and integral $\boldsymbol{K}_i$ gains are constant diagonal matrices with terms k_{pf}, $k_{p\tau}$ and k_{if}, $k_{i\tau}$, respectively, and $\hat{\lambda}$ is the observed stator flux magnitude.

It can be discerned from Fig. 10.4 that the τ-axis is coupled with f-axis through the cross-coupling gain a. Furthermore, the self-axis term b acts as a loop gain, making dynamics dependent on the operating point. To date, the constant-gain PI regulator implementation underestimated the bandwidth variability associated to the term b (was b'), as well as the weight of the cross-coupling term a (was a').

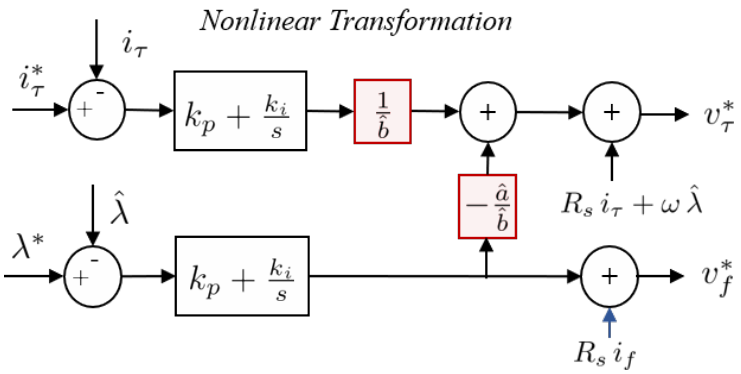

Figure 10.5: Decoupled DFVC with nonlinear transformation matrix for constant bandwidth and uniform dynamic performance at all operating points.

It is worth pointing out that the control approaches singularity at the MTPV limit ($b = 0$) which is an inherent limitation of the DFVC control.

10.3.2 Decoupled DFVC

Using (10.13), the voltage reference with decoupling transformation, shown in Fig. 10.5, is computed as

$$\boldsymbol{v}^*_{f\tau} = R_s\, \boldsymbol{i}_{f\tau} + \mathbf{J}\, \omega\, \boldsymbol{\lambda}_{f\tau} + \hat{\boldsymbol{T}} \left[\boldsymbol{K}_p + \frac{\boldsymbol{K}_i}{s} \right] \begin{bmatrix} \lambda^* - \hat{\lambda} \\ i^*_\tau - i_\tau \end{bmatrix} \tag{10.15}$$

where $\hat{\boldsymbol{T}}$ in (10.13) is computed using the observed stator flux. Likewise, the components of $\hat{\boldsymbol{T}}$ are denoted by $\hat{a}$ and $\hat{b}$.

The controller gains can be calibrated for a constant bandwidth in all operating points with $\boldsymbol{K}_p = k_p\, \mathbf{I}$ and $\boldsymbol{K}_i = k_i\, \mathbf{I}$ where the gains tuned for critical damping at $s = -\Omega$ are

$$k_p = 2\,\Omega \qquad k_i = \Omega^2 \tag{10.16}$$

10.3.3 Conventional LUTs-based Reference Generation

The optimal reference block diagram is shown in Fig. 10.4. The stator flux linkage for the reference torque at MTPA is computed as

$$\lambda_{\text{MTPA}} = \boldsymbol{f}_\lambda\Big(|T^*|\Big) \tag{10.17}$$

where $\boldsymbol{f}_\lambda$ is the MTPA LUT computed offline using flux-map LUTs. The maximum stator flux linkage is a function of operating speed as

$$\lambda_{\max} = k_v\, \frac{v_{dc}}{\sqrt{3}\, \omega} \tag{10.18}$$

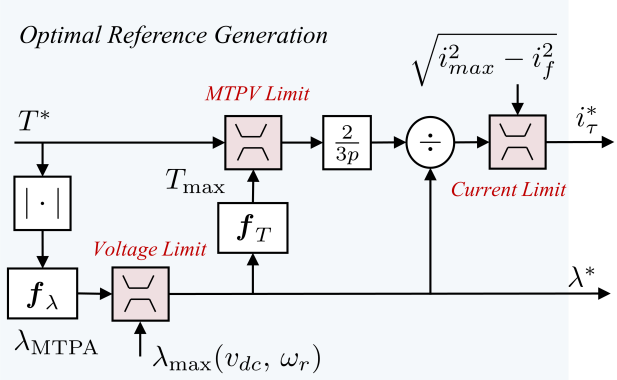

Figure 10.6: Decoupled DFVC with nonlinear transformation matrix for constant bandwidth and uniform dynamic performance at all operating points.

where k_v defines the voltage margin (≈10%). Thus, the stator flux reference is obtained as

$$\lambda^* = \min\Big(\lambda_{\text{MTPA}}, \lambda_{\max}\Big). \tag{10.19}$$

The maximum torque $T_{\max}$ is a function of λ^*, determined by the MTPV limit $\boldsymbol{f}_T$ as

$$T_{\max} = k_T\, \boldsymbol{f}_T\Big(\lambda^*\Big) \tag{10.20}$$

where $\boldsymbol{f}_T$ is a MTPV LUT and k_T defines the torque margin. When the torque limit is in effect, $T_{\max}$ is relayed back to speed controller for anti-windup. Note that DFVC approaches singularity at MTPV limit ($b = 0$); hence, a small margin ($\approx 10\%$) is necessary in implementation.

The aforementioned choice of controlled variables (λ^* & i_τ^*) enables the DFVC to accommodate MTPA and flux-weakening operations with MTPV and current limits in a simple and straightforward fashion. This is a unique advantage over the commonly used CVC.

10.3.4 Adaptive Reference Generation: LUTs-less Online

The block diagram of the proposed online LUT-less adaptive reference generation is shown in Fig. 10.7.

Online MTPA Adaptation

To make the preprocessing of MTPA LUT obsolete, the flux adaptation for real-time MTPA tracking is designed from the analytical expression (2.9) as

$$\lambda_{\text{MTPA}} = \frac{k_A}{s}\left(\hat{\boldsymbol{\lambda}}_{dq}^{a}\right)^{\mathrm{T}} \mathbf{J}\, \boldsymbol{i}_{dq} \tag{10.21}$$

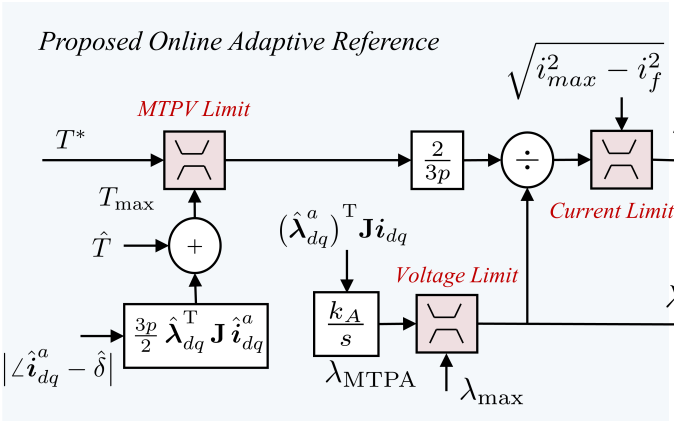

Figure 10.7: Decoupled DFVC with nonlinear transformation matrix for constant bandwidth and uniform dynamic performance at all operating points.

where k_A is an integral gain and the estimated auxiliary-flux vector $\hat{\boldsymbol{\lambda}}_{dq}^a$ is computed from the observed stator flux. The adaptation law ensures that the auxiliary-flux and the current vectors are in phase. Note that the MTPA adaptation must be disabled in flux-weakening region to prevent the saturation of integrator in (10.21).

Online Computed MTPV limit

Akin to the former section, the preprocessed MTPV LUT is avoided by real-time computation of the MTPV limit using the analytical expression (2.16). As DFVC is unstable on the MTPV trajectory, an instantaneous hard constraint to limit torque is necessary.

The maximum permissible torque is computed from the estimated torque and load angle margin relating to the MTPV limit as

$$T_{\max} = k_T \left(|\hat{T}| + \left.\frac{\mathrm{d}T}{\mathrm{d}\delta}\right|_\lambda \cdot \left|\angle \hat{\boldsymbol{i}}_{dq}^a - \hat{\delta}\right| \right) \tag{10.22}$$

where $k_T < 1$ is a margin factor to avoid reaching the MTPV condition and thus instability. It follows from the derivative of torque w.r.t load angle (2.16) that

$$T_{\max} = k_T \left(|\hat{T}| + \frac{3p}{2} \hat{\boldsymbol{\lambda}}_{dq}^{\mathrm{T}} \mathbf{J} \hat{\boldsymbol{i}}_{dq}^a \cdot \left|\angle \hat{\boldsymbol{i}}_{dq}^a - \hat{\delta}\right| \right) \tag{10.23}$$

where $\hat{\boldsymbol{i}}_{dq}^a$ is the estimated auxiliary-current vector. Thus, the proposed adaptive torque limit in (10.23) makes the offline processing for MTPV LUTs obsolete.

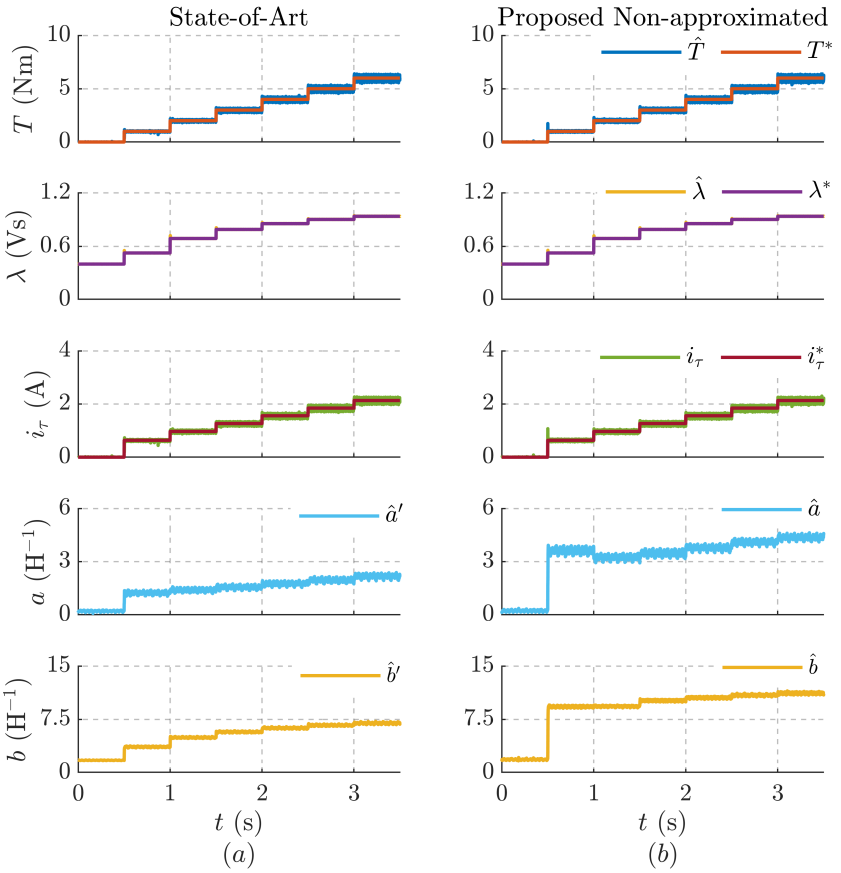

Figure 10.8: Torque control at half rated speed, $\omega_r = 750$ rpm, using decoupled DFVC with the controller poles at $\Omega = 2\pi \cdot 100$ rad/s: (a) State-of-Art ($\hat{a}'$ & $\hat{b}'$); (b) Proposed Non-approximated ($\hat{a}$ & $\hat{b}$). Motor: A.

10.3.5 Experimental Results

The proposed decoupled DFVC is validated experimentally on the SyR motor A at a sampling frequency of 5 kHz. The flux observer gain is $g = 2\,\pi \cdot 5$ rad/s. The speed PI controller is tuned for critical damping at $s = -2\pi \cdot 1$ rad/s. The MTPA adaptive gain is $k_A = 60$.

Significance of Accurate Modeling

To illustrate the significance of the proposed non-approximated dynamic model, the steady-state performance is evaluated at two different bandwidths of the stator flux regulators, $\Omega = 2\pi \cdot 100$ rad/s and $\Omega = 2\pi \cdot 200$ rad/s; the gains are tuned according to (10.16).

Figs. 10.8(a) and 10.8(b) report the torque control response of the decoupled

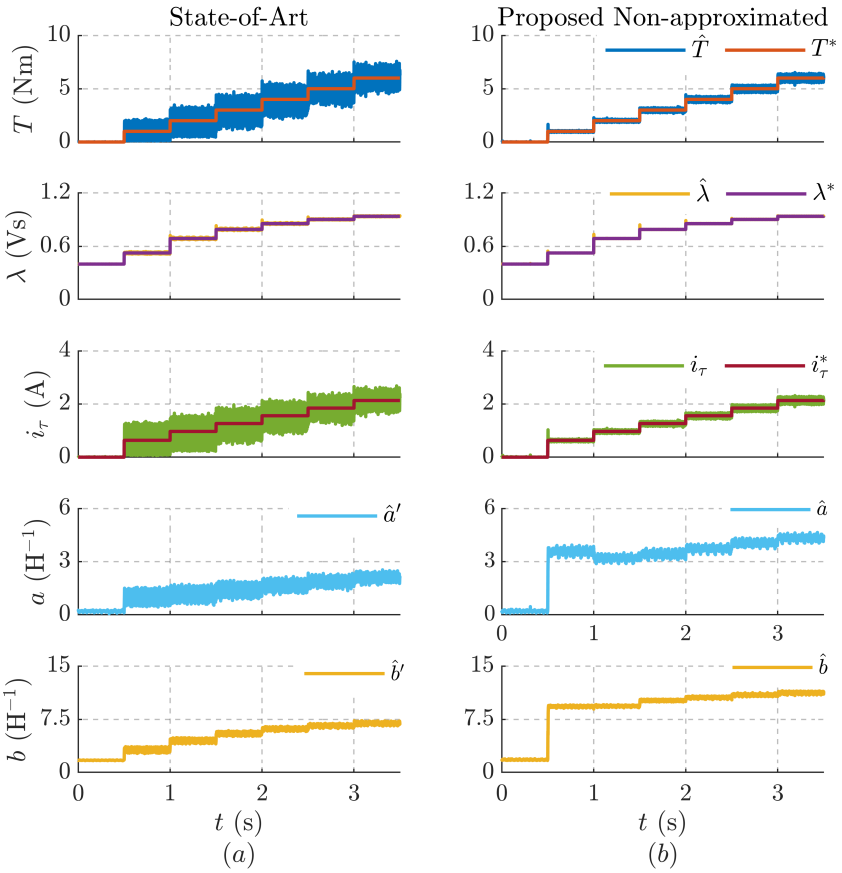

Figure 10.9: Torque control at half rated speed, $\omega_r = 750$ rpm, using decoupled DFVC with the controller poles at $\Omega = 2\pi \cdot 200$ rad/s: (a) State-of-Art ($\hat{a}'$ & $\hat{b}'$); (b) Proposed Non-approximated ($\hat{a}$ & $\hat{b}$). Motor: *A*.

DFVC at $\Omega = 2\pi \cdot 100$ rad/s for the state-of-art and the proposed non-approximated model, respectively, where a similar steady-state response is observed. For a low bandwidth stator flux controller, the shift of poles due to under-compensation of the self-axis gain ($\hat{b}' < \hat{b}$) is not discernible in steady-state performance.

In Fig. 10.9(a) where the stator flux controller poles are designated at higher bandwidth $\Omega = 2\pi \cdot 200$ rad/s, the under-compensation of self-axis gain b for the state-of-art model shifts the poles to even higher frequency, resulting in a persistent high-frequency noise in τ axis. On the other hand, the proposed non-approximated in Fig. 10.9(b) has no high-frequency noise due to the precise compensation of the self-axis and cross-coupling gains. This results in a uniform and stable performance at all operating points. Besides permitting a higher control bandwidth, the proposed (a & b) approach also demonstrates a better robustness towards parameters detuning.

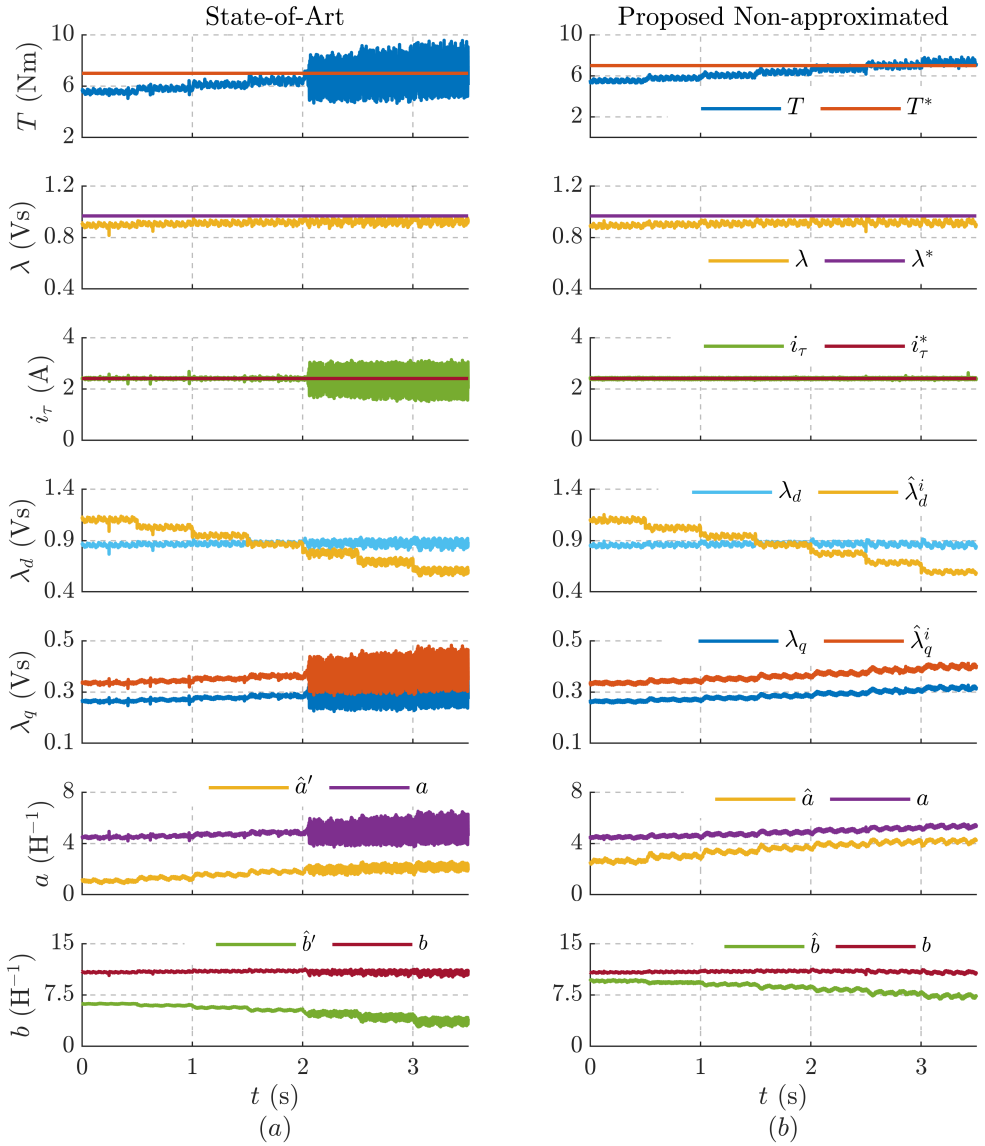

Figure 10.10: Sensitivity analysis to parameter errors at $\omega_r = 300$ rpm (0.2 p.u.) and reference torque $T^* = 7.1$ Nm (1 p.u.): (a) State-of-art model; (b) Proposed non-approximated model. Varying error in d-axis from -30% to +30%, $\hat{\lambda}_d^i = 1.3\,\lambda_d \rightarrow \hat{\lambda}_d^i = 0.7\,\lambda_d$, in steps of 10% increment every 0.5 s; fixed error in q-axis, $\hat{\lambda}_q^i = 1.25\,\lambda_q$. Stator flux controller poles $\Omega = 2\pi \cdot 200$ rad/s. Motor: A.

Sensitivity Analysis to Parameter Error

The sensitivity to parameter errors is evaluated in Fig. 10.10 with a varying error in d-axis from -30% ($\hat{\lambda}_d^i = 1.3\,\lambda_d$) to +30% ($\hat{\lambda}_d^i = 0.7\,\lambda_d$) in steps of 10%

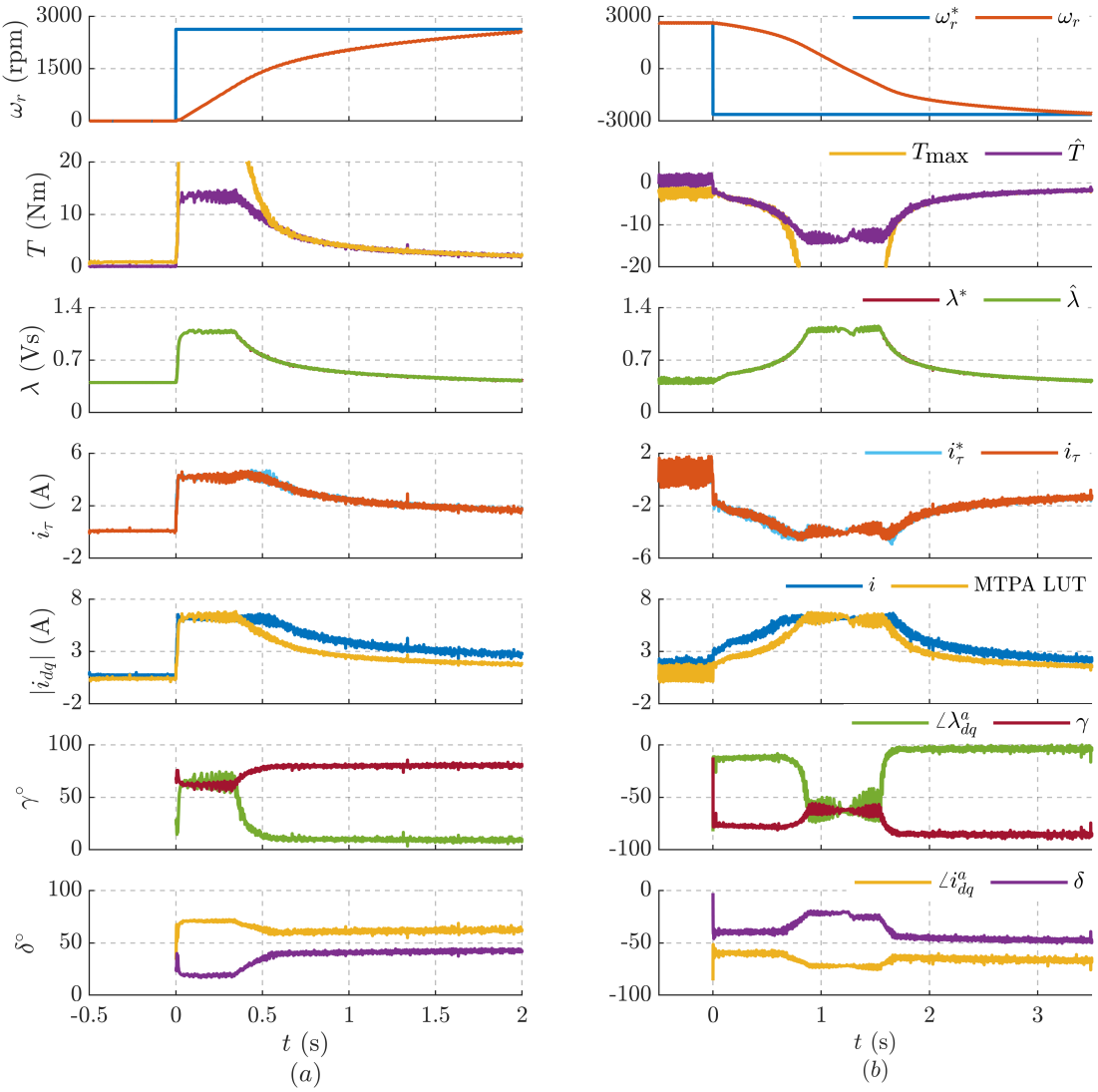

Figure 10.11: Dynamic response of proposed DFVC with online optimal reference: (a) speed step $\omega_r^* = 0 \rightarrow 2625$ (1.75 p.u) at $t = 0$ s; (b) speed step reversal $\omega_r^* = 2625 \rightarrow -2625$ (1.75 p.u) at $t = 0$ s. Motor: *A*.

increment every 0.5 s and a fixed error in q-axis of -25% ($\hat{\lambda}_q^i = 1.25\,\lambda_q$). The results correspond to operation at low speed of 300 rpm (0.2 p.u.) where the impact of the erroneous current-model flux-map on the flux observer is pronounced. The stator flux controller is tuned at $\Omega = 2\pi \cdot 150$ rad/s.

Fig. 10.10(a) shows the performance at rated torque with the state-of-art model; it is observed to suffer from high-frequency noise for the time $t > 2$ s as the self-axis gain is progressively under-compensated. At $t = 3.5$ s, the self-axis gain is under-compensated by a factor of $b/\hat{b}' = 3$. The proposed non-approximated model in

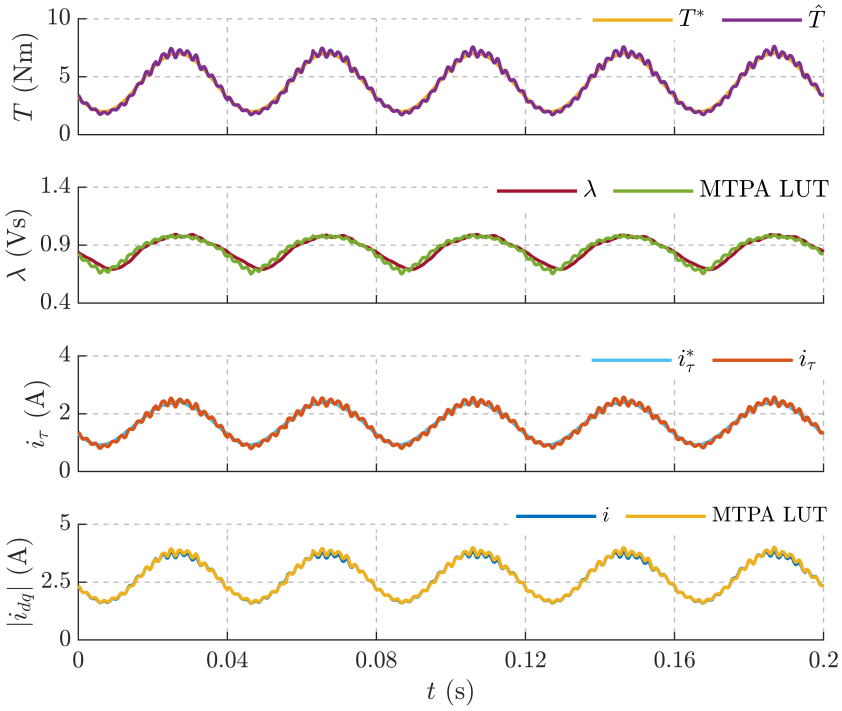

Figure 10.12: Validation of adaptive flux reference for MTPA condition for a sinusoidal torque reference at 25 Hz at $\omega_r = 750$ rpm (0.5 p.u.). Motor: *A*.

Fig. 10.10(b) is observed to be more resilient as the under-compensation of the self-axis gain at $t = 3.5$ s is $b/\hat{b} = 1.5$. The non-ideal compensation of the cross-coupling gain a is observed to be less significant in steady-state conditions.

Speed Control Response

The online optimal reference scheme is validated with a speed control response at no load. In Fig. 10.11(a), a speed step reference $\omega_r^* = 0 \rightarrow 2625$ rpm (1.75 p.u) is commanded at $t = 0$ s.

- *MTPA Operation:* The control operates at the MTPA and the current limit for time $0 < t < 0.35$ s where the auxiliary-flux vector is observed to be in phase with the current vector. The maximum torque is constrained by the current limit, permitting 50% overload ($i_{\max} = 1.5\sqrt{2}\, I_n$). The stator current magnitude is observed to be coincident with the values from MTPA LUT, validating the adaptive reference generation.
- *Constant Current Locus:* Due to the voltage limit, the control is prompted into flux-weakening at $t = 0.35$ s upon which the optimal operating point

traverses the locus of the maximum current limit for the time interval $0.35 < t < 0.55$ s.

- *MTPV Limit:* For time $t > 0.55$ s, the torque is constrained by the MTPV limit $T_{\max}$ computed from (10.23). Note that the load angle and the phase of auxiliary-current vector do not converge due to the margin $k_t = 0.9$ necessary for stability.

The Fig. 10.11(b) shows the dynamic response for a step speed reversal $\omega_r = 2625 \rightarrow -2625$ rpm at $t = 0$ s to validate the performance in braking operation. Similar discussions that of Fig. 10.11(a) applies to Fig. 10.11(b) where the various stages of optimal operations can be identified.

Adaptive Stator Flux for MTPA Tracking

The high dynamic response of the proposed stator flux adaptation for MTPA tracking in (10.21) is validated with a sinusoidal torque reference at 25 Hz in Fig. 10.12. It can be observed that the stator flux and the stator current magnitude are coincident with the values from the MTPA LUT, illustrating the feasibility of dynamic MTPA tracking.

10.4 DFVC: Small-Signal Model

The shortcoming of the former decoupled DFVC model is the inability to operate at MTPV limit. To this end, a new scheme is investigated where the second controlled variable, besides the stator flux linkage magnitude, is the load angle in place of the torque producing current to circumvent the instability and permit operation at the MTPV limit. The optimal flux magnitude and load angle references are calculated using the small-signal approximation of the motor model, without dedicated preprocessed LUTs.

Torque accuracy and the respect of control trajectories (MTPA, MTPV, voltage and current limits) rely on the accurate knowledge of the motor flux-map LUTs in the flux observer. Thus, in the presence of an erroneous flux-map LUTs, the optimal operation and efficiency can be compromised. Hence, the proposed optimal reference is supplemented with an online current-model flux adaptation scheme for accurate stator flux estimation.

The block diagram of the proposed small-signal model based DFVC optimal reference scheme using the stator flux magnitude and the load angle as the controlled variables is shown in Fig. 10.13.

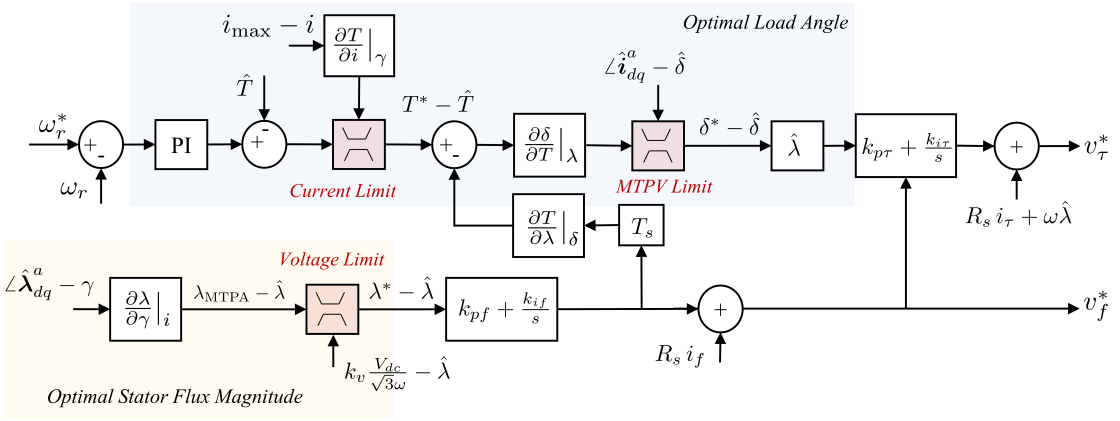

Figure 10.13: Overview of the DFVC scheme with model-based optimal reference generation block highlighting the MTPA flux adaptation with voltage-limited flux reference, current-limited torque reference and MTPV-limited load angle reference. Note that no LUTs are employed.

10.4.1 Optimal Load Angle

For a given stator flux magnitude, the load angle is regulated to track the reference torque. The maximum achievable torque is determined by the current and the MTPV limits.

Reference Torque Tracking

The small-signal torque perturbation is expressed as the functions of the load angle and the stator flux magnitude as

$$\mathrm{d}T = \frac{\partial T}{\partial \delta}\bigg|_{\lambda} \mathrm{d}\delta + \frac{\partial T}{\partial \lambda}\bigg|_{\delta} \mathrm{d}\lambda \tag{10.24}$$

where the derivative of torque w.r.t load angle is derived in the MTPV formulation (2.14). Manipulating (10.24), the load angle reference is computed from the discrepancy between reference and estimated torque as

$$\delta^* = \hat{\delta} + \frac{\mathrm{d}\delta}{\mathrm{d}T}\bigg|_{\lambda} \cdot \left(T^* - \hat{T} - \frac{\partial T}{\partial \lambda}\bigg|_{\delta} \mathrm{d}\lambda \right) \tag{10.25}$$

where the change in flux magnitude is computed from the f-axis reference voltage as $\mathrm{d}\lambda = T_s(v_f^* - R_s\, i_f)$, illustrated in Fig. 10.13. The derivative of torque w.r.t load angle (2.14) reduces to zero along the MTPV trajectory as shown in Fig. 2.1(b). As the expression (10.25) uses the inverse of (2.14), care must to taken for operation in the vicinity of the MTPV limit; in practice, a minimum value ($\approx$1) is imposed on (2.14).

According to (10.25), the change in stator flux magnitude introduces perturbations in torque; it is compensated using the derivative of torque w.r.t stator flux,

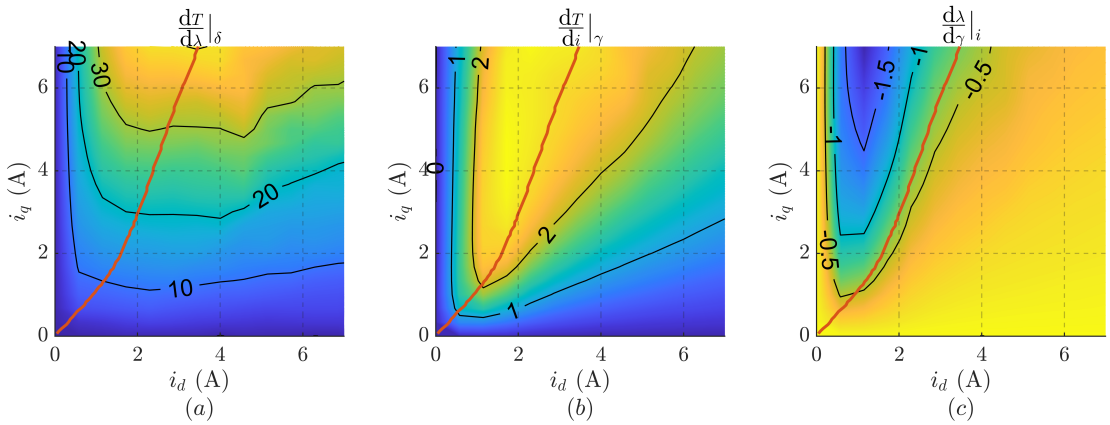

Figure 10.14: (a) Contour of derivative of torque w.r.t stator flux magnitude in A for the reference load angle computation; (b) Contour of derivative of torque w.r.t stator current magnitude in Vs for the adaptive torque limit computation respecting current limitation; (c) Contour of derivative of stator flux magnitude w.r.t current angle in Vs for the MTPA flux adaptation. Motor: *A*.

given by

$$\left.\frac{\partial T}{\partial \lambda}\right|_\delta = \frac{3p}{2}\frac{1}{\lambda}\left(\boldsymbol{L}_\partial^{-1}\boldsymbol{\lambda}_{dq} + \boldsymbol{i}_{dq}\right)^{\mathrm{T}} \mathbf{J}\,\boldsymbol{\lambda}_{dq}. \tag{10.26}$$

Having a dimension of A, the contour of the gain (10.26) is shown in Fig. 10.14(a); it is worth pointing out that this gain maximizes along the MTPV trajectory in the dq flux plane.

Current Limitation

The permissible maximum stator current $i_{\max}$ limits the torque reference that is analytically expressed as an adaptive torque limit as

$$T^i_{max} = \hat{T} + \left.\frac{\partial T}{\partial i}\right|_\gamma \cdot \left(i_{max} - i\right) \tag{10.27}$$

where $\hat{T}$ is the estimated torque from the observed stator flux and measured current. The derivative of torque w.r.t stator current magnitude at a given current angle is expressed as

$$\begin{aligned}\left.\frac{\partial T}{\partial i}\right|_\gamma &= \frac{3p}{2}\left(\frac{\boldsymbol{i}_{dq}^{\mathrm{T}}}{i}\mathbf{J}\,\boldsymbol{\lambda}_{dq} + \boldsymbol{i}_{dq}^{\mathrm{T}}\mathbf{J}\,\boldsymbol{L}_\partial\frac{\boldsymbol{i}_{dq}}{i}\right)\\ &= \frac{3p}{2}\frac{\boldsymbol{i}_{dq}^{\mathrm{T}}}{i}\mathbf{J}\left(\boldsymbol{\lambda}_{dq} + \boldsymbol{L}_\partial\,\boldsymbol{i}_{dq}\right).\end{aligned} \tag{10.28}$$

Fig. 10.14(b) shows the contour of the gain (10.28) for the motor under test; it is worth pointing out that the gain (10.28) is a representative of the torque factor (Nm/A) with dimension Vs, being maximum along the MTPA trajectory. The magnitude of torque reference T^* is limited to T^i_{max}.

MTPV Limitation

The reference load angle δ^* is limited by the phase of auxiliary-current vector to respect the MTPV limitation (see (2.16)) as

$$\delta_{max} = |\angle \hat{\boldsymbol{i}}^a_{dq}| \tag{10.29}$$

where the estimated auxiliary-current vector $\hat{\boldsymbol{i}}^a_{dq}$ is computed from the observed stator flux.

10.4.2 Optimal Stator Flux Magnitude

The optimal stator flux magnitude is designed to comply with the MTPA law for operations under the rated speed and with the voltage limit (flux-weakening) for operations over the rated speed.

MTPA Criterion

Following (2.9), the MTPA condition is found by imposing the phase of the auxiliary-flux vector as the current angle. Thus, the stator flux magnitude for the MTPA condition λ_{MTPA} is calculated as

$$\lambda_{\text{MTPA}} = \hat{\lambda} + \frac{\partial \lambda}{\partial \gamma}\Big|_i \cdot \left(\angle \hat{\boldsymbol{\lambda}}^a_{dq} - \gamma \right) \tag{10.30}$$

where the derivative of stator flux w.r.t current angle at a given current magnitude is a gain, expressed as

$$\frac{\partial \lambda}{\partial \gamma}\Big|_i = \frac{1}{\lambda}\, \hat{\boldsymbol{\lambda}}^{\mathrm{T}}_{dq}\, \boldsymbol{L}_{\partial}\, \mathbf{J}\, \boldsymbol{i}_{dq}. \tag{10.31}$$

Fig. 10.14(c) is the contour plot of the gain (10.31) with dimension Vs for the SyR motor under test. It is observed to vary little along the MTPA trajectory and could be replaced with a constant to decrease computational load.

Voltage Limitation

The stator flux magnitude is limited by the voltage as a function of operating speed. The maximum flux magnitude is given by

$$\lambda_{max} = k_v\, \frac{V_{dc}}{\sqrt{3}\,\omega} \tag{10.32}$$

where k_v is a small voltage margin ($\approx$10%). Finally, the optimal stator flux magnitude reference λ^* is the λ_{MTPA} limited by λ_{max}.

Thus, the optimal references are computed entirely relying on the small-signal model around the operating point without additional LUTs. Note that the small-signal terms (10.31), (10.28) and (10.26) are gains; hence, any reasonable approximation does not affect the steady-state performance.

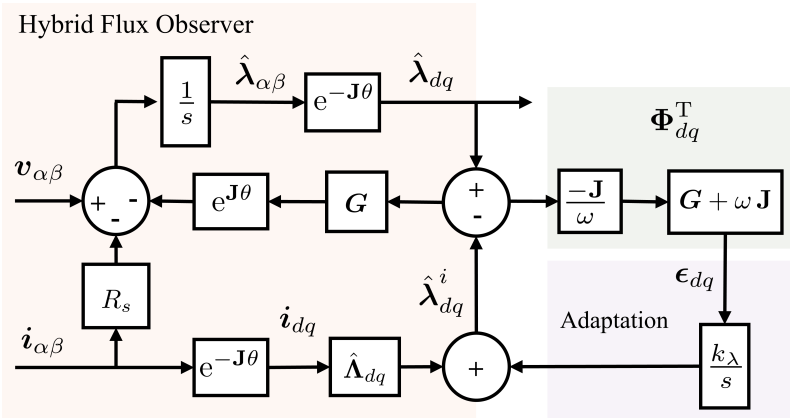

Figure 10.15: Hybrid flux observer with projection vectors approach for current-model flux adaptation.

10.4.3 Stator Flux Oriented Controller

It follows from (10.2) that the voltage reference can be computed with a proportional-integral (PI) regulator and feed-forward terms as

$$\boldsymbol{v}^*_{f\tau} = R_s\,\boldsymbol{i}_{f\tau} + \mathbf{J}\,\omega\,\hat{\boldsymbol{\lambda}}_{f\tau} + \left[\boldsymbol{K}_p + \frac{\boldsymbol{K}_i}{s}\right]\begin{bmatrix}\lambda^* - \hat{\lambda}\\ \hat{\lambda}(\delta^* - \hat{\delta})\end{bmatrix} \tag{10.33}$$

where $\hat{\boldsymbol{\lambda}}_{f\tau}$ is the observed stator flux, the proportional $\boldsymbol{K}_p$ and integral $\boldsymbol{K}_i$ gains are diagonal matrices with terms k_{pf}, $k_{p\tau}$ and k_{if}, $k_{i\tau}$, respectively. The f-axis gains are tuned for critical damping at $s = -\Omega_f$ as

$$k_{pf} = 2\,\Omega_f \qquad k_{if} = \Omega_f^2. \tag{10.34}$$

The τ-axis gains are tuned in a similar fashion for critical damping at $s = -\Omega_\tau$. The torque loop is recommended to be faster than the flux loop to curtain overshoot in torque during transients. Moreover, the PI regulator in the f-axis is limited to one third of the rated voltage. As the controlled variable in the τ-axis is δ, the nonlinear transformation matrix (10.13) is no longer necessary. Provided that the torque reference is translated into corresponding λ and δ references, and that the feed-forward terms are accurate, the controller (10.33) is linear and decoupled.

10.4.4 Current-Model Flux Adaptation

Under erroneous flux-map LUTs, the optimal operation and torque accuracy become compromised. Hence, an online current-model flux adaptation is devised to mitigate the errors in real-time.

The projection vector approach used in sensorless control is here revisited to design parameters adaptation. The presence of encoder is reflected in the error

signal (3.28) with $\tilde{\theta} = 0$. The current-model flux error signal is given by

$$\boldsymbol{\epsilon}_{dq} = \boldsymbol{\Phi}_{dq}^{\mathrm{T}} \, (\hat{\boldsymbol{\lambda}}_{dq} - \hat{\boldsymbol{\lambda}}_{dq}^{\,i}) \tag{10.35}$$

where $\boldsymbol{\Phi}_{dq}^{\mathrm{T}}$ is the 2×2 projection vector matrix, given by

$$\boldsymbol{\Phi}_{dq}{}^{\mathrm{T}} = \frac{-\mathbf{J}}{\omega} \, (\boldsymbol{G} + \mathbf{J} \, \omega). \tag{10.36}$$

It can be shown from (3.28) that the current-model flux error signal $\boldsymbol{\epsilon}_{dq}$ is equal to the parameter error in steady-state condition, i.e., $\boldsymbol{\epsilon}_{dq}|_{s=0} = \tilde{\boldsymbol{\lambda}}_{dq}$. An integral regulator is therefore set up to rectify the flux-map LUTs error, according to the flux estimate error function (9.11)-(10.36) as

$$\hat{\boldsymbol{\lambda}}_{dq}^{\,i} = \hat{\boldsymbol{\Lambda}}_{dq}(\boldsymbol{i}_{dq}) + \frac{k_\lambda}{s} \, \boldsymbol{\epsilon}_{dq} \tag{10.37}$$

where k_λ is integral gain as depicted in Fig. 10.15.

Note that the proposed adaption mitigates error in the flux estimation but error in incremental inductance (3.20) remains; this can be mitigated with high frequency signal injection techniques although not viable at high speeds operation. Dealing with the proposed control scheme, flux adaptation (10.37) guarantees that the steady-state value of controlled torque is accurately tracked, though the effect of parameter detuning during torque transients is unavoidable, as shown later.

10.4.5 Experimental Results

The flux observer gain is $g = 2\,\pi \cdot 10$ rad/s. The speed PI controller is tuned for critical damping at $s = -2\pi \cdot 1.5$ rad/s. The torque loop is recommended to be faster than the flux loop to curtain overshoot in torque during transients. Hence, $\Omega_\tau = 2\pi \cdot 150$ rad/s and $\Omega_f = 2\pi \cdot 30$ rad/s are chosen. The flux adaptation gain is $k_\lambda = 2\pi \cdot 5$ rad/s.

Comparison against State-of-Art DFVC Scheme

The considered state-of-art DFVC scheme is the same adopted in Section 10.3.5, namely, the decoupled control using λ and i_τ proposed in [141]. The merit of the new scheme over the state-of-art is evaluated with a step speed in reference $\omega_r^* = 0 \rightarrow 2625$ rpm (1.75 p.u.) at $t = 0$ s as shown in Fig. 10.16. A 50% overload in current is permitted in this test, i.e., $i_{max} = 1.5 \cdot \sqrt{2}\, I_n$ A.

The two schemes are observed to be nearly identical in the MTPA and the maximum current locus operation until $t = 0.7$ s. For stability reasons, a torque margin of 10% from the MTPV limit is imposed in the state-of-art DFVC; this is reflected in the difference between the phase of auxiliary-current and the load

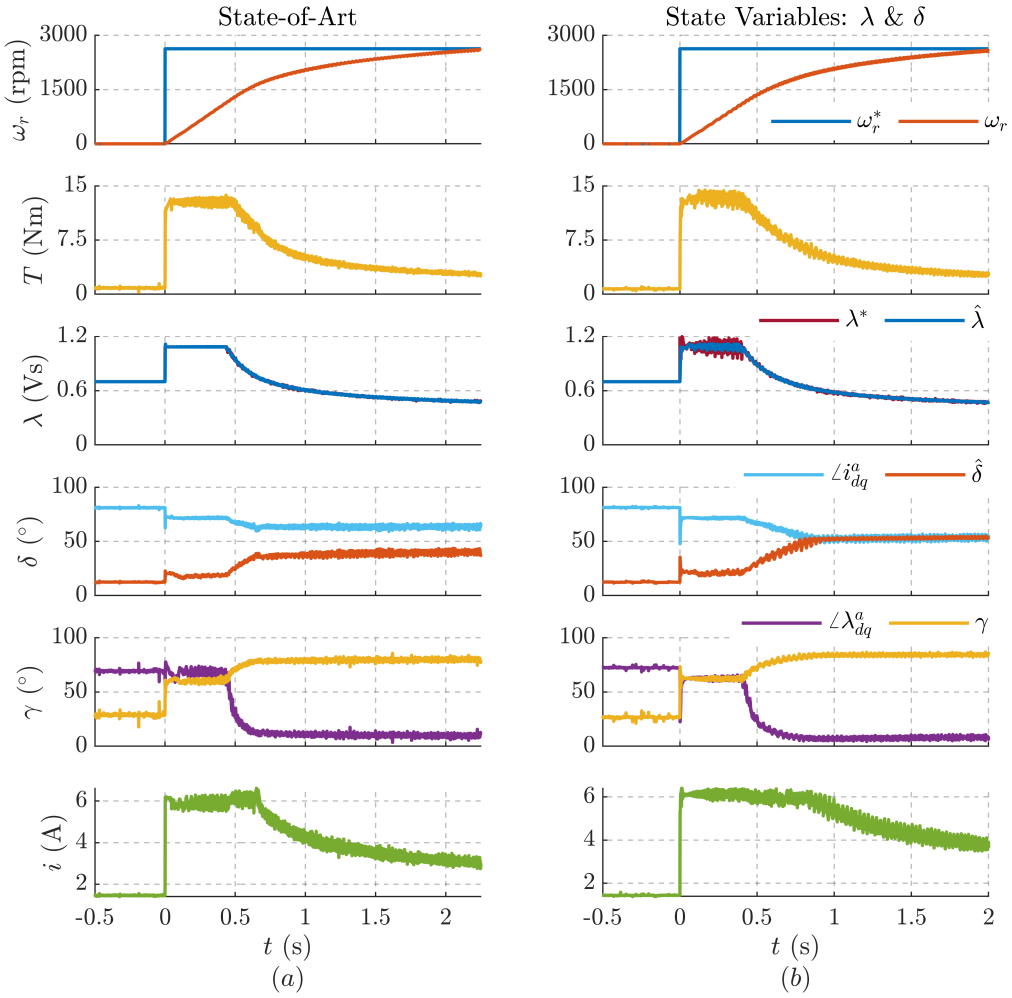

Figure 10.16: Speed control with a step reference $\omega_r = 0 \rightarrow 2625$ rpm (1.75 p.u.) commanded at $t = 0$ s to illustrate the efficacy of the proposed optimal reference scheme. A 50% overload in current is allowed. Motor: *A*.

angle for $t > 0.7$ s in Fig. 10.16(a). The torque saturation below the MTPV limit increases the settling time by about 15% w.r.t to the proposal small-signal scheme in Fig. 10.16(b). The major advantage of the proposed scheme is the alleviation of instability of the state-or-art DFVC at the MTPV limit.

Speed Step Response

The different stages of the result in Fig. 10.16(b) are analyzed in detail at various time segments:

- *(i) MTPA Operation* - $0 < t \leq 0.4$ *s*: In response to the step in speed

reference, the control operates at the maximum torque $\hat{T} = T^i_{max}$ in (10.27), limited by the current i_{max}. The MTPA operation is evidenced by the current angle coincident with the phase of auxiliary-flux vector, i.e., $\gamma = \angle \boldsymbol{\lambda}^a_{dq}$.

- *(ii) Maximum Current Locus* - $0.4 < t \leq 0.85$ *s*: At $t = 0.4$ s marks the onset of the flux-weakening region due to voltage limit at the speed $\omega_r = 1100$ rpm (0.73 p.u). The flux-weakening is enforced prior to the rated speed due to the permitted 50% overload in the current. As the speed increases, the control traverses along the maximum current locus with progressively decreasing torque output.

- *(iii) MTPV Limit* - $t > 0.85$ *s*: The intersection of the maximum current locus with the MTPV trajectory occurs at $t = 0.85$ s. For speeds beyond, the maximum torque is dictated by the MTPV limit; the MTPV operation is evidenced by the load angle coincident with the phase of auxiliary-current vector, i.e., $\delta = \angle \boldsymbol{i}^a_{dq}$. Furthermore, the achievable torque at the speed 1.75 p.u is observed to be about 35% of rated torque ($\approx$ 2.5 Nm). It illustrates the poor capability of SyR machines to operate in the deep flux-weakening regions.

Torque Transient Response

Under the torque control mode with speed regulated by the auxiliary drive, a step reference $T^* = 10$ Nm (1.5 p.u.) is commanded at $t = 0$ s at half the rated speed in Fig. 10.17(a). At the onset, the stator flux and the load angle references that are computed based on the small-signal quantities of the present operating point are initially inaccurate but converge as the operating point moves closer to the final steady-state value.

No torque overshoot is discerned; a small overshoot in load angle is observed which is due to the higher bandwidth of torque loop relative to the flux loop. The settling time of torque is about 1 ms while stator flux to MTPA condition is about 5 ms.

To ascertain steady-state stability at all torque levels, an incremental reference of $T^* = 1 \rightarrow 10$ Nm (1.5 p.u.) in steps of 1 Nm is imposed at 750 rpm (0.5 p.u.) in Fig. 10.17(b). Besides the stator harmonics exhibited by the motor under test, the noise is more related to reference values than the controlled values due to the small-signal based search for the optimal reference.

Dynamic MTPA Tracking

The dynamic MTPA tracking capability of the drive is validated at 750 rpm in Fig. 10.18 with a sinusoidal perturbation in reference torque at 25 Hz. The

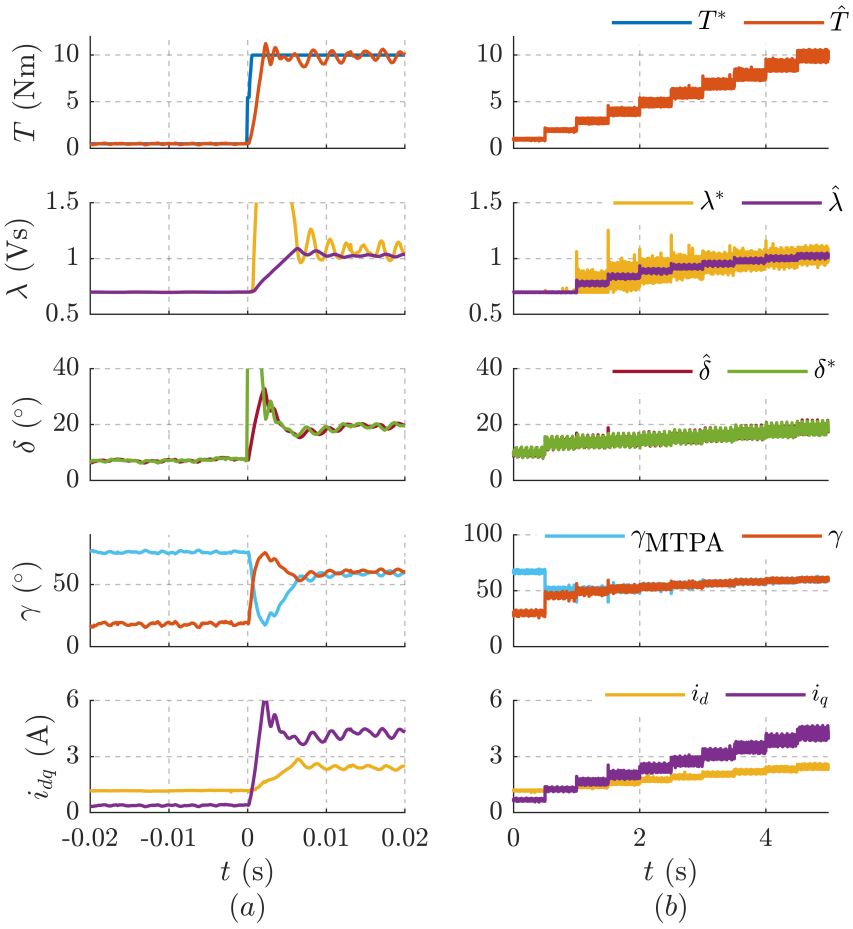

Figure 10.17: (a) Torque control with a step reference $T^* = 10$ Nm (1.5 p.u.) commanded at $t = 0$ s at half 750 rpm (0.5 p.u) to illustrate the transient dynamics; (b) Torque control with a incremental reference $T^* = 1 \rightarrow 10$ Nm (1.5 p.u.) in steps of 1 Nm at 750 rpm (0.5 p.u.) to illustrate steady-state stability. Motor: *A*.

stator flux is adapted seamlessly to traverse along the MTPA trajectory where the current angle is observed to be coincident with the phase of the auxiliary-flux vector, $\gamma = \angle \boldsymbol{\lambda}^a_{dq}$.

Parameter Error Adaptation

The hybrid flux observer reflects parameter errors in the flux-map LUTs, especially in the low speed regions. Hence, the validation of current model flux adaptation is demonstrated at 0.33 p.u. (500 rpm) and at rated torque reference in Fig. 10.19 where the quantity T is the torque estimated with accurate parameters.

Any error in observed flux propagates to the estimated torque $\hat{T}$ and ultimately, results in a discrepancy between the reference and the actual torque. A 25% error

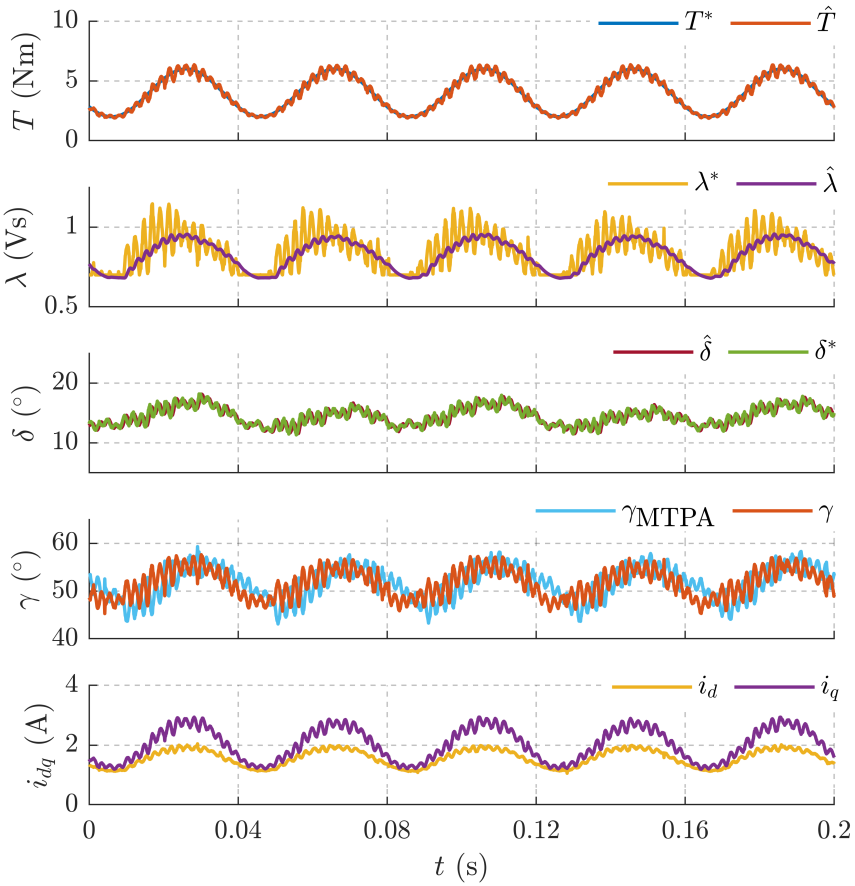

Figure 10.18: Sinusoidal perturbations at 25 Hz imposed on the reference torque at 750 rpm to illustrate the dynamic MTPA tracking capability. Motor: *A*.

in d-axis flux-map LUTs, $\hat{\lambda}_d^i = 0.75\,\lambda_d$, is considered in Fig. 10.19(a). While the reference torque is $T^* = 7.1$ Nm, the actual torque is $T \approx 8$ Nm which is approximately -14% error. The flux adaptation is enabled at $t = 0$ s upon which the observed and current model flux estimates converge and accurate torque control is realized.

Similar test at -25% error in d-axis flux-map LUTs, $\hat{\lambda}_d^i = 1.25\,\lambda_d$, is shown in Fig. 10.19(b) where the error between the reference and actual torque prior to flux adaptation is approximately +18%. Once the flux adaptation is enabled, the errors in stator flux and torque are mitigated. A small inaccuracy in MTPA tracking remains as seen from the discrepancy between the phase of the real auxiliary-flux (computed using accurate flux-maps) and the current angle; this is due to the error in the incremental inductance (3.20) which affects the accuracy of the auxiliary-flux estimation.

The impact of the gain k_λ on the flux adaptation is evaluated at +25% error in d-axis for values $k_\lambda = 2\pi \cdot 15$ rad/s and $k_\lambda = 2\pi \cdot 35$ rad/s in Figs. 10.20(a) and

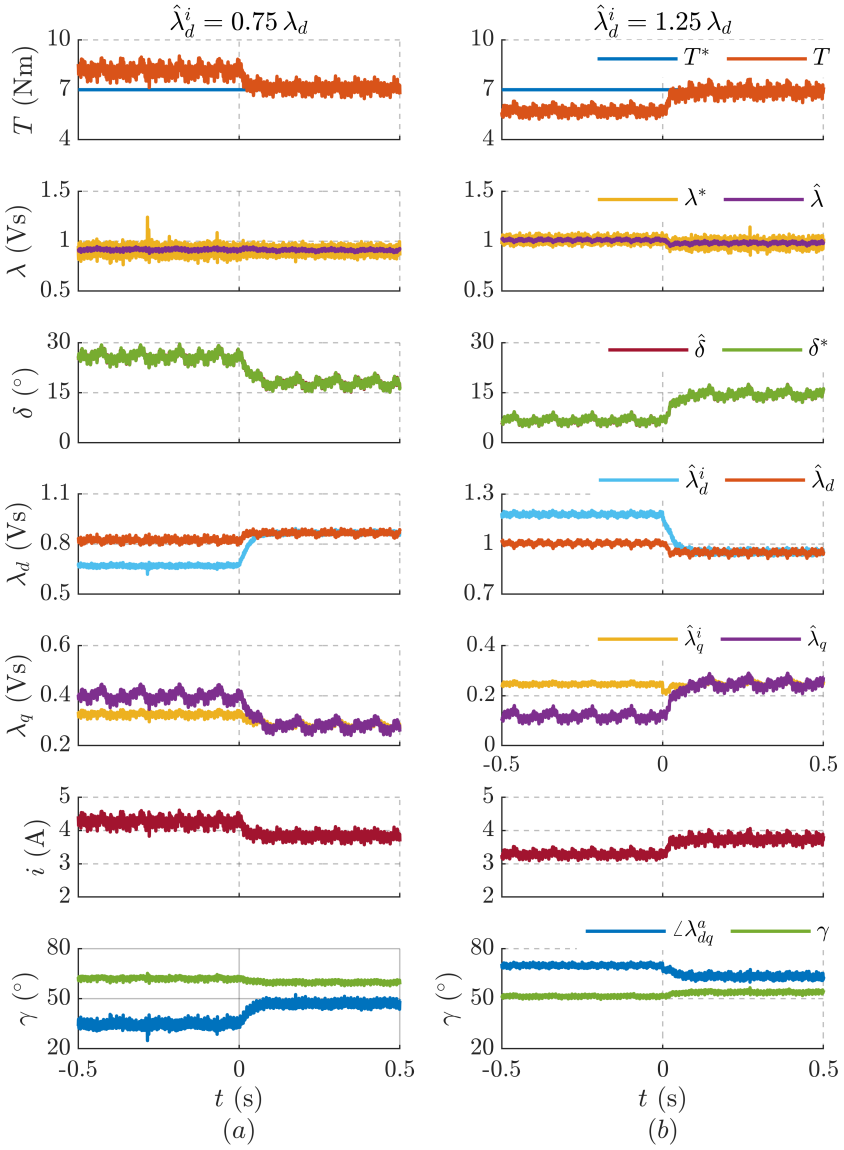

Figure 10.19: Torque control under parameter at 500 rpm (0.33 rpm) and $T^* = 7.1$ Nm (1 p.u.): (a) +25% error in d-axis flux-map LUTs, $\hat{\lambda}_d^i = 0.75\,\lambda_d$; (b) -25% error in d-axis flux-map LUTs, $\hat{\lambda}_d^i = 1.25\,\lambda_d$. The current model flux adaptation is enabled at $t = 0$ s. Motor: A.

10.20(b), respectively. It can be discerned that while 15 Hz shows good dynamics, the adaptation at 35 Hz shows under-damped oscillations. Hence, a very high k_λ is not recommended.

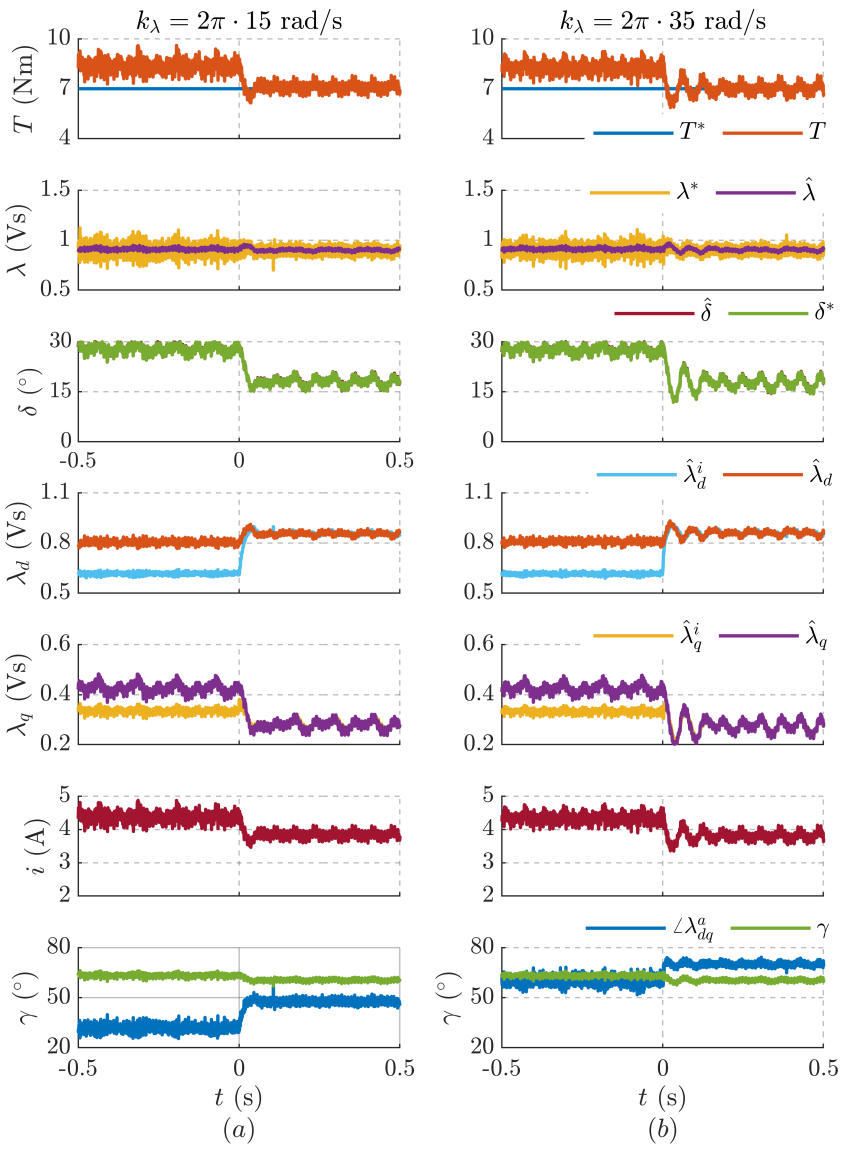

Figure 10.20: Impact of the gain k_λ on the flux adaptation at +25% error in d-axis flux-map LUTs, $\hat{\lambda}_d^i = 0.75\,\lambda_d$, 500 rpm (0.33 rpm) and $T^* = 7.1$ Nm (1 p.u.): (a) $k_\lambda = 2\pi \cdot 15$ rad/s; (b) $k_\lambda = 2\pi \cdot 35$ rad/s. The current-model flux adaptation is enabled at $t = 0$ s. Motor: A.

10.5 Summary of the Chapter Contributions

The major contributions of the improved dynamic model and the decoupled control in Sections 10.2 and 10.3, respectively, are:

1. The dynamic model of DFVC with the coupled f and τ-axes in stator flux oriented reference frame is improved over the state-of-art model with the inclusion of magnetic saturation.

2. A nonlinear transformation matrix is proposed for decoupling in order to have an uniform bandwidth at all operating points. With the proposed non-approximated decoupling, high bandwidth of stator flux controllers can be realized. In addition, improved resilience to parameter detuning is obtained.

3. The online optimal generation is designed for MTPA and MTPV criteria using auxiliary-flux and auxiliary-current vectors, respectively. The proposed adaptation schemes demonstrate the prospect of tracking both laws without the offline preprocessed LUTs. Moreover, the proposed MTPA adaptive tracking is highly dynamic, as the test at sinusoidal torque reference demonstrates.

The major contributions of the small-signal based DFVC scheme in Section 10.4 are:

1. A DFVC control with the stator flux and the load angle as the controlled variables is developed, contrary to the conventional stator flux and the quadrature torque producing current i_τ. This choice of controlled variables circumvents the singularity problem of the i_τ current loop and permits operation on the MTPV trajectory to exploit the maximum torque-speed characteristics of the machine. Besides, the new scheme obtains linear and decoupled torque control.

2. The optimal stator flux and load angle references are computed from the small-signal model around the present operating point. Besides the flux-map LUTs, no additional tables are necessary.

3. Furthermore, a current-model flux adaptation is supplemented to mitigate parameter errors in flux-map LUTs. Unlike the control relying on preprocessed MTPA and MTPV LUTs, an improved optimal operation is feasible under flux adaptation; thus, the proposed scheme becomes more resilient to parameter error. In addition, mitigating error in flux estimation assists in accurate torque control.

The proposed decoupled DFVC, the small-signal based optimal reference scheme and flux adaptation are experimentally validated on a 1.1 kW SyR motor test-bench.

Chapter 11

Conclusions

The work conducted during the course of three years of PhD resulted in some new findings that broadly touches on three topics: *(i)* Sensorless control; *(ii)* Self-Commissioning; *(iii)* Direct flux vector control. A brief summary of the significant findings are summarized below.

11.1 Findings in Sensorless Control

Chapters 3 - 8 discussed the sensorless control techniques whose major findings are summarized below:

- A generalized projection vector-based sensorless control framework was developed in Chapter 3. It is a powerful tool for design and analysis of position observers based on the flux observers, considering the parameter errors. A magnetic model accounting position error was introduced to better represent the nonlinearity in the flux-map under position error.
- Through the common prism of projection-vectors, three flux observer-based sensorless techniques were reviewed to identify regions of instability in Chapter 4. This exposed the shortcomings of flux cross-product, active-flux and fundamental saliency-based position observers.
- Within the projection vector framework, a new auxiliary-flux position observer (AUX), based on the accurate magnetic model accounting for position error (MMAP) was developed in Chapter 5 to circumvent the stability problems. The sensitivity of AUX scheme to parameter errors was evaluated analytically and corroborated experimentally.
- The adaptive projection vector for position error estimation (APP) scheme was developed from the linearized dynamics of flux observer in Chapter 6 and was shown to have a stable operation at all operating points. In addition,

using a low-pass-filtered derivative term, the orthogonal projection vector to APP carries the speed error information that can be retrieved independently to the position error.

- Differing from the AUX scheme, the APP technique is immune from stator resistance variations and voltage error due to non-ideal inverter compensation for operations on the MTPA trajectory.

- Based on the sensitivity analysis, the d-axis current-model flux error has a relatively higher influence over the APP scheme. Using the orthogonal projection vector, the parameter adaptation for the d-axis current-model flux was designed. Alternatively, under accurate flux-map, stator resistance adaptation for good torque and flux estimation was explored.

- A model-based closed-loop torque control scheme was proposed for MTPA tracking in Chapter 7. Based on the orthogonal projection to APP, a new current-model flux adaptation law was designed for accurate torque estimation that is decoupled from the position observer. In turn, accurate torque control under parameter error was realized.

- Following the brief review of high-frequency excitation schemes in Chapter 8, a generalized high-frequency projection vector framework was introduced as a counterpart and analogous to that of the fundamental-wave excitation. This matches elegantly with the high speed sensorless schemes based also on projection vector.

- An injection-less sensorless technique for sustained operation at zero to low speeds region based on finite-control-set model-predictive-control was proposed in Chapter 8. The position information was retrieved from the high-frequency machine response to the discrete voltage vectors. A speed-dependent linear fusion was designed for smooth transition between the two models.

11.2 Findings in Self-Commissioning

Two self-commissioning of SyR machines for magnetic model identification were discussed in Chapter 9. The highlights of the first technique are:

- A sensorless self-commissioning technique with rotor self-locking mechanism at standstill condition was investigated for a stable and systematic identification. The proposed scheme permits wider exploration of dq plane while holding the rotor firmly still.

- The high-frequency current response in d-axis induced by the hysteresis control in q-axis was exploited for cross-saturation identification. Experimental

validation showed good correlation with reference maps with the error <3% of rated flux.

The major findings of the second self-commissioning technique are:

- An alternating acceleration-deceleration test procedure was proposed for self-commissioning at free-shaft and using a position transducer. A low-frequency modulated q-axis current regulates the speed with a constant frequency of speed reversals by alternating positive and negative values of current value i_q under test.
- An online stator flux adaptation was developed using the projection vector framework. Experimental validation showed promising results with an error <1.5% of rated flux.
- In addition, a stator resistance adaptation was also devised to be independent and decoupled from the flux adaptation.

11.3 Findings in Direct Flux Vector Control

Chapter 10 presented the findings in direct flux vector control; the highlights of the proposed decouple DFVC are briefly summarized in the following:

- DFVC is implemented in stator flux oriented reference where the torque producing current loop (τ-axis) is nonlinear. With respect to the state-of-art, an accurate model of the nonlinear dynamics in the stator flux oriented control was developed that accounts for magnetic saturation.
- Accordingly, a nonlinear transformation was designed to decouple the two axes and to have fixed poles for the stator flux oriented controllers. This results in a uniform dynamic performance at all operating points. The proposed decoupling with accurate dynamic model enhances resilience to parameter detuning.
- To refrain from the offline preprocessed optimal reference LUTs, the stator flux adaptation for MTPA and the torque limit for MTPV are evaluated in real-time based on the analytical expressions.

The major findings of the small-signal model-based DFVC are as follows:

- DFVC approaches singularity on the MTPV trajectory as the torque producing current loop becomes uncontrollable. To circumvent this, the load angle is chosen as the second controlled variable in addition to the stator flux magnitude, permitting operation at the MTPV limit. The optimal references are computed from the small-signal model of the machine.

- A current-model flux adaptation was developed to mitigate errors in flux-map. This helps in accurate torque and flux estimation, leading to the optimal operation point.
- With respect to the decoupled control, this method is relatively more noisier due to small-signal nature for optimal search but benefits from stability and uniform bandwidth in all operating points.

11.4 Future Works

Had time been more accommodating, some of the following tasks could have already been in the body of the thesis but are now relegated to future. They are:

- Hitherto, the proposed sensorless control techniques have only been validated on a SyR machines. Experimental validation on a PM machine is the natural progression to demonstrate the generality and bring closure to the proposed schemes. Tests are ongoing on a ferrite-assisted SyR machine for industrial applications.
- Once more, the thesis showed that - different from MTPA and MTPV LUTs - the flux-map LUTs are a hard to eliminate necessity, being the bare footprint of the machine under control. Sensorless techniques with limited or no dependency on flux-map LUTs are appealing and is of interest to investigate for general purpose drives.
- Beyond the control paradigm, the design of machines to be conducive to sensorless control is worthy of exploration.
- The applicability of the self-commissioning techniques to PM motors will be assessed. Besides, it is also of practical interest to implement on an industrial microcontroller in the spirit of plug-and-play systems.

Bibliography

[1] P. Waide and C. U. Brunner, "Energy-Efficiency Policy Opportunities for Electric Motor-Driven Systems", Internationale energy agency, Tech. Rep., 2011.

[2] A. T. D. Almeida, F. J. T. E. Ferreira, and A. Q. Duarte, "Technical and Economical Considerations on Super High-Efficiency Three-Phase Motors", *IEEE Transactions on Industry Applications*, vol. 50, no. 2, pp. 1274–1285, 2014, ISSN: 1939-9367 VO - 50. DOI: 10.1109/TIA.2013.2272548.

[3] S.-M. Lu, "A review of high-efficiency motors: Specification, policy, and technology", *Renewable and Sustainable Energy Reviews*, vol. 59, pp. 1–12, 2016, ISSN: 1364-0321. DOI: https://doi.org/10.1016/j.rser.2015.12.360. [Online]. Available: http://www.sciencedirect.com/science/article/pii/S1364032116000265.

[4] M. van Werkhoven, R. Werle, and C. Brunner, "Policy Guidelines for Motor Driven Units", International Energy Agency, Tech. Rep., 2016.

[5] M. van Werkhoven and A. Advani, "Energy-efficient Electric Motors and Motor Systems: U4E Policy Guide Series", The United Nations Enivronment Programme, Tech. Rep., 2017.

[6] F. J. T. E. Ferreira and A. T. de Almeida, "Reducing Energy Costs in Electric-Motor-Driven Systems: Savings Through Output Power Reduction and Energy Regeneration", *IEEE Industry Applications Magazine*, vol. 24, no. 1, pp. 84–97, 2018, ISSN: 1558-0598 VO - 24. DOI: 10.1109/MIAS.2016.2600685.

[7] "Rotating electrical machines – Part 30-1: Efficiency classes of line operated AC motors (IE code), Ed. 1", IEC 60034-30-1, Tech. Rep., 2014.

[8] A. T. de Almeida, F. J. T. E. Ferreira, and G. Baoming, "Beyond Induction Motors—Technology Trends to Move Up Efficiency", *IEEE Transactions on Industry Applications*, vol. 50, no. 3, pp. 2103–2114, 2014, ISSN: 1939-9367 VO - 50. DOI: 10.1109/TIA.2013.2288425.

[9] H. Kärkkäinen, L. Aarniovuori, M. Niemelä, J. Pyrhönen, and J. Kolehmainen, "Technology comparison of induction motor and synchronous reluctance motor", in *IECON 2017 - 43rd Annual Conference of the IEEE Industrial Electronics Society*, 2017, pp. 2207–2212, ISBN: VO -. DOI: 10.1109/IECON.2017.8216371.

[10] P. Guglielmi, M. Pastorelli, and A. Vagati, "Impact of cross-saturation in sensorless control of transverse-laminated synchronous reluctance motors", *IEEE Transactions on Industrial Electronics*, vol. 53, no. 2, pp. 429–439, 2006, ISSN: 02780046. DOI: 10.1109/TIE.2006.870716.

[11] A. Varatharajan and G. Pellegrino, "Sensorless Synchronous Reluctance Motor Drives: A Sensitivity Analysis Framework and Design to Achieve Stator Resistance Immunity", in *2019 IEEE 10th International Symposium on Sensorless Control for Electrical Drives, SLED 2019*, 2019, pp. 1–6, ISBN: 9781728107660. DOI: 10.1109/SLED.2019.8896282.

[12] A. Varatharajan and G. Pellegrino, "Sensorless Synchronous Reluctance Motor Drives: A Projection Vector Approach for Stator Resistance Immunity and Parameter Adaptation", *IEEE Transactions on Industry Applications*, vol. 56, no. 5, pp. 5003–5012, 2020, ISSN: 1939-9367 VO -. DOI: 10.1109/TIA.2020.3009641.

[13] G. Pellegrino, A. Vagati, B. Boazzo, and P. Guglielmi, "Comparison of Induction and PM Synchronous Motor Drives for EV Application Including Design Examples", *IEEE Transactions on Industry Applications*, vol. 48, no. 6, pp. 2322–2332, 2012, ISSN: 1939-9367 VO - 48. DOI: 10.1109/TIA.2012.2227092.

[14] A. M. El-Refaie and T. M. Jahns, "Comparison of synchronous PM machine types for wide constant-power speed range operation", in *Fourtieth IAS Annual Meeting. Conference Record of the 2005 Industry Applications Conference, 2005.*, vol. 2, 2005, 1015–1022 Vol. 2, ISBN: 0197-2618 VO - 2. DOI: 10.1109/IAS.2005.1518478.

[15] P. Xue and J. Lin, "Discussion on the Rare earth resources and its development potential of Inner Mongolia of China", in *2011 International Conference on Materials for Renewable Energy & Environment*, vol. 1, 2011, pp. 9–12, ISBN: VO - 1. DOI: 10.1109/ICMREE.2011.5930752.

[16] C. Jeong, J. Park, and N. Bianchi, "Alternatives to Replace Rare-Earth Permanent Magnet Motors in Direct Drive Applications", in *2020 International Symposium on Power Electronics, Electrical Drives, Automation and Motion (SPEEDAM)*, 2020, pp. 276–281, ISBN: VO -. DOI: 10.1109/SPEEDAM48782.2020.9161958.

[17] G. Pellegrino, T. Jahns, N. Bianchi, W. Soong, and F. Cupertino, *The Rediscovery of Synchronous Reluctance and Ferrite Permanent Magnet Motors*. Jan. 2016. DOI: 10.1007/978-3-319-32202-5.

[18] A. Vagati, "The synchronous reluctance solution: a new alternative in AC drives", in *Industrial Electronics, Control and Instrumentation, 1994. IECON '94., 20th International Conference on*, vol. 1, 1994, 1–13 vol.1, ISBN: VO - 1. DOI: 10.1109/IECON.1994.397741.

[19] J. K. Kostko, "Polyphase reaction synchronous motors", *Journal of the American Institute of Electrical Engineers*, vol. 42, no. 11, pp. 1162–1168, 1923, ISSN: 2376-7723 VO - 42. DOI: 10.1109/JoAIEE.1923.6591529.

[20] R. E. Doherty and C. A. Nickle, "Synchronous machines I; An extension of Blondel's two-reaction theory", *Journal of the A.I.E.E.*, vol. 45, no. 10, pp. 974–987, 1926, ISSN: 0095-9804 VO - 45. DOI: 10.1109/JAIEE.1926.6537307.

[21] H. A. A. Awan, T. Tuovinen, S. E. Saarakkala, and M. Hinkkanen, "Discrete-time observer design for sensorless synchronous motor drives", *IEEE Transactions on Industry Applications*, vol. 52, no. 5, pp. 3968–3979, 2016, ISSN: 00939994. DOI: 10.1109/TIA.2016.2572105.

[22] E. Armando, R. I. Bojoi, P. Guglielmi, G. Pellegrino, and M. Pastorelli, "Experimental identification of the magnetic model of synchronous machines", *IEEE Transactions on Industry Applications*, vol. 49, no. 5, pp. 2116–2125, 2013, ISSN: 00939994. DOI: 10.1109/TIA.2013.2258876.

[23] A. Varatharajan and G. Pellegrino, "Sensorless Control of Synchronous Reluctance Motor Drives: Improved Modeling and Analysis Beyond Active Flux", in *2019 IEEE International Electric Machines & Drives Conference (IEMDC)*, IEEE, May 2019, pp. 419–426, ISBN: 978-1-5386-9350-6. DOI: 10.1109/IEMDC.2019.8785315.

[24] ——, "Sensorless Synchronous Reluctance Motor Drives: A General Adaptive Projection Vector Approach for Position Estimation", *IEEE Transactions on Industry Applications*, vol. 56, no. 2, pp. 1495–1504, 2020, ISSN: 19399367. DOI: 10.1109/TIA.2019.2961986. [Online]. Available: https://ieeexplore.ieee.org/document/8941242/.

[25] M. Hinkkanen, S. E. Saarakkala, H. A. A. Awan, E. Mölsä, and T. Tuovinen, "Observers for Sensorless Synchronous Motor Drives: Framework for Design and Analysis", *IEEE Transactions on Industry Applications*, vol. 54, no. 6, pp. 6090–6100, 2018, ISSN: 00939994. DOI: 10.1109/TIA.2018.2858753.

[26] T. Tuovinen, H. A. A. Awan, J. Kukkola, S. E. Saarakkala, and M. Hinkkanen, "Permanent-Magnet Flux Adaptation for Sensorless Synchronous Motor Drives", in *2018 IEEE 9th International Symposium on Sensorless Control for Electrical Drives (SLED)*, 2018, pp. 138–143, ISBN: VO -. DOI: 10.1109/SLED.2018.8485899.

[27] I. R. Bojoi, E. Armando, G. Pellegrino, and S. G. Rosu, "Self-commissioning of inverter nonlinear effects in AC drives", *2012 IEEE International Energy Conference and Exhibition, ENERGYCON 2012*, pp. 213–218, 2012. DOI: 10.1109/EnergyCon.2012.6347755.

[28] A. Varatharajan, G. Pellegrino, E. Armando, and M. Hinkkanen, "Sensorless Synchronous Motor Drives: A Review of Flux Observer-based Position Estimation Schemes using the Projection Vector Framework", *IEEE Transactions on Power Electronics*, pp. 1–10, 2021. DOI: 10.1109/TPEL.2020.3048922.

[29] J.-I. Ha, S.-J. Kang, and S. K. Sul, "Position-controlled synchronous reluctance motor without rotational transducer", *IEEE Transactions on Industry Applications*, vol. 35, no. 6, pp. 1393–1398, 1999, ISSN: 0093-9994 VO - 35. DOI: 10.1109/28.806054.

[30] E. Capecchi, P. Guglielmi, M. Pastorelli, and A. Vagati, "Position-sensorless control of the transverse-laminated synchronous reluctance motor", *IEEE Transactions on Industry Applications*, vol. 37, no. 6, pp. 1768–1776, 2001, ISSN: 0093-9994 VO - 37. DOI: 10.1109/28.968190.

[31] A. Yousefi-Talouki, P. Pescetto, and G. Pellegrino, "Sensorless Direct Flux Vector Control of Synchronous Reluctance Motors Including Standstill, MTPA, and Flux Weakening", *IEEE Transactions on Industry Applications*, vol. 53, no. 4, pp. 3598–3608, 2017, ISSN: VO - 53. DOI: 10.1109/TIA.2017.2679689.

[32] T. Hanamoto, H. Ikeda, T. Tsuji, and Y. Tanaka, "Sensorless speed control of synchronous reluctance motor using RTLinux", in *Proceedings of the Power Conversion Conference-Osaka 2002 (Cat. No.02TH8579)*, vol. 2, 2002, 699–703 vol.2, ISBN: VO - 2. DOI: 10.1109/PCC.2002.997604.

[33] I. Boldea, M. C. Paicu, G. Andreescu, and F. Blaabjerg, ""Active Flux" DTFC-SVM Sensorless Control of IPMSM", *IEEE Transactions on Energy Conversion*, vol. 24, no. 2, pp. 314–322, 2009, ISSN: 0885-8969 VO - 24. DOI: 10.1109/TEC.2009.2016137.

[34] S. C. Agarlita, I. Boldea, and F. Blaabjerg, "High-frequency-injection-assisted 'active-flux'-based sensorless vector control of reluctance synchronous motors, with experiments from zero speed", *IEEE Transactions on Industry Applications*, vol. 48, no. 6, pp. 1931–1939, 2012, ISSN: 00939994. DOI: 10.1109/TIA.2012.2226133.

[35] F. J. Barnard, W. T. Villet, and M. J. Kamper, "Hybrid Active-Flux and Arbitrary Injection Position Sensorless Control of Reluctance Synchronous Machines", *IEEE Transactions on Industry Applications*, vol. 51, no. 5, pp. 3899–3906, 2015, ISSN: 00939994. DOI: 10.1109/TIA.2015.2425802.

[36] P. Landsmann, R. Kennel, H. W. De Kock, and M. J. Kamper, "Fundamental saliency based encoderless control for reluctance synchronous machines", *19th International Conference on Electrical Machines, ICEM 2010*, 2010. DOI: 10.1109/ICELMACH.2010.5607906.

[37] S. Morimoto, K. Kawamoto, M. Sanada, and Y. Takeda, "Sensorless control strategy for salient-pole PMSM based on extended EMF in rotating reference frame", *IEEE Transactions on Industry Applications*, vol. 38, no. 4, pp. 1054–1061, 2002, ISSN: 0093-9994 VO - 38. DOI: 10.1109/TIA.2002.800777.

[38] Z. Chen, M. Tomita, S. Doki, and S. Okuma, "An extended electromotive force model for sensorless control of interior permanent-magnet synchronous motors", *IEEE Transactions on Industrial Electronics*, vol. 50, no. 2, pp. 288–295, 2003, ISSN: 0278-0046 VO - 50. DOI: 10.1109/TIE.2003.809391.

[39] Y. Inoue, Y. Kawaguchi, S. Morimoto, and M. Sanada, "Performance Improvement of Sensorless IPMSM Drives in a Low-Speed Region Using Online Parameter Identification", *IEEE Transactions on Industry Applications*, vol. 47, no. 2, pp. 798–804, 2011, ISSN: 0093-9994 VO - 47. DOI: 10.1109/TIA.2010.2101994.

[40] Y. Lee and S. K. Sul, "Model-Based Sensorless Control of an IPMSM With Enhanced Robustness Against Load Disturbances Based on Position and Speed Estimator Using a Speed Error", *IEEE Transactions on Industry Applications*, vol. 54, no. 2, pp. 1448–1459, 2018, ISSN: 0093-9994 VO - 54. DOI: 10.1109/TIA.2017.2777390.

[41] H. Kim, J. Son, and J. Lee, "A High-Speed Sliding-Mode Observer for the Sensorless Speed Control of a PMSM", *IEEE Transactions on Industrial Electronics*, vol. 58, no. 9, pp. 4069–4077, 2011, ISSN: 0278-0046 VO - 58. DOI: 10.1109/TIE.2010.2098357.

[42] S. Bolognani, L. Tubiana, and M. Zigliotto, "EKF-based sensorless IPM synchronous motor drive for flux-weakening applications", *IEEE Transactions on Industry Applications*, vol. 39, no. 3, pp. 768–775, 2003, ISSN: 00939994. DOI: 10.1109/TIA.2003.810666.

[43] D. Liang, J. Li, and R. Qu, "Sensorless Control of Permanent Magnet Synchronous Machine Based on Second-Order Sliding-Mode Observer With Online Resistance Estimation", *IEEE Transactions on Industry Applications*, vol. 53, no. 4, pp. 3672–3682, 2017, ISSN: 0093-9994 VO - 53. DOI: 10.1109/TIA.2017.2690218.

[44] A. Piippo, M. Hinkkanen, and J. Luomi, "Analysis of an Adaptive Observer for Sensorless Control of Interior Permanent Magnet Synchronous Motors", *IEEE Transactions on Industrial Electronics*, vol. 55, no. 2, pp. 570–576, 2008, ISSN: 0278-0046 VO - 55. DOI: 10.1109/TIE.2007.911949.

[45] T. Tuovinen, M. Hinkkanen, L. Harnefors, and J. Luomi, "Comparison of a Reduced-Order Observer and a Full-Order Observer for Sensorless Synchronous Motor Drives", *IEEE Transactions on Industry Applications*, vol. 48, no. 6, pp. 1959–1967, 2012, ISSN: 0093-9994 VO - 48. DOI: 10.1109/TIA.2012.2226200.

[46] M. Hinkkanen, T. Tuovinen, L. Harnefors, and J. Luomi, "A Combined Position and Stator-Resistance Observer for Salient PMSM Drives: Design and Stability Analysis", *IEEE Transactions on Power Electronics*, vol. 27, no. 2, pp. 601–609, 2012, ISSN: 0885-8993 VO - 27. DOI: 10.1109/TPEL.2011.2118232.

[47] A. Varatharajan, G. Pellegrino, and E. Armando, "Sensorless Synchronous Reluctance Motor Drives: Auxiliary Flux based Position Observer", *IEEE Journal of Emerging and Selected Topics in Power Electronics*, pp. 1–1, 2020. DOI: 10.1109/JESTPE.2020.3019568.

[48] A. Varatharajan, G. Pellegrino, E. Armando, and M. Hinkkanen, "Sensorless Control of Synchronous Motor Drives: Accurate Torque Estimation and Control under Parameter Errors", *IEEE Journal of Emerging and Selected Topics in Power Electronics*, pp. 1–10, 2020. DOI: 10.1109/JESTPE.2020.3037792.

[49] J. Yoo, Y. Lee, and S. Sul, "Back-EMF Based Sensorless Control of IPMSM with Enhanced Torque Accuracy Against Parameter Variation", in *2018 IEEE Energy Conversion Congress and Exposition (ECCE)*, 2018, pp. 3463–3469, ISBN: 2329-3721 VO -. DOI: 10.1109/ECCE.2018.8557803.

[50] A. Varatharajan, P. Pescetto, and G. Pellegrino, "Injectionless Sensorless Control of Synchronous Reluctance Machine for Zero to Low Speeds Region", in *2018 IEEE 9th International Symposium on Sensorless Control for Electrical Drives (SLED)*, 2018, pp. 72–77, ISBN: 2166-6733 VO -. DOI: 10.1109/SLED.2018.8486061.

[51] A. Varatharajan, P. Pescetto, and G. Pellegrino, "Sensorless Synchronous Reluctance Motor Drives: A Full-Speed Scheme using Finite-Control-Set MPC in a Projection Vector Framework", *IEEE Transactions on Industry Applications*, vol. 56, no. 4, pp. 3809–3818, 2020, ISSN: 0093-9994. DOI: 10.1109/tia.2020.2990834.

[52] P. D. C. Perera, F. Blaabjerg, J. K. Pedersen, and P. Thogersen, "A sensorless, stable V/f control method for permanent-magnet synchronous motor drives", *IEEE Transactions on Industry Applications*, vol. 39, no. 3, pp. 783–791, 2003, ISSN: 1939-9367 VO - 39. DOI: 10.1109/TIA.2003.810624.

[53] I. Boldea, "Driving control without motion sensors", in *Reluctance Synchronous Machines and Drives*, London, U.K.: Oxford Uni. Press, 1996, ch. 7, ISBN: 9780198593911.

[54] M. Fatu, R. Teodorescu, I. Boldea, G. Andreescu, and F. Blaabjerg, "I-F starting method with smooth transition to EMF based motion-sensorless vector control of PM synchronous motor/generator", in *2008 IEEE Power Electronics Specialists Conference*, 2008, pp. 1481–1487, ISBN: 2377-6617 VO -. DOI: 10.1109/PESC.2008.4592146.

[55] Z. Wang, K. Lu, and F. Blaabjerg, "A Simple Startup Strategy Based on Current Regulation for Back-EMF-Based Sensorless Control of PMSM", *IEEE Transactions on Power Electronics*, vol. 27, no. 8, pp. 3817–3825, 2012, ISSN: 1941-0107 VO - 27. DOI: 10.1109/TPEL.2012.2186464.

[56] S. V. Nair, K. Hatua, N. D. Prasad, and D. K. Reddy, "A Smooth and Stable Open-Loop I-F Control for a Surface Mount PMSM Drive by Ensuring Controlled Starting Torque", in *IECON 2018 - 44th Annual Conference of the IEEE Industrial Electronics Society*, 2018, pp. 355–360, ISBN: 2577-1647 VO -. DOI: 10.1109/IECON.2018.8591856.

[57] F. Briz and M. W. Degner, "Rotor Position Estimation", *IEEE Industrial Electronics Magazine*, vol. 5, no. 2, pp. 24–36, 2011, ISSN: 1932-4529. DOI: 10.1109/MIE.2011.941118.

[58] L. A. S. Ribeiro, M. W. Degner, F. Briz, and R. D. Lorenz, "Comparison of carrier signal voltage and current injection for the estimation of flux angle or rotor position", in *Conference Record of 1998 IEEE Industry Applications Conference. Thirty-Third IAS Annual Meeting (Cat. No.98CH36242)*, vol. 1, 1998, 452–459 vol.1, ISBN: 0197-2618 VO - 1. DOI: 10.1109/IAS.1998.732341.

[59] M. Bugsch, A. Held, and B. Piepenbreier, "Sensorless control of SynRMs using an adaptive 2DoF current control including a comparison of two alternating HF signal injection-based methods", in *IECON 2016 - 42nd Annual Conference of the IEEE Industrial Electronics Society*, 2016, pp. 2910–2916, ISBN: VO -. DOI: 10.1109/IECON.2016.7793793.

[60] M. Corley and R. Lorenz, "Rotor position and velocity estimation for a salient-pole permanent magnet synchronous machine at standstill and high speeds", *Industry Applications, IEEE Transactions on*, vol. 34, no. 4, pp. 784–789, 1998, ISSN: 00939994. DOI: 10.1109/28.703973.

[61] S. Shinnaka, "A new speed-varying ellipse voltage injection method for sensorless drive of permanent-magnet synchronous motors with pole saliency - New PLL method using high-frequency current component multiplied signal", *IEEE Transactions on Industry Applications*, vol. 44, no. 3, pp. 777–788, 2008, ISSN: 00939994. DOI: 10.1109/TIA.2008.921446.

[62] J. I. Ha, K. Ide, T. Sawa, and S. K. Sul, "Sensorless rotor position estimation of an interior permanent-magnet motor from initial states", *IEEE Transactions on Industry Applications*, vol. 39, no. 3, pp. 761–767, 2003, ISSN: 00939994. DOI: 10.1109/TIA.2003.811781.

[63] T. Ohnuma, S. Doki, and S. Okuma, "Extended EMF observer for wide speed range sensorless control of salient-pole synchronous motor drives", in *The XIX International Conference on Electrical Machines - ICEM 2010*, 2010, pp. 1–6, ISBN: VO -. DOI: 10.1109/ICELMACH.2010.5608087.

[64] B. Guan, S. Doki, T. Furukawa, and N. Minoshima, "The position-sensorless control of low voltage high power permanent magnet synchronous motors in zero/low-speed regions", in *IECON 2016 - 42nd Annual Conference of the IEEE Industrial Electronics Society*, 2016, pp. 2963–2968, ISBN: VO -. DOI: 10.1109/IECON.2016.7793736.

[65] P. Guglielmi, A. Yousefi-Talouki, G. Iabichino, and G. Pellegrino, "Sensorless direct torque control for PM-assisted synchronous motors with injection high-frequency signal into stator flux reference frame", in *2017 IEEE International Symposium on Sensorless Control for Electrical Drives (SLED)*, 2017, pp. 139–144, ISBN: 2166-6733 VO -. DOI: 10.1109/SLED.2017.8078444.

[66] J. M. Liu and Z. Q. Zhu, "Novel Sensorless Control Strategy With Injection of High-Frequency Pulsating Carrier Signal Into Stationary Reference Frame", *IEEE Transactions on Industry Applications*, vol. 50, no. 4, pp. 2574–2583, 2014, ISSN: 0093-9994 VO - 50. DOI: 10.1109/TIA.2013.2293000.

[67] T. H. Liu, H. S. Haslim, and S. K. Tseng, *Predictive controller design for a high-frequency injection sensorless synchronous reluctance drive system*, 2017. DOI: 10.1049/iet-epa.2016.0054.

[68] Y. D. Yoon, S. K. Sul, S. Morimoto, and K. Ide, "High-bandwidth sensorless algorithm for AC machines based on square-wave-type voltage injection", *IEEE Transactions on Industry Applications*, vol. 47, no. 3, pp. 1361–1370, 2011, ISSN: 00939994. DOI: 10.1109/TIA.2011.2126552.

[69] A. Yousefi-Talouki, P. Pescetto, G. Pellegrino, and I. Boldea, "Combined Active Flux and High-Frequency Injection Methods for Sensorless Direct-Flux Vector Control of Synchronous Reluctance Machines", *IEEE Transactions on Power Electronics*, vol. 33, no. 3, pp. 2447–2457, 2018, ISSN: 08858993. DOI: 10.1109/TPEL.2017.2697209. [Online]. Available: http://ieeexplore.ieee.org/document/7907329/.

[70] L. Harnefors and H. P. Nee, "A general algorithm for speed and position estimation of AC motors", *IEEE Transactions on Industrial Electronics*, vol. 47, no. 1, pp. 77–83, 2000, ISSN: 02780046. DOI: 10.1109/41.824128.

[71] A. Piippo, M. Hinkkanen, and J. Luomi, "Sensorless control of PMSM drives using a combination of voltage model and HF signal injection", in *Conference Record - IAS Annual Meeting (IEEE Industry Applications Society)*, vol. 2, 2004, pp. 964–970, ISBN: 0780384865. DOI: 10.1109/IAS.2004.1348530.

[72] J.-H. Jang, J.-I. Ha, M. Ohto, K. Ide, and S. K. Sul, "Analysis of permanent-magnet machine for sensorless control based on high-frequency signal injection", *IEEE Transactions on Industry Applications*, vol. 40, no. 6, pp. 1595–1604, 2004, ISSN: 0093-9994 VO - 40. DOI: 10.1109/TIA.2004.836222.

[73] Á. Oliveira, D. Cavaleiro, R. Branco, H. Hadla, and S. Cruz, "An encoderless high-performance synchronous reluctance motor drive", in *2015 IEEE International Conference on Industrial Technology (ICIT)*, 2015, pp. 2048–2055, ISBN: VO -. DOI: 10.1109/ICIT.2015.7125398.

[74] M. Morandin, D. Da Ru, S. Bolognani, and N. Bianchi, "An Integrated Starter-Alternator Based on a Sensorless Synchronous Reluctance Machine Drive", in *2015 IEEE Vehicle Power and Propulsion Conference, VPPC 2015 - Proceedings*, 2015, pp. 1–6, ISBN: 9781467376372. DOI: 10.1109/VPPC.2015.7352896.

[75] Z. Q. Zhu, Y. Li, D. Howe, and C. M. Bingham, "Compensation for Rotor Position Estimation Error due to Cross-Coupling Magnetic Saturation in Signal Injection Based Sensorless Control of PM Brushless AC Motors", in *2007 IEEE International Electric Machines & Drives Conference*, vol. 1, 2007, pp. 208–213, ISBN: VO - 1. DOI: 10.1109/IEMDC.2007.383578.

[76] Y. Li, Z. Q. Zhu, D. Howe, C. M. Bingham, and D. A. Stone, "Improved Rotor-Position Estimation by Signal Injection in Brushless AC Motors, Accounting for Cross-Coupling Magnetic Saturation", *IEEE Transactions on Industry Applications*, vol. 45, no. 5, pp. 1843–1850, 2009, ISSN: 0093-9994 VO - 45. DOI: 10.1109/TIA.2009.2027518.

[77] T. Tuovinen and M. Hinkkanen, "Adaptive Full-Order Observer With High-Frequency Signal Injection for Synchronous Reluctance Motor Drives", *IEEE Journal of Emerging and Selected Topics in Power Electronics*, vol. 2, no. 2, pp. 181–189, 2014, ISSN: 21686785. DOI: 10.1109/JESTPE.2013.2294359.

[78] Y. Kwon, J. Lee, and S. Sul, "Extending Operational Limit of IPMSM in Signal-Injection Sensorless Control by Manipulation of Convergence Point", *IEEE Transactions on Industry Applications*, vol. 55, no. 2, pp. 1574–1586, 2019, ISSN: 1939-9367 VO - 55. DOI: 10.1109/TIA.2018.2882483.

[79] V. Manzolini and S. Bolognani, "On the Rotor Position Self-Sensing Capability of Reluctance and IPM Synchronous Motors", *IEEE Transactions on Industry Applications*, vol. 56, no. 4, pp. 3755–3766, 2020, ISSN: 1939-9367 VO - 56. DOI: 10.1109/TIA.2020.2984406.

[80] J. Lee, Y.-C. Kwon, and S.-K. Sul, "Signal-Injection Sensorless Control with Tilted Current Reference for Heavily-Saturated IPMSMs", *IEEE Transactions on Power Electronics*, vol. 8993, no. c, pp. 1–1, 2020, ISSN: 0885-8993. DOI: 10.1109/tpel.2020.2984029.

[81] P. L. Jansen and R. D. Lorenz, "Transducerless position and velocity estimation in induction and salient AC machines", *IEEE Transactions on Industry Applications*, vol. 31, no. 2, pp. 240–247, 1995, ISSN: 0093-9994 VO - 31. DOI: 10.1109/28.370269.

[82] M. W. Degner and R. D. Lorenz, "Using multiple saliencies for the estimation of flux, position, and velocity in AC machines", *IEEE Transactions on Industry Applications*, vol. 1, no. 5, 760–767 vol.1, 1997, ISSN: 0093-9994 VO - 34. DOI: 10.1109/IAS.1997.643153.

[83] Z. Chen, J. Gao, F. Wang, Z. Ma, Z. Zhang, and R. Kennel, "Sensorless Control for SPMSM With Concentrated Windings Using Multisignal Injection Method", *IEEE Transactions on Industrial Electronics*, vol. 61, no. 12, pp. 6624–6634, 2014, ISSN: 0278-0046 VO - 61. DOI: 10.1109/TIE.2014.2316257.

[84] S. Kondo, M. Tomita, M. Hasegawa, S. Doki, and S. Kato, "Position sensorless control of SynRM at low speeds by estimating high-frequency extended EMF using disturbance observer", in *2015 IEEE 2nd International Future Energy Electronics Conference (IFEEC)*, 2015, pp. 1–5, ISBN: VO -. DOI: 10.1109/IFEEC.2015.7361401.

[85] N. Bianchi, E. Fornasiero, and S. Bolognani, "Effect of stator and rotor saturation on sensorless rotor position detection", in *IEEE Transactions on Industry Applications*, vol. 49, 2013, pp. 1333–1342, ISBN: 2329-3721 VO -. DOI: 10.1109/TIA.2013.2253437.

[86] S. Kim, Y. Kwon, S. K. Sul, J. Park, and S. Kim, "Position sensorless operation of IPMSM with near PWM switching frequency signal injection", in *8th International Conference on Power Electronics - ECCE Asia*, 2011, pp. 1660–1665, ISBN: 2150-6086 VO -. DOI: 10.1109/ICPE.2011.5944422.

[87] S. Kim, J. Im, E. Song, and R. Kim, "A New Rotor Position Estimation Method of IPMSM Using All-Pass Filter on High-Frequency Rotating Voltage Signal Injection", *IEEE Transactions on Industrial Electronics*, vol. 63, no. 10, pp. 6499–6509, 2016, ISSN: 0278-0046 VO - 63. DOI: 10.1109/TIE.2016.2592464.

[88] G. Wang, D. Xiao, G. Zhang, C. Li, X. Zhang, and D. Xu, "Sensorless Control Scheme of IPMSMs Using HF Orthogonal Square-Wave Voltage Injection Into a Stationary Reference Frame", *IEEE Transactions on Power Electronics*, vol. 34, no. 3, pp. 2573–2584, 2019, ISSN: 0885-8993 VO - 34. DOI: 10.1109/TPEL.2018.2844347.

[89] R. Ni, D. Xu, F. Blaabjerg, K. Lu, G. Wang, and G. Zhang, "Square-Wave Voltage Injection Algorithm for PMSM Position Sensorless Control With High Robustness to Voltage Errors", *IEEE Transactions on Power Electronics*, vol. 32, no. 7, pp. 5425–5437, 2017, ISSN: 0885-8993 VO - 32. DOI: 10.1109/TPEL.2016.2606138.

[90] S. Kim, J. I. Ha, and S. K. Sul, "PWM switching frequency signal injection sensorless method in IPMSM", *IEEE Transactions on Industry Applications*, vol. 48, no. 5, pp. 1576–1587, 2012, ISSN: 00939994. DOI: 10.1109/TIA.2012.2210175.

[91] D. Kim, Y. Kwon, S. K. Sul, J. Kim, and R. Yu, "Suppression of Injection Voltage Disturbance for High-Frequency Square-Wave Injection Sensorless Drive With Regulation of Induced High-Frequency Current Ripple", *IEEE Transactions on Industry Applications*, vol. 52, no. 1, pp. 302–312, 2016, ISSN: 0093-9994 VO - 52. DOI: 10.1109/TIA.2015.2478887.

[92] C. E. Hwang, Y. Lee, and S. K. Sul, "Analysis on position estimation error in position-sensorless operation of IPMSM using pulsating square wave signal injection", *IEEE Transactions on Industry Applications*, vol. 55, no. 1, pp. 458–470, 2019, ISSN: 00939994. DOI: 10.1109/TIA.2018.2864117.

[93] M. Bugsch and B. Piepenbreier, "Bandwidth Extending Approach for Sensorless Control of Synchronous Reluctance Machines Using an HF Square-Wave-Shaped-Voltage-Injection-Based Method for Low Speed Range", in *SPEEDAM 2018 - Proceedings: International Symposium on Power Electronics, Electrical Drives, Automation and Motion*, 2018, pp. 1239–1244, ISBN: 9781538649411. DOI: 10.1109/SPEEDAM.2018.8445350.

[94] M. Schroedl and P. Weinmeier, "Sensorless control of reluctance machines at arbitrary operating conditions including standstill", *IEEE Transactions on Power Electronics*, vol. 9, no. 2, pp. 225–231, 1994, ISSN: 0885-8993 VO - 9. DOI: 10.1109/63.286816.

[95] M. Schroedl, "Sensorless control of AC machines at low speed and standstill based on the "INFORM" method", in *IAS '96. Conference Record of the 1996 IEEE Industry Applications Conference Thirty-First IAS Annual Meeting*, vol. 1, 1996, 270–277 vol.1, ISBN: 0197-2618 VO - 1. DOI: 10.1109/IAS.1996.557028.

[96] M. Schroedl and C. Simetzberger, "Sensorless control of PM synchronous motors using a predictive current controller with integrated INFORM and EMF evaluation", in *2008 13th International Power Electronics and Motion Control Conference*, 2008, pp. 2275–2282, ISBN: VO -. DOI: 10.1109/EPEPEMC.2008.4635602.

[97] E. Robeischl and M. Schroedl, "Optimized INFORM measurement sequence for sensorless PM synchronous motor drives with respect to minimum current distortion", *IEEE Transactions on Industry Applications*, vol. 40, no. 2, pp. 591–598, 2004, ISSN: 0093-9994 VO - 40. DOI: 10.1109/TIA.2004.824510.

[98] M. Hofer, M. Nikowitz, and M. Schroedl, "Sensorless control of a reluctance synchronous machine in the whole speed range without voltage pulse injections", in *2017 IEEE 3rd International Future Energy Electronics Conference and ECCE Asia (IFEEC 2017 - ECCE Asia)*, 2017, pp. 1194–1198, ISBN: VO -. DOI: 10.1109/IFEEC.2017.7992211.

[99] M. Mamo, K. Ide, M. Sawamura, and J. Oyama, "Novel rotor position extraction based on carrier frequency component method (CFCM) using two reference frames for IPM drives", *IEEE Transactions on Industrial Electronics*, vol. 52, no. 2, pp. 508–514, 2005, ISSN: 0278-0046 VO - 52. DOI: 10.1109/TIE.2005.844234.

[100] G. Xie, K. Lu, S. K. Dwivedi, J. R. Rosholm, and F. Blaabjerg, "Minimum-Voltage Vector Injection Method for Sensorless Control of PMSM for Low-Speed Operations", *IEEE Transactions on Power Electronics*, vol. 31, no. 2, pp. 1785–1794, 2016, ISSN: 0885-8993 VO - 31. DOI: 10.1109/TPEL.2015.2426200.

[101] Q. Gao, G. M. Asher, M. Sumner, and P. Makys, "Position Estimation of AC Machines Over a Wide Frequency Range Based on Space Vector PWM Excitation", *IEEE Transactions on Industry Applications*, vol. 43, no. 4, pp. 1001–1011, 2007, ISSN: 0093-9994 VO - 43. DOI: 10.1109/TIA.2007.900464.

[102] Q. Gao, G. M. Asher, M. Sumner, and L. Empringham, "Position estimation of a matrix-converter-fed AC PM machine from zero to high speed using PWM excitation", *IEEE Transactions on Industrial Electronics*, vol. 56, no. 6, pp. 2030–2038, 2009, ISSN: 02780046. DOI: 10.1109/TIE.2009.2014903.

[103] R. Morales-Caporal and M. Pacas, "Suppression of saturation effects in a sensorless predictive controlled synchronous reluctance machine based on voltage space phasor injections", *IEEE Transactions on Industrial Electronics*, vol. 58, no. 7, pp. 2809–2817, Jul. 2011, ISSN: 02780046. DOI: 10.1109/TIE.2010.2080652. [Online]. Available: http://ieeexplore.ieee.org/document/5585821/.

[104] S. Nalakath, Y. Sun, M. Preindl, and A. Emadi, "Optimization-Based Position Sensorless Finite Control Set Model Predictive Control for IPMSMs", *IEEE Transactions on Power Electronics*, vol. 33, no. 10, pp. 8672–8682, 2018, ISSN: 0885-8993 VO - 33. DOI: 10.1109/TPEL.2017.2784816.

[105] P. Landsmann, D. Paulus, P. Stolze, and R. Kennel, "Saliency based encoderless Predictive Torque Control without signal injection for a reluctance synchronous machine", in *Proceedings of 14th International Power Electronics and Motion Control Conference EPE-PEMC 2010*, 2010, S1–10–S1–17, ISBN: VO -. DOI: 10.1109/EPEPEMC.2010.5606557.

[106] L. Rovere, A. Formentini, A. Gaeta, P. Zanchetta, and M. Marchesoni, "Sensorless Finite-Control Set Model Predictive Control for IPMSM Drives", *IEEE Transactions on Industrial Electronics*, vol. 63, no. 9, pp. 5921–5931, 2016, ISSN: 02780046. DOI: 10.1109/TIE.2016.2578281.

[107] A. Varatharajan, G. Pellegrino, and E. Armando, "Self-Commissioning of Synchronous Reluctance Motor Drives: Magnetic Model Identification with Online Adaptation", in *2020 IEEE Energy Conversion Congress and Exposition (ECCE)*, 2020, pp. 5353–5360. DOI: 10.1109/ECCE44975.2020.9236307.

[108] A. Varatharajan, P. Pescetto, and G. Pellegrino, "Sensorless Self-Commissioning of Synchronous Reluctance Machine with Rotor Self-Locking Mechanism", in *2019 IEEE Energy Conversion Congress and Exposition (ECCE)*, 2019, pp. 812–817, ISBN: 2329-3721 VO -. DOI: 10.1109/ECCE.2019.8913023.

[109] H. A. A. Awan, Z. Song, S. E. Saarakkala, and M. Hinkkanen, "Optimal Torque Control of Saturated Synchronous Motors: Plug-and-Play Method", *IEEE Transactions on Industry Applications*, p. 1, 2018, ISSN: 0093-9994 VO -. DOI: 10.1109/TIA.2018.2862410.

[110] G. Pellegrino, R. I. Bojoi, and P. Guglielmi, "Unified direct-flux vector control for AC motor drives", *IEEE Transactions on Industry Applications*, vol. 47, no. 5, pp. 2093–2102, 2011, ISSN: 00939994. DOI: 10.1109/TIA.2011.2161532.

[111] IEEE, *IEEE Trial-Use Guide for Testing Permanent Magnet Machines*, 2015. DOI: 10.1109/IEEESTD.2015.7047988.

[112] B. Stumberger, G. Stumberger, D. Dolinar, A. Hamler, and M. Trlep, "Evaluation of saturation and cross-magnetization effects in interior permanent-magnet synchronous motor", *IEEE Transactions on Industry Applications*, vol. 39, no. 5, pp. 1264–1271, 2003, ISSN: 1939-9367 VO - 39. DOI: 10.1109/TIA.2003.816538.

[113] S. A. Odhano, R. Bojoi, Ş. G. Roşu, and A. Tenconi, "Identification of the Magnetic Model of Permanent-Magnet Synchronous Machines Using DC-Biased Low-Frequency AC Signal Injection", *IEEE Transactions on Industry Applications*, vol. 51, no. 4, pp. 3208–3215, 2015, ISSN: 00939994. DOI: 10.1109/TIA.2015.2413383.

[114] L. Peretti, P. Sandulescu, and G. Zanuso, "Self-commissioning of flux linkage curves of synchronous reluctance machines in quasi-standstill condition", *IET Electric Power Applications*, vol. 9, no. 9, pp. 642–651, 2015, ISSN: 1751-8660 VO - 9. DOI: 10.1049/iet-epa.2015.0070.

[115] G. Pellegrino, B. Boazzo, and T. M. Jahns, "Magnetic Model Self-Identification for PM Synchronous Machine Drives", *IEEE Transactions on Industry Applications*, vol. 51, no. 3, pp. 2246–2254, 2015. DOI: 10.1109/TIA.2014.2365627.

[116] K. Liu, J. Feng, S. Guo, L. Xiao, and Z. Zhu, "Identification of Flux Linkage Map of Permanent Magnet Synchronous Machines Under Uncertain Circuit Resistance and Inverter Nonlinearity", *IEEE Transactions on Industrial Informatics*, vol. 14, no. 2, pp. 556–568, 2018, ISSN: 1941-0050 VO - 14. DOI: 10.1109/TII.2017.2722470.

[117] S. A. Odhano, P. Pescetto, H. A. A. Awan, M. Hinkkanen, G. Pellegrino, and R. Bojoi, "Parameter Identification and Self-Commissioning in AC Motor Drives: A Technology Status Review", *IEEE Transactions on Power Electronics*, vol. 34, no. 4, pp. 3603–3614, 2019, ISSN: 08858993. DOI: 10.1109/TPEL.2018.2856589.

[118] N. Bedetti, S. Calligaro, and R. Petrella, "Stand-Still Self-Identification of Flux Characteristics for Synchronous Reluctance Machines Using Novel Saturation Approximating Function and Multiple Linear Regression", *IEEE Transactions on Industry Applications*, vol. 52, no. 4, pp. 3083–3092, 2016. DOI: 10.1109/TIA.2016.2535413.

[119] M. Hinkkanen, P. Pescetto, E. Mölsä, S. E. Saarakkala, G. Pellegrino, and R. Bojoi, "Sensorless Self-Commissioning of Synchronous Reluctance Motors at Standstill Without Rotor Locking", *IEEE Transactions on Industry Applications*, vol. 53, no. 3, pp. 2120–2129, 2017. DOI: 10.1109/TIA.2016.2644624.

[120] P. Pescetto and G. Pellegrino, "Automatic Tuning for Sensorless Commissioning of Synchronous Reluctance Machines Augmented with High-Frequency Voltage Injection", *IEEE Transactions on Industry Applications*, vol. 54, no. 5, pp. 4485–4493, 2018, ISSN: 00939994. DOI: 10.1109/TIA.2018.2839600.

[121] ——, "Standstill determination of PM flux linkage based on minimum saliency tracking for PM-SyR machines", in *2019 IEEE Energy Conversion Congress and Exposition, ECCE 2019*, 2019, pp. 4888–4894, ISBN: 9781728103952. DOI: 10.1109/ECCE.2019.8913077.

[122] T. M. Jahns, "Flux-weakening regime operation of an interior permanent-magnet synchronous motor drive", *IEEE Transactions on Industry Applications*, vol. IA-23, no. 4, pp. 681–689, 1987, ISSN: 19399367. DOI: 10.1109/TIA.1987.4504966.

[123] W. L. Soong and T. J. E. Miller, "Field-weakening performance of brushless synchronous AC motor drives", *IEE Proceedings - Electric Power Applications*, vol. 141, no. 6, pp. 331–340, 1994, ISSN: 1350-2352 VO - 141. DOI: 10.1049/ip-epa:19941470.

[124] N. Bianchi, S. Bolognani, and B. J. Chalmers, "Salient-rotor PM synchronous motors for an extended flux-weakening operation range", *IEEE Transactions on Industry Applications*, vol. 36, no. 4, pp. 1118–1125, 2000, ISSN: 1939-9367 VO - 36. DOI: 10.1109/28.855968.

[125] S. Morimoto, Y. Takeda, T. Hirasa, and K. Taniguchi, "Expansion of Operating Limits for Permanent Magnet Motor by Current Vector Control Considering Inverter Capacity", *IEEE Transactions on Industry Applications*, vol. 26, no. 5, pp. 866–871, 1990, ISSN: 19399367. DOI: 10.1109/28.60058.

[126] B. Cheng and T. R. Tesch, "Torque feedforward control technique for permanent-magnet synchronous motors", *IEEE Transactions on Industrial Electronics*, vol. 57, no. 3, pp. 969–974, 2010, ISSN: 02780046. DOI: 10.1109/TIE.2009.2038951.

[127] J. M. Kim and S. K. Sul, "Speed control of interior permanent magnet synchronous motor drive for the flux weakening operation", *IEEE Transactions on Industry Applications*, vol. 33, no. 1, pp. 43–48, 1997, ISSN: 00939994. DOI: 10.1109/28.567075.

[128] B. H. Bae, N. Patel, S. Schulz, and S. K. Sul, "New Field Weakening Technique for High Saliency Interior Permanent Magnet Motor", *Conference Record - IAS Annual Meeting (IEEE Industry Applications Society)*, vol. 2, no. 2, pp. 898–905, 2003, ISSN: 01972618.

[129] S. Bolognani, S. Calligaro, and R. Petrella, "Adaptive Flux-Weakening Controller for Interior Permanent Magnet Synchronous Motor Drives", *IEEE Journal of Emerging and Selected Topics in Power Electronics*, vol. 2, no. 2, pp. 236–248, 2014, ISSN: 21686785. DOI: 10.1109/JESTPE.2014.2299153.

[130] V. Manzolini, D. D. Rù, and S. Bolognani, "An Effective Flux Weakening Control of a SyRM Drive Including MTPV Operation", *IEEE Transactions on Industry Applications*, vol. 55, no. 3, pp. 2700–2709, 2019, ISSN: 1939-9367 VO - 55. DOI: 10.1109/TIA.2018.2886328.

[131] N. Bedetti, S. Calligaro, and R. Petrella, "Analytical Design and Autotuning of Adaptive Flux-Weakening Voltage Regulation Loop in IPMSM Drives With Accurate Torque Regulation", *IEEE Transactions on Industry Applications*, vol. 56, no. 1, pp. 301–313, 2020, ISSN: 1939-9367 VO - 56. DOI: 10.1109/TIA.2019.2942807.

[132] Y. D. Yoon, W. J. Lee, and S. K. Sul, "New flux weakening control for high saliency interior permanent magnet synchronous machine without any tables", *2007 European Conference on Power Electronics and Applications, EPE*, 2007. DOI: 10.1109/EPE.2007.4417350.

[133] G. S. Buja and M. P. Kazmierkowski, "Direct torque control of PWM inverter-fed AC motors - A survey", *IEEE Transactions on Industrial Electronics*, vol. 51, no. 4, pp. 744–757, 2004, ISSN: 02780046. DOI: 10.1109/TIE.2004.831717.

[134] M. F. Rahman, L. Zhong, and K. W. Lim, "A direct torque-controlled interior permanent magnet synchronous motor drive incorporating field weakening", *IEEE Transactions on Industry Applications*, vol. 34, no. 6, pp. 1246–1253, 1998, ISSN: 00939994. DOI: 10.1109/28.738985.

[135] Y. Inoue, S. Morimoto, and M. Sanada, "Comparative study of PMSM drive systems based on current control and direct torque control in flux-weakening control region", *IEEE Transactions on Industry Applications*, vol. 48, no. 6, pp. 2382–2389, 2012, ISSN: 00939994. DOI: 10.1109/TIA.2012.2227134.

[136] X. Zhang, G. H. B. Foo, D. M. Vilathgamuwa, and D. L. Maskell, "An Improved Robust Field-Weakeaning Algorithm for Direct-Torque-Controlled Synchronous-Reluctance-Motor Drives", *IEEE Transactions on Industrial Electronics*, vol. 62, no. 5, pp. 3255–3264, 2015. DOI: 10.1109/TIE.2014.2386798.

[137] G. Pellegrino, E. Armando, and P. Guglielmi, "Direct flux field-oriented control of IPM drives with variable DC link in the field-weakening region", *IEEE Transactions on Industry Applications*, vol. 45, no. 5, pp. 1619–1627, 2009, ISSN: 00939994. DOI: 10.1109/TIA.2009.2027167.

[138] G. Pellegrino, B. Boazzo, and T. M. Jahns, "Direct flux control of PM synchronous motor drives for traction applications", *2014 IEEE Transportation Electrification Conference and Expo: Components, Systems, and Power Electronics - From Technology to Business and Public Policy, ITEC 2014*, no. c, pp. 1–6, 2014. DOI: 10.1109/ITEC.2014.6861836.

[139] B. Boazzo and G. Pellegrino, "Model-Based Direct Flux Vector Control of Permanent-Magnet Synchronous Motor Drives", *IEEE Transactions on Industry Applications*, vol. 51, no. 4, pp. 3126–3136, Jul. 2015, ISSN: 0093-9994 VO - 51. DOI: 10.1109/TIA.2015.2399619.

[140] G. Pellegrino, E. Armando, and P. Guglielmi, "Direct-flux vector control of IPM motor drives in the maximum torque per voltage speed range", *IEEE Transactions on Industrial Electronics*, vol. 59, no. 10, pp. 3780–3788, 2012, ISSN: 02780046. DOI: 10.1109/TIE.2011.2178212.

[141] H. A. A. Awan, M. Hinkkanen, R. Bojoi, and G. Pellegrino, "Stator-Flux-Oriented Control of Synchronous Motors: A Systematic Design Procedure", *IEEE Transactions on Industry Applications*, vol. 55, no. 5, pp. 4811–4820, 2019, ISSN: VO - 55. DOI: 10.1109/TIA.2019.2927316.

[142] S. Bolognani, R. Petrella, A. Prearo, and L. Sgarbossa, "Automatic Tracking of MTPA Trajectory in IPM Motor Drives Based on AC Current Injection", *IEEE Transactions on Industry Applications*, vol. 47, no. 1, pp. 105–114, 2011, ISSN: 1939-9367 VO - 47. DOI: 10.1109/TIA.2010.2090842.

[143] Y. Lee and S.-K. Sul, "Position-Sensorless MTPA Control of IPMSM Based on High-Frequency Signal Injection", in *2019 10th International Conference on Power Electronics and ECCE Asia (ICPE 2019 - ECCE Asia)*, 2019, pp. 2562–2567, ISBN: VO -.